Karlsruher Institut für Technologie

Development of a highly sensitive hollow waveguide based Raman system for the compositional analysis of the KATRIN tritium source gas

Zur Erlangung des akademischen Grades eines
DOKTORS DER NATURWISSENSCHAFTEN
von der Fakultät für Physik des
Karlsruher Instituts für Technologie

genehmigte
DISSERTATION
von

Diplom-Physikerin

Simone Isabel Rupp

aus Karlsruhe

Referent:	Prof. Dr. Guido Drexlin Institut für Experimentelle Kernphysik Karlsruher Institut für Technologie
Korreferent:	Prof. Dr. Helmut H. Telle Instituto Pluridisciplinar Universidad Complutense de Madrid
Tag der mündlichen Prüfung:	24. Juni 2016

Contents

List of Figures

List of Tables

1. Introduction

The topic of this work is the development of a highly sensitive Raman spectroscopic system for compositional analyses of tritiated gases within the framework of the next-generation neutrino mass experiment KATRIN. This introduction gives a brief overview of the scientific background and the motivation of this thesis.

Neutrinos are the lightest particles in the Standard Model of particle physics and were long considered to be massless, being unable to interact with the Higgs boson [Zub12]. However, the discovery of neutrino oscillations [Sup98a, SNO01, SNO02], recently honored with the Nobel Prize in Physics [Nob15], proved that neutrinos have a non-zero mass [PDG14]. The determination of the absolute neutrino mass scale is of major interest both for particle physics and for astrophysics and cosmology, in the context of such highly topical research issues as the origin of the neutrino mass and the role of neutrinos in the structure formation in the universe [Zub12, Aba11].

A multitude of neutrino mass experiments have been conducted up to today, leading to an upper limit on the neutrino mass of $2\,\mathrm{eV}/c^2$ (95 % C.L.) [PDG14]. The next-generation neutrino mass experiment KATRIN, the Karlsruhe Tritium Neutrino experiment, will be able to discover a neutrino mass of $350\,\mathrm{meV}/c^2$ with 5σ significance, or to improve the current upper limit by one order of magnitude to a value of $200\,\mathrm{meV}/c^2$ (90 % C.L.) in case no neutrino mass signal is detected [KAT05]. KATRIN will measure the neutrino mass in a model-independent way by high-precision spectroscopy of tritium β-decay electrons close to their kinematic endpoint.

The use of a high-luminosity Windowless Gaseous Tritium Source (WGTS) with an activity of the order of 10^{11} Bq will enable low statistical uncertainties to be reached within an effective measurement time of three years. In addition, the source has to fulfill stringent stability and monitoring requirements to minimize systematic uncertainty contributions. One key parameter in this respect is the isotopic composition of the source gas. Due to its influence on the measured β-spectrum, the gas composition has to be continuously monitored with a precision of at least 0.1% [Bab12] and a calibration accuracy of at least 10% [Höt12, Sch13b]. Raman spectroscopy was selected as the method of choice for this purpose: it allows for simultaneous detection of all hydrogen isotopologues – the main gas constituents – in automated, in-line and contact-free measurements. A Laser Raman system (LARA) fulfilling the precision and trueness requirements has been developed over the last years in cooperation between the Karlsruhe Institute of Technology and Swansea University [Sch15b].

This Raman system is integrated into the tritium supply loop in a distance of several meters from the actual source tube due to technical and experimental constraints. There are a range of effects such as wall interactions and gas separation phenomena which can influence the composition of the gas on its way towards the WGTS from the point of measurement. Therefore, it is currently unknown to which extent the gas composition

measured by the LARA system can be assumed to represent the composition in the actual source tube. In order for KATRIN to produce a neutrino mass result with reliable uncertainties, however, this knowledge is indispensable.

Since the gas composition cannot be measured directly in the source tube, the use of an additional Raman measurement system after the WGTS is proposed. A quantitative understanding of changes in the isotopic composition of the source gas can be gained based on the difference between the compositions measured before and after the source, combined with theoretical input by gas dynamical simulations. The position of said Raman system would ideally be as close as possible to the exit from the WGTS, with the caveat that at the same time it has to encounter molecular densities which are within the realm of the Raman system sensitivity. Owing to the low gas pressure of the order of few millibars at the possible measurement location after the source, the standard LARA system for KATRIN cannot be employed, having been developed for gas pressures of about 150 to 200 mbar. As the performance of the current LARA system is considered to be close to the ultimate reachable limit in this type of Raman configuration [Sch11a], the significant sensitivity enhancement required for a measurement at a pressure almost two orders of magnitude lower than previously can only be achieved by alterations to the current implementation.

The principal goal of this work is thus to develop the optical design of a Raman system which is sensitive enough to measure the gas composition after the WGTS. In particular, this task includes the following objectives:

- To provide for a sufficiently high sensitivity, the new system should be able to reach a tritium detection limit of the order of 10^{-3} mbar within acquisition times of a minute or less.
- In addition, the new Raman system has to be fully tritium compatible. For optical systems intended for long-term use in KATRIN, it has to be particularly ensured that the functionality of the measurement system is not substantially impeded by the influence of tritium exposure on optical components. Also, an easy-to-align and robust setup should be envisaged in order to render reliable operation within a tritium glove box environment possible.

The thesis is structured as follows: first, an introduction into neutrino physics and the KATRIN experiment is given in chapter 2. In this context, the motivation and objectives of this work are further detailed towards the end of the chapter. Chapter 3 provides the theoretical background of Raman spectroscopy, before appropriate sensitivity enhancement methods are discussed. Afterwards, the setup and test of a signal-enhanced prototype system for tritium gas analysis is described in chapter 4, and necessary steps towards a fully tritium compatible, highly sensitive Raman system are identified based on the results obtained and observations made. In chapter 5, a test of the durability of reflective surfaces under tritium exposure as well as further improvements of the suitability of such a system for operation in tritium environments are presented. Chapter 6 describes investigations concerning the optimization of the optical design and measurement parameters in order to maximize the sensitivity of the new Raman system. The results achieved with the optimized system are presented in chapter 7. Finally, a summary of the work and an outlook are given in chapter 8.

2. The neutrino mass experiment KATRIN

This chapter provides an introduction into the topic of neutrinos and neutrino mass experiments, with a focus on the next-generation neutrino mass experiment KATRIN. The latter is targeted to measure the neutrino mass with a sensitivity of $200\,\mathrm{meV}/c^2$, improving the current upper limit by one order of magnitude. Based on this introduction, the motivation and objectives of the present work are explained.

The chapter is structured as follows: first, an overview of neutrino physics is given in section 2.1. Afterwards, the relevance of neutrino masses in particle physics and cosmology is addressed in section 2.2, before possible methods to determine the neutrino mass experimentally are discussed in section 2.3. In section 2.4, the physical principles of tritium β-decay experiments are described, and current limits on the neutrino mass achieved by such experiments are presented. Finally, the aim and experimental setup of the KATRIN experiment is explained in section 2.5. The focus in this section is on systematic effects related to the Windowless Gaseous Tritium Source of the experiment, leading to the motivation and objectives of this work.

2.1. Introduction to neutrino physics

The following subsections give a short introduction into the history of neutrino physics, their properties and the phenomenon of neutrino oscillations.

2.1.1. Discovery and properties of neutrinos

At the beginning of the last century, the β-decay was assumed to be a two-body decay just like the α- and γ-decay. The discovery of a continuous instead of a discrete electron spectrum in the β-decays of ^{214}Pb and ^{214}Bi by Chadwick in 1914 [Cha14] therefore seemed to violate the law of conservation of energy. In order to 'save' this fundamental physical principle, W. Pauli – in his famous letter from 1930 [Pau30] – suggested the existence of a new particle hitherto undetected. This particle, which was later called neutrino, should

- be electrically neutral,
- have a spin of 1/2,

- have a small mass ("not larger than 0.01 proton mass" [Pau30][1]), and
- interact only weakly with matter ("the same or perhaps a 10 times larger ability to get through [material] than a gamma ray" [Pau30][1]).

Assuming the emission of this hypothetical particle in addition to the electron in a β-decay would make the process a three-body decay and thus explain the observed spectrum. In 1934, a theoretical description of the β-decay was published by E. Fermi [Fer34]. In this work, Fermi already discussed how the shape of the β-spectrum depends on the neutrino mass, and concluded that the mass must be very small in comparison to the electron mass. In the same year, H. Bethe and R. Peierls estimated the cross section for interactions of neutrinos with nuclei to be only of the order of $10^{-44}\,\mathrm{cm}^2$, concluding that "there is no practically possible way of observing the neutrino" [Bet34].

Nevertheless, a possibility to observe the neutrino despite its extremely small interaction probability emerged in the following decades with the development of ever more powerful nuclear fission reactors, a very intense source of electron anti-neutrinos. F. Reines and C. L. Cowan utilized the inverse β-decay reaction

$$\overline{\nu}_\mathrm{e} + \mathrm{p} \rightarrow \mathrm{n} + \mathrm{e}^+ \tag{2.1}$$

to detect reactor neutrinos in their 'Project Poltergeist' [Rei56]. Liquid scintillator detectors around tanks of water with dissolved cadmium chloride allowed detection based on a delayed-coincidence signature: two 511 keV photons from the annihilation of the positron followed by delayed MeV gammas from the $^{113}\mathrm{Cd}(\mathrm{n},\gamma)^{114}\mathrm{Cd}$ neutron capture reaction [Zub12].

The second neutrino flavor, ν_μ, was discovered in 1962 at the Brookhaven accelerator AGS [Dan62]. The neutrinos were produced by pion decay and could be shown to give rise to muon production only, by observing the muons in a spark chamber. Finally, the tau neutrino ν_τ was discovered in the DONUT experiment at the Tevatron in 2000 [Kod01]. The number of light neutrino generations (with $m_\mu < 45\,\mathrm{GeV}/c^2$) was determined at the $\mathrm{e}^+\mathrm{e}^-$ collider LEP from the total decay width of the Z^0 resonance [ALE06]:

$$N_\nu = 2.9840 \pm 0.0082\ . \tag{2.2}$$

Neutrinos interact only via the weak interaction, with parity being maximally violated according to the V-A theory [Fey58, Sud58]. For this reason, only left-handed neutrinos and right-handed anti-neutrinos take part in the weak interaction, as was confirmed experimentally in the Goldhaber experiment [Gol58]. However, in order to generate neutrino masses by the same mechanism as for all other particles in the Standard Model of particle physics, i.e. via Yukawa couplings, right-handed neutrinos and left-handed antineutrinos would be required as well [Zub12]. Neutrinos are therefore considered to be massless particles in the Standard Model. Nevertheless, the discovery of neutrino oscillations revealed that neutrinos must have a non-zero rest mass. This is the topic of the following subsection.

[1] Translation by K. Riesselmann.

2.1.2. Neutrino oscillations

The first experiment hinting at the existence of neutrino oscillations was the Homestake experiment [Dav68], which had been proposed by R. Davis in 1964 in order to test J. Bahcall's theoretical predictions of the solar neutrino flux [Dav64, Bah64]. The experiment utilized a target of 615 tons of liquid C_2Cl_4 in order to detect solar neutrinos based on the reaction

$$\nu_e + {}^{37}\mathrm{Cl} \underset{\text{decay}}{\overset{\text{capture}}{\rightleftharpoons}} {}^{37}\mathrm{Ar} + e^- \ . \tag{2.3}$$

^{37}Ar produced in the interaction of solar neutrinos with ^{37}Cl was extracted from the tank by a radiochemical process. When decaying back to ^{37}Cl, 2.7 keV Auger electrons were emitted which could be detected in a proportional counter [Dav68]. The neutrino flux determined by this means turned out to be a factor of 3 to 4 lower than the predicted value [Bah76], which came as a surprise for the scientific community at that time. This deficit became known as the 'solar neutrino problem'; it was later confirmed by a range of further experiments based on radiochemical methods – GALLEX [GAL99], SAGE [SAG02] and GNO [GNO05] – as well as the Super-Kamiokande experiment based on water Cerenkov detectors [Sup98b].

A possible explanation for the observed deficit was offered by the theory of neutrino oscillations. As early as 1957/58, B. Pontecorvo considered the possibility of transitions between neutrinos and anti-neutrinos similar to the oscillation of neutral kaons [Pon58]. After the discovery of the muon neutrino, he extended the concept to oscillations between different neutrino flavors [Pon68]; a similar idea was developed by Z. Maki, M. Nakagawa and S. Sakata [Mak62]. The mechanism was proposed as a possible solution for the solar neutrino problem in a publication by V. Gribov and B. Pontecorvo [Gri69], according to which the measured flux of solar neutrinos was decreased by the number of neutrinos oscillated into muon neutrinos, since the solar neutrino experiments were only sensitive to electron neutrinos.

The theory of neutrino oscillations is based on a difference between the flavor eigenstates ν_α ($\alpha = e, \mu, \tau$) and the mass eigenstates ν_i ($i = 1, 2, 3$) of the neutrino. These states are connected via a unitary mixing matrix U according to

$$|\nu_\alpha\rangle = \sum_i U_{\alpha i} \, |\nu_i\rangle \, , \tag{2.4}$$

$$|\nu_i\rangle = \sum_\alpha U^*_{\alpha i} \, |\nu_\alpha\rangle \tag{2.5}$$

with the Pontecorvo-Maki-Nakagawa-Sakata or PMNS matrix [Kay08]

$$U = \begin{pmatrix} 1 & 0 & 0 \\ 0 & c_{23} & s_{23} \\ 0 & -s_{23} & c_{23} \end{pmatrix} \times \begin{pmatrix} c_{13} & 0 & s_{13}e^{-\mathrm{i}\delta} \\ 0 & 1 & 0 \\ -s_{13}e^{\mathrm{i}\delta} & 0 & c_{13} \end{pmatrix} \times \begin{pmatrix} c_{12} & s_{12} & 0 \\ -s_{12} & c_{12} & 0 \\ 0 & 0 & 1 \end{pmatrix} \times \begin{pmatrix} \mathrm{e}^{\mathrm{i}\frac{\varphi_1}{2}} & 0 & 0 \\ 0 & \mathrm{e}^{\mathrm{i}\frac{\varphi_2}{2}} & 0 \\ 0 & 0 & 1 \end{pmatrix} . \tag{2.6}$$

In this expression, $c_{ij} \equiv \cos\theta_{ij}$ and $s_{ij} \equiv \sin\theta_{ij}$ with the mixing angles θ_{ij}. δ is the CP violating Dirac phase, which can be observed in neutrino oscillations. If neutrinos are Majorana particles, they also have CP-violating Majorana phases (φ_1 and φ_2); however, these are inaccessible in oscillation experiments [Kun08].

The mass eigenstates are solutions of the Schrödinger equation and show a time dependence according to

$$|\nu_i(x,t)\rangle = \mathrm{e}^{-\mathrm{i}E_i t/\hbar}\,|\nu_i(x,0)\rangle \tag{2.7}$$

with

$$E_i = \sqrt{m_i^2c^4 + p_i^2c^2} \approx p_ic + \frac{m_i^2c^4}{2p_ic} \approx E + \frac{m_i^2c^4}{2E} \tag{2.8}$$

for $pc \gg m_ic^2$ and the total energy $E \approx pc$ [Zub12]. A neutrino produced via weak interaction in a certain flavor eigenstate represents a superposition of mass eigenstates, which propagate each with a different phase due to the dependence between the energy and the mass of a neutrino. The flavor content of the state in a certain distance $L = ct$ from the source therefore differs from the initial one, leading to a probability $P(\nu_\alpha \to \nu_\beta)$ that a neutrino created with flavor α is detected in a different flavor state β [Zub12]:

$$P(\nu_\alpha \to \nu_\beta) = \delta_{ij} - 4\sum_{j>i} U_{\alpha i}U_{\alpha j}U_{\beta i}U_{\beta j}\sin^2\left(\frac{\Delta m_{ij}^2 \cdot L \cdot c^3}{4\hbar E}\right) \tag{2.9}$$

with $\Delta m_{ij} = m_i^2 - m_j^2$. According to this expression, the transition probability shows an oscillatory behavior under the conditions that there is (i) mixing between the flavors, i.e. non-diagonal terms in U, and (ii) a difference between the neutrino mass eigenstates so that $\Delta m_{ij} \neq 0$. Based on the second condition, the observation of neutrino oscillations would thus imply non-zero neutrino masses, in contrast to the assumption in the Standard Model.

The existence of neutrino oscillations was confirmed experimentally around the turn of the millennium: in 1998, the Cerenkov-based Super-Kamiokande experiment proved the disappearance of atmospheric muon neutrinos – i.e. muon neutrinos produced in the interaction of cosmic rays with the earth's atmosphere – with a probability depending on the distance between their point of origin and the detector [Sup98a]. In 2001/02, the Sudbury Neutrino Observatory (SNO) Collaboration was able to solve the solar neutrino

Table 2.1.: Best-fit values of the neutrino oscillation parameters in dependence of the neutrino mass hierarchy. Data from [PDG14], based on [Cap14]. The values were derived from a global fit of neutrino oscillation data. Δm^2 is defined as $\Delta m^2 = m_3^2 - (m_2^2 + m_1^2)/2$.

Parameter	Best fit ($\pm 1\sigma$)	
	normal	inverted
Δm^2_{21} ($10^{-5}\,\mathrm{eV}^2/c^4$)	$7.54^{+0.26}_{-0.22}$	
$\lvert\Delta m^2\rvert$ ($10^{-3}\,\mathrm{eV}^2/c^4$)	2.43 ± 0.06	2.38 ± 0.06
$\sin^2\theta_{12}$	0.308 ± 0.017	
$\sin^2\theta_{23}$	$0.437^{+0.033}_{-0.023}$	$0.455^{+0.039}_{-0.031}$
$\sin^2\theta_{13}$	$0.0234^{+0.0020}_{-0.0019}$	$0.0240^{+0.0019}_{-0.0022}$
δ/π (2σ range)	$1.39^{+0.38}_{-0.27}$	$1.31^{+0.29}_{-0.33}$

problem by measuring for the first time the solar neutrino flux of all neutrino flavors in addition to the one of electron neutrinos only [SNO01, SNO02]. The measured total flux was well in accordance with the predicted value, while a fraction of only around 1/3 of the neutrinos produced in the sun as electron neutrinos arrived in their original flavor. In 2015, T. Kajita from the Super-Kamiokande Collaboration and A. B. McDonald from SNO were awarded the Nobel Prize of Physics "for the discovery of neutrino oscillations, which shows that neutrinos have mass" [Nob15].

Since the experimental discovery of neutrino oscillations, a number of different experiments have been performed to further study this topic and determine the parameters of the PMNS matrix, exploiting a range of different neutrino sources, energies and baseline lengths between source and detector. Apart from experiments studying atmospheric neutrinos (e.g. Super-Kamiokande [Sup13]) and solar neutrinos (SNO [SNO16], Borexino [BC14]), there are various experiments like KamLAND [Kam11], Double Chooz [Dou12], RENO [REN15] and Daya Bay [Day16] which utilize reactor neutrinos, while others (MINOS [MIN14], T2K [T2K15]) use beams of muon neutrinos produced at particle accelerators. Table 2.1 lists the present values of the oscillation parameters.

It should be noted that neutrino oscillation experiments are only sensitive on the squared mass difference between neutrino eigenstates, but not on the absolute mass scale. Since neither the sign of Δm^2_{31} (or Δm^2_{32}) nor the absolute value of one of the mass eigenstates is known, there are three possible scenarios:

- Normal hierarchy: $m_1 < m_2 \ll m_3$.
- Inverted hierarchy: $m_3 \ll m_1 < m_2$.
- Quasi-degenerate scenario: $m_1 \approx m_2 \approx m_3$.

In the normal and the inverted hierarchy case, the mass of the lightest eigenstate is small compared to the mass differences, leading to three distinct neutrino masses. In

the quasi-degenerate scenario, the mass of the lightest eigenstate is so large compared to the mass splittings that all masses are approximately equal. The sign of Δm^2_{31} or Δm^2_{32} will be studied in a range of further oscillation experiments such as NOνA [NOv07], PINGU [Ice14] or JUNO [JUN16]. The question how to determine the absolute mass scale will be the topic of section 2.3. First, the relevance of determining the neutrino mass will be outlined in the next section.

2.2. Relevance of neutrino masses in physics

The determination of the absolute mass scale of neutrinos is of high interest in various fields of physics, in particular particle physics and cosmology.

2.2.1. Particle physics

As stated previously, neutrinos are considered to be massless particles in the Standard Model of particle physics. The discovery of non-zero neutrino masses is therefore an indication for physics beyond the standard model [Zub12]. A range of theoretical models have been developed to explain the tremendous difference of at least six orders of magnitude between the masses of the neutrinos and those of the lightest charged fermions, many based on the so-called seesaw mechanism [Moh07]. Heavy right-handed Majorana neutrinos are introduced in the type I seesaw mechanism, which leads to smaller masses of the observed left-handed neutrinos the higher the mass of the Majorana neutrino is [Zub12]. A hierarchical neutrino mass scenario is expected in this case. In the type II seesaw mechanism, an additional mass term is added which includes coupling to the Higgs vacuum expectation value, leading to a quasi-degenerate scenario [Zub12]. An experimental determination of the neutrino mass scenario realized in nature would thus be an important step to identify the underlying mechanism, enabling us to improve our understanding of the origin of neutrino masses.

2.2.2. Cosmology

Although it has not yet been directly detected, an intense cosmic neutrino background is assumed to have been left over from the Big Bang according to the Standard Hot Big Bang Model [Pas08]. Being relativistic at the time of decoupling from matter, these abundant amounts of neutrinos played a certain role in the structure formation of the universe as so-called neutrino hot dark matter (νHDM) [Han04]: the neutrinos could freely stream out of any primordial density fluctuations and thus slow down their growth [Per09]. The strength of this damping effect depends on the neutrino mass. As illustrated in figure 2.1, heavier neutrinos suppress small structures more efficiently. By directly measuring the neutrino mass, the contribution of the neutrino density $\Omega_\nu h^2 = \sum m_\nu / 93\,\mathrm{eV}$ [Han04] to the total dark matter content of the universe could be determined. The knowledge of this additional parameter would allows us to probe cosmological models and improve our understanding of structure formation in the universe.

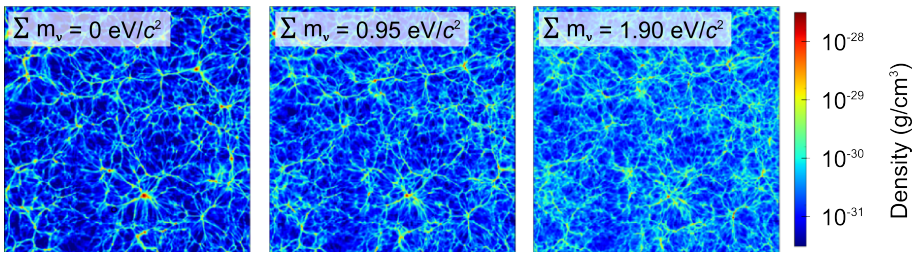

Figure 2.1.: Simulation of the dependence of the baryon density distribution in the universe on the neutrino masses. The slices shown are 200 h^{-1} Mpc wide and show the baryonic mass averaged over the volume of a grid cell of size $\sim 391\,h^{-1}$ kpc [Aga11]. The figure demonstrates how small structures smear out increasingly with rising neutrino masses. Figure adapted from [Aga11].

2.3. Methods to determine the neutrino mass

Methods for neutrino mass determination are divided into two different types: direct and indirect methods. Direct methods enable neutrino mass determination purely based on kinematics. By making use of the relativistic energy-momentum relation

$$E^2 = p^2c^2 + m^2c^4 \ , \tag{2.10}$$

these methods are sensitive to the neutrino mass squared. Indirect methods, in contrast, are based on theoretical and modeling assumptions. Additional systematic and model-dependent uncertainties are therefore connected to the neutrino mass determination in this case. Representatives of both methods are discussed in the following subsections.

2.3.1. Indirect methods

Cosmological and astrophysical observations: As outlined in the previous section, the formation of the large-scale structures visible in the universe today has been influenced by neutrinos smearing out small-scale fluctuations in the early universe, with the strength of this effect depending on the sum of the neutrino masses. It is therefore possible to gain information about $\sum m_\nu$ by studying (i) today's structure of the universe by means of large galaxy surveys like SDSS [SDS15], and (ii) the cosmic microwave background (CMB), which maps the tiny temperature differences connected to density fluctuations in the early universe. A very detailed map of the cosmic microwave background has recently been provided by the Planck Collaboration based on data from the Planck satellite [Pla15b]. One of the currently most stringent upper limits on $\sum m_\nu$ obtained by combining large-scale structure and CMB results is reported by the Planck Collaboration [Pla14, Pla15a]:

$$\sum m_\nu < 0.23\,\mathrm{eV}/c^2 \ (95\,\%\ \mathrm{C.L.}) \ . \tag{2.11}$$

However, it should be noted that this upper limit depends both on the data sets considered and the model assumptions used [Pla15a, Aba15].

Neutrinoless double β-decay: A neutrinoless double β-decay ($0\nu\beta\beta$) is a weak interaction process which can only be observed if the neutrino is a massive Majorana particle and thus its own anti-particle [Giu12]. In this case, a simultaneous decay of two neutrons in the same nucleus can occur without emission of neutrinos as in the normal double β-decay ($2\nu\beta\beta$): the neutrino produced at one vertex as a right-handed anti-neutrino $\overline{\nu}_{\mathrm{R}}$ is absorbed as a left-handed neutrino ν_{L} at the other vertex, leading to the following effectively neutrinoless decay pattern of a nucleus N with mass number A and charge Z:

$$N(A, Z) \rightarrow N'(A, Z + 2) + 2\mathrm{e}^{-} \ . \tag{2.12}$$

As a spin-flip of the neutrino is required for such a process to take place, the probability of this process and thus the decay rate $\Gamma_{0\nu\beta\beta}$ depends on the neutrino mass according to [Giu12]:

$$\Gamma_{0\nu\beta\beta} = (T_{1/2}^{0\nu\beta\beta})^{-1} = G_{01} \cdot \left| M^{0\nu\beta\beta} \right|^2 \cdot \left(\frac{\langle m_{\nu_{\mathrm{e}}} \rangle}{m_{\mathrm{e}}} \right)^2 \ . \tag{2.13}$$

In this equation, $T_{1/2}^{0\nu\beta\beta}$ is the half-life of the $0\nu\beta\beta$ process, G_{01} a phase-space factor which depends on charge, mass and available energy of the process, $M^{0\nu\beta\beta}$ the nuclear matrix element, m_{e} the electron mass and $\langle m_{\nu_{\mathrm{e}}} \rangle$ the so-called effective Majorana neutrino mass. The latter is defined as the coherent sum of the neutrino mass eigenvalues, which takes into account the neutrino mixing matrix U [Zub12]:

$$\langle m_{\nu_{\mathrm{e}}} \rangle = \left| \sum_i U_{\mathrm{e}i}^2 m_i \right| \ . \tag{2.14}$$

It should be noted that the calculation of the nuclear matrix element $M^{0\nu\beta\beta}$ leads to a significant uncertainty in the determination of the effective Majorana neutrino mass from the observed decay rate [Giu12].

The observation of neutrinoless double β-decay at $\langle m_{\nu_{\mathrm{e}}} \rangle = (0.32 \pm 0.03)\,\mathrm{eV}/c^2$ in ^{76}Ge was claimed by parts of the Heidelberg-Moscow collaboration [Kla06]. The result has been discussed controversially in the community; recent limits on the effective Majorana neutrino mass set by other experiments such as EXO-200, KamLAND-Zen and GERDA (see e.g. [Gar14]) challenge the claim. In 2015, the GERDA Collaboration has published results excluding the previous claim with 99 % probability [GER15].

2.3.2. Direct methods

Time-of-flight measurements of supernova neutrinos: The time-of-flight of a neutrino with velocity v_ν and total energy E_ν, which starts at a time t_0 from a certain point (source) and is detected at a time t in a distance L to the source, is given by [Zub12]

$$T_\nu = t - t_0 = \frac{L}{v_\nu} = \frac{L}{c}\frac{E_\nu}{p_\nu c} = \frac{L}{c} \cdot \frac{E_\nu}{\sqrt{E_\nu^2 - m_\nu^2 c^4}} \approx \frac{L}{c} \cdot \left(1 + \frac{m_\nu^2 c^4}{2E_\nu^2} \right) \tag{2.15}$$

and is thus dependent on the neutrino mass. In practice, very long baselines and thus very strong neutrino sources are required in order to determine the neutrino mass from the kinematics of time-of-flight measurements [Dre13]. Suitable sources are core-collapse supernovae (type II supernovae), in which tremendous amounts of neutrinos are released. For instance, about 10^{58} neutrinos were emitted from the type II supernova SN1987A, leading to a flux of still over 10^{10} neutrinos per cm^{-2} at the earth, in a distance of about 170 000 light years [Per09].

The measured arrival times of two neutrinos with energies E_1 and E_2 ($E_2 > E_1$), which are emitted with a time difference of Δt_0 in a supernova in the distance L from earth, differs by [Zub12]

$$\Delta t = t_2 - t_1 = \Delta t_0 + \frac{L m_\nu^2 c^3}{2} \left(\frac{1}{E_2^2} - \frac{1}{E_1^2} \right) . \tag{2.16}$$

While Δt, L, E_1 and E_2 can be measured, Δt_0 is unknown and has to obtained based on theoretical models describing the time evolution of the supernova neutrino burst, thus introducing a certain model-dependence in this method as well. It should also be noted that nearby supernova explosions are very rare events, which makes this method less favorable than laboratory neutrino mass experiments: only one suitable supernova explosion occurred since the setup of the first neutrino detectors, namely above-mentioned 1987A. Detailed analysis of the neutrinos from this event yielded upper limits on the neutrino mass of $5.7\,\mathrm{eV}/c^2$ [Lor02] or $5.8\,\mathrm{eV}/c^2$ [Pag10] at a confidence level of 95 %, depending to a certain extent on the supernova model used.

Kinematics of weak decays: Studying the kinematics of weak decays allows for a purely laboratory-based neutrino mass measurement. In principle, all neutrino flavors can be investigated. Muon and tau neutrino mass measurements utilize the decay of pions and taus produced in particle accelerators, e.g. the following decays [Bar56, ALE98]:

$$\pi^+ \to \mu^+ + \nu_\mu \quad \text{and} \quad \pi^- \to \mu^- + \overline{\nu}_\mu , \tag{2.17}$$

$$\tau^- \to 2\pi^- + \pi^+ + \nu_\tau \quad \text{and} \quad \tau^- \to 3\pi^- + 2\pi^+ (+\pi^0) + \nu_\tau . \tag{2.18}$$

By precisely measuring the energies and momenta of all other particles involved, information about the mass of the undetected neutrino can be gained. The current upper limits obtained this way have been achieved at the Paul Scherrer Institute in the case of m_{ν_μ} [Ass96], and the ALEPH experiment at LEP in the case of m_{ν_τ} [ALE98]:

$$m_{\nu_\mu} < 0.17\,\mathrm{MeV}/c^2 \quad (90\,\%\ \text{C.L.}) , \tag{2.19}$$

$$m_{\nu_\tau} < 18.2\,\mathrm{MeV}/c^2 \quad (95\,\%\ \text{C.L.}) . \tag{2.20}$$

It is noticeably that the upper limits obtained by these approaches are still several orders of magnitude higher than the expected mass range of the neutrino eigenstates. A significantly more sensitive method is the measurement of the electron neutrino mass via precision investigations of the β-electron spectrum near its endpoint. The method makes use of the fact that an energy equivalent to the neutrino rest mass is required for the production of a neutrino in a β-decay

$$\mathrm{n} \to \mathrm{p} + \mathrm{e}^- + \overline{\nu}_\mathrm{e} . \tag{2.21}$$

Since the neutrino mass is not available as kinetic energy for the emitted electron, the shape of the β-electron energy spectrum depends on the neutrino mass. The relative effect on the shape is most prominent near the kinematic endpoint, so that the focus of β-decay neutrino mass experiments is on precision spectroscopy of the endpoint region. There are several different techniques to reach this goal:

- One approach utilizes microcalorimeters to investigate β-decays of rhenium or electron capture decays of holmium [Dre13]. This approach is based on a 'source = detector' concept, with the rhenium or holmium source material being embedded in the detector. The deposited energy is measured either by a change of temperature [Kra08], resistance [Vac08] or magnetization [Ran12]. An advantage of this approach is that the complete decay energy apart from the fraction carried away by the neutrino can be measured, including nuclear recoil and excitation of the daughter molecule. On the other hand, the method is prone to pile-up effects in the detectors, so that large arrays of small detectors are required [Dre13]. Current microcalorimeter experiments comprise the MARE experiment planning to use both ^{187}Re and ^{163}Ho for neutrino mass measurements [MAR13], and the ECHo experiment using metallic magnetic calorimeters to investigate the electron capture of ^{163}Ho [ECH14]. So far, the best upper limit on the neutrino mass achieved by a microcalorimeter approach has been reached by the Milano neutrino mass experiment with $m_{\nu_e} < 15\,\mathrm{eV}/c^2$ (90 % C.L.) [Sis04].

- Another possibility is based on the cyclotron motion of electrons around magnetic field lines: β-decay electrons brought into a magnetic field emit cyclotron radiation with a frequency that depends on the electron energy [Mon09]. Using the β-decay of tritium, a strong magnetic field in the 1 T range and radio-frequency antennas to detect the coherent cyclotron radiation, Project 8 currently investigates the feasibility of this approach for neutrino mass determination [Pro13].

- Currently, the most sensitive direct method for neutrino mass determination utilizes the β-decay of tritium, $\mathrm{T} \rightarrow {}^3\mathrm{He}^+ + \mathrm{e}^- + \overline{\nu}_\mathrm{e}$, and a spectrometer of MAC-E-Filter type. Details about this approach as well as current neutrino mass limits obtained using this method will be given in the following section.

2.4. Tritium β-decay experiments

2.4.1. The tritium β-decay spectrum

In order to understand the advantages of using tritium for β-decay neutrino mass experiments, it is worthwhile to take a closer look at the properties and dependencies of the β-electron spectrum. Where not stated otherwise, the following equations and explanations are based on [Wei03].

The transition rate for a β-decay can be calculated according to Fermi's Golden Rule from the transition matrix element M and the density of final states $\varrho(E)$:

$$\frac{\mathrm{d}^2N}{\mathrm{d}t\mathrm{d}E} = \frac{2\pi}{\hbar}\left|M^2\right|\varrho(E) \tag{2.22}$$

$$= C \cdot F(E, Z+1) \cdot p \cdot (E + m_\mathrm{e}c^2) \cdot (E_0 - E) \cdot \sqrt{(E_0 - E)^2 - m_{\nu_\mathrm{e}}^2 c^4} \cdot \Theta(E_0 - E - m_{\nu_\mathrm{e}}c^2) \ , \tag{2.23}$$

where E, p and m_e are the energy, momentum and mass of the electron, respectively, E_0 is the total decay energy and m_{ν_e} the neutrino mass. $F(E, Z+1)$ is the Fermi function, which takes into account the Coulomb interaction between the β-electron and the daughter nucleus with charge $Z+1$. The Heaviside step function $\Theta(E_0 - E - m_{\nu_\mathrm{e}}c^2)$ ensures energy conservation in the decay. The factor C is given by

$$C = \frac{G_\mathrm{F}^2}{2\pi^3\hbar^7c^5}\cos^2\theta_\mathrm{c}\,|M_\mathrm{nuc}|^2 \tag{2.24}$$

with the Fermi constant G_F, the Cabibbo angle θ_c and the nuclear matrix element M_nuc.

Equation 2.23 is an approximation holding only for the decay of a bare, infinitely heavy nucleus and neglecting the existence of more than one mass eigenstate. If realistic atoms or molecules are considered, it has to be taken into account that the daughter atom or molecule will end up in an excited state of excitation energy V_j with a certain probability P_j. For this reason, the total spectrum is actually given by a sum of different β-spectra with amplitudes P_j and different endpoint energies $E_{0,j} = (E_0 - V_j)$. Similarly, neutrino mixing has to be taken into account by summing over all mass eigenstates m_i weighted by the squares of the mixing matrix elements $U_{\mathrm{e}i}$. This leads to the following expression for the β-decay transition rate:

$$\frac{\mathrm{d}^2N}{\mathrm{d}t\mathrm{d}E} = C \cdot F(E, Z+1) \cdot p \cdot (E + m_\mathrm{e}c^2) \cdot \sum_j P_j(E_{0,j} - E)\left(\sum_i |U_{\mathrm{e}i}|^2 \sqrt{(E_{0,j} - E)^2 - m_i^2c^4} \cdot \Theta(E_{0,j} - E - m_ic^2)\right) \ . \tag{2.25}$$

However, as the spectral resolution of current spectrometers for β-spectroscopy is large compared to the difference between the neutrino mass eigenstates, the contributions from the different eigenstates cannot be resolved. Instead, analysis of the measured spectrum yields the following mean squared electron neutrino mass:

$$m_{\nu_\mathrm{e}}^2 = \sum_i |U_{\mathrm{e}i}|^2\, m_i^2 \ . \tag{2.26}$$

A significant influence of the neutrino mass on the shape of the β-spectrum can only be observed in the region around the kinematic endpoint, as the neutrino mass term in the square root in equation 2.25 is no longer negligible at energies $E \approx E_{0,j}$. The effect of a non-zero neutrino mass on the spectrum is illustrated in figure 2.2. In order to determine the neutrino mass from a fit to the β-spectrum, the tiny change of the spectral shape in a region with a very low count rate has to be resolved. For these reasons, it

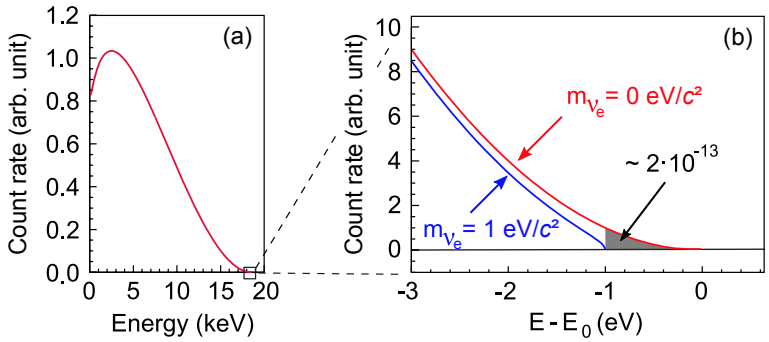

Figure 2.2.: Electron spectrum of the tritium β-decay. *(a)* Full tritium β-spectrum. *(b)* Energy range around the kinematic endpoint. The simulated spectra for m_ν=0 eV/c^2 and an arbitrarily chosen neutrino mass of m_ν=1 eV/c^2 are shown in order to demonstrate the effect of the neutrino mass on the shape of the curve. In the case of tritium, a fraction of only $2 \cdot 10^{-13}$ of all β-decays is found in the region 1 eV below the endpoint (gray-shaded area). Figure according to [KAT05].

is vital that the β-emitter used for a neutrino mass measurement provides a very high activity as well as a low endpoint energy, the latter facilitating a high relative energy resolution $\Delta E/E$ to be achieved experimentally [Dre13]. Tritium has been identified as a particularly advantageous β-emitter for neutrino mass experiments for the following reasons [Bor08]:

- The half-life of tritium is 12.3 y and thus comparatively short, providing a high specific activity. This reduces the amount of source material needed and thus the fraction of inelastically scattered β-electrons, which represent a source of systematic uncertainties.
- Due to the low nuclear charge of tritium, inelastic scattering of β-electrons with source molecules is further reduced compared to high-Z materials.
- The tritium endpoint energy of about 18.6 keV is the second lowest endpoint energy of all β-emitters. Only ^{187}Re has a lower endpoint, which is however accompanied by a very long half-life of more than 10^{10} years.
- The simple electronic shell configuration of tritium and its daughter nucleus ^{3}He$^+$ allows for precise calculations of the final state spectrum, so that related systematic uncertainties are minimized.
- The β-decay of tritium is a super-allowed nuclear transition, so that the nuclear matrix element M_{nuc} is independent of the electron energy. For this reason, no corrections from M_{nuc}, which would contribute to the systematic uncertainties, have to be taken into account.

2.4.2. Working principle of the MAC-E-Filter

In order to investigate the shape of the β-spectrum near its endpoint in detail, a high energy resolution as well as a high luminosity at low background is required [Dre13].

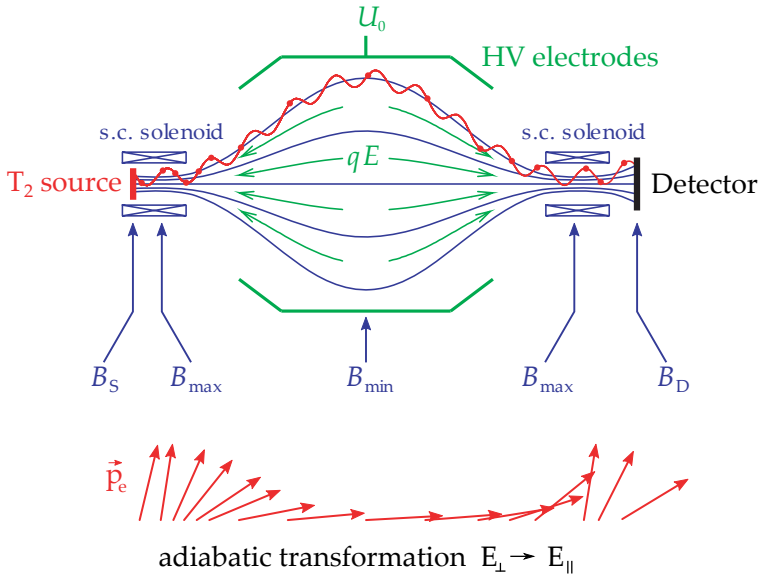

Figure 2.3.: Principle of the MAC-E-Filter. *Top:* Experimental setup. *Bottom:* Adiabatic transformation of the momentum vector. Figure adapted from [KAT05].

These features are combined in a type of spectrometer developed independently at the Mainz and Troitsk neutrino mass experiments [Pic92, Lob85] based on pioneering work by Kruit and Read [Kru83]: the MAC-E-Filter ("Magnetic Adiabatic Collimation with an Electrostatic Filter").

Figure 2.3 illustrates the main features of the MAC-E-Filter. It makes use of an electrostatic high-pass filter to energetically analyze the β-decay electrons: only electrons with kinetic energies above a threshold $|eU_0|$ are transmitted, with the threshold being defined by the voltage U_0 of the electrostatic retarding potential. The integrated β-spectrum can be determined by measuring the rate of transmitted electrons as a function of the retarding voltage.

As the retarding field acts only on the component of motion along the electric field lines, magnetic adiabatic collimation is used in order to parallelize the β-electrons in the analyzing plane. For this purpose, the tritium source is located in a superconducting solenoid, so that the emitted electrons are guided magnetically in a cyclotron motion along the magnetic field lines into the spectrometer. The magnetic guidance allows for an accepted solid angle of almost 2π. In the spectrometer, the magnetic field B decreases gradually by several orders of magnitude until it reaches its minimum value B_{min} approximately in the center of the spectrometer. This slow variation keeps the magnetic orbital moment of the electron invariant,

$$\mu = \frac{E_\perp}{B} = \text{const.} \,, \tag{2.27}$$

so that almost all cyclotron energy $E_\perp$ is transformed into longitudinal motion, as shown in the bottom of figure 2.3. The ratio between the minimum and the maximum value of the magnetic guiding field (cf. figure 2.3, top) defines the relative sharpness of the filter:

$$\frac{\Delta E}{E} = \frac{B_{\mathrm{min}}}{B_{\mathrm{max}}} \ . \tag{2.28}$$

2.4.3. Results of previous tritium β-decay experiments

Spectrometers of the MAC-E-Filter type were first applied in the tritium β-decay experiments in Mainz and Troitsk, leading to a significantly improved neutrino mass sensitivity compared to previous experiments using magnetic spectrometers [Dre13]. The Mainz experiment utilized a quenched-condensed tritium source. They obtained a result of [Kra05]

$$m_\nu^2 = (-0.6 \pm 2.2_{\mathrm{stat}} \pm 2.1_{\mathrm{syst}})\,\mathrm{eV}^2/c^4 \ . \tag{2.29}$$

Using the Feldman and Cousins approach [Fel98], this value can be translated into an upper limit on the neutrino mass of

$$m_\nu < 2.3\,\mathrm{eV}/c^2 \quad (95\%\ \mathrm{C.L.}) \ . \tag{2.30}$$

The Troitsk group refined the concept of a windowless gaseous tritium source pioneered earlier in the Los Alamos experiment [Wil87, Rob91]. In 2011 the results of a reanalysis of the Troitsk data taken between 1997 and 2002 were published [Tro11]:

$$m_\nu^2 = (-0.67 \pm 1.89_{\mathrm{stat}} \pm 1.68_{\mathrm{syst}})\,\mathrm{eV}^2/c^4 \ , \tag{2.31}$$

corresponding to an upper limit of

$$m_\nu < 2.05\,\mathrm{eV}/c^2 \quad (95\%\ \mathrm{C.L.}) \ . \tag{2.32}$$

An evaluation of the same data by the Particle Data Group [PDG14] resulted in an upper mass limit of

$$m_\nu < 2\,\mathrm{eV}/c^2 \quad (95\%\ \mathrm{C.L.}) \ . \tag{2.33}$$

2.5. The KATRIN experiment

2.5.1. Aim of the experiment

The next-generation neutrino mass experiment KATRIN is presently being constructed and commissioned at the Karlsruhe Institute of Technology (KIT) in Germany. Pushing the precision of β-spectroscopy to the current technological limits, KATRIN has been designed to improve the current experimental sensitivity on the neutrino mass as set by its predecessor experiments (cf. subsection 2.4.3) by an order of magnitude.

As the actual observable in tritium β-decay experiments is the squared neutrino mass m_ν^2, this ambitious sensitivity goal requires an improvement of both systematic and statistical uncertainties by at least two orders of magnitude compared to previous experiments. A maximum systematic uncertainty of $\sigma_{\mathrm{sys,tot}} = 1.7 \cdot 10^{-2}\,\mathrm{eV}^2/c^4$ is tolerable, which corresponds to an individual uncertainty budget of $\sigma_{\mathrm{sys,ind}} \leq 7.5 \cdot 10^{-3}\,\mathrm{eV}^2/c^4$ for each of the five main sources of uncertainty [KAT05]. Two of these uncertainty sources which are linked to the KATRIN tritium source are directly related to the topic of this thesis; they will be discussed in detail in subsection 2.5.3.

After three years of effective measurement time (equivalent to five calender years), the statistical uncertainty for the determination of m_ν^2 will have reached a level comparable to the systematic uncertainty with $\sigma_{\mathrm{stat}} = 1.8 \cdot 10^{-2}\,\mathrm{eV}^2/c^4$. The total uncertainty is obtained by adding up both uncertainties quadratically:

$$\sigma_{\mathrm{tot}} = \sqrt{\sigma_{\mathrm{stat}}^2 + \sigma_{\mathrm{sys,tot}}^2} \approx 2.5 \cdot 10^{-2}\,\mathrm{eV}^2/c^4 \ . \tag{2.34}$$

This corresponds to a 5σ significance level for detecting a neutrino mass of

$$m_\nu = \sqrt{5 \cdot \sigma_{\mathrm{tot}}} \tag{2.35}$$

$$\approx 350\,\mathrm{meV}/c^2 \ . \tag{2.36}$$

In case of a measurement result consistent with zero, the total uncertainty would lead to a new upper limit for the neutrino mass of

$$m_\nu \leq \sqrt{1.64 \cdot \sigma_{\mathrm{tot}}} \tag{2.37}$$

$$\approx 200\,\mathrm{meV}/c^2 \quad (90\,\%\ \mathrm{C.L.}) \ . \tag{2.38}$$

This sensitivity will allow KATRIN to probe a neutrino mass range of particular relevance for cosmology and particle physics [KAT05].

2.5.2. Experimental setup

A short description of the main components of the KATRIN experiment is given in the following, with a focus on the WGTS and Inner Loop system, which are of particular relevance for this work. An overview of the KATRIN setup is shown in figure 2.4.

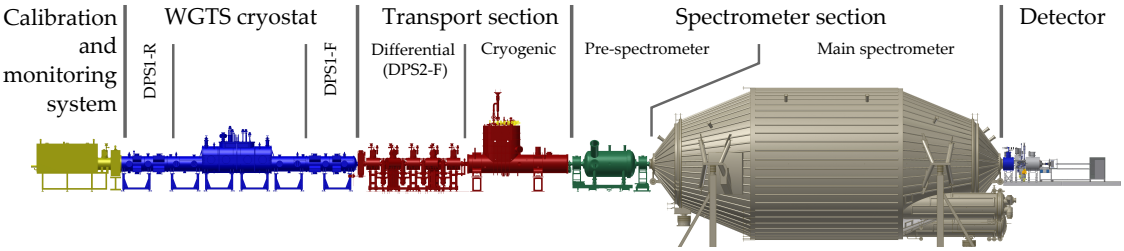

Figure 2.4.: Setup of the KATRIN experiment. The KATRIN sub-components form a continuous beam line of 70 m length, along which the β-electrons are guided magnetically. Not shown here is the system of air coils which surrounds the main spectrometer.

The Windowless Gaseous Tritium Source and the Inner Loop

The Windowless Gaseous Tritium Source (WGTS) is the high-luminosity source of tritium β-electrons. The concept of using a source of molecular, gaseous tritium was pioneered in the LANL neutrino mass experiment at Los Alamos [Wil87, Rob91] and refined later in the Troitsk neutrino mass experiment [Bel95a], allowing for minimized effects of scattering on the spectrum and less complex final-states calculations than solid sources [Bod15]. In the following, an outline of the concept and setup of the WGTS will be given. Source-related systematic effects will be discussed in detail in subsection 2.5.3.

The working principle of the WGTS is illustrated in figure 2.5. The source tube is a 10 m long stainless steel tube with an inner diameter of 90 mm. Molecular tritium is injected continuously into the middle of this tube at a rate of 1.853 mbar·l/s and pumped off again by turbomolecular pumps at both ends of the source tube (differential pumping sections DPS1-F and DPS1-R, cf. figure 2.4). By these means, a tritium gas column with a stable density profile – as shown at the top of figure 2.5 – is formed inside the source tube, providing about 10^{11} β-electrons per second. The column density value of $\varrho d = 5 \cdot 10^{17}\,\mathrm{cm}^{-2}$ is chosen such that the β-activity is maximized while keeping energy losses due to electron scattering in the source low [KAT05]. A system of superconducting solenoids around the source tube provides a magnetic field of 3.6 T by which the β-electrons are guided adiabatically along the tube. The WGTS cryostat keeps the source gas at a stable temperature of around 30 K; this temperature is low enough to keep Doppler broadening as well as the required T_2 inventory low, but not so low as to induce clustering and condensation of the source molecules [Bab12]. The gas processing loops connected to the WGTS provide tritium injection into the source on a 0.1 % stability level (Inner Loop) and with a high isotopic tritium purity of $\geq 95\,\%$ (Outer Loop) [Stu10]. A simplified flow diagram of the Inner Loop is shown and explained in figure 2.5.[2]

After delivery of the WGTS cryostat in 2015 and the recent successful completion of all installation works, commissioning is currently ongoing and will be finished by the end of 2016. The Loop system has been set up and tested; details are given in [Pri15a]. It is currently being integrated into the overall KATRIN setup and will then be further commissioned and characterized.

The WGTS will be operated with a daily tritium throughput of 40 g. The extensive infrastructure required for this task is provided by the Tritium Laboratory Karlsruhe (TLK) at the Karlsruhe Institute of Technology. The TLK has a license to handle up to 40 g of tritium and long-standing expertise in the field of tritium technology [Bor11]. It features a closed tritium cycle comprising facilities for such processing steps as tritium purification and isotopologue separation which are vital for the KATRIN experiment. All tritium-bearing components of KATRIN – WGTS and loops, calibration and monitoring system as well as the transport section – are located inside the TLK.

[2] An unsimplified flow diagram of the Inner Loop directly around the source tube can be found in appendix B.

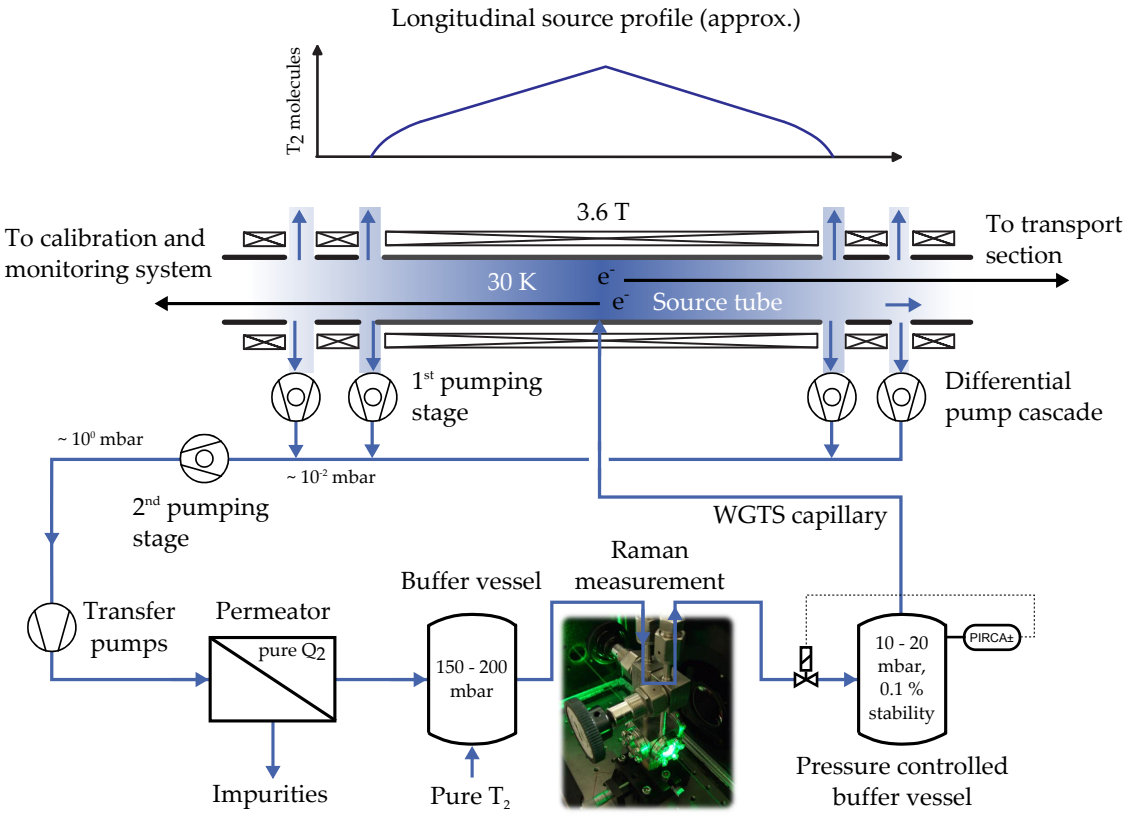

Figure 2.5.: Schematic representation of WGTS concept and Inner Loop flow diagram. A stable tritium gas profile in the source tube *(top)* is provided by the Inner Loop *(bottom)*: tritium gas is injected into the source tube from a pressure-controlled buffer vessel. The gas is pumped off at both ends of the source tube and subsequently purified by a permeator, which consists of a palladium membrane only permeable by hydrogen isotopologues. Impurities like ^{3}He and tritiated methanes are thus removed from the gas circulation and replaced by highly purified T_2 gas (purity $\geq 95\,\%$) from the Outer Loop via another buffer vessel. The composition of the gas fed from here into the pressure controlled buffer vessel is measured continuously by an inline Raman spectroscopic system; this will be described in detail in subsection 2.5.4. Figure adapted from [Stu10, Fis14].

The calibration and monitoring system

A calibration and monitoring system is located at the rear side of the WGTS. It has three major tasks:

1. It houses the so-called rear wall, which represents the effective rear end of the WGTS. The rear wall defines the electrical potential of the source relative to the spectrometer retarding voltage [Bab12, Sch16].

2. It monitors the source activity via beta-induced X-ray spectrometry (BIXS): β-electrons hitting the gold surface of the rear wall generate X-rays which are detected by a silicon drift detector [Röl13]. According to recent Monte Carlo simulations, the BIXS system will allows for activity measurements with an uncertainty of $\leq 0.1\,\%$ in $\leq 70\,\mathrm{s}$ of measurement time [Röl15].

3. It houses an angle and energy selective electron gun [Val11] allowing for systematic scans of the complete KATRIN beam line. The e-gun is used for a range of monitoring and calibration purposes such as determination of the energy loss and transmission function as well as periodical measurements of the WGTS column density [KAT05].

The different components of the calibration and monitoring section are currently being set up and tested. Commissioning is planned for the beginning of 2017.

The transport section

The task of the transport section is to adiabatically guide the β-electrons from the WGTS towards spectrometer and detector while at the same time reducing the tritium flow rate by a factor of 10^{14}. Such a powerful tritium retention is necessary to limit the amount of tritium molecules entering the spectrometer, as these would produce background events and thus disturb the measurement of the β-endpoint spectrum [Mer13]. The transport section comprises two separate pumping sections: the Differential Pumping Section (DPS) and the Cryogenic Pumping Section (CPS). The DPS is designed to reduce the tritium flux by four to five orders of magnitudes by means of four turbo molecular pumps [Luk12]; note that the DPS1-F and the end of the WGTS (cf. figure 2.4) contributes about two to three additional orders of magnitude of tritium flow reduction by differential pumping. The cryogenic pumping section makes use of cryosorption, a passive pumping method where tritium molecules are adsorbed on an argon frost layer cooled down to 3 K. It is targeted to reduce the tritium flow by at least seven orders of magnitude [Jan15]. Superconducting magnets with central fields of up to 5.7 T provide adiabatic guidance of the β-electrons along the approximately 14 m long transport section. The DPS was delivered in 2014; its installation and connection to the WGTS are currently being finalized. Since the arrival of the CPS at KIT in the middle of 2015, mechanical installation works, position measurements and tests of the electronics have been completed, and the system is now prepared for cool-down.

The spectrometer and detector section

Two spectrometers of the MAC-E-Filter type (cf. subsection 2.4.2) are employed in the KATRIN experiment in a tandem configuration. A pre-spectrometer of 3.4 m length and 1.7 m diameter acts as a pre-filter by rejecting all β-electrons with energies lower than 300 eV below the endpoint, which are of no use for the neutrino mass determination [KAT05, Pra12]. The high-energy electrons transmitted by the pre-spectrometer enter the main spectrometer, which is 23 m long and has a diameter of 10 m. There, they are energetically analyzed with a resolution of $\Delta E = 0.93\,\text{eV}$ at $E = 18.6\,\text{keV}$ [KAT05]. Two solenoids with $B = 4.5\,\text{T}$ at the side facing the pre-spectrometer and $B = 6.0\,\text{T}$ at the detector end provide the magnetic field, which is fine-tuned by a system of air-coils surrounding the main spectrometer [Glü13]. The retarding potential is directly applied to the spectrometer vessel and fine-tuned by an inner wire-electrode system [Val10].

The β-electrons with sufficient energy to be transmitted through the spectrometers are counted by the focal plane detector at the end of the KATRIN beam line. It is a segmented

silicon PIN-diode array with 148 equal-area pixels which cover the entire transmitted flux tube of 191 Tcm^2 focused onto the detector wafer by the detector magnet. Due to this segmentation, inhomogeneities in the tritium source and the analyzing plane of the spectrometer can be detected [Ams15]. The detector has a measured detection efficiency of about 95 % [Ams15].

The spectrometer and detector section has been extensively tested in the past (see e.g. [Lei14, Sch14b, Gro15, KAT16]) and is currently being prepared for its final commissioning phase in the summer of 2016.

2.5.3. Source-related systematic effects

As outlined in subsection 2.5.1, the KATRIN experiment requires exceptionally low statistical and systematic uncertainties in order to reach its ambitious design sensitivity. With respect to the WGTS, there are two key parameters which have to be carefully considered when speaking about both types of uncertainties: the column density and the isotopic composition of the source. These parameters and the uncertainties connected to them will be discussed in the following.

The column density ϱd is defined as the number of molecules within a flux tube volume of unit cross section in the source [Bab12]. The isotopic composition specifies the content of different hydrogen isotopologues in the source gas: although the ideal source gas would consist of pure T_2, in reality there are always small admixtures of the other hydrogen isotopologues DT, HT, D_2, HD and H_2. The tritium purity ϵ_T is defined as the ratio of the number of tritium atoms to the total number of atoms in the source [Bab12]. The measured signal rate S is proportional to these two parameters:

$$S = C \cdot \varrho d \cdot \epsilon_T \ . \tag{2.39}$$

The proportionality constant C contains experimental properties like detector efficiency, acceptance angles etc. [Bab12].

Evidently, a high signal rate is essential for KATRIN to achieve a high statistical sensitivity. For this reason, a high tritium purity of $\epsilon_T > 95\,\%$ of the WGTS source gas is targeted: the source gas will consist of approximately 90 % T_2, $< 10\,\%$ DT and trace admixtures of the other hydrogen isotopologues. The column density, on the other hand, cannot be increased arbitrarily, as a higher column density leads to an increase of scattering probabilities and thus higher energy losses of the β-electrons. Some will not be able to pass the spectrometer retarding potential any more due to these losses, so that the signal measured at the detector will saturate for large values of ϱd [Bab12]. In this case, equation 2.39 is not strictly valid any more. However, for the targeted column density value of $\varrho d = 5 \cdot 10^{17}\,\mathrm{cm}^{-2}$, the resulting non-linearity of above relation has been shown to be negligible [Bab12].

Apart from their influence on the statistical uncertainty of KATRIN, the column density and the isotopic composition of the WGTS are of high significance with respect to systematic uncertainties. Therefore, stringent requirements concerning the stabilization and monitoring of these parameters have to be met, as will be detailed in the following.

The column density

According to the proportionality given in equation 2.39, every fluctuation of the column density ϱd directly influences the measured count rate. In addition, the column density is related to the probability of inelastic scattering of β-electrons off the source gas molecules and thus to the associated energy losses [KAT05, Bab12]. For this reason, both a precise knowledge and a high stability of this parameter are vital for the neutrino mass determination [Pri15a]. In order to stay within the limits of the systematic uncertainty budget of $\sigma_{\mathrm{sys,ind}} \leq 7.5 \cdot 10^{-3}\,\mathrm{eV}^2/c^4$ (cf. subsection 2.5.1), the column density has to be monitored and stabilized to the 0.1 % precision level [KAT05]. ϱd is measured periodically between the actual neutrino mass measurement runs by using the electron gun; during runs, monitoring is achieved by combining BIXS measurements of the source activity and Raman measurements of the tritium purity ϵ_{T} to determine the column density via the relation

$$\varrho d = \frac{N(\mathrm{T})}{\epsilon_{\mathrm{T}} \cdot A_{\mathrm{S}}} \,. \tag{2.40}$$

In this expression, A_{S} is the cross section of the source tube and $N(\mathrm{T})$ the number of tritium atoms in the source, which is proportional to the activity measured by BIXS. Details on the measurement of the tritium purity will be given further below in subsection 2.5.4. The required stabilization of the column density to the 0.1 % level is achieved by stabilizing the related WGTS operating parameters to the same level, namely

- the gas injection rate into the source tube,
- the pumping speed of the turbo molecular pumps at both ends of the source tube,
- the beam tube temperature.

The pumping speed of the turbo molecular pumps depends mainly on their rotation frequency and is stable approximately to the 0.01 % level [Bab12]. For this reason, the stability of the gas injection rate into the WGTS is mainly determined by the pressure stability of the buffer vessel. In a test experiment, a pressure stability of almost one order of magnitude better than the required 0.1 % could be achieved [Pri15a]. Furthermore, the performance of the WGTS cryostat was tested in the so-called Demonstrator setup. The achieved temperature stability was more than one order of magnitude better than specified [Gro13].

The isotopic composition

As it directly affects the measured signal rate S as well, also the tritium purity ϵ_{T} has to be monitored on the 0.1 % level. However, knowing only the relative amount of tritium atoms is not sufficient; the isotopic composition of the source gas in its entirety has to be taken into account, as there are several systematic effects related to the differences of the molecular species in the WGTS:

- **Nuclear recoil:** In a β-decay, the daughter molecule experiences a recoil due to the emission of the produced lepton pair. The recoil energy, being not available as kinetic energy for the β-electron, reduces the endpoint energy of the spectrum

accordingly. Close to the tritium β-endpoint, the recoil energy corresponding to an electron energy E can be approximated by the following expression [KAT05]:

$$E_{\mathrm{rec}} \approx E \cdot \frac{m_{\mathrm{e}}}{m_{\mathrm{daughter}}} \ . \tag{2.41}$$

This expression is dependent on the mass of the daughter molecule, m_{daughter}, which differs significantly for the three daughter molecules of the tritiated hydrogen isotopologues: for instance, the mass of the $^3HeT^+$ daughter molecule from a T_2 decay is 1.5 times the mass of a $^3HeH^+$ nucleus from a HT decay. The resulting differences in the recoil energy translate directly into the endpoint energy. For this reason, the observed β-spectrum actually represents a superposition of the single spectra of the T_2, DT and HT β-decays with their respective endpoint energies, weighted by the relative concentration of each molecular species in the source gas.

- **Doppler effect:** The source gas molecules are subject to a random thermal motion according to the Maxwell-Boltzmann distribution [Höt12] as well as to a bulk motion due to their diffusion towards the ends of the WGTS tube. For this reason, the observed energies of the β-electrons are changed by the Doppler effect. In the non-relativistic approximation, the Doppler shift of an electron with mass m_{e} and velocity v_{e} (in the center-of-mass system of the decaying molecule) is given by [KAT05]

$$\Delta E \approx m_{\mathrm{e}} \cdot v_{\mathrm{e}} \cdot v_{\parallel,\mathrm{mol}} \ , \tag{2.42}$$

with $v_{\parallel,\mathrm{mol}}$ being the velocity component of the decaying molecule in the direction of the emitted electron. For KATRIN, the Doppler effect has to be considered in the spectral fit since the shift is of about the same order as the targeted neutrino mass sensitivity [Bab12]. As molecular velocities at a certain gas temperature depend mainly on the molecular masses, the Doppler broadening differs for the three tritiated hydrogen isotopologues T_2, DT and HT.

- **Elastic electron scattering:** β-decay electrons will scatter elastically and inelastically off source molecules. Inelastic scattering is accounted for by energy loss measurements by the e-gun in the calibration and monitoring system. However, elastic scattering processes also lead to a loss of electron energy [KAT05]:

$$\Delta E = 2 \cdot \frac{m_{\mathrm{e}}}{m_{\mathrm{mol}}} \cdot E_{\mathrm{e}} \cdot (1 - \cos\theta) \tag{2.43}$$

with the polar scattering angle θ. The energy loss depends on the mass m_{mol} of the molecule involved in the scattering process, and thus in total on the source gas composition. Although the average energy loss is rather low with only 16 meV since the scattering angles are typically small (about 3°), it can reach maximum values in the eV range [KAT05].

- **Final state distribution:** As briefly outlined in subsection 2.4.1, the daughter molecule in a tritium β-decay ends up in an excited state of excitation energy V_j, thus leading to an endpoint energy $E_{0,j} = E_0 - V_j$ below the total decay energy E_0 (cf. equation 2.25). The shape of the spectrum close to the endpoint thus depends on the probability distribution of these final states. While electronic excitations of

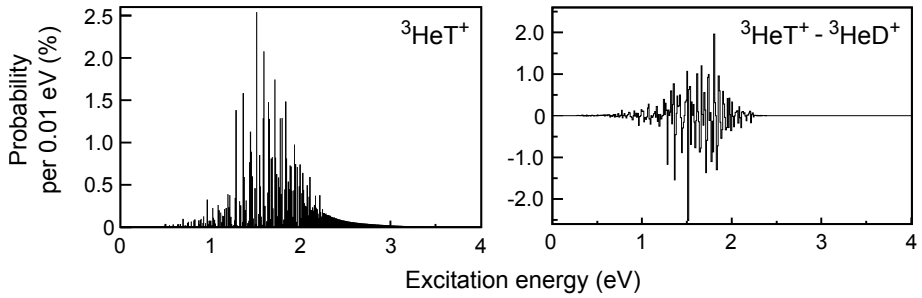

Figure 2.6.: Calculated final state distributions. *Left:* Final state distribution of the daughter molecule $^3HeT^+$ of a T_2 decay. *Right:* Difference between the final distribution of $^3HeT^+$ and $^3HeD^+$, the daughter molecules of the β-decays of the hydrogen isotopologues T_2 and DT. The nuclear recoil is already accounted for in these plots. Figure from [Sch13b], based on data from [Dos07].

hydrogen isotopologues play no role in the region of interest for the neutrino mass determination, i.e. the region of about 20 eV below E_0, rotational and vibrational excitations have to be taken into account [Bod15]. The final state distribution of the daughter molecule of a T_2 decay is shown in the left panel of figure 2.6; it was obtained via high-precision, ab initio calculations by N. Doss [Dos06, Dos07]. Due to the different masses of the hydrogen isotopologues, their final state distributions deviate from each other, as can be seen in the right panel of figure 2.6. This introduces another dependence of the measured β-spectrum on the gas composition.

The gas dynamical model of the WGTS, which will be used to analyze the measured β-spectra, takes into account these systematic effects [Kuc16, Höt12, Käf12]. For this purpose, the isotopic composition of the source gas during a measurement run has to be available as an input parameter, which requires continuous monitoring of the WGTS gas composition. Simulations have shown that the calibration uncertainty of the measurement system should not surpass about 10 % in order to achieve a systematic shift well below $\sigma_{\mathrm{syst}}(m_\nu^2) = 3 \cdot 10^{-3}\,\mathrm{eV}^2/c^4$ [Höt12, Sch13b]; the total uncertainty is in this case dominated by the uncertainty related to the theoretical description of the final states, which is estimated to be $6 \cdot 10^{-3}\,\mathrm{eV}^2/c^4$ [Bod15].

The measurement system chosen for the monitoring of the isotopic composition of the WGTS is a Raman spectroscopic system: LARA, the Laser Raman system for the KATRIN experiment. Its advantages and current performance are discussed in the following.

2.5.4. Monitoring of the source gas composition via Raman spectroscopy

Raman spectroscopy is a spectroscopic method based on inelastic scattering of light off molecules. The basic process is illustrated in the left panel of figure 2.7: an energy transfer between the photon and the molecule involved takes place, which changes both the rovibrational state of the molecule and the wavelength of the scattered photon [Dem08b].

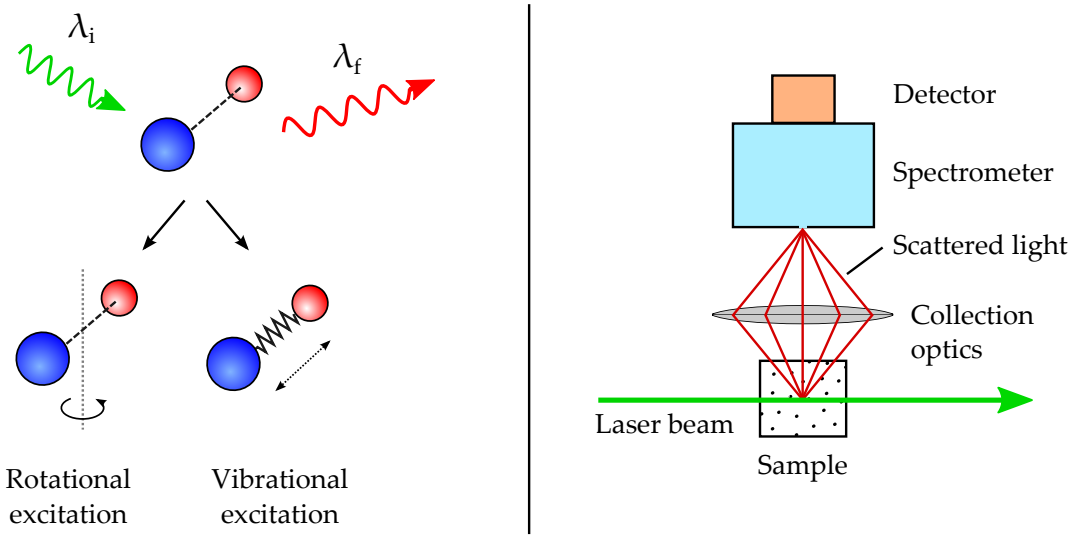

Figure 2.7.: Schematic illustration of the Raman scattering process *(left)* and a typical Raman setup *(right)*. In the left panel, the Stokes Raman scattering process is shown: incident light of the wavelength λ_i is scattered inelastically off a molecule. Parts of the photon energy are transferred into rotational and/or vibrational excitations, so that the wavelength of the scattered photon is shifted to the longer wavelength λ_f. Note that the inverse process is also possible; it is called anti-Stokes Raman scattering. The effect is utilized in compositional measurements with Raman systems as sketched in the right panel. A laser is usually used as the excitation light source since Raman scattering cross sections are extremely low, with typical scattering probabilities of the order of 10^{-7} for a single photon [Atk06]. The scattered light is collected by appropriate optics and analyzed by a spectrometer and a detector. Shown here is a conventional 90° observation geometry, in which the scattered light is observed perpendicular to the excitation beam to reduce the intensity of collected primary light. Other observation geometries will be discussed in section 3.3.

Details on the theoretical background of the Raman effect will be discussed in the following chapter. In the right panel of figure 2.7, a typical Raman measurement setup comprising an excitation light source, the sample and a light collection and detection system is shown. The gaseous, liquid or solid sample is probed by a laser beam, and a spectrum of the scattered light is acquired. The composition of the sample can be determined by analyzing this spectrum, since the wavelength change of the scattered light (Raman shift) is characteristic for the type of molecule the light is scattered off. Such a spectrum is shown in figure 2.8 for a gas mixture of hydrogen isotopologues.

Raman spectroscopy has been identified as an particularly advantageous technique for the composition monitoring task detailed in the previous subsection for a number of reasons. First of all, it allows for simultaneous detection of all hydrogen isotopologues using only one excitation wavelength, as demonstrated in figure 2.8. Molecular contaminations of the source gas – if present – can be detected as well. In addition, measurements can be performed in-line, without the need for potentially time-consuming sample-taking. Instead, automated and real-time data acquisition is possible. As the method is contact-

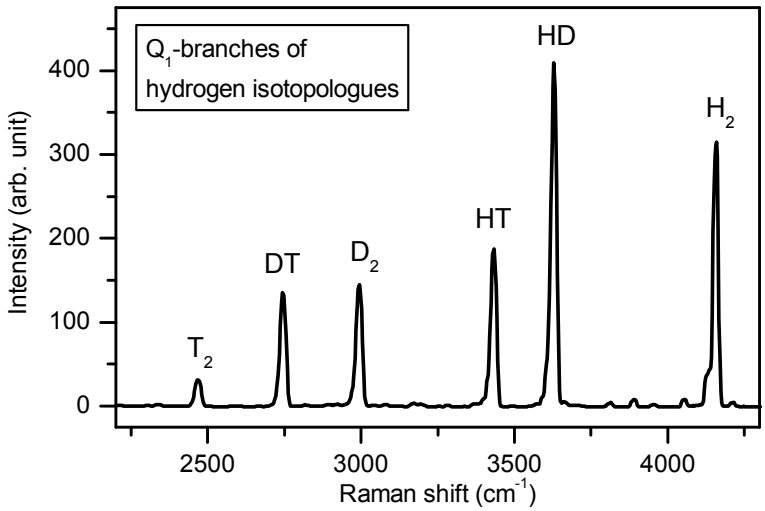

Figure 2.8.: Typical Raman spectrum of a gas mixture containing all hydrogen isotopologues. This spectrum was obtained by probing the sample gas with a 532 nm laser. Each peak visible in the spectrum can be assigned to a molecular species present in the sample by its characteristic Raman shift. Due to the large relative mass differences of the hydrogen isotopologues, their Q_1-branches are clearly separated from each other. This facilitates an unambiguous identification of the hydrogen-type gas constituents. In addition, quantitative information about the gas composition can be extracted from the peak intensities. Figure adapted from [Sch13b].

free, the environments of sample gas and optical system can furthermore be spatially separated to a certain extent in order to avoid contaminations.

For these reasons, a Laser Raman (LARA) system has been developed for the KATRIN experiment over the last years in cooperation between the Karlsruhe Institute of Technology and Swansea University [Sch15b]. The LARA system is a conventional 90° Raman system as sketched in the right panel of figure 2.7; a detailed description of its setup and components can be found in appendix A. The LARA system is integrated into the Inner Loop as illustrated in figure 2.5, measuring the composition of the tritium gas just before it enters the pressure controlled buffer vessel from which the gas is injected into the actual WGTS tube. At the place of measurement, the gas has a pressure of about 150 to 200 mbar and is still at room temperature before being cooled down to 30 K on its way towards the source tube.

A relative precision of better than the required 0.1 % was reached for measurement periods of 30 s each in a long-term performance test of the LARA system in the tritium test loop LOOPINO under realistic KATRIN Inner Loop conditions [Fis14]. In addition, a calibration uncertainty of only about 3 % was achieved [Sch13b, Sch13c], which is well within the uncertainty budget outlined in subsection 2.5.3. The KATRIN requirements with respect to precision and trueness can thus be fulfilled by the LARA system.

2.5.5. Compositional changes in the Inner Loop

In the previous subsections, the importance of accurately determining the isotopic composition of the source gas was stressed, and the high-performance Raman system used for compositional analyses was presented. However, one important question has still to be answered:

To which extent can the gas composition measured by LARA *at a certain position in the Inner Loop* be assumed to represent the gas composition *in the WGTS tube*?

Even though the uncertainty on the isotopic composition measured by LARA is well within the requirements, it does not yet include the additional uncertainty resulting from the fact that the composition of the gas might change by a certain extent on its way from the LARA measurement cell towards the WGTS source tube. If unsolved, this may constitute a serious limitation on the reliability of the uncertainty values connected to source systematics.

Possible effects leading to gas composition changes

In order to understand which effects could lead to a change of the gas composition, it is necessary to have a look at the gas system between the point of measurement and the source first. Before entering the actual WGTS tube, the gas from the LARA measurement cell passes a multitude of stainless steel pipes and other vacuum components while undergoing substantial pressure and temperature changes. This is illustrated in the schematic sketch in figure 2.9: the measurement cell is followed by about 2 m of tubing, before the gas enters the pressure-controlled buffer vessel by a regulating valve. At this point, the gas is still at room temperature. After several more meters of larger tubing, it reaches the injection capillary which has a substantially smaller inner diameter of 2.1 mm. This capillary runs along the WGTS cooling tube to cool the gas down to the source temperature of 30 K over a length of 5 m. Finally, the cold gas arrives at the injection chamber; its pressure at this point is about five orders of magnitude lower than at the point of measurement. From here, the gas is injected into the actual source tube through 415 holes with 2 mm diameter in order to prevent turbulences or jets in the injection process [KAT05].

A range of composition-changing effects may occur within this gas system:

(a) **Wall interactions:** There are a number of effects related to the stainless steel walls of the source tube and the tubing of the Inner Loop. Hydrogen can adsorb on the wall surface in molecular form or split into the individual atoms [Jou08], with a sticking coefficient which depends on the type of isotopologue or atom [Sou86]. In addition, atoms can diffuse into the walls and be absorbed [Jou08]. When atoms desorb from the surface, they recombine to form molecules again. The gas composition is influenced by these effects in various ways:

   (i) *Outgassing from walls:* A certain amount of absorbed hydrogen atoms is generally present in stainless steel walls. Apart from protium, there will also be deuterium present in the walls of the WGTS and Inner Loop, since the loop system will be tested with inactive D_2 gas prior to tritium operation.

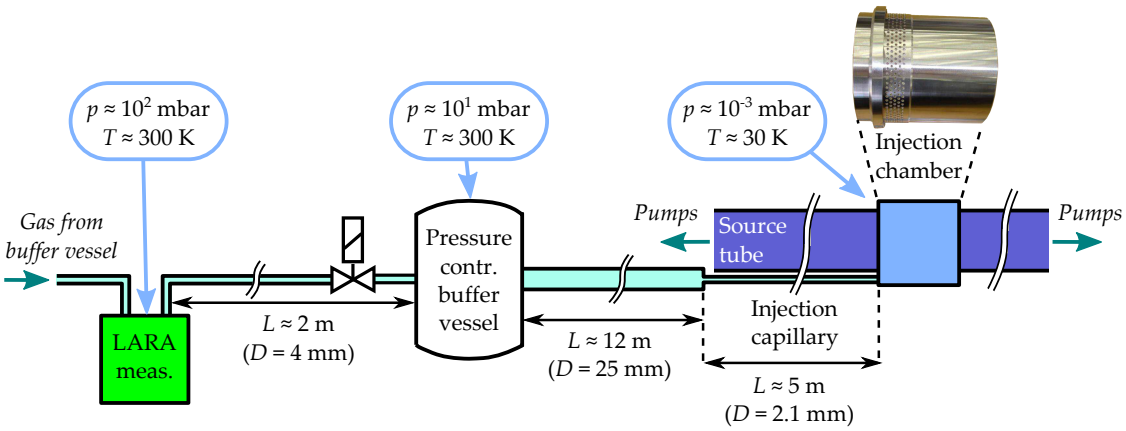

Figure 2.9.: Schematic illustration of the gas system between the LARA measurement point and the source tube. L stands for the approximate length and D for the inner diameter of the tubing. See main text for details. The picture of the injection chamber is taken from [Stu10].

When the system is evacuated or operated at low pressures, parts of this hydrogen and deuterium will diffuse out of the walls ("outgassing") [Jou08] and thus reduce the purity of the tritium gas by formation of H_2, HD and D_2. Although this effect is reduced by baking out the WGTS at temperatures around 500 K [KAT05] to minimize the amount of absorbed hydrogen, outgassing in the source cannot be fully avoided; besides, it is not possible to bake out the surfaces of the complete Inner Loop tubing as well.

(ii) *Isotopic exchange reactions:* Protium and deuterium atoms diffusing out of the walls can also recombine with tritium from the source gas, which is partly adsorbed on the wall. This process increases the fraction of HT and DT in the gas, as reported e.g. in [Gil80] and [Fis11].

(iii) *Diffusion into the walls:* The reverse process to the above-mentioned outgassing is absorption of source gas by diffusion into the walls. The gas composition is influenced as the probability for this process differs for the different source constituents.[3]

(iv) *Formation of secondary impurities:* Another effect linked to tritium-wall interactions is the formation of hydrocarbons, in particular of tritiated methanes such as CT_4, CHT_3 and CDT_3 [Gil80, Fis11]. As the carbon atoms originate from the steel walls themselves, this impurity formation cannot be reduced by such measures as baking out the system.

[3] Note that after exposing the loop to high-purity tritium for a long enough time, it can be expected that the walls will adapt to the prevailing composition, so that an approximate equilibrium with respect to compositional changes by diffusion both into and out of the walls will be reached. However, this process can take a long time. In the TriToP experiment, to name but one long-term measurement of the processes in a closed tritium loop, a continuous decrease of the tritium partial pressure was observed over 60 days of operation and almost half a year of total tritium exposure [Pri13b]. For this reason, it is not to be expected that an equilibrium will be reached in the much larger WGTS loops before the start of the actual KATRIN measurements.

(b) **Self-equilibration:** The β-activity of tritium can trigger the self-equilibration of gas mixtures whose composition does not correspond to the thermal equilibrium, even without catalytic materials present [Uda92].

(c) **Gas separation phenomena:** When mixtures of gases flow through long tubes such as the WGTS injection capillary, separation effects can occur due to the differing mean velocities, leading to a reduction of the concentration of lighter components along the tube [Sha05]. Apart from the length and diameter of the tube, the magnitude of this effect depends on the mass ratio of the involved molecules. The mass ratio is 6:5 and thus comparatively low for the main components of the WGTS source gas, T_2 and DT, but increases quickly to higher values for the minor, lighter gas constituents.

(d) **Radioactive decays:** For the sake of completeness, the decay of the radioactive isotopologues should also be mentioned as a composition-changing effect. However, with a half-life of 12.3 years for tritium, the fraction of tritiated molecules decaying inside the Inner Loop is well below 1 ppm and thus easily negligible.

Methods to estimate the compositional changes

In order for KATRIN to produce a neutrino mass result with reliable uncertainties, a quantitative understanding of the possible changes in isotopic composition of the source gas is indispensable. The ideal case would be to directly measure the composition inside the WGTS. However, the calibration and monitoring system of KATRIN (see subsection 2.5.2) provides only the possibility to determine the tritium purity ϵ_T directly in the source, and only in intervals of about every two hours: using on the one hand the electron gun to determine the column density ϱd in the intervals between the actual neutrino mass measurement runs, and on the other hand activity monitoring by the beta-induced X-ray spectrometry (BIXS) system, ϵ_T can be obtained via the relation given in equation 2.40. This value can be compared to the one measured by the LARA system, thus making it possible to detect deviations at least in the tritium fraction due to composition-changing effects between the LARA measurement and the source tube. However, while the number of tritium atoms in a certain amount of source gas molecules can be determined, the knowledge of the tritium purity fails to provide information about

- the distribution of the tritium atoms across the source molecules, and
- the ratio of inactive H and D atoms in the gas.

For instance, from a tritium purity point of view there is no difference between (T_2+H_2), (T_2+D_2), (T_2+HD), (HT + DT), 2 HT or 2 DT. Yet, in order to properly take into account composition-dependent systematic effects like the final state distribution (cf. subsection 2.5.3), it is vital to determine the actual molecular composition.

This is hard to accomplish in the source itself: a measurement system would not only have to be sensitive enough to achieve the required measurement precision at sub-μbar total pressures, but would also have to be implemented without interfering with the

sophisticated WGTS design required for an undisturbed source gas column.[4] For this reason, other possibilities to estimate the compositional changes have to be considered.

One approach is detailed modeling of the gas dynamics and composition-related effects in the whole gas system from the LARA measurement cell to the source tube. Certainly, simulations will be essential to our understanding of composition-related processes. However, the usefulness and reliability of such simulations is highly dependent on detailed experimental input about (i) above-mentioned effects – which is partly not yet available, especially for tritium-related topics – and (ii) characteristics of the setup at hand which cannot be predicted by simulations. To name but one example for the latter, virtual leaks might occur e.g. due to material defects in vacuum components: volumes of gas trapped in such a way that the gas is not effectively pumped off during evacuation, but is gradually released into the system later on [Cha89]. Such virtual leaks affect the system similarly to normal leaks, apart from not being detectable by helium leak tests beforehand.

For these reasons, any simulation approach will always have to be accompanied by appropriate measurements. Due to the system characteristics mentioned in item (ii), at least a certain part of these measurements have to be performed at the very Inner Loop and WGTS gas system under KATRIN-like conditions. The results of previous measurements using e.g. the simplified loop LOOPINO [Fis11, Fis14] or testing the Inner Loop system only with nitrogen and deuterium in order not to contaminate the system yet [Pri15a] have provided many helpful insights, but not all of them can be transferred one-to-one to the final system in operation. Therefore, it has been considered to test the compositional behavior in the Inner Loop by bypassing the permeator and the buffer vessel before the LARA system (cf. figure 2.5) for a certain period of time[5]. By this means, it would be possible to measure both the input and the output of the WGTS source tube in a quasi-batched way by the same measurement system. However, without the permeator removing impurities from the gas, there is a risk that high-mass hydrocarbon molecules possibly generated from non-metallic surfaces of the turbo molecular pumps (see [Pri13a, Pri13b]) could freeze out inside the WGTS source tube[6]. For this reason, another measurement option has to be considered.

Instead of just conducting a range of pre-measurements in a modified loop, the most reliable possibility would be to monitor the source gas composition not only before, but also after the source tube throughout KATRIN operation. Of course, there will be components between the source and the measurement system in this case as well – starting from the pumps needed to pump off the gas from the source tube in the first place. The data obtained after the WGTS will thus not directly represent the composition in the

[4] It should be noted that a rest gas analyzer (RGA) suitable for the required pressure range (MKS Instruments, HPQ3 [MKS16]) will be located directly after the WGTS in one of the differential pumping ports [KAT05]. However, it provides an accuracy of only about 10 to 15 %. In addition, proper interpretation of the acquired mass spectrometry data is not trivial. Parts of the analyte gas are fragmented in the ionization process required for this method, so that the fragments themselves as well as new molecules recombined from such fragments appear in the mass spectrum [Gro06, Pri13a]. Quantitative interpretation of the spectra would thus require precise knowledge of the different fragmentation probabilities. However, in-line calibration of the device is not possible, while any off-line calibration is rendered useless as the strong magnetic fields in the vicinity of the WGTS tube interfere with the internal magnetic field of the RGA.

[5] Internal suggestion by M. Schlösser, KATRIN collaboration, August 2015.

[6] Internal discussion contribution by B. Bornschein, KATRIN collaboration, September 2015.

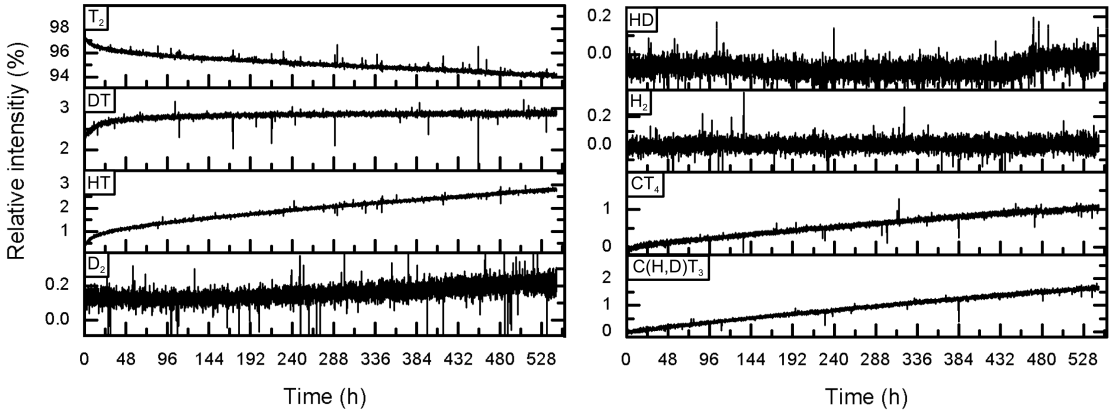

Figure 2.10.: Time evolution of the measured relative Raman intensities of gas constituents in the tritium test loop LOOPINO. The loop was tested under KATRIN-like conditions, with an initial high tritium purity of $> 98\,\%$. The plot shows the time evolution of the six hydrogen isotopologues as well as different types of tritiated methanes. Figure adapted from [Fis11].

source tube, but still provide very valuable input to probe our understanding and modeling of the processes in the gas system. Most of the composition-changing effects mentioned above can be expected to lead to the same trend of compositional changes at any position in the loop, as these changes are mainly driven by concentration differences. Thus, one expects a steady decrease of T_2 along with an increase in HT, DT and impurities such as tritiated methanes, as was already observed in previous tests with circulating T_2 gas [Fis11, Fis14, Pri13b]; an example of the measured time evolution in such a test is shown in figure 2.10. In this case, the values for the different molecular concentrations in the source could be assumed to lie at some point between the concentrations measured before and after the WGTS. The only one of the aforementioned effects which might counteract the expected trends in some parts of the Inner Loop, e.g. by locally increasing the T_2 concentrations, is the gas separation effect. Its local influences will have to be carefully simulated. In combination, simulations and composition measurements before and after the tube would provide a much improved understanding of the gas composition inside the actual gas tube and thus allow for a reliable estimation of the uncertainties connected to source systematics.

Framework conditions for a composition measurement after the WGTS

Ideally, one would like to use the same type of measurement system before and after the source tube, due to the advantages of Raman spectroscopy in general and the already demonstrated excellent performance of the LARA system in particular (cf. subsection 2.5.4). However, differences in the experimental conditions at the respective locations have to be taken into account, specifically the altered pressure regime.

At both ends of the WGTS, the source gas is being continuously pumped off by a number of turbo molecular pumps in two pumping stages (first pumping stage: Oerlikon Leybold Vacuum GmbH, TURBOVAC MAG W 2800 [Oer16]; second pumping stage: Pfeiffer

Vacuum, HiPace 300 [Pfe16]). Additional transfer pumps further downstream provide the low pressure required for operation of the turbo molecular pumps. This is shown schematically in figure 2.5. Actually, each pump icon in this figure represents several pumps; a more realistic flow diagram of the section of the Inner Loop at the WGTS comprising the first two pumping stages can be found in appendix B. The pressure after the first pumping stage is estimated to be of the order of 10^{-2} mbar, after the second pumping stage in the single-digit mbar range.[7]

A Raman system after the WGTS would have to be placed after the second pumping stage because of (i) space restrictions and (ii) the low total pressure after the first pumping stage. Even after the second pumping stage, the pressure is still about two orders of magnitude lower than at the LARA system before the WGTS. This means that the sensitivity of the system has to be enhanced by about two orders of magnitude in order to analyze the gas composition with equal quality at this position. Such an enhancement, however, is no trivial task. The performance of the LARA system for KATRIN – the result of years of development and optimization – is considered to be close to the ultimate reachable limit in conventional 90° configurations [Sch11a]. For this reason, alterations to the current implementation are required for a significant sensitivity enhancement. This constitutes the motivation of this thesis, which will be detailed in the following.

2.6. Objectives of this work

The principal goal of this work is to develop the optical design of a Raman system suitable to measure the gas composition after the WGTS. In particular, this task includes the following objectives:

- **Sensitivity:** The detection limit for tritium of the new system should be of the order of 10^{-3} mbar within acquisition times of a minute or less.

  This number arises from two reasons. Primarily, as discussed above, the new system should be about two orders of magnitude more sensitive compared to the standard LARA system to achieve a comparable performance at a pressure two orders of magnitude lower. The detection limit, i.e. the minimal partial pressure required to still be able to detect a certain gas species with sufficient confidence within a certain acquisition time, can serve as a measure for the sensitivity of a system; this will be explained in detail in subsection 3.2.1. With the standard LARA system, a detection limit of the order of 10^{-1} mbar in 20 s total acquisition time was achieved for hydrogen isotopologues [Sch13b]. A maximum acquisition time of about a minute is envisaged for KATRIN monitoring purposes.

  The main constituents of the source gas will occur at partial pressures substantially above the detection limit of the measurement system, so that they can be adequately monitored and quantified. This may not be the case for impurities being formed inside the WGTS gas system in trace amounts, e.g. tritiated methanes. Nevertheless, in order to obtain a comprehensive understanding of the processes in the loop, it would be highly desirable to be able to at least detect such impurities – especially

[7] M. Sturm, KATRIN Collaboration, private communication, January 2016.

as this is not possible with the standard LARA system due to its location after the gas-purifying permeator. The envisaged detection limit of the order of 10^{-3} mbar at total pressures in the millibar range will thus also allow the detection of trace impurities down to the permille level.

- **Tritium compatibility:** In addition, the new Raman system has to be fully tritium compatible.

  This requirement is connected to the material-degrading properties of tritium. Polymers, for instance, are known to deteriorate under tritium exposure, which can e.g. inhibit sealing functions [Cla07]. Halogenated polymers have to be particularly avoided in tritium systems, as their exposure can lead to the formation of corrosive acids and subsequent damages of components in the system [Cla07, Fis15]. For optical systems intended for long-term use in KATRIN, it has to be particularly ensured that the influence of tritium exposure on optical components such as coated windows or reflective surfaces does not substantially impede the functionality of the measurement system.

  Furthermore, it has to be taken into account that the new Raman system will have to be incorporated into a glove box for tritium-related safety reasons. Glove boxes offer very limited possibilities for fine-adjustments due to the thickness of the gloves, the lower box pressure sucking the gloves into the box, and constraints in viewing and accessing components or beam paths. In addition, measurement conditions in a glove box are normally less controlled than in optical experiments outside, so that vibrations and temperature changes in the range of few Kelvins have to be expected. For this reason, an easy-to-align and robust setup should be envisaged.

The structuring of this thesis reflects these main aims: after a discussion of appropriate sensitivity enhancement methods in chapter 3, the setup and test of a signal-enhanced prototype for tritium gas analysis is described in chapter 4. Based on the results obtained in this test, chapter 5 focuses on improvements of the suitability of such a system for operation in tritium environments. The topic of chapter 6 is the optimization of the optical design and measurement parameters in order to maximize the sensitivity of the new Raman system. Finally, the results achieved with the optimized system are presented in chapter 7.

3. High-sensitivity Raman spectroscopy: Basic concepts and enhancement strategies

This chapter has two aims: first, it provides the theoretical background and terminology required for the understanding of this thesis. Second, it gives an introduction into the topic of high-sensitivity Raman spectroscopy in general and hollow waveguide based Raman spectroscopy – the main focus of this thesis – in particular.

The chapter starts with a theoretical overview of the principles of Raman spectroscopy and the calculation of Raman line positions and intensities in section 3.1. In section 3.2, relevant terms and definitions connected to high-sensitivity Raman spectroscopy are explained. Afterwards, methods to enhance the Raman signal are discussed in section 3.3. The chapter ends with an introduction to the enhancement method employed within this work, namely hollow waveguide based Raman spectroscopy: section 3.4 outlines the concept of this method and the current state of research in this field.

3.1. Theoretical description of the Raman effect

The Raman effect is named after C. V. Raman, who discovered it in 1928 together with K. S. Krishnan [Ram28], after it had been theoretically predicted by A. Smekal five years earlier [Sme23]. As introduced in subsection 2.5.4, it describes an inelastic scattering process between photons and molecules, with the wavelength of the scattered light being characteristic for the type of molecule the light is scattered off. For this reason, the Raman effect can be utilized for compositional analysis of molecular samples such as the WGTS source gas.

In the previous chapter, the basic concept as well as the various advantages of this spectroscopic technique for the KATRIN source composition monitoring task were presented, and the motivation for this work on high-sensitivity Raman spectroscopy was explained. In the following, the theoretical background of the Raman effect will be treated as far as necessary for the understanding of this thesis. The reader is referred to the following textbooks for further reading: [Lon02], [Dem08b], [Hak06] and [Atk06]. If not stated otherwise, the contents of this section is based on these textbooks.

3.1.1. Rotational and vibrational states of diatomic molecules

Molecular spectroscopic techniques in general utilize photon-molecule-interactions which are connected to transitions between different molecular quantum states. In order to understand the Raman effect, it is thus necessary to study the quantum states of molecules. Since the focus in this thesis is on Raman spectroscopy of hydrogen isotopologues, the theory given here is restricted to the special case of diatomic molecules.

There are three different types of excited states of molecules: electronic, vibrational and rotational ones. Electronic excitations of hydrogen isotopologues are outside of the energy range considered here – visible light and room temperature – and are thus not of relevance for this work. For this reason, the following theoretical treatment of rotational and vibrational states assumes molecules in the electronic ground state.

Semi-classical models of rotating and vibrating two-body systems can be employed to obtain approximate terms for the energy levels of molecular excitations. Basic models are illustrated in figure 3.1: the so-called rigid rotator serves as a simple model for the rotation of diatomic molecules, while molecular vibrations can be approximated within an oscillator model. By combining both models, a non-rigid, oscillating rotator can be used to describe rovibrational excitations. The related energy level calculations are presented in the following paragraphs.

Note that in the field of molecular spectroscopy, it is common to express energies in wavenumbers $\bar{\nu}$, which are related to the frequency $\nu = \omega/2\pi$ and the wavelength λ of a photon according to

$$\bar{\nu} = \frac{E}{hc} = \frac{\nu}{c} = \frac{1}{\lambda} \tag{3.1}$$

with Planck's constant h and the speed of light c.

Rotational states: In a purely classical description, a simple rigid rotator with angular frequency ω as shown in figure 3.1 (a) has a rotational energy of

$$E_{\mathrm{rot}} = \frac{1}{2}\Theta\omega^2 = \frac{L^2}{2\Theta} \tag{3.2}$$

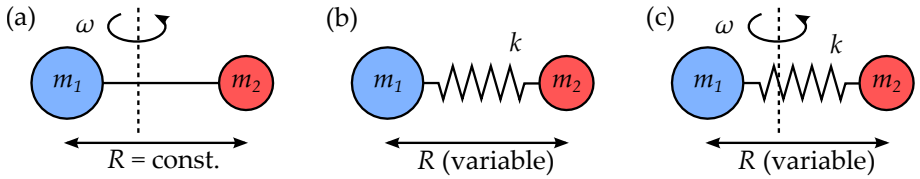

Figure 3.1.: Models of excited diatomic molecules. *(a)* Rigid rotator. Two atoms with masses m_1 and m_2 are located in a fixed distance R to each other. They rotate around the center of mass of the molecule with the angular frequency ω. *(b)* Oscillator. The two atoms oscillate with the spring constant k. *(c)* Rotating oscillator. In this case, the molecule rotates and oscillates at the same time.

with the molecule's moment of inertia Θ and the angular momentum $L = \Theta\omega$. For molecules as quantum mechanical systems, however, this angular momentum is quantized according to

$$L = \hbar\sqrt{J(J+1)}\ , \quad J = 0, 1, 2, ... \tag{3.3}$$

with the rotational quantum number J. This leads to the quantized energy levels of rotational eigenstates:

$$E_{\mathrm{rot}} = \frac{\hbar^2}{2\Theta} J(J+1)\ . \tag{3.4}$$

Expressed in wavenumbers, the rotational energy eigenvalues are given by

$$\tilde{F}_{\mathrm{rot}} = \frac{E_{\mathrm{rot}}}{hc} = BJ(J+1) \quad \text{with} \quad B = \frac{h}{8\pi^2 c\Theta}\ . \tag{3.5}$$

B is the so-called rotational constant. Depending solely on the moment of inertia of the molecule, it is characteristic for each molecular species.

While this approximation leads to evenly spaced rotational levels of a molecule, in reality the levels move closer together with increasing J due to centrifugal stretching of the molecule. This can be better accounted for by using the model of a non-rigid rotator, in which the moment of inertia increases progressively with increasing J. In this model, equation 3.5 is modified to

$$\tilde{F}_{\mathrm{rot}} = BJ(J+1) - DJ^2(J+1)^2 \tag{3.6}$$

with the centrifugal stretching constant $D > 0$. It should be noted that the ratio D/B is typically of the order of 10^{-4}, so that the corrections are relatively small. In high resolution spectroscopy, however, additional correction terms might be necessary in order to achieve a good description of the spectra [Her63].

Vibrational states: A very basic model for diatomic vibration is the (harmonic) oscillation of two masses connected by a spring, as illustrated in figure 3.1 (b). In this first approximation, the potential is assumed to be quadratic:

$$V(R) = \frac{k}{2}(R - R_{\mathrm{e}})^2 \tag{3.7}$$

with the internuclear distance R, the equilibrium distance R_{e} and the spring constant k. The energy levels of the resulting harmonic oscillations are given by [Coh77]

$$\tilde{G}_{\mathrm{vib,h}} = \frac{E_{\mathrm{vib,h}}}{hc} = \frac{\hbar\omega}{hc}\left(v + \frac{1}{2}\right) = \tilde{\nu}_{\mathrm{e}}\left(v + \frac{1}{2}\right) \quad \text{with} \quad \tilde{\nu}_{\mathrm{e}} = \frac{1}{2\pi c}\sqrt{\frac{k}{\mu}}\ . \tag{3.8}$$

The vibrational quantum number is $v = 0, 1, 2, ...$. The wavenumber $\tilde{\nu}_{\mathrm{e}}$ corresponds to the eigenfrequency ν_{e} of the harmonic oscillator; μ is the reduced mass of the molecule. The equidistant energy levels resulting from the quadratic potential are shown in figure 3.2 (a).

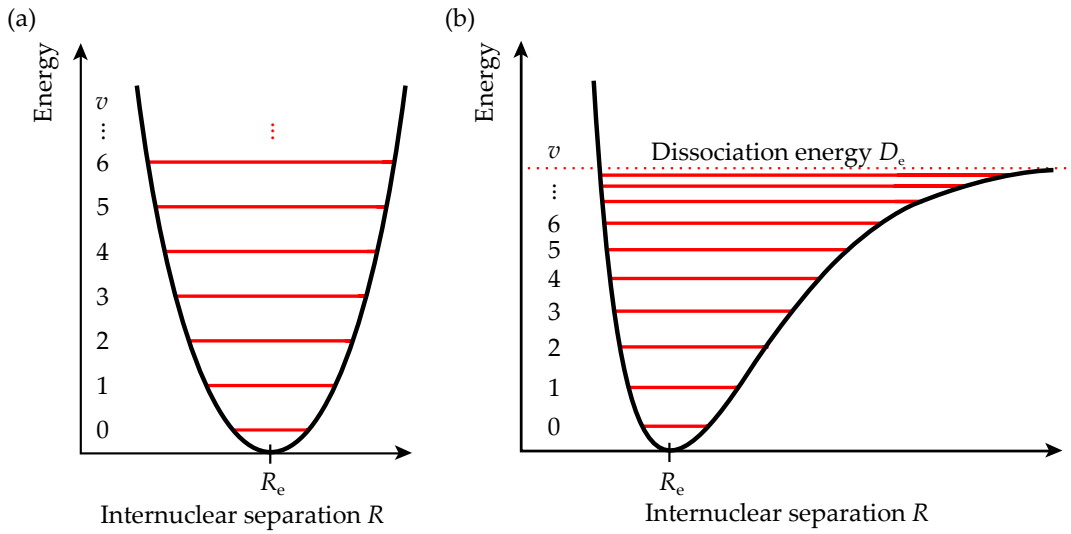

Figure 3.2.: Potential curves and energy levels of oscillating systems.
(a) Quadratic potential (harmonic oscillation). *(b)* Morse potential (anharmonic oscillation).

This approximation of a harmonic oscillator works only for small values of v. In reality, the atomic bond is weakened to the point of dissociation of the molecule if the internuclear distance R is increased significantly. A better approximation of the molecular potential and thus for an anharmonic oscillator is e.g. the Morse potential shown in panel (b) of the figure:

$$V(R) = D_e \cdot \left(1 - e^{-a(R-R_e)}\right)^2 \quad \text{with} \quad a = \tilde{\nu}_e \cdot \sqrt{\frac{\mu}{2D_e}} \,. \tag{3.9}$$

D_e is the dissociation energy. In this approximation, an anharmonicity term with anharmonicity constant $x_e > 0$ is added to equation 3.8:

$$\tilde{G}_{\text{vib,anh}} = \tilde{\nu}_e \left(v + \frac{1}{2}\right) - \tilde{\nu}_e x_e \left(v + \frac{1}{2}\right)^2 \,. \tag{3.10}$$

Thus, the energy levels move closer together for higher quantum numbers v. This is illustrated in figure 3.2 (b).

Rovibrational states: So far, rotational and vibrational excitations have been treated as being completely decoupled from each other. However, when rotations and vibrations are excited at the same time, as is generally the case under the conditions considered in this work, the influence on each other has to be taken into account: as seen before, the mean internuclear separation R becomes larger for higher values of the vibrational quantum number v. Similarly to the centrifugal stretching discussed above, this vibrational stretching increases the moment of inertia of the molecule, Θ, and thus decreases the rotational constant B according to equation 3.5. For this reason, the rotational constant

B and the stretching constant D have to be expressed by terms dependent on v in order to describe rovibrational excitations:

$$B_v = B - \alpha\left(v + \frac{1}{2}\right) \ , \tag{3.11}$$

$$D_v = D - \beta\left(v + \frac{1}{2}\right) \ . \tag{3.12}$$

α and β are correction factors which are characteristic for the molecule type. Using these modified terms, one obtains the following rovibrational energy levels:

$$\tilde{T}(v, J) = \tilde{G}(v) + \tilde{F}(v, J) \tag{3.13}$$

$$= \tilde{\nu}_\mathrm{e}\left(v + \frac{1}{2}\right) - \tilde{\nu}_\mathrm{e}x_\mathrm{e}\left(v + \frac{1}{2}\right)^2 + B_v J(J+1) - D_v J^2(J+1)^2 \ . \tag{3.14}$$

Again, additional minor correction terms (as discussed e.g. in [Her63]) can be added to further improve the description of these energy levels. With regard to the spectra obtained in the scope of this work, however, the approximation given above is sufficient.

3.1.2. Basic principle of Raman scattering

Transitions between the energy states of a molecule can be mediated by photons:

A photon of energy $h\nu$ can be absorbed or emitted when the resonance condition is met, i.e. $\Delta E = h\nu$ with ΔE being the energy difference between two molecular quantum states. This interaction is described by the Hamiltonian

$$H = -\vec{p} \cdot \vec{E} \tag{3.15}$$

with the electric dipole moment $\vec{p}$ of the molecule and the electric field vector $\vec{E}$ of the electromagnetic wave. Only molecules with a permanent electric dipole moment can absorb or emit light, which excludes homonuclear diatomic molecules such as H_2, D_2 and T_2 from this kind of interaction. For this reason, these molecules cannot be detected for instance in infrared absorption spectroscopy.

Another possibility is scattering of light off molecules, in which case the resonance condition does not have to be met. The Raman effect is such a scattering process, as sketched in the left panel of figure 2.7 in the previous chapter. In the classical description of the Raman effect, an incident electromagnetic wave with electric field vector $\vec{E} = \vec{E_0} \cdot \cos(\omega t)$ induces an oscillating dipole moment

$$\vec{p}_\mathrm{ind} = \boldsymbol{\alpha} \cdot \vec{E} \tag{3.16}$$

in a molecule with polarizability tensor $\boldsymbol{\alpha}$. In addition, the molecule may have a permanent dipole moment $\vec{\mu}_0$. Both the polarizability and the permanent dipole moment, if existing, depend on the configuration of the nuclei in the molecule. An incoming light wave polarizing the electron shell will lead to small oscillations of the nuclei around the equilibrium position, so that an expansion into a Taylor series with respect to the normal coordinates of vibration q_n is possible. Neglecting second- and higher-order terms, this

leads to the following expression for the electric dipole moment and the polarizability tensor components:

$$\vec{\mu} = \vec{\mu}(0) + \sum_n \left(\frac{\partial \vec{\mu}}{\partial q_n}\right)_0 q_n \ , \tag{3.17}$$

$$\alpha_{ij}(q) = \alpha_{ij}(0) + \sum_n \left(\frac{\partial \alpha_{ij}}{\partial q_n}\right)_0 q_n \ . \tag{3.18}$$

$\vec{\mu}(0)$ and $\vec{\alpha}(0)$ are the dipole moment and the polarizability in the equilibrium $q_n = 0$.

Assuming harmonic oscillations for the normal coordinates q_n of the vibrating molecule, i.e. $q_n(t) = q_{n0}\cos(\omega_n t)$ with the amplitude q_{n0} and the frequency ω_n of the n-th normal vibration, the total time-dependent dipole moment is given by

$$\vec{p} = \vec{\mu}_0 + \boldsymbol{\alpha}\vec{E} \tag{3.19}$$

$$= \vec{\mu}_0 + \sum_n \left(\frac{\partial \vec{\mu}}{\partial q_n}\right)_0 q_{n0}\cos(\omega_n t) + \alpha_{ij}(0)\vec{E}_0\cos(\omega t) + \frac{E_0}{2}\sum_n \left(\frac{\partial \alpha_{ij}}{\partial q_n}\right)_0 q_{n0}\left[\cos(\omega-\omega_n)t + \cos(\omega+\omega_n)t\right] \ . \tag{3.20}$$

In the last term, the trigonometric identity $\cos x \cos y = \frac{1}{2}(\cos(x-y) + \cos(x+y))$ was used.

Apart from the first term, which describes the (potential) permanent dipole moment in the equilibrium configuration, all terms of this time-dependent dipole moment are subject to oscillations. Oscillating dipole moments, however, lead to the generation of new electromagnetic waves:

- The second term describes the part of the permanent dipole moment which follows the molecular vibration and thus accounts for the infrared spectrum of the molecule.
- The third term describes the induced dipole moment, which depends on the polarizability and is modulated by the incident wave. It gives rise to elastic scattering of light: the frequency of incident and scattered light are the same. This scattering process is called Rayleigh scattering.
- The last term is the one describing the Raman effect. It depends on the change of the polarizability connected to the oscillation of the nuclei. Since the frequency of the emitted light is shifted with respect to the incident light, this type of scattering is called "inelastic". There are two possibilities for a frequency shift: in the so-called Stokes Raman process, the Raman light is shifted to lower angular frequencies $(\omega - \omega_n)$. The reverse process, anti-Stokes Raman scattering, can only take place when the molecule is in an excited state prior to the scattering, so that energy can be transferred to the photon and give rise to a higher angular frequency $(\omega + \omega_n)$. In contrast to infrared spectroscopy, Raman spectroscopy is sensitive to all hydrogen isotopologues as even the homonuclear ones undergo non-vanishing polarizability changes under light exposure.

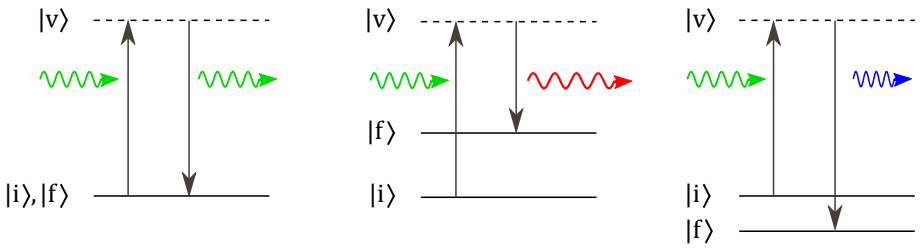

Figure 3.3.: Different types of photon scattering in the quantum mechanical picture. $|\mathrm{i}\rangle$ denotes the initial, $|\mathrm{f}\rangle$ the final and $|\mathrm{v}\rangle$ the virtual state. *Left:* Rayleigh scattering (elastic, $E_\mathrm{i} = E_\mathrm{f}$). *Center:* Stokes Raman scattering (inelastic, $E_\mathrm{i} < E_\mathrm{f}$, red-shifted). *Right:* Anti-Stokes Raman scattering (inelastic, $E_\mathrm{i} > E_\mathrm{f}$, blue-shifted).

The processes connected to the polarizability of a molecule, i.e. Rayleigh scattering and the two types of Raman scattering, are illustrated in figure 3.3 in the quantum mechanical picture. In this picture, a molecule in a certain initial state is excited into a virtual state by absorbing a photon. The final state is reached by emitting a photon again. While initial and final state are the same for elastic Rayleigh scattering, the differ by a certain amount of energy in the case of inelastic Raman scattering. The difference between the energy levels of initial and final state, $\Delta E = E_\mathrm{f} - E_\mathrm{i}$, is equal to the energy difference between incident and emitted photon and thus determines the frequency difference. It is expressed by the shift in wavenumbers, the so-called Raman shift:

$$\Delta\bar{\nu} = \bar{\nu}_\mathrm{i} - \bar{\nu}_\mathrm{f} = \frac{E_\mathrm{i} - E_\mathrm{f}}{hc} = \frac{\Delta E}{hc} \ . \tag{3.21}$$

Taking into account the rovibrational energy levels $\tilde{T}(v, J)$ of a diatomic molecule given in equation 3.14, the line position in a Raman spectrum corresponding to a transition between two rovibrational states with quantum numbers (v', J') and (v'', J''), respectively, is described by the following Raman shift:

$$\Delta\bar{\nu} = \frac{\Delta E}{hc} = \Delta\tilde{T} = \tilde{T}(v', J') - \tilde{T}(v'', J'') \ . \tag{3.22}$$

Raman transitions between molecular states are constrained by the following selection rules:

- **Rotational transitions:** Since Raman scattering involves two photons, i.e. spin-1 particles, only transitions with $\Delta J = 0, \pm 2$ can take place.
- **Vibrational transitions:** Assuming a harmonic oscillator, the selection rule for transitions between vibrational states is $\Delta v = 0, \ \pm 1$. In the anharmonic case, overtone transitions with $\Delta v = \pm 2, \ 3, \ \ldots$ are also possible, although much less probable [Hak06].

In figure 3.4, the schematic Raman spectrum of a diatomic molecule as resulting from the allowed transitions between the energy levels discussed above is shown. The spectral lines related to the different scattering types – Stokes Raman, Anti-Stokes Raman and Rayleigh scattering – in a Raman spectrum are classified according to above selection rules by grouping transitions with the same ΔJ and Δv into spectral branches. An overview of these branches and their nomenclature is given in table 3.1.

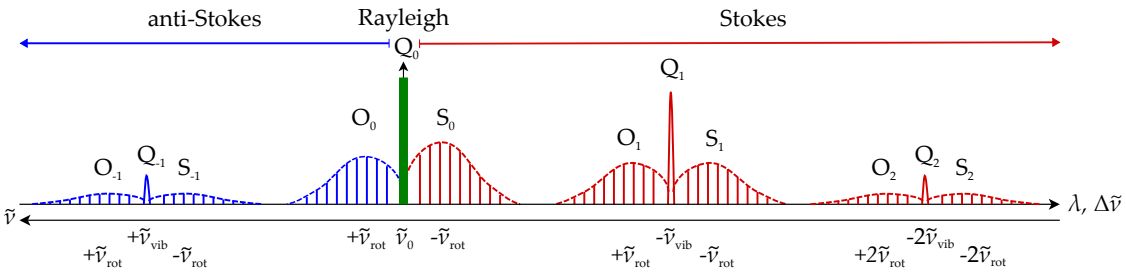

Figure 3.4.: Schematic Raman spectrum of a diatomic molecule at room temperature. The branches corresponding to the different transitions are labeled in the plot. It is clearly visible that the Raman shift connected to vibrational excitations is much larger in comparison to rotational excitations. In addition, the spectrum shows that not only the overtone transitions discussed in the text but also the anti-Stokes Raman lines are less intense than the Stokes Raman lines. This is associated with the fact that the anti-Stokes process requires the molecule to be initially in an excited state. As the number of excited molecules is described by the Boltzmann distribution, the intensity of anti-Stokes Raman lines decreases for lower temperatures. Figure adapted from [Hak06].

Table 3.1.: Classification of branches in the Raman spectrum according to selection rules. This work uses the branch nomenclature introduced by Richard Lewis [Lew07]: the letters O, Q and S represent a ΔJ of $-2\,,0$ and $+2$, respectively, while the index of each letter indicates the Δv value. Overtone and anti-Stokes Raman transitions are of no further relevance for this thesis and are thus not included in the table.

Scattering type	Δv	ΔJ	Branch name	Raman shift
Rayleigh	0	0	Q_0	-
Stokes Raman (pure rotation)	0	+2	S_0	$\tilde{\nu}_\mathrm{i} - \tilde{\nu}_\mathrm{rot}$
Stokes Raman (rotation-vibration)	1	−2	O_1	$\tilde{\nu}_\mathrm{i} - \tilde{\nu}_\mathrm{vib} + \tilde{\nu}_\mathrm{rot}$
	1	0	Q_1	$\tilde{\nu}_\mathrm{i} - \tilde{\nu}_\mathrm{vib}$
	1	+2	S_1	$\tilde{\nu}_\mathrm{i} - \tilde{\nu}_\mathrm{vib} - \tilde{\nu}_\mathrm{rot}$

With respect to the analysis of Raman spectra, it should be noted that the single rotational lines of Q branches are much closer together than those of S and O branches, a fact reflected in the schematic spectrum in figure 3.4. While these lines can still be resolved in high-resolution spectroscopy, this is often not the case in overview spectra as required for the simultaneous monitoring of all six hydrogen isotopologues. Instead, these lines add up to what seems to be one very intense spectral peak, as is clearly visible in the spectrum of a hydrogen gas mixture shown in figure 2.8 in the previous chapter. Due to this high intensity and the clear separation of the Q_1 branches of the hydrogen isotopologues resulting from their large relative mass differences, these peaks are used for the analysis of the Raman spectra for KATRIN.

3.1.3. Raman line intensities

Apart from the line positions discussed so far, the other important parameter characterizing a Raman spectrum is the intensity of each line. Line intensities are already included qualitatively in the schematic spectrum in figure 3.4; they will be discussed in a quantitative way in the following.

When a population of diatomic molecules is exposed to irradiation, the line intensity related to a given transition of a certain molecule type is given by [Lon02]

$$I(\varphi,\theta)_{p^\mathrm{s},p^\mathrm{i}} = k_{\tilde{\nu}} \cdot \mathcal{I} \cdot \tilde{\nu}_\mathrm{s}^4 \cdot \Phi(\varphi,\theta,a,\gamma)_{p^\mathrm{s},p^\mathrm{i}} \cdot N_\mathrm{i} \ . \tag{3.23}$$

Before the individual factors are explained, it should be noted that this equation applies only if the scattered intensity is measured in units of power [McC06]. In many detector systems, in particular also the charged-coupled device (CCD) detector employed in this work, the number of scattered photons is measured instead. In this case, above equation has to be modified by replacing the factor $\tilde{\nu}_\mathrm{s}^4$ by $\tilde{\nu}_\mathrm{i} \cdot \tilde{\nu}_\mathrm{s}^3$ to take into account the energy carried by each scattered photon [McC06]:

$$I(\varphi,\theta)_{p^\mathrm{s},p^\mathrm{i}} = k_{\tilde{\nu}} \cdot \mathcal{I} \cdot \tilde{\nu}_\mathrm{i} \cdot \tilde{\nu}_\mathrm{s}^3 \cdot \Phi(\varphi,\theta,a,\gamma)_{p^\mathrm{s},p^\mathrm{i}} \cdot N_\mathrm{i} \ . \tag{3.24}$$

The terms and constants in this equation are briefly discussed in the following. A detailed discussion can be found in [Lon02].

$k_{\tilde{\nu}}$ is a constant given by

$$k_{\tilde{\nu}} = \frac{\pi^2}{\epsilon_0^2} \approx 1.259 \cdot 10^{23}\,\mathrm{m^2F^{-2}} \tag{3.25}$$

with the vacuum permittivity ϵ_0.

$\mathcal{I}$ denotes the irradiance of the incident light, i.e. the radiant flux incident per unit area (measured in $\mathrm{W/m^2}$) [Dem08a].

$\tilde{\nu}_\mathrm{i}$, $\tilde{\nu}_\mathrm{s}$ are the wavenumbers of the incident laser ($\tilde{\nu}_\mathrm{i}$) and the scattered Raman light ($\tilde{\nu}_\mathrm{s}$).

$\Phi(\varphi,\theta,a,\gamma)_{p^\mathrm{i},p^\mathrm{s}}$ is the so-called line strength function. It describes the transition probability of a certain Raman transition. The line strength function can be calculated using components of the polarizability tensor $\boldsymbol{\alpha}$ which was introduced in subsection 3.1.2. By taking the isotropic averages of quadratic products of polarizability tensor components, one obtains molecule-dependent tensor invariants, two of which are of relevance in the case of diatomic molecules: the average polarizability, a, and the anisotropy of the polarizability, γ [Lon02].

The line strength function depends on the polarization of incident and scattered light (p^i, p^s) as well as on the scattering geometry. The latter is described by the angles θ and φ which define the direction of the scattered beam relative to the reference coordinate system. A figure illustrating the definition of the scattering angles and the polarization states can be found in appendix C, together with the expressions of the line strength functions for $\perp$- and $\parallel$-polarized light.

N_i represents the number of molecules in the initial state of the considered transition. In thermodynamic equilibrium, it is defined by a Boltzmann distribution; this leads to the characteristic intensity distribution the lines in the O and S branches in figure 3.4. N_i is described by the following equation:

$$N_\mathrm{i} = N \cdot \frac{g_\mathrm{i} \cdot \exp\left(-\frac{E_\mathrm{i}}{k_\mathrm{B}T}\right)}{Z} \ . \tag{3.26}$$

In this expression, N is the total number of irradiated molecules, E_i and g_i are the energy and the statistical weight of the initial state, $k_\mathrm{B}T$ is the thermal energy at a given temperature T, and Z is the molecular partition function:

$$Z = \sum_j g_j \cdot \exp\left(-\frac{E_j}{k_\mathrm{B}T}\right) \ . \tag{3.27}$$

The statistical weight, which accounts for the degeneracy of molecular states, consists of the respective statistical weights of vibrational and rotational states: $g_\mathrm{i} = g_v \cdot g_{J''}$ with J'' being the rotational quantum number of the lower energetic state involved in the scattering process. The vibrational levels are non-degenerate in the case of diatomic molecules considered here, i.e. $g_v = 1$. On the other hand, $g_{J''}$ depends on the rotational quantum number and the nuclear spin degeneracy g_N:

$$g_{J''} = g_\mathrm{N} \cdot (2J'' + 1) \ . \tag{3.28}$$

The nuclear spin degeneracy depends on the type of molecule involved. In the case of the heteronuclear diatomic molecules HD, HT and DT, no parity can be defined, so that $g_\mathrm{N} = 1$. The homonuclear hydrogen isotopologues, in contrast, are subject to nuclear spin statistics, so that the value of g_N depends on the nuclear spin of the atoms involved and differs for odd and even J'' values. Details on the underlying theory can be found for instance in [Her63]. The values of g_N for the six hydrogen isotopologues and odd/even J'' values are listed in table 3.2.

To understand the factors influencing Raman intensities is essential for this thesis, as the main objective is to increase the sensitivity of a Raman system. The sensitivity is closely related to the Raman signal measured with a certain system, and thus to the intensity of the emitted light. The relation between intensity, signal and sensitivity will be discussed in detail in the following section.

Table 3.2.: Nuclear spin degeneracy g_N of the hydrogen isotopologues.

	H_2, T_2	D_2	HD, HT, DT
g_N for J'' odd	3	3	1
g_N for J'' even	1	6	1

3.2. Important terms in high-sensitivity Raman spectroscopy

The previous section provided the theoretical input to understand the spectrum and the factors influencing the intensity of light emitted in Raman scattering processes. In order to achieve high sensitivities in Raman spectroscopy, however, high Raman intensities at the point of emission are not enough: the actually measured spectrum is equally dependent on a number of experimental and setup-related factors. This section will clarify the definition of important terms related to to the sensitivity of a Raman system and discuss the experimental prerequisites for achieving high sensitivities.

3.2.1. Definition of detection limit and signal-to-noise ratio

In order to assess the sensitivity of a Raman system, it is necessary to be able to quantify it. One possibility which is very common in the field of chemical analysis is the detection limit (also 'limit of detection', LOD). It denotes the smallest quantity of an analyte which can still be detected with reasonable certainty [IUP76, IUP97]. As the focus of this work is on the compositional analysis of gas mixtures, it is convenient to express analyte quantities in terms of their respective partial pressure in the gas mixture. Thus, within the scope of this work, the detection limit will be defined as the minimal partial pressure an analyte can have and still be detected.

According to the IUPAC definition, the detection limit can be derived from the smallest detectable analyte amount, x_L, which is given by [IUP76]

$$x_\mathrm{L} = \overline{x}_\mathrm{blank} + k \cdot s_\mathrm{blank} \ . \tag{3.29}$$

The numerical factor k represents the desired confidence level. A value of $k = 3$ is recommended by IUPAC, corresponding – in the case of background fluctuations following a normal distribution – to a 99.86 % probability that a signal at the detection limit is really a positive signal rather than a random background fluctuation [Lon83]. $\overline{x}_\mathrm{blank}$ and s_blank are the mean and the standard deviation of the blank measures, i.e. measurements of a sample of basically the same composition as the sample of interest but which does not contain the analyte. In order to determine the detection limit of a Raman system using equation 3.29, the corresponding quantities have to be extracted from measured Raman spectra. Figure 3.5 illustrates spectra-related terms which are important for the analysis:

The background is an undesired, but not fully avoidable byproduct of a Raman measurement; its origins will be discussed in subsection 3.2.3. It is in general independent of the analyte and corresponds thus to the blank measurement. However, it can be subtracted by appropriate background removal routines in the analysis of Raman spectra; this is commonly done to obtain pure Raman signals. In this case, a value of $\overline{x}_\mathrm{blank} = 0$ can be used in equation 3.29.

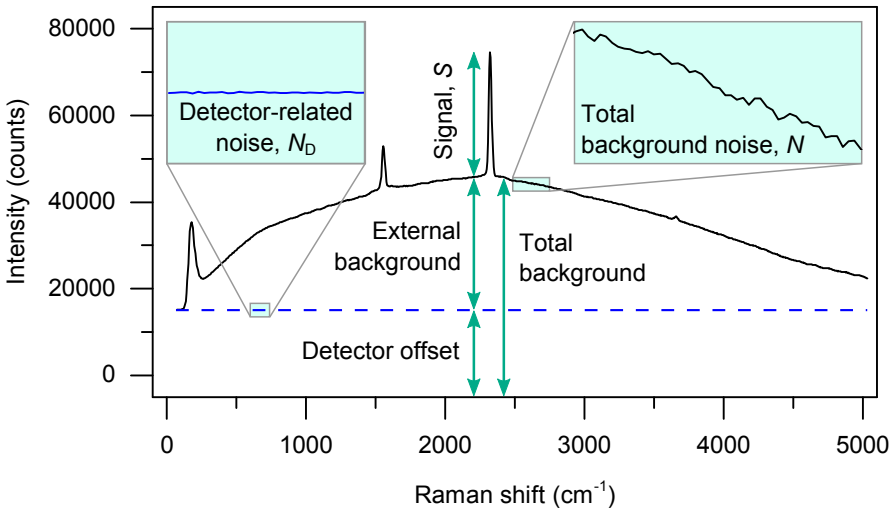

Figure 3.5.: Illustration of important terms connected to Raman spectra.
Black, solid line: Raman spectrum of air with a pronounced fluorescence background.
Blue, dashed line: "Dark" spectrum acquired with the laser turned off.
The single terms illustrated in the figure are explained in more detail in the following subsections. Data taken from [Sei14].

The Raman signal, S, is connected to the intensity of a Raman peak in the measured spectrum[1]; details about this topic will be given in the following subsection. The smallest detectable amount from above equation corresponds to the smallest signal of a certain peak which is still distinguishable in a Raman spectrum, S_{LOD}.

The noise, N, denotes statistical fluctuations of the measured intensities. These fluctuations limit the detectability of small signals; although connected to the background, the noise cannot be simply subtracted like the latter due to its statistical nature. The different contributions to the total background noise in a spectrum will be discussed in subsection 3.2.3. The noise in a certain part of the background-subtracted spectrum is quantified by the standard deviation of the intensities in this part. It corresponds to the standard deviation of the blank measures, s_{blank}.

Using the recommend value of $k = 3$, these considerations lead to the following form of equation 3.29:

$$S_{\mathrm{LOD}} = 0 + 3N \quad \Leftrightarrow \quad \frac{S_{\mathrm{LOD}}}{N} = 3 \ . \tag{3.30}$$

This means that a signal has to exceed the noise level by at least a factor of 3 in order to be considered as a detected signal rather than a background fluctuation (see also [Des15]).

[1] It should be noted that either the peak height or the peak area can be used as a measure for the Raman signal. For comparison measurements within the scope of this thesis, the peak height is used for reasons of simplicity and to maintain comparability to earlier LARA measurements. For analysis applications, however, it is recommended to use the peak area instead due to better precision and accuracy properties [Sch09].

It should be noted that the ratio of a measured signal to the background noise in a spectrum, the so-called signal-to-noise ratio

$$\mathrm{SNR} = \frac{S}{N} \ , \tag{3.31}$$

can itself be used to compare sensitivities as long as the partial pressure of the analyte stays constant. According to equation 3.30, the actual detection limit represents the partial pressure p for which a signal-to-noise ratio of 3 is obtained in the Raman spectrum:

$$\mathrm{LOD} = \frac{3p}{\mathrm{SNR}} = \frac{3pN}{S} \ . \tag{3.32}$$

In order to achieve high sensitivities, i.e. low detection limits, the signal has to be maximized while keeping the noise as low as possible. The factors influencing the Raman signal and the noise will be discussed in the following subsections.

3.2.2. Measured Raman signals

The measured Raman signal of a certain analyte depends not only on the theoretical line intensities given in equation 3.24, but also on further experimental factors. It can be described by the following equation:

$$S = C \cdot t_{\mathrm{acq}} \cdot I_{\mathrm{b}} \ . \tag{3.33}$$

The single elements will be briefly explained in the following:

- $\mathbf{C}$ is the so-called collection function [McC05]. It contains the system characteristics connected to light collection and detection, namely (i) the detected area and collection angle, (ii) the transmission of collection optics and spectrometer and (iii) the quantum efficiency of the detector [McC05].

- $\mathbf{t_{acq}}$ is the acquisition time.

- $\mathbf{I_b}$ is related to the intensity of the Raman line or branch chosen for analysis. In the case of a single, separated Raman line, I_{b} is equal to the intensity I described by equation 3.24. As motivated in subsection 3.1.1, however, it is often advantageous to use the peak associated to the Q_1 branch for analysis. This peak is composed of multiple not individually resolved lines, so that I_{b} is rather a function of the individual intensities of several lines, its precise value depending on such parameters as the resolution of the detection system.

The question how the Raman signal can be maximized will be addressed in detail in section 3.3.

3.2.3. Background and noise in Raman spectra

Apart from the desired pure Raman lines, a measured spectrum always contains a certain background. As the background is closely related to the sensitivity-limiting noise in a spectrum, it is worthwhile to have a closer look at its origins.

The total background consists of two contributions, as illustrated in figure 3.5: one is related to the detector, the second to undesired external light superimposing the Raman light. The detector-related background is an unavoidable property of each detector and constant over the whole wavelength range. It traces back to two different effects, which will be explained in the following before the external light is addressed:

Detector dark current: CCD detectors are based on the production of electron-hole pairs in a photosensitive semiconductor. However, a certain amount of electron-hole pairs is also spontaneously generated by thermal excitations, independent of the intensity of incident light [McC05]. The resulting dark current, I_d, contributes thus as a temperature-dependent background to the measured spectrum. Since the generation of thermal electron-hole pairs is a statistical process following a Poisson distribution, it gives rises to the so-called dark or thermal noise [McC05]:

$$N_\mathrm{T} = \sqrt{I_\mathrm{d} \cdot t}\ . \tag{3.34}$$

The dark current can be reduced by cooling the CCD detector. The CCDs employed in this work can be cooled down to -75 °C.

CCD detector read-out: In the read-out process of the CCD after each acquisition, the charge of each pixel or binned groups of pixels is converted into a voltage signal and the analog into a digital signal. A non-zero voltage value is set by the CCD manufacturer for conversion purposes, leading to a certain offset in the spectrum independent of the number of electrons being read out (see figure 3.5). This voltage offset itself does not contribute to the noise. However, the process of reading out each packet of electrons leads to a noise contribution, the so-called read-out noise N_R [McC05]. It depends on the read-out speed and the model of the CCD. Since each single read-out contributes to the read-out noise, the latter can be reduced by using less bins. Other than the thermal noise, the read-out noise is independent of the acquisition time.

Together, thermal noise and read-out noise yield the purely detector-related noise

$$N_\mathrm{D} = \sqrt{N_\mathrm{T}^2 + N_\mathrm{R}^2} \tag{3.35}$$

which remains even in the absence of any detected Raman light or external background, as illustrated in figure 3.5.

External background: The external background consists basically of any light which reaches the detector in addition to the Raman light. Background contributions by room light and stray light of a range of other light sources can be avoided by an enclosure around the Raman system as well as by filters and properly placed screens inside the system. More difficult is the elimination of contributions from light sources close to or directly in the optical path of the Raman light: background light in the same wavelength range as the Raman lines of interest cannot be eliminated by optical filters as these would block the Raman light as well. The main contributor to background in Raman spectra is thus often fluorescence produced by the excitation laser beam in optical components in the Raman light path. The detected fluorescence background can be reduced for instance by reducing the number of fluorescent components in the setup or by utilizing non-fluorescent materials. The reduction of fluorescence is one of the main issues encountered in this work. It will be treated in detail in chapter 6. The external background gives rise to another noise contribution, the shot noise N_S. Like the thermal noise, it is governed by Poisson statistics due to the inherent statistical variation in the arrival rate of background photons [McC05]:

$$N_\mathrm{S} = \sqrt{B_\mathrm{ext}(t)} \ , \tag{3.36}$$

where $B_\mathrm{ext}(t)$ is the time-dependent intensity of the external background. In general, a constant flux of external photons can be assumed, so that $B_\mathrm{ext}(t) \propto t$.

Taking all individual background contributions into account, the total background noise is given by the combination of detector-related and shot noise:[2]

$$N = \sqrt{N_\mathrm{D}^2 + N_\mathrm{S}^2} = \sqrt{N_\mathrm{T}^2 + N_\mathrm{R}^2 + N_\mathrm{S}^2} \ . \tag{3.37}$$

This noise has to be reduced as far as possible in order to achieve high sensitivities. As the detector-related noise is mainly fixed when a certain detector is chosen, the main focus in this work is on the reduction of the external background.

3.3. Enhancing the Raman signal

In this section the question is addressed how a considerable Raman signal increase can be achieved. In order to obtain sensitivity enhancements of about two orders of magnitude in comparison to the standard 90° KATRIN Raman system, the signal has to be increased by at least the same factor. An even higher signal increase is necessary in the case that the noise level rises as well by the measures taken.

Based on the expressions for Raman line intensities and measured Raman signals introduced earlier in this chapter (see equations 3.24 and 3.33), the different factors influencing the signal can be summarized in the following proportionality expression:

$$S \propto t_\mathrm{acq} \cdot C \cdot \mathcal{I} \cdot \tilde{\nu}_\mathrm{i} \tilde{\nu}_\mathrm{s}^3 \cdot \Phi(\varphi, \theta, a, \gamma)_{p^\mathrm{s}, p^\mathrm{i}} \cdot N_\mathrm{i} \ . \tag{3.38}$$

[2] It should be mentioned that this equation for N is valid only in the absence of any Raman signal; otherwise another shot noise contribution by the signal photons would have to be included. However, for the determination of the detection limit according to equation 3.32, the pure background noise is required as the LOD is related to the signal which rises just above background noise level [Des15].

In the following subsections, each factor contributing to the total signal will be discussed with respect to a possible signal enhancement.

3.3.1. Acquisition time, t_{acq}

In general, the maximal allowable acquisition time is specified for a certain measurement task, e.g. acquisition times of about one minute or less for KATRIN. For this reason, an increase of this parameter to maximize the signal is not possible.

3.3.2. Collection function, C

In order to maximize the collection function C, all optical components of the Raman system including the spectrometer setup should exhibit good transmission properties, and a highly efficient detector should be used. In the standard LARA system, these components have already been optimized: optics in the setup are in general anti-reflection coated, a spectrometer with high light throughput was chosen, and the detector provides a high quantum efficiency of about 95 % (cf. appendix A). For this reason, no significant further signal increase can be expected from a different choice of optical system components.

In addition, it is important that the overall optical design of the Raman system is chosen appropriately to maximize the detected scattering region. One important parameter in this respect is the choice of scattering geometry. In a Raman system, there are basically three different standard scattering geometries: 90° scattering, forward (0°) and backward (180°) scattering. They are illustrated in figure 3.6.

In the standard 90° configuration, light is collected only from a certain limited scattering region as shown in the figure. This region is 6 mm long in the case of the KATRIN Raman system; the length is limited by the size of the spectrometer entrance slit. In forward or backward measurements, on the other hand, the Raman light is collected along the direction of the incident laser beam, so that the scattering region concurs with the optical

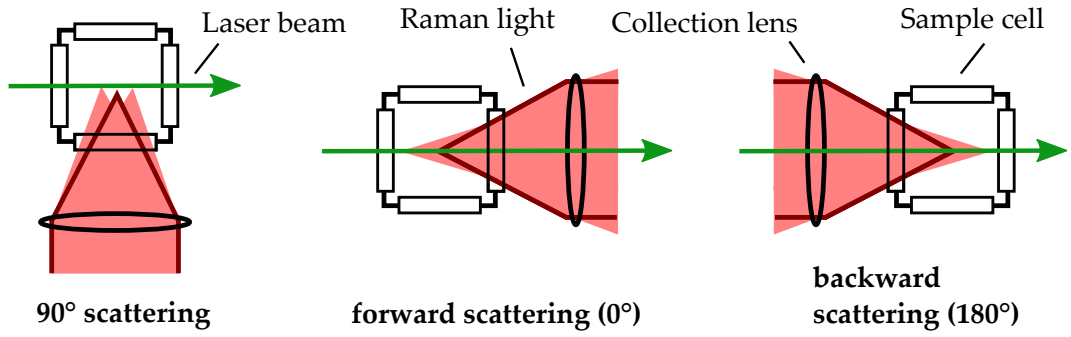

Figure 3.6.: Illustration of common Raman scattering geometries. In Raman spectroscopy, the Raman light is usually detected in a 90° angle to the laser beam or in forward or backward direction. In the figure, the areas in light red represent the total collected Raman light. The path of the detectable Raman light which is emitted in the focal point of the collection lens and its optical axis is highlighted by dark red contours.

axis of the collection optics. Due to the focal depth of these optics, not only the Raman light emitted in the very focal point of the collection lens is collected, but light from a larger region along the optical axis.

Comparison measurements between a standard 90° LARA setup and a backward Raman setup performed by LARA group member T. James demonstrated a signal enhancement of about a factor of 15 due to the improved collection properties [Jam13a]. On the other hand, an advantage of 90° setups is that the sample cell can be designed in such a way that fluorescence generated in the laser entrance and exit windows does scarcely reach the collection optics. By this means, the fluorescence background is kept very low. This is not possible in forward or backward Raman configurations, where fluorescence is generated in the path of the Raman light (see figure 3.6) and will thus be detected more efficiently. Accordingly, the sensitivity gain reported in [Jam13a] for backward scattering instead of 90° detection was much lower than the pure signal gain with enhancement factors of only 1.5 to 10 for different acquisition times. This shows that a variation of the scattering geometry alone is not enough to obtain significant sensitivity enhancements compared to the standard LARA system.

3.3.3. Laser irradiance, $\mathcal{I}$

The emitted Raman intensity is directly proportional to the irradiance of the incident light, $\mathcal{I}$, which is defined as the radiant flux incident per unit area. There are several possibilities to increase the irradiance:

Laser focusing: A tighter focus of the laser beam leads to a local increase of the laser irradiance. However, as a consequence the number of irradiated molecules decreases, and the product $\mathcal{I} \cdot N$ remains constant, so that effectively the signal is not increased.

High laser power: High-power lasers are usually employed in Raman systems to achieve a high irradiance. The LARA system for KATRIN uses a 532 nm continuous wave laser with a maximum power of 5 W in double-pass configuration, so that effective laser powers of up to 10 W can be reached. While this is already a high value compared to the majority of Raman spectroscopic experiments described in the literature, 532 nm solid-state lasers are available with output powers of up to 100 W, thus in principle allowing for a signal enhancement by about one order of magnitude. However, apart from the associated high costs, high powers involve the risk to damage optical components like the Raman cell windows. In a LARA commissioning run at the LOOPINO facility, laser-induced coating damages were observed within five days of LARA operation at full power [Fis14], so that the LARA system will eventually be operated at reduced power to enable stable long-term operation. Based on these experiences, it does not seem advisable to envisage a considerable laser power increase compared to the current LARA system.

Cavity enhancement: The concept of increasing the Raman signal by employing high irradiances is also adopted in the so-called CERS approach, which stands for cavity-enhanced Raman scattering. It was first demonstrated in 2001 by Taylor et al. at the TLK [Tay01]. In this approach, a resonant optical cavity is used to enhance the power of incident laser light. For measurements with H_2 and other gases, a power increase by about three orders of magnitude was reported by Salter et al. and Hippler [Sal12, Hip15]. Using just a 10 mW laser diode as the light source and a cavity inside the gas system, detection limits of 0.42 mbar (3σ) were obtained for H_2 in 30 s acquisition time [Hip15]. On the downside, however, CERS systems are very sensitive to vibrations and temperature variations and have to be elaborately stabilized [Tay01], which is especially complex in glove box environments. Moreover, although low-power light sources can be effectively enhanced, the maximum achievable power is still limited by the damage threshold of the cavity mirrors employed.

Nevertheless, the approach is further pursued as quite promising results have been shown to be within reach: Keiner et al. report a power build-up to up to 100 W in a cavity system stabilized by passive frequency-locking and feedback-coupling, by which means they reached a 3σ detection limit for CO_2 of about 0.05 mbar within measurement times of 1 s [Kei14]. While this demonstrates the overall potential of this approach, detection limits reported so far are still more than one order of magnitude higher than the one targeted in this work. Also, those systems were generally not designed for applications with corrosive gases like tritium.

Altogether, it seems currently not feasible to achieve the targeted sensitivity enhancement of about two orders of magnitude for tritium gas analysis by means of a laser power increase only.

3.3.4. Excitation laser wavelength, λ_i

The frequency or wavelength dependence of the Raman signal according to equation 3.38 can be crudely approximated by

$$S \propto \tilde{\nu}_i \tilde{\nu}_s^3 = \tilde{\nu}_i \cdot (\tilde{\nu}_i - \Delta\tilde{\nu})^3 \approx \tilde{\nu}_i^4 \ , \tag{3.39}$$

due to the frequency of excitation laser light ($\tilde{\nu}_i$) and Raman light ($\tilde{\nu}_s = \tilde{\nu}_i - \Delta\tilde{\nu}$) being similar in magnitude. The approximate $\tilde{\nu}_i^4$ law demonstrates that the measured signal can be significantly increased by using shorter excitation laser wavelengths:

For instance, frequency-doubling a 532 nm laser while maintaining the same output power yields a signal gain by a factor of $532^4/266^4 = 16$. In addition, short enough wavelengths (in the middle to far UV region) lead to a separation of Raman and fluorescence wavelengths and thus a very low noise level [Sem16c]. On the downside, a UV-based Raman system requires not only a new laser, but also special optics and detectors, and would therefore be a rather expensive solution. Furthermore, optical alignment of an invisible beam inside a tritium glove box is not trivial. For these reasons, other possibilities to enhance the signal would be preferable to a UV system.

Alternatively, the wavelength can be shifted not as far, but just into the blue or violet region in order to still be able to use standard optics and components for visible light.

In that case, however, the signal gain is not only much smaller – merely a factor of 3 for a 405 nm laser diode compared to the current 532 nm laser –, but the broadband fluorescence background in a system and thus the noise tends to increase at first for shorter wavelengths in the blue region [McC05]. The overall sensitivity would thus barely improve, or it might even become worse due to the higher noise. Consequently, blue or violet lasers are no feasible alternative to the current wavelength choice.

3.3.5. Line strength function, Φ

The line strength function, $\Phi(\varphi, \theta, a, \gamma)_{p^{\mathrm{i}}, p^{\mathrm{s}}}$, depends critically on the overall experimental configuration. On the one hand, there is a dependence on polarization directions and the scattering geometry. In appendix C, it is shown that Φ assumes the same maximal value for each geometry when the scattering angles and polarization configurations are chosen such that the direction in which the Raman light is collected is perpendicular to the polarization axis of the incident laser light. These parameters are already optimized in the LARA system. On the other hand, the transition probability between different molecular states and thus the line strength function can be considerably influenced by certain enhancement techniques like surface-enhanced or stimulated Raman scattering. The most common enhancement techniques suitable for gases will be discussed in the following with respect to their signal enhancing properties and their suitability for the task at hand.

To avoid misunderstandings, it should be noted that in general only the achievable signal enhancement is stated in the literature. A potential simultaneous increase in noise is often not considered, so that the actual sensitivity enhancement is – more often than not – lower than the pure gain in signal stated in the following.

Surface-enhanced Raman spectroscopy (SERS): The SERS effect was first observed in 1974 by Fleischmann et al. who found Raman signals of their analyte much enhanced when those were adsorbed on a roughened silver electrode [Fle74]. The underlying enhancement mechanism is still an active research topic, but there is evidence that two different effects contribute to the signal enhancement [Smi05, Hay05]. Both depend on molecules being adsorbed on a roughened metallic surface:

- The so-called chemical enhancement is linked to the chemical bond formed between metal surface and analyte molecules. Electrons can be transferred between the metal and the molecule in the so-called charge-transfer effect, by which the polarizability $\boldsymbol{\alpha}$ (cf. subsection 3.1.2) is increased [Smi05]. The resulting enhancement factor is assumed to be of the order of 100 [Hay05].
- The second effect is electromagnetic enhancement. By interactions of the laser beam with irregularities of the metal surface, conduction electrons at the metal surface are excited. Large electromagnetic fields at the metal surface confine the analyte molecules and lead to enhancement factors of more than 10,000 [Hay05].

The SERS effect depends critically on the choice of substrate and the surface size; in total, the enhancement may even approach factors of 10^{10} to 10^{11} for highly optimized

surfaces [Sha12]. However, the SERS effect relies also on an effective adsorption of the analyte on the substrate. This makes its utilization for gas sensing applications more challenging, since the adsorption coefficient of many gases is rather low on common substrates [Rae10], especially in the case of hydrogen [Løv02]. SERS spectra of hydrogen were first presented by Li et al., but with hydrogen generated by dissociation of water in an electrochemical cell and measured within an electrolyte solution instead of in the gas phase [Li11]. Preliminary investigations about using SERS for gaseous hydrogen have failed to lead to any significant enhancements [Las04].

Even if a suitable substrate – providing sufficient adsorption properties for hydrogen isotopologues and not degrading in tritium atmospheres – should be identified, continuous monitoring of changes in a gas flow using SERS proves difficult: molecules adsorbed to the observed surface do not interchange quickly enough to reflect short-time fluctuations in the gas composition. Thus, heating and cooling of the surface would be required to trigger alternately adsorption and desorption [Rae10]. For all these reasons, the SERS technique is not considered suitable for the KATRIN monitoring purposes at hand.

Resonance, stimulated and coherent anti-Stokes Raman scattering: A range of enhancement techniques are in principle based on adjusting incident light to a certain Raman transition to increase the corresponding transition probability. The working principles of resonance, stimulated and coherent anti-Stokes Raman scattering are sketched in figure 3.7.

In resonance Raman spectroscopy, the excitation laser is chosen in such a way that its wavelength is close to an electronic transition of the analyte in order to enhance the probability of this transition taking place by several orders of magnitude [Smi05, Efr08]. However, an energy of more than 15 eV is required to excite an electronic transition in a hydrogen molecule in the ground state [Hak06]. This corresponds to wavelengths smaller than 100 nm, i.e. in the extreme ultraviolet regime, where there are hardly lasers available, nor other light sources feasible for the task at hand.

In contrast, stimulated Raman spectroscopy (SRS) and coherent anti-Stokes Raman scattering (CARS) utilize effects in principle accessible with lasers in the visible range, typically pulsed ones. SRS is based on stimulating the emission of Raman light by means

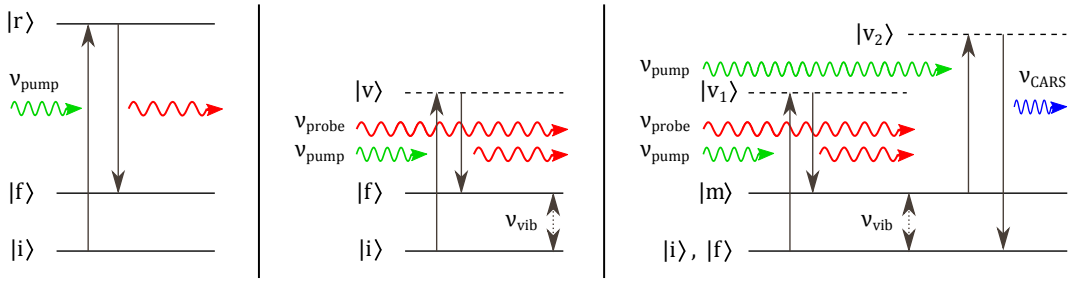

Figure 3.7.: Principles of resonance *(left)*, stimulated *(center)* and coherent anti-Stokes Raman scattering *(right)*. $|i\rangle$ denote initial, $|f\rangle$ final, $|r\rangle$ real, $|v\rangle$ virtual and $|m\rangle$ intermediate states. Details about each process are given in the main text.

of two lasers: a pump laser with frequency ν_{pump} excites a virtual state in the analyte molecule. An additional probe laser with frequency ν_{probe} will stimulate the emission of Raman light with increased transition probability if the frequency difference $\nu_{\text{pump}} - \nu_{\text{probe}}$ corresponds to the frequency of a vibrational transition, ν_{vib} [Dem08b]. It should be noted that the Raman light of interest has the same frequency as the probe laser, so care has to be taken to distinguish it from laser fluctuations.

In the case of CARS, a four-wave mixing process is utilized in which the pump and probe laser pulses are focused together in a sample to produce a coherent beam of anti-Stokes radiation with $\nu_{\text{CARS}} = 2\nu_{\text{pump}} - \nu_{\text{probe}}$ [Tol77] (see figure 3.7). Since the emitted light is blue-shifted in the case of anti-Stokes processes, it can be well separated from red-shifted fluorescence light, thus keeping the background and noise level low. Enhancement factors of 10^5 using CARS [Dem08b] and even up to 10^9 for the detection of hydrogen using SRS have been reported [Kry96].

However, there are serious drawbacks connected to both SRS and CARS. In contrast to spontaneous Raman scattering, one single-frequency laser is not enough to detect all hydrogen isotopologues – plus impurities – simultaneously, but two laser are required, including an (expensive) tunable laser which covers a wide wavelength range of about 85 nm width to match transitions of all analytes of interest. Unexpected constituents in a gas mixture might be missed if they lie outside the wavelength range of the excitation laser. In addition, an effective enhancement requires a certain amount of analyte molecules to be present in the sample [Blo67, Dem08b][3]: for low-pressure and trace gas applications as required for KATRIN, these techniques are thus not suitable.

3.3.6. Number of molecules, N

So far, the parameters discussed did not provide the possibility for a significant sensitivity enhancement, or could not be feasibly increased within the KATRIN frame conditions. The last remaining parameter is the number of irradiated molecules imaged by the Raman system.

Since the gas pressure is fixed by the KATRIN measurement task, the number of molecules cannot simply be raised by increasing the molecule density in the scattering region. However, there is in principle the possibility to make the scattering region very large, so that many gas molecules are irradiated even at low pressures. The challenge is to design the optical setup in such a way that light from such an extended scattering region can still be efficiently collected and detected. In the following section, a concept will be discussed which comprises both a large amount of irradiated molecules and the means to detect a large fraction of the emitted Raman light.

[3] Note that the SRS signal enhancement by a factor of 10^9 for hydrogen mentioned above was achieved at a pressure of 45 bar [Kry96].

3.4. Signal enhancement by hollow waveguide based Raman spectroscopy

In the following, the basic concept of hollow waveguide based Raman spectroscopy is explained, and the current state of research of this enhancement method is presented.

3.4.1. Concept of hollow waveguide based Raman spectroscopy

Hollow waveguide based Raman spectroscopy is an elegant approach to enhance measured Raman signals by substantially increasing the number of irradiated sample molecules. The basic concept is to use a hollow waveguide – with decent light guiding properties in the wavelength range of both laser and Raman light – as the sample cell, as illustrated in figure 3.8. When the excitation laser beam is guided through the gas-filled waveguide, it interacts with gas molecules over the entire length of the waveguide, so that the scattering region is greatly extended compared to conventional 90° Raman systems. The emitted light is confined in the same waveguide and thus guided towards the waveguide exit, where it can be collected. For this reason, a much larger fraction of the total emitted Raman light than in 90° systems is detected.

The resulting Raman signal depends on several experimental parameters, in particular the length, guiding loss coefficient and diameter of the waveguide. For an ideal, loss-free waveguide, the scattering length would be equal to the length of the waveguide, so that the measured signal would be proportional to the waveguide length. However, due to attenuation losses of both laser and Raman light in realistic waveguides, the scattering length is actually a function of the waveguide length l and the loss coefficients α_{L} and α_{R} of laser and Raman light. It can be described in terms of an effective waveguide length l_{eff}, which depends also on the chosen scattering geometry.

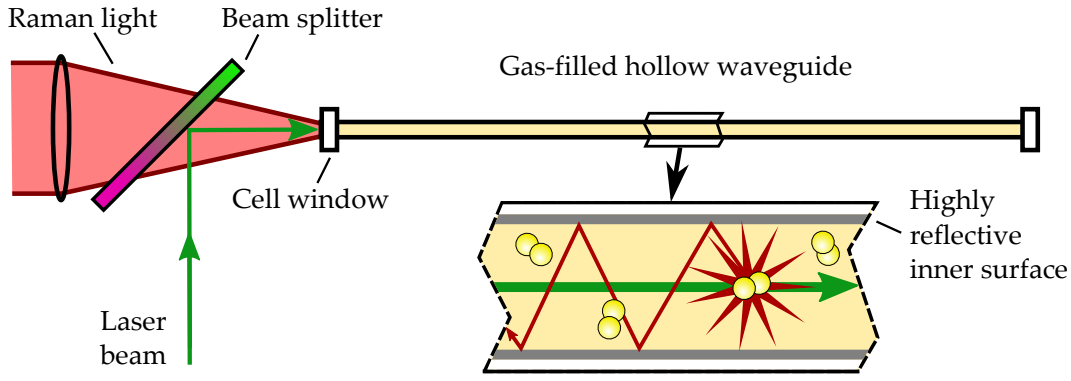

Figure 3.8.: Concept of hollow waveguide based Raman spectroscopy. A laser beam is coupled into the hollow waveguide which serves as the sample gas cell. The emitted Raman light is guided towards the waveguide exit where it can be collected. A dichroic beam splitter can be used to separate the light paths of laser and Raman light. A backward collection geometry is shown in this illustration; other collection geometries are presented in figure 3.9.

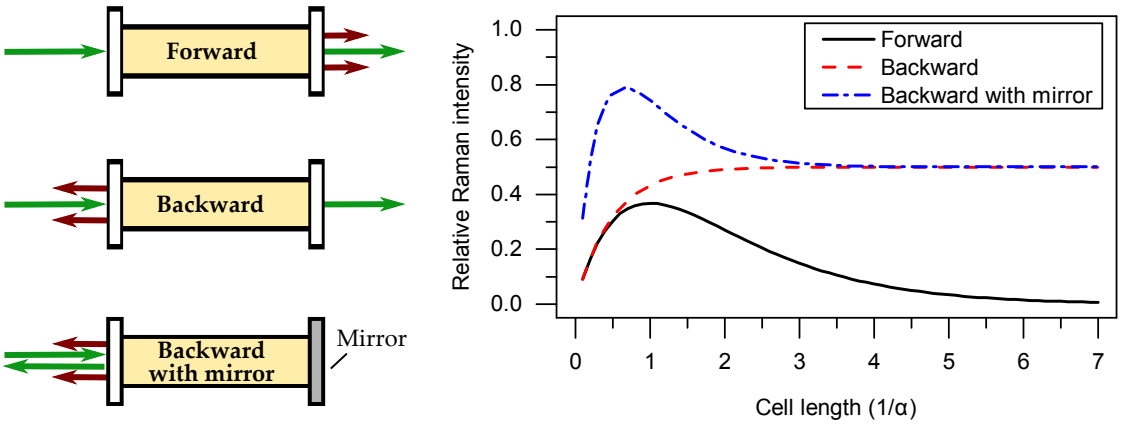

Figure 3.9.: Scattering geometries and corresponding relative Raman intensities in hollow waveguide based Raman spectroscopy. Different collection geometries are sketched schematically on the left side of the figure. Green arrows stand for the direction of the laser light entering and exiting the waveguide, short red arrows for the direction in which the Raman light is collected. The plot on the right side illustrates the relative Raman intensities at the waveguide exit as a function of the waveguide length. The latter is given in units of attenuation length, i.e. the waveguide length after which the intensity has decreased to $1/e$ of its original value. The plot assumes the same attenuation coefficient and the same mirror reflectance for laser and Raman light. A value of $R = 0.95$ was used. Figure adapted from [Alt01].

Possible collection configurations for hollow waveguide based Raman systems and the corresponding relative Raman intensities are shown in figure 3.9. The effective waveguide lengths for these configurations are given by the following expressions [Alt01]:

$$l_{\text{eff,forward}} = \frac{\mathrm{e}^{-\alpha_\mathrm{L} l} - \mathrm{e}^{-\alpha_\mathrm{R} l}}{\alpha_\mathrm{R} - \alpha_\mathrm{L}} \,, \tag{3.40}$$

$$l_{\text{eff,backward}} = \frac{1 - \mathrm{e}^{-(\alpha_\mathrm{L}+\alpha_\mathrm{R}) l}}{\alpha_\mathrm{L} + \alpha_\mathrm{R}} \,, \tag{3.41}$$

$$\begin{aligned} l_{\text{eff,backward+mirror}} = &\frac{1 - \mathrm{e}^{-(\alpha_\mathrm{L}+\alpha_\mathrm{R}) l}}{\alpha_\mathrm{L} + \alpha_\mathrm{R}} + \frac{R(\mathrm{e}^{-2\alpha_\mathrm{L} l} - \mathrm{e}^{-2\alpha_\mathrm{R} l})}{\alpha_\mathrm{R} - \alpha_\mathrm{L}} \\ &+ \frac{R^2(\mathrm{e}^{-(\alpha_\mathrm{L}+\alpha_\mathrm{R}) l} - \mathrm{e}^{-2(\alpha_\mathrm{L}+\alpha_\mathrm{R}) l})}{\alpha_\mathrm{L} + \alpha_\mathrm{R}} \,. \end{aligned} \tag{3.42}$$

R is the reflectance of the optional mirror at the waveguide end; for the sake of simplicity, it is assumed in above formula that R is the same for laser and Raman light.

In the following, the different factors influencing the Raman signal achievable with a hollow waveguide based Raman system are discussed.

Scattering geometry and waveguide length: The right panel of figure 3.9 illustrates the characteristics of the different geometries with respect to the resulting Raman signal. In all configurations, the collected Raman signal profits at first from increasing waveguide lengths. However, while it simply runs into saturation for backward Raman, it starts to decrease again in case of forward Raman when a certain optimum cell length is exceeded: after that point, the forward-scattered Raman light produced at the beginning of the waveguide – where the laser is still powerful – is attenuated too much until it is collected at the waveguide end, and only little Raman light is still produced at the end of the waveguide due to the attenuation of the laser beam itself. A backward Raman configuration can thus be considered superior to a forward one in the case of hollow waveguide based Raman spectroscopy, as higher total signals can be collected while the choice of waveguide length is less critical. In the third configuration shown in the figure, the laser beam and forward-scattered Raman light are reflected by a mirror at the end of the waveguide and transmitted back towards the collection optics. By this means, even higher signals can be achieved if the optimal length is chosen.

Attenuation losses: Independent of the scattering geometry chosen, low loss coefficients are of course advantageous with respect to high signals. Waveguide losses depend on the guiding mechanism used. Standard light guiding based on total internal reflection is generally not applicable for hollow waveguides in the field of gas analysis, as this would require a waveguide material with a lower refraction index than the gas. For this reason, hollow waveguides for this type of spectroscopy are usually simply based on "normal" reflection of the light, with highly reflective inner surfaces ensuring low attenuation losses. According to the Fresnel equations [Dem13], the reflectance e.g. of metal surfaces approaches 100 % for grazing angles, so that a laser beam coupled in with a small entrance angle will be able to propagate with especially low losses; this could also be concluded from a theoretical treatment using mode propagation theory by Buric et al. [Bur10].

Waveguide diameter: The investigation of Buric et al. also included the influence of the waveguide diameter on the Raman signal. They found that the Raman intensity at the waveguide exit is higher for larger diameters as more light modes can propagate with low losses. At the same time, however, the collection angle required to collect all low-loss rays increases for larger-diameter waveguides as well, so that large diameters can also lead to lower signals if the acceptance angle of the collection optics and detection system is not large enough [Bur10]. With respect to high signals, the diameter should thus be chosen in such a way that the étendue $A\Omega$, given by the product of the cross-section area A of the waveguide and the solid angle Ω into which light is emitted, matches the étendue of the detection system. For gas flow measurements, however, it has to be additionally taken into account that the diameter has to be large enough to allow a sufficiently high gas flow through the waveguide, even if this should go along with reduced signals.

3.4.2. Discussion of the current state of research

The use of hollow waveguides for low-loss transmission of laser light or optical signals was considered already in the 1960s: Eaglesfield discussed optical pipelines made of hollow steel pipes with reflective silver coating [Eag62], and Marcatili and Schmeltzer contributed theoretical studies of mode propagation and attenuation in hollow waveguides [Mar64]. Laser transmission was also the goal of more recent studies by Matsuura et al. and Osawa et al. in which the production of glass waveguides with highly reflective inner coatings was investigated [Mat90, Mat98, Osa95]. The group around Matsuura have since commercialized their manufacturing technique; silver-lined glass capillaries obtained from their company 'Doko engineering' were used in parts of this work (see chapter 4). Other groups describe the use of hollow waveguides as Raman probes for remote sensing applications, where the waveguide serves as a compact and background-reduced alternative to common silica fibers to transport laser light to a sample and Raman light back to the spectrometer [Kom05, Bor10].

The idea to use a hollow waveguide not just for light transmission but as the actual sample cell was first proposed by Walrafen and Stone in 1972 [Wal72]. However, these considerations were at first purely focused on waveguides based on total internal reflection and thus limited to the analysis of liquid samples due to the required high reflective index. It was not until 1996 that highly reflective hollow waveguides were first proposed as Raman sample cells for gas analysis applications [Car96, Mit96]. The principle was adopted later by groups in the USA and Japan who employed glass waveguides lined with silver on the inside for their tests:

- Pearman et al. reported about 15-fold signal enhancements for their fiber-coupled waveguide probe compared to standard fiber-optic probes when using a capillary with 2 mm inner diameter as the gas cell [Pea08a, Pea08b].
- Okita et al. utilized a silver-lined glass waveguide with 700 µm inner diameter and back-reflecting mirror at the waveguide end for breath analysis [Oki10]. Focused on compactness, they characterized their system with respect to bending losses and the optimal waveguide length, which they found to be 80 cm. Their estimated 1σ detection limit was 0.2 % for exhaled gases, corresponding to 0.6 % at 3σ.
- The group around Buric set up a direct-focusing Raman system for the monitoring of fuel gases at high pressures up to 44.8 bar [Bur12]. They thoroughly examined the underlying theory of mode propagation through metal-lined hollow waveguides and means to optimize the collected signal [Bur10]. Using a 1 m long metal-lined glass fiber with an inner diameter of 300 µm as the gas cell, they obtained a 1σ detection limit of 0.12 % N_2 at a total pressure of 1 bar, a laser power of 150 mW and an acquisition time of 1 s [Bur13], corresponding to a 3σ detection limit of 3.6 mbar.

The detection limit achievable with higher laser powers P_{new} and longer acquisition times t_{new} can be roughly approximated by $\mathrm{LOD}_{\mathrm{new}} = \mathrm{LOD}_{\mathrm{old}} \cdot \sqrt{P_{\mathrm{old}}/P_{\mathrm{new}} \cdot t_{\mathrm{old}}/t_{\mathrm{new}}}$, as detailed in appendix D. Assuming an increased laser power of 5 W and an acquisition time of 60 s, the Buric detection limit of 3.6 mbar would translate into an improved detection limit of 0.08 mbar for N_2. Although promising, these numbers indicate that the goal

envisaged in this work – a detection limit of the order of 10^{-3} mbar within acquisition times of a minute or less – is still not quite within reach. Despite successful signal enhancement, the overall sensitivity enhancement is somewhat limited by fluorescence occurring from interactions between laser and the waveguide glass substrate, as reported e.g. in [Bur13, Oki10].

It should be noted that another type of hollow waveguide, so-called hollow-core photonic crystal fibers (HC-PCF), have also been investigated as Raman gas cells. Light guiding properties are in this case often achieved by a photonic band gap effect: light is confined inside a waveguide by a photonic band gap which prohibits photons of certain wavelengths to propagate into the fiber material [Cha05]. Charlton et al. demonstrated the usage of HC-PCFs as gas cells first for absorption spectroscopy [Cha05], but the technique has recently been investigated for Raman measurements as well. Yang et al. report a sensitivity enhancement of a factor of about 700 using a 30 cm long HC-PCF with 7.5 µm core diameter [Yan13]. Hanf et al. have set up a system based on a 7 µm core HC-PCF, which reaches detection limits of 9 ppm for N_2 in a gas mixture at 20 bar total pressure within acquisition times of only 40 ms [Han14]. Despite these excellent results, an application of HC-PCFs for the intended measurements for KATRIN is not feasible due to the extremely small hollow cores, which would preclude sufficient gas throughput[4] and lead to severe gas separation effects for individual constituents in a gas mixture.

In summary, the potential of using hollow waveguides as Raman cells in order to achieve significant signal enhancements compared to free-space solutions has in principle been demonstrated in the literature. However, the reported system configurations are not suitable for KATRIN purposes in their current form due to (i) still insufficient sensitivities, (ii) partly too small diameters in the sub-mm range and (iii) designs not optimized for tritium applications.

For this reason, a hollow waveguide based prototype system for the use with tritium was set up within the scope of this thesis based on results of first investigations by LARA group member T. James [Jam13a]. This will be the topic of the following chapter.

[4] For instance, Yang et al. report filling times of 1 h for toluene vapor until stable signals are reached in their 30 cm long HC-PCF [Yan13].

4. Setup and test of a hollow waveguide based prototype system for tritium gas analysis

In order to explore the potential of hollow waveguide based Raman spectroscopy for KATRIN, a prototype setup was constructed, tested with tritium gas and evaluated within the scope of this work. The prototype was based on preliminary studies carried out by LARA group member T. James in his PhD thesis [Jam13a], and on subsequent studies conducted in a collaboration between Swansea University and KIT [Jam15].

The prototype setup and its performance are the topic of this chapter, which is structured as follows: first, the experimental setup of the prototype system is presented in section 4.1, comprising the optical setup and the design of the gas handling system. Afterwards, section 4.2 addresses the measurement procedure and the conducted measurement runs as well as the analysis of acquired spectra. Results of the different measurement runs are discussed in section 4.3 with a focus on the achieved sensitivity. Finally, section 4.4 focuses on limitations of the prototype system encountered during construction, commissioning and tritium operation. Based on these, necessary steps towards a fully tritium compatible, highly sensitive Raman system are identified.

4.1. Experimental setup

In the following, the optical setup of the prototype system is explained, followed by an outline of the gas handling system.

4.1.1. Optical setup

A backward Raman configuration with a back-reflecting mirror at the far end of the waveguide is used for the measurements in order to achieve highest-possible signals (cf. figure 3.9 and the related discussions in subsection 3.4.1). The optical setup of the prototype system is shown in figure 4.1. It is further explained in the following; details about the main components can be found in table 4.1.

The waveguide utilized in the prototype setup is a hollow, silver-lined glass fiber with an inner diameter of 1 mm and a length of 650 mm. It was produced by Doko Engineering, the company founded by the group around Matsuura who performed extensive studies on the production of hollow waveguides for laser-related applications (cf. subsection 3.4.2 and [Mat98]). The largest available inner diameter was chosen to provide sufficient

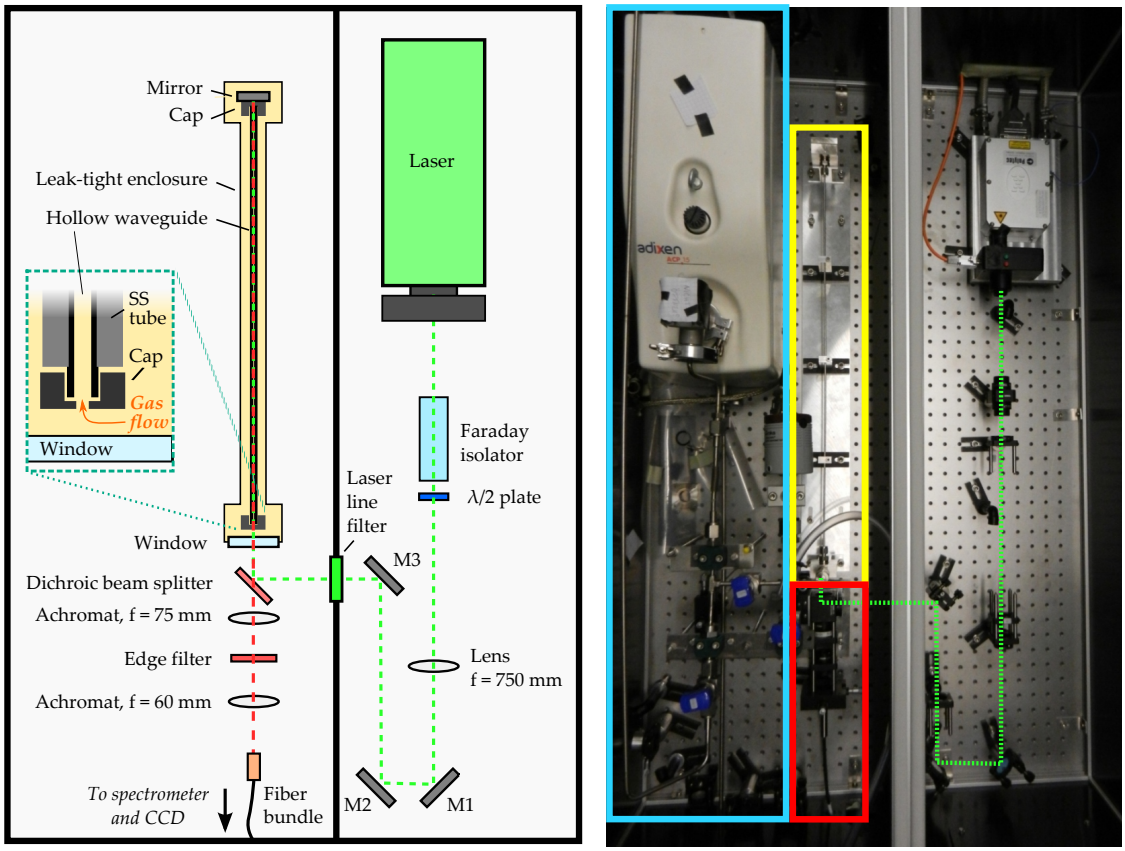

Figure 4.1.: Optical setup of the hollow waveguide based prototype system. *Left:* Schematic drawing of the optical setup. The light paths and the purposes of the different components in the setup are explained in the main text. M1 – M3 are 532 nm narrowband mirrors. The inset shows a detail of the fiber-cap assembly. *Right:* Picture of the system in top view. The orientation of the picture corresponds to the schematic drawing. Some additional components are visible here which are not included in the former: in the right compartment of the light-tight enclosure, there are two beam dumps visible used to dump laser reflections. In the left compartment, components of the gas handling system *(blue box)* such as the vacuum pump in the upper left corner are located next to the waveguide enclosure *(yellow box)* and the Raman light collection optics *(red box)*.

gas throughput. The inner surface of the waveguide is coated with a silver layer of about 200 nm thickness. It should be noted that this fiber is generally provided by the manufacturer with an additional polymer film [Dok07] to protect the silver lining from oxidation and to further improve the reflectance. However, such a polymer coating is not compatible with tritium and was thus not applied to the waveguide used in this work.[1]

[1] Prior long-term use of the same type of waveguide in air by our group showed that degradation of the waveguide reflectance due to oxidation of the silver lining is minimal for small-diameter waveguides as the air flow through the core is very low. In addition, the waveguide used for the measurements presented here was rarely exposed to air: it is housed in a gas system which was closed after initial alignment measurements with air and subsequently either evacuated or flushed with pure nitrogen between tritium measurements.

Table 4.1.: Overview of the main components of the prototype setup. The following abbreviations were used: ID = inner diameter; OD = outer diameter; UVFS = UV grade fused silica; AR = anti-reflection; DPSS = diode pumped solid state; cw = continuous wave; NA = numerical aperture.

Component	Manufacturer	Model	Details
Waveguide	Doko Engineering Sendai, Japan	VSS1000/1600	hollow, silver-lined glass fiber, ID = 1 mm, OD = 1.6 mm, $L = 650$ mm
Back-reflecting mirror	Thorlabs Inc. Newton, NJ, USA	BB05-E02	broadband dielectric mirror, $R_{\text{avg}} > 99\,\%$ for 400 – 750 nm
Window	EKSMA OPTICS, Optolita UAB Vilnius, Lithuania	226-1221M + 3217i0	2 mm UVFS precision window, $\lambda/10$, 30 arcsec, broadband AR coating for 400 – 700 nm
Laser	Laser Quantum Ltd. Stockport, Cheshire, UK	Excel	DPSS Nd:YVO_4 laser, $\lambda = 532$ nm, $P_{\text{max}} = 2$ W, cw
Dichroic beam splitter	Semrock, Inc. Rochester, NY, USA	Razor Edge LPD01-532RS	$R_{\text{abs}} > 94\%$ @ 532 nm, $T_{\text{avg}} > 93\,\%$ for 544.2 – 824.8 nm
Fiber bundle	Ceram Optec GmbH Bonn, Germany	*custom*	48 fibers with core diameter 100 µm, NA = 0.22, dot-to-slit config., dot $d = 1$ mm, slit $h = 6$ mm
Spectrometer	PI Acton Trenton, NJ, USA	SP500i	Czerny-Turner, 600 gr/mm grating, focal length 500 mm, aperture ratio $f/6.5$
CCD detector	Princeton Instruments Trenton, NJ, USA	PIXIS:400B	1340 x 400 array, 20 x 20 µm pixel, cooled down to -75 °C

The laser is a 532 nm continuous wave laser with a maximum power output of 2 W.[2] A Faraday isolator behind the laser output is used to prevent back-reflected laser light from re-entering the laser cavity. The laser polarization can be adjusted by the subsequent half-wave plate: although the Raman signal is in principle independent of the laser polarization direction in case of forward or backward scattering due to the rotational symmetry of these configurations (see also appendix C), the laser polarization should be adjusted for minimum reflection losses at the mirrors and the dichroic beam splitter each reflecting at an 45° angle.

The beam is coupled into the waveguide by a long focal length lens ($f = 750\,\mathrm{mm}$) in order to achieve optimum coupling with only little excitation of lossy high-order modes. Fluorescence generated in the beam path before the waveguide is rejected by a laser line filter. A dichroic beam splitter is used to spatially separate the light paths of laser and Raman light: it reflects the laser towards the waveguide and couples the back-reflected beam out of the Raman beam path, but is transparent for the longer-wavelength Raman light. The latter is subsequently collected and imaged onto a fiber bundle by two achromatic lenses with focal lengths $f_1 = 75\,\mathrm{mm}$ and $f_2 = 60\,\mathrm{mm}$, both with a diameter of 25.4 mm. The fiber bundle transports the Raman light towards the spectrometer and detector. It consists of 48 individual fibers which are arranged in a custom 'dot-to-slit' configuration: the circular configuration on the collection end of the fiber bundle has a diameter of 1 mm in order to match the waveguide core diameter, while the output end is arranged in a slit configuration of 6 mm in height to fit the entrance slit of the spectrometer. A 532 nm edge filter is placed between the collection lenses in order to prevent stray laser light and Rayleigh-scattered light from entering the fiber bundle where it could generate additional background light. The whole optical system is surrounded by a light-tight enclosure closed by a lid to block ambient light from being detected.

As briefly outlined in the previous chapter in subsection 3.2.3, external background in Raman spectra is often dominated by fluorescence produced by the laser beam in optical components in the Raman light path. Since an increased external background leads to increased shot noise in a spectrum and thus worsens the signal-to-noise ratio and the detection limit, it is desirable to minimize fluorescence contributions in Raman spectra as far as possible. In preliminary studies by T. James, several possibilities for fluorescence background reduction in hollow waveguide based Raman systems have been investigated. The measures identified in these studies are already implemented in the prototype setup described here. They will be briefly outlined in the following. For a detailed description of the individual studies and their results, the reader is referred to [Jam15].

- The first step to minimize fluorescence contributions from optical components which are exposed to laser light and located within line-of-sight of the Raman light collection is simply to minimize the number of these components. For this reason, the optical setup used in this work deviates somewhat from other setups described in the literature such as the one used by Buric et al. [Bur13], who use a joint laser focusing and Raman collection lens between the beam splitter and the entrance window of the gas system. By using two separate lenses instead, the laser focusing lens can be placed before the beam splitter and thus outside of the Raman

[2] Note that higher laser powers can be employed in a final setup for KATRIN in order to reach higher sensitivities.

light collection line-of-sight, while the collection lens is moved behind the beam splitter where it is not exposed to laser light (cf. figure 4.1). A noise reduction of approximately a factor of 2 was achieved by this measure [Jam15].

- An additional advantage of the configuration just described is that the focal lengths for laser focusing and Raman light collection can be chosen independently of each other. While a short focal length is required to maximize the solid angle for light collection, a longer focal length is ideal for low-loss coupling of the laser into the waveguide. In a comparison of several lenses with long focal lengths, a value of $f = 750\,\mathrm{mm}$ was found to lead to the highest signal-to-noise ratio for the type of waveguide used here [Jam15].

- As suggested by Okita et al. [Oki10], a metal sleeve or cap with central aperture can be used to cover the waveguide front face in order to avoid direct exposure of the front face to laser light on the one hand, and to block fluorescence generated in the waveguide glass from exiting on the other hand. A central aperture of 0.8 mm diameter was found to yield the best SNR results for the 1 mm waveguide used [Jam15]: larger apertures do not sufficiently suppress fluorescence background, while smaller apertures block Raman light as well. In the prototype system, caps are used at both ends of the waveguide (see figure 4.1). The front cap can be fixed inside the system by a metal clamp; this design was developed within the scope of this work after misalignments of the system during evacuation or gas filling had been observed when a loose cap was used. A picture of the front cap is shown in figure 4.2.

- The window sealing the gas system is close to the waveguide end and thus to the focus of the collection optics. For this reason, fluorescence generated in the window is collected relatively efficiently, so that it is crucial to choose a window contributing as little fluorescence as possible. The relevant parameters in this case are the thickness and material of the window. In accordance with the findings reported in [Jam15], a window made of UV grade fused silica with a broadband anti-reflection coating is used for the prototype setup (see table 4.1). The window should ideally be as thin as possible with respect to fluorescence, but has to be stable enough for use in a vacuum system. For this reason, a thickness of 2 mm was chosen.

4.1.2. Gas handling system

The waveguide is located inside of a leak-tight enclosure connected to a gas handling system for measurements with tritium gas. The gas handling system will be explained in the following. First, however, it should be noted that the prototype is intended for a proof-of-principle test with tritium and does not yet fully represent the system setup intended for later measurements for KATRIN: to allow for flexible handling of components and facilitated alignment, it is not set up inside of a glove box, but under a fume hood. For this reason, a maximum tritium inventory of $10^{10}\,\mathrm{Bq}$ is permitted. The consequences from this limitation are the following:

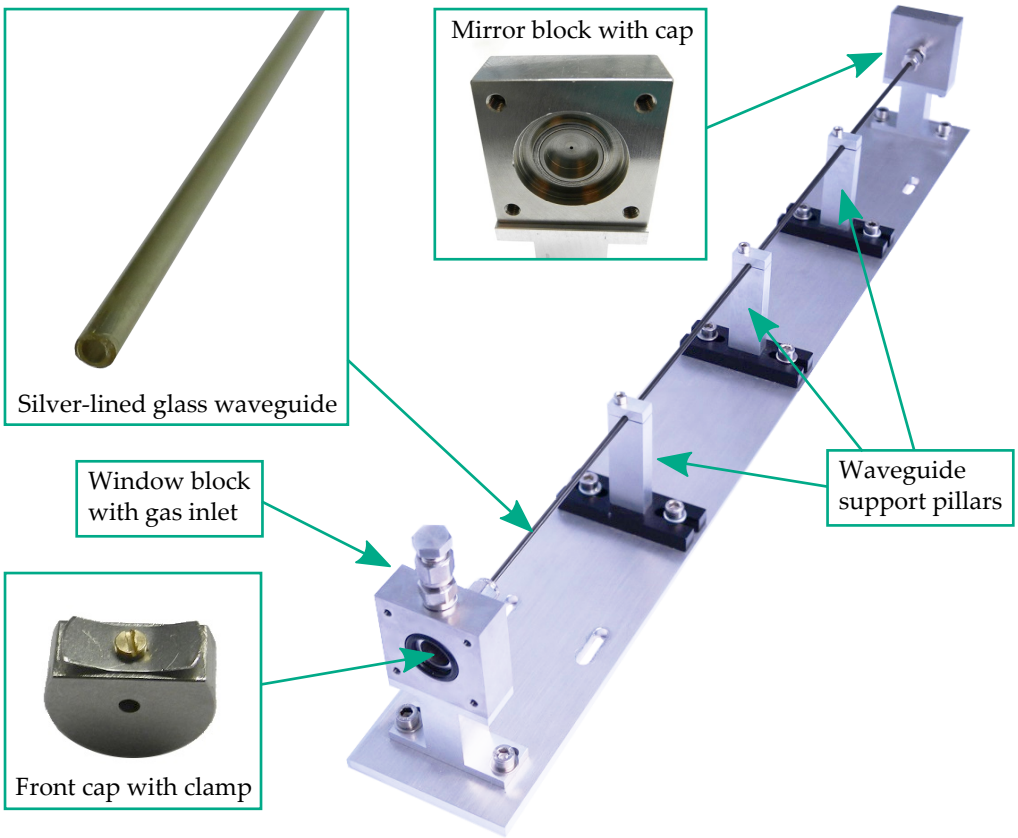

Figure 4.2.: Picture of the Raman gas cell. The window block is open in this picture, so that the inner chamber is visible through which the waveguide is filled with gas via the gas inlet on top of the block. The gas inlet is closed by a blind cap in this picture. The front cap shown in the lower left is clamped into the inner chamber. The O-ring which provides the sealing between the steel cell body and the window is visible at the front of the window block. The steel tube housing the waveguide is kept straight by three support pillars. The rear block houses the back-reflecting mirror, which is inserted into the rear cap. A schematic drawing of the gas cell design with sectional views of the blocks can be found in appendix E.

- Care had to be taken to keep the volume of the gas system small in order to be able to work with tritium partial pressures in the single-digit mbar range without exceeding the activity limit. For this reason, the waveguide was constructed for static measurements only with a single gas inlet, instead of setting up a full circulation loop with gas in- and outlets at both ends of the waveguide. By this means, the volume of the primary gas system could be restricted to 19 ml. Since sample cylinders with a volume of 10 ml are used to fill the system with tritium gas, the total volume amounts to 29 ml. This corresponds to a maximum allowed tritium partial pressure of 4.01 mbar, or 3.82 mbar taking into account a safety margin of 5 % on the accuracy of the tritium amount.

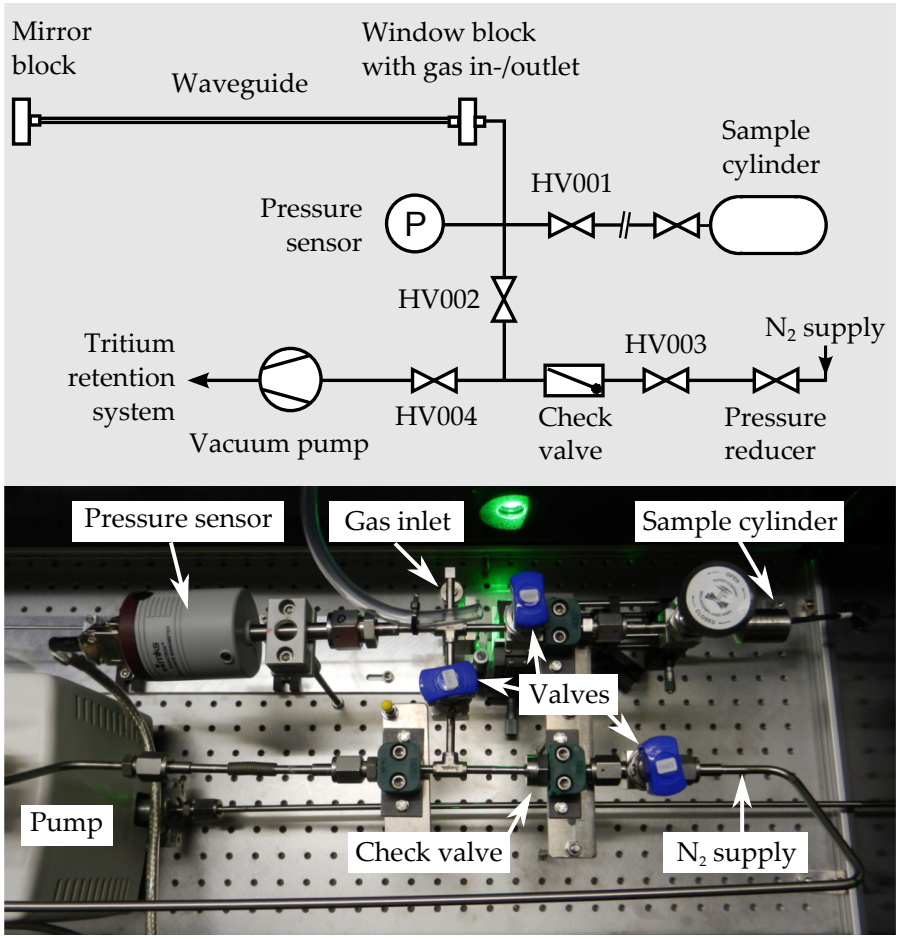

Figure 4.3.: Flowchart *(top)* and picture *(bottom)* of the gas handling system. The abbreviation HV in the flowchart stands for hand valve.

- The low total activity made it possible to use a Viton O-ring as the window sealing, which is not possible for high tritium activities due to degradation of the sealing material. Using an O-ring sealing for the prototype setup reduced manufacturing time and costs. For later non-prototype setups, the design can easily be altered to fully tritium compatible metal-glass sealings instead.

The gas cell is shown in figure 4.2: the waveguide is mounted in a stainless steel tube with an inner diameter of about 1.7 mm, which is connected at each end to a stainless steel block by a copper-sealed Swagelok fitting. The rear block houses the back-reflecting mirror, the front block contains the window through which laser and Raman light are coupled in or out of the system (see appendix E for a schematic drawing showing the inside of the blocks). A gas inlet on top of the front block connects the waveguide to a gas handling system which allows to evacuate the system and to fill it with gas. A flowchart and a picture of the gas handling system are shown in figure 4.3. The system provides the following functionalities:

Tritium supply: Tritium gas mixtures are provided by the TLK CAPER facility (see e.g. [Bor05, Dem11]). The gas is transported to the prototype system in a 10 ml sample cylinder, which can be connected to the evacuated system at valve HV001.

Nitrogen supply: The system is connected to a nitrogen supply line to be able to flush the system after a measurement. By this means, contamination of the system is kept low. In addition, nitrogen can be used for reference Raman measurements, e.g. to check the system alignment. The nitrogen flow is controlled by a pressure reducer and a hand valve; an additional check valve prevents contamination of the N_2 supply line.

Pressure monitoring: The pressure in the system is monitored by an absolute pressure transducer (MKS Baratron Type 626B12MBE) suitable to measure pressures of ≤ 100 mbar (accuracy 0.25 % of reading).

Evacuation: The system can be evacuated using an ACP 15 vacuum pump by Pfeiffer vacuum. This pump is oil-free, which is important for tritium operation. The pumping speed is 14 m^3/h, end pressures in the range of $3{\cdot}10^{-2}$ mbar can be reached. The pump exit is connected to the tritium retention system of the TLK.

All valves used have Vespel seats for reasons of tritium compatibility. Before measurements with the full tritium inventory were performed, the system was thoroughly leak-tested and commissioned with inactive gas mixtures. In addition, the activity in the fume hood air is continuously monitored by an ionization chamber to be able to quickly detect major leaks or contaminations.

4.2. Measurement and analysis procedure

4.2.1. Measurement procedure

After the commissioning with inactive hydrogen gas, two measurement runs with tritiated gases were performed: the first one with low tritium concentration (activity $\sim 10^8$ Bq) to ensure the safety of tritium operation in the system, and the second one with an activity close to the maximum allowed value ($\sim 8.6 \cdot 10^9$ Bq). Central measurement parameters of each run are collated in table 4.2. In addition, reference spectra with pure nitrogen gas at a constant pressure of approximately 80 mbar were taken prior to and between the measurements to ascertain the stability of the alignment and hence the measurement reproducibility.

For the initial low-activity measurement (run 'T-low'), a hydrogen gas mixture at an overall system pressure of 42.8 mbar was used. The mixture was prepared by the CAPER facility and analyzed by the standard 90° LARA system; it consisted of approximately 98.4 % H_2, 0.4 % HD, 0.2 % HT, 0.1 % D_2 and 0.8 % N_2. The high-activity measurement (run 'T-high') was performed with 3.4 mbar of almost pure tritium gas, consisting of about 93.2 % T_2, 4.0 % HT and 2.8 % DT according to a gas chromatographic analysis (measurement uncertainty approximately 5%). For each of the tritium runs, measurements were performed with a range of acquisition times, reaching from 0.1 s up to a maximum acquisition time $t_{\mathrm{acq,max}}$ for which the measured spectra were just not saturated (see

Table 4.2.: Measurement parameters of different prototype runs.

Run	Analyte x	p_{tot} (mbar)	p_x (mbar)	P (W)	$t_{\mathrm{acq,max}}$ (s)
T-low	H_2	42.8	42.1	1.00	2.35
T-high-1000	T_2	3.4	3.2	1.00	2.6
T-high-1750	T_2	3.4	3.2	1.75	1.6

table 4.2). Processing and analysis of the acquired data will be described in detail in the following subsection.

The measurement procedure for each tritium run comprised the following steps:

1. Filling of the sample cylinder at the CAPER facility and compositional analysis.
2. Evacuation of the gas system. (Turn on pump, open valves HV001, HV002, HV004.)
3. Connection of the sample cylinder to the evacuated system (Close valve HV001, remove blind cap at VCR connection behind valve HV001, attach sample cylinder to VCR connection.)
4. Evacuation of the gas system up to the sample cylinder valve. (Open valve HV001.)
5. Start of laser exposure for system warm-up.
6. End of evacuation. (Close valves HV002, HV004, turn off pump.)
7. Monitoring of the pressure sensor and the spectrum of the evacuated cell to check for leaks.
8. Filling of the gas system with sample gas. (Open sample cylinder valve.)
9. Acquisition of Raman spectra of the sample gas.
10. Evacuation of the gas system up to the sample cylinder valve. (Close sample cylinder valve, turn on pump, open valves HV002, HV004.)
11. Flushing of the system with nitrogen. (Close valve HV004, open valve HV003, fill system with $\leq 100\,\mathrm{mbar}$ of N_2, close valve HV003, open valve HV004. Repeat procedure several times.)
12. Removal of sample cylinder. (Close all valves, remove sample cylinder, attach blind cap to VCR connection.)
13. Acquisition of dark spectra.
14. Transport of sample cylinder back to CAPER facility.

The system warm-up (step 5) was performed not only to reach stable laser operation, but also to guarantee a stable background level in the spectra: when the waveguide system was exposed to laser light, a noticeable decrease of fluorescence background could be observed. The decrease slowed down with time. For this reason, the system was exposed for at least 20 min prior to each measurement until the background level was stable.

For radiation safety purposes, the activity of the fume hood air was controlled using an ionization chamber during each measurement. Only a small part of the lid was removed to open and close valves in order to maintain sufficient air exchange in the fume hood. In addition, proper connection of the sample cylinder to the system was ascertained by monitoring of the pressure sensor and the Raman spectrum of the evacuated cell (step 7): a leak at the connection would lead to ambient air entering the system and thus rising pressure and a rising nitrogen peak in the continuously monitored Raman spectrum.

At the end of each measurement run, dark measurements were performed to be able to quantify the detector-related noise, i.e. the combination of detector read-out noise and thermal noise (c.f. subsection 3.2.3).

4.2.2. Analysis of the spectra

The spectroscopic data was acquired using the integrated acquisition and analysis routine LARASoft [Sch15b, Fis14], which combines the Raman acquisition routines with post-acquisition cosmic ray removal, background correction and peak fitting routines [Jam13b]. Data analysis was done using parts of these routines plus a dedicated routine for determination of the signal-to-noise ratio of a spectrum written within the scope of this thesis. The single analysis steps are explained in the following.

Data acquisition: For each measurement setting, 50 back-to-back acquisitions were taken and averaged for shot noise reduction. All spectra were acquired with a CCD read-out speed of 100 kHz and CCD gain 3. The CCD was cooled to $-75\,^{\circ}\mathrm{C}$ to reduce thermal noise, and the 400 vertical CCD pixels were combined to 5 bins of 80 pixels each to reduce read-out noise.

Dead pixel removal and region of interest: Single dead CCD pixels were removed from the spectra. In addition, the first ten pixels were removed in each bin to eliminate a CCD-related distortion present at the low-pixel margin of each spectrum.

Cosmic ray removal: Cosmic rays were removed by the temporal removal routine described in [Jam13b] with a threshold of 200.

Binning and averaging: After the described processing steps, all bins of a single spectrum were added up pixel-wise to obtain the total count rate per pixel. Afterwards, the 50 back-to-back spectra acquired for each single measurement were averaged for shot noise reduction.

Signal extraction: As outlined in section 3.2, the maximum height of the peak associated to the Q_1 branch of the analyte of interest is taken as the Raman signal S for signal-to-noise calculation within the scope of this work. In order to obtain this signal from an acquired spectrum, the underlying background as shown in figure 3.5

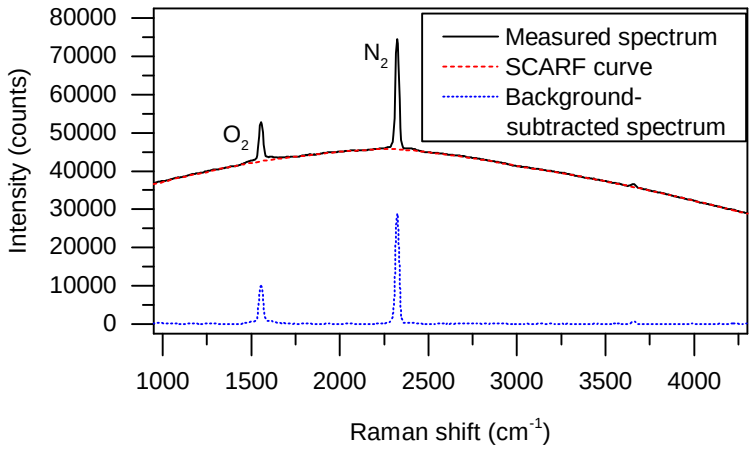

Figure 4.4.: SCARF background removal for signal extraction. A Raman spectrum of air with an intense fluorescence background is shown. The background curve is obtained by a SCARF routine and subtracted, so that the signal can be extracted from the resulting spectrum by taking the height of the peak of interest. Data taken from [Sei14].

has to be subtracted first. This is done using the background removal routine described in [Jam13b], which is based on a Savitzky-Golay Coupled Advanced Rolling Circle Filter (SCARF). In this routine, a rolling circle filter algorithm applied to a Raman spectrum is used to obtain the shape of the background curve, which is subsequently smoothed by means of a Savitzky-Golay filter and subtracted from the spectrum. The SCARF routine is applied twice to obtain even better background curves. A spectrum which is background-subtracted via SCARF is shown in 4.4. The signal is extracted from the background-subtracted spectrum by taking the maximum value inside a specified pixel region. The SCARF settings used for each measurement analysis are listed in appendix F.

Noise extraction: The noise can be obtained by taking the standard deviation of a flat part of the spectrum, ideally close to the Raman peak of interest as the noise can differ in different parts of the spectrum. Since measured spectra are rarely flat over a sufficiently large pixel range, the overall spectral shape is subtracted in this case as well to obtain the pure fluctuations. A polynomial fitting routine based on least square fitting and using a Cholesky algorithm to compute the best polynomial fit is utilized to obtain the background curve in this case.[3] Figure 4.5 illustrates this approach. The background is fitted over a certain range of pixels which is somewhat larger than the pixel range from which the noise is determined in order to account for possible small distortions of the fit curve at its start and end. The obtained background curve is subtracted from the spectrum and the standard deviation of the residual taken as the noise. The noise extraction settings used for each measurement analysis are listed in appendix F as well.

[3]The SCARF routine works well to separate spectral peaks which span across a certain range of pixels from a broad background curve. However, in the case of random pixel-to-pixel fluctuations as required for noise extraction, polynomial fitting allows for a closer approximation of the background curve than an approach based on a rolling circle filter.

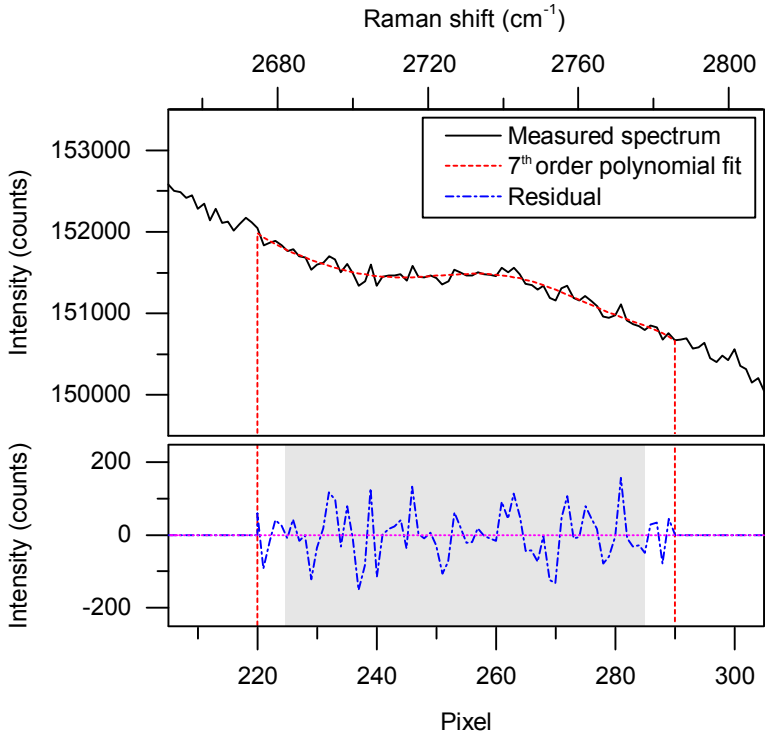

Figure 4.5.: Determination of the noise in a spectrum. The measured background curve is fitted in a certain pixel range *(marked here by vertical red lines)* in order to obtain the fluctuations of the curve only. The noise is determined as the standard deviation of a smaller pixel range *(gray area)*.

Calculation of uncertainties: The uncertainties of the signal-to-noise ratio and the detection limit for a certain measurement configuration can be obtained by using Gaussian error propagation:

$$\Delta\mathrm{SNR} = \mathrm{SNR} \cdot \sqrt{\left(\frac{\Delta S}{S}\right)^2 + \left(\frac{\Delta N}{N}\right)^2}\,, \tag{4.1}$$

$$\Delta\mathrm{LOD} = \mathrm{LOD} \cdot \sqrt{\left(\frac{\Delta p}{p}\right)^2 + \left(\frac{\Delta\mathrm{SNR}}{\mathrm{SNR}}\right)^2}\,. \tag{4.2}$$

The uncertainties of signal and noise required here are calculated as follows:

- **ΔS:** The total signal uncertainty is calculated by summing up three individual contributions quadratically:

$$\Delta S = \sqrt{\left(\frac{\sqrt{S_\mathrm{B}}}{\sqrt{n_\mathrm{acq}}}\right)^2 + N_\mathrm{D}^2 + \left(\frac{\Delta P}{P} \cdot S\right)^2}\,. \tag{4.3}$$

The first contribution is the uncertainty related to the statistical nature of the photon arrival rate at the detector (shot noise, c.f. subsection 3.2.3). Since the arrival rate follows a Poisson distribution, the uncertainty is given by the square

root of the total photon signal at the Raman peak of interest, S_B. Not only the Raman photons have to be taken into account here, but also the external background photons. For this reason, S_B is obtained by subtracting the detector offset from the total measured peak intensity (c.f. figure 3.5). This uncertainty contribution is reduced by a factor $\sqrt{n_{acq}}$ when n_{acq} back-to-back spectra are averaged.

The second uncertainty contribution is the detector-related noise N_D, i.e. the combination of detector read-out noise and thermal noise (c.f. subsection 3.2.3). It is obtained by taking a dark spectrum and evaluating its standard deviation as described above in the 'noise extraction' paragraph. The same pixel range as for the background noise determination is used.

The third contribution arises from the uncertainty of the incident laser power. The Raman signal is proportional to the laser power, so that the corresponding uncertainty is given by the percentage power uncertainty $\Delta P/P$ multiplied by the total signal.

- **ΔN:** The noise uncertainty is calculated by

$$\Delta N = \sqrt{\left(\frac{N}{\sqrt{n}}\right)^2 + \left[\left(\sqrt{1+\frac{\Delta P}{P}} - 1\right) \cdot N\right]^2} \ . \tag{4.4}$$

The first contribution is connected to the determination of the noise by taking the standard deviation of the spectrum over a certain limited pixel range: the more pixels are used, the better is the estimation of the noise. The uncertainty related to this method is the so-called standard deviation of the mean, which decreases with the square root of the number n of data points used to calculate the noise [GUM08].

The second uncertainty contribution is again related to the laser power uncertainty, which influences the shot noise of the background. The approximation is made that the total noise is proportional to the square root of the laser power according to equation 3.36, i.e. $N = C \cdot \sqrt{P}$ with proportionality constant C.[4] In this case, the power-related uncertainty contribution can be calculated as follows:

$$N + \Delta N_P = C \cdot \sqrt{P + \Delta P} = C \cdot \sqrt{P} \cdot \sqrt{1+\frac{\Delta P}{P}} = N \cdot \sqrt{1+\frac{\Delta P}{P}} \tag{4.5}$$

$$\Leftrightarrow \qquad \Delta N_P = \left(\sqrt{1+\frac{\Delta P}{P}} - 1\right) \cdot N \ . \tag{4.6}$$

Wavelength calibration: A wavelength calibration is done using a Ne(Pb) spectral lamp in order to transfer pixels into Raman shifts in the x-axis of the spectra.

[4] In fact, only the shot noise due to external background light is proportional to the laser power, while the detector-related noise contributions are constant. The approximation assumes that these small constant contributions are negligible compared to the external shot noise. In case the external background becomes so low that the total noise is dominated by detector-related noise, equation 4.4 leads to an upper limit on the total uncertainty.

Table 4.3.: Overview of obtained detection limits. Note that the number of averaged spectra, n_{acq}, is the same for all measurements. It is listed below nonetheless to stress the fact that the total acquisition time to obtain the stated LOD values is 50 x t_{acq}.

Run	Analyte	P (W)	n_{acq}	t_{acq} (s)	LOD (mbar)
T-low	H_2	1.00	50	2.35	0.20 ± 0.03
T-high-1000	T_2	1.00	50	2.6	0.21 ± 0.03
T-high-1750	T_2	1.75	50	1.6	0.17 ± 0.02
T-low	H_2	1.00	50	0.1	0.66 ± 0.09
T-high-1000	T_2	1.00	50	0.1	0.68 ± 0.11
T-high-1750	T_2	1.75	50	0.1	0.43 ± 0.06

4.3. Achieved sensitivity

The detection limits obtained for each run are summarized in table 4.3. The top part of the table shows the minimum detection limits, i.e. the ones obtained for the maximum acquisition time which could still be used in a measurement without saturating the CCD detector. The bottom part of the table lists detection limits obtained within the same acquisition time to allow for direct comparison of the tritium runs. It should be noted that the only detectable analytes in the tritium runs are H_2 in the 'T-low' run and T_2 in the 'T-high' run, since the partial pressures of all other hydrogen isotopologues (≤ 0.17 mbar for 'T-low', ≤ 0.14 mbar for 'T-high') are below the respective detection limits. The detection limits of H_2 and T_2 obtained for the same laser power and similar acquisition times are basically the same within the measurement uncertainty, which is expected due to the similar Raman cross sections for the hydrogen isotopologues.[5]

The table shows that the best detection limits are of the order of 10^{-1} mbar and thus about two orders of magnitude higher (i.e. worse) than aimed for. Of course, the system performance depends to a certain extent on the chosen measurement settings:

The comparison between measurements with 1 W and 1.75 W laser power demonstrates that better detection limits can in principle be reached by using higher laser powers. However, as discussed before, the sensitivity does not scale linearly with increasing laser power since not only the signal, but also the fluorescence background and thus the shot noise are increased. The same is true for longer acquisition times, as shown in figure 4.6: the detection limit improves approximately with only the inverse square root of laser power or acquisition time. Exorbitantly high laser powers and/or acquisition times would thus be required to increase the prototype sensitivity by two orders of magnitude. This is

[5] The Raman cross sections for all hydrogen isotopologues are listed in appendix G. The scattering cross section is approximately 20% higher for H_2 than for T_2. In the data of table 4.3, this difference cannot be resolved due to the comparatively high uncertainties of the determined LOD values. Note that the relative intensity of different Raman lines also depends to a certain extent on the spectral sensitivity of the Raman system used, i.e. its wavelength-dependent light detection efficiency (see e.g. [Sch13b]).

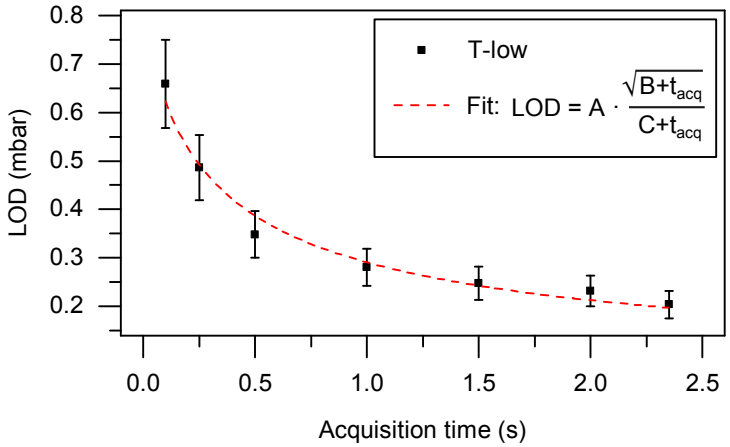

Figure 4.6.: Dependence of the detection limit on the acquisition time. The plot shows detection limits of H_2 from the 'T-low' run for a range of acquisition times between 0.1 s and 1.6 s. The progression of the curve can be explained by the approximate proportionality of the noise to $\sqrt{t_{\mathrm{acq}}}$ and the signal to t_{acq} in the detection limit LOD $\propto N/S$. The additional parameters B and C used to fit the curve take into account time-independent read-out noise contributions to the total noise (B), and the small constant signal offset due to additional light being detected during the CCD read-out process (C).

not possible – not only due to the reasons discussed already in section 3.3, namely the damage threshold of optics and the limited time frame for analytical measurements for KATRIN, but also due to detector saturation: even with the current settings, acquisitions of more than two or three seconds were not possible without saturating the detector. This limitation can be partly overcome by averaging multiple spectra as was the case here, or by combining the 400 vertical CCD pixels in more single bins with less pixels each. However, both alternatives go along with an increased read-out noise. The optimal choice of such measurement settings will be discussed in more detail in subsection 6.7.3. In any case, the target sensitivity does not yet seem to be within reach with the current prototype implementation even with optimized measurement settings.

It is worthwhile to compare the obtained results with the performance of the standard LARA system, which achieved a detection limit of the order of 0.068 mbar in an acquisition time of 2 x 10 s for the inactive hydrogen isotopologues [Sch13b]. This value is lower than the minimum LODs achieved with the current waveguide prototype. However, it has to be taken into account that a spectrometer with approximately 2.64 times higher light throughput and a higher laser power of 5 W was used for said standard measurements. Scaling the LOD reported there with a factor of $\sqrt{2.64 \cdot 5} \approx 3.6$ leads to a value of about 0.24 mbar, which is close to the detection limits stated above. The performance of the hollow waveguide based prototype system is thus similar, but not superior to the standard 90° implementation. The reasons for this are discussed in the following section, along with further findings and conclusions drawn from the experiences made with the prototype setup.

4.4. Discussion of limitations of the prototype setup

The prototype setup was intended to explore the potential of hollow waveguide based Raman spectroscopy for KATRIN. The experiences gained during construction, commissioning and tritium operation provided many helpful insights into shortcomings of the current implementation with respect to the goals defined in subsection 2.6, and thus allowed for identification of the necessary steps towards a fully tritium compatible, highly sensitive Raman system. The detailed findings are discussed in the following subsections.

4.4.1. High fluorescence background

In figure 4.7, spectra acquired in the run 'T-high-1000' are shown together with a dark spectrum. Evidently, the external background level is very high: for a 2.6 s measurement, a T_2 Raman signal of about 3300 counts is accompanied by a fluorescence background of more than 150000 counts. This high background level is the reason why the CCD detector saturates within seconds, and above all gives rise to a non-negligible shot noise. The insets in the figure illustrate the noticeable noise increase by external background contributions. This high noise more or less neutralizes the signal enhancement by the hollow waveguide based Raman approach, and thus severely constrains the overall sensitivity gain. This explains why the sensitivity of the prototype setup is not significantly better than the one achieved with the standard LARA system, as discussed in the previous section.

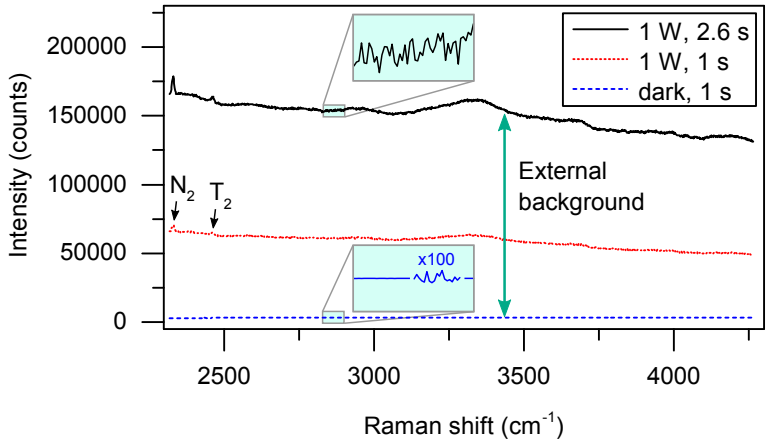

Figure 4.7.: Fluorescence background of the hollow waveguide based prototype system. The plot shows data from run 'T-high-1000' at two different acquisition times, and a dark spectrum for comparison. The positions of the peaks associated to the Q_1 branches of T_2 and N_2 are labeled in the plot. The nitrogen Raman signal arises from ambient air outside the gas cell, which is excited by the laser beam between the cell window and the dichroic beam splitter. The insets show zoomed-in views of the background curves of Raman measurement and dark spectrum at a Raman shift of 2835 – 2909 cm^{-1} and over an intensity range of 3350 counts each.

The detector-related noise obtained from the dark spectrum shown here is of the order of 1 count, while a 1 s measurement at 1 W laser power leads already to a total noise of 47 ± 6 counts. For a five times higher laser power – as currently employed in the standard LARA system, and as would be used for a hollow waveguide based Raman system for KATRIN as well – even a noise of about $47 \cdot \sqrt{5}$ counts ≈ 105 counts could be expected, i.e. a value two orders of magnitude higher than in the absence of external background. Since the detection limit is directly proportional to the noise value, the targeted sensitivity increase by a factor of 100 could in principle be reached by eliminating the external background. For this reason, fluorescence reduction is a major topic of this work. It will be treated in detail in chapter 6: after an introduction into the phenomenon of fluorescence in optical systems in section 6.1, the individual fluorescence sources in the prototype setup are identified in section 6.2. Based on this, detailed investigations of fluorescence-reducing measures are described in the following sections.

4.4.2. Damage of optical components

Damage of optical components was observed during commissioning and after the high-activity tritium run. The two incidents were probably due to different damage mechanisms, namely laser-induced and mechanical damage in the one case and radiation-induced damage in the other.

Damage of optics during commissioning: After a first incarnation of the system had been closed, leak-tested and commissioned with an inactive gas mixture of H_2, D_2 and HD, the fluorescence background suddenly increased by about a factor of 3 over night. Spectra taken before and after the fluorescence increase are shown in figure 4.8. The signal decreased only slightly by about 3 %. The system had been evacuated after the inactive commissioning and filled with air the following morning. The fluorescence

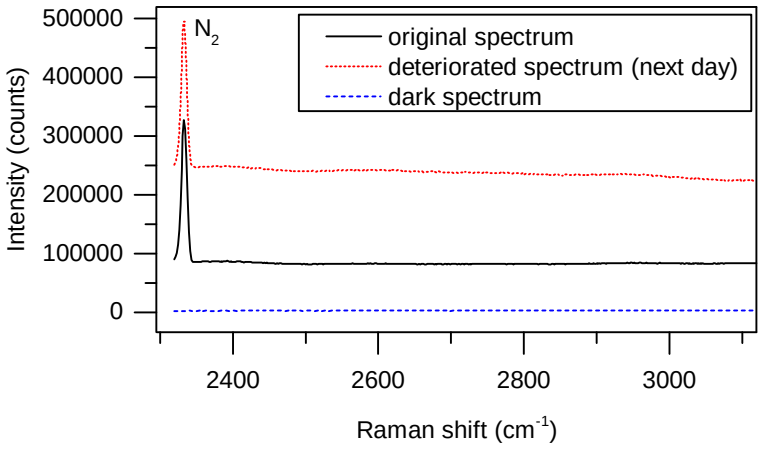

Figure 4.8.: Comparison of spectra of air before and after the fluorescence rise. All spectra were acquired at an acquisition time of 0.5 s. A laser power of 2 W was used for the Raman measurement of air.

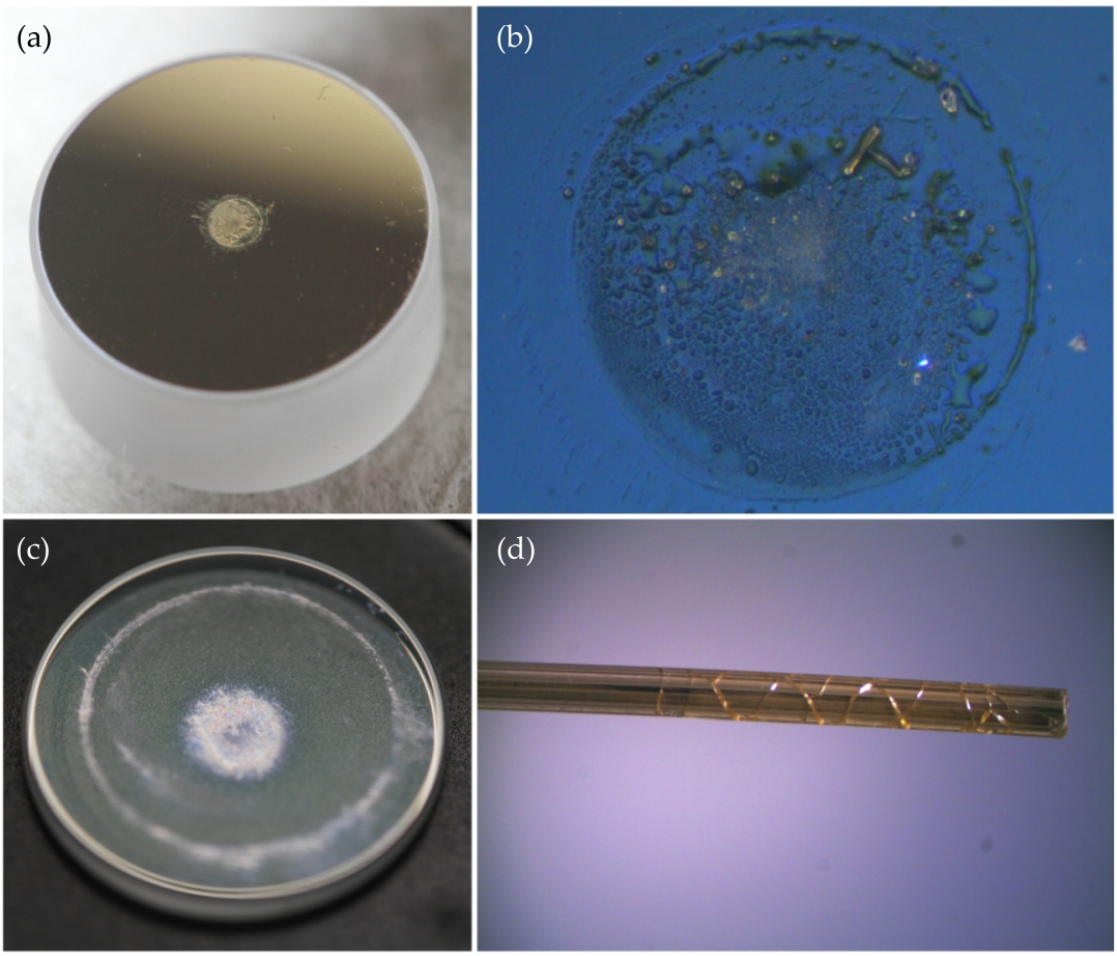

Figure 4.9.: Damage of components during commissioning. *(a)* Deposition on the back-reflecting mirror. *(b)* Microscopic image of the mirror deposition. *(c)* Deposition on the inner surface of the window. Note that the deposition looks very white due to reflections in this picture, while it is perceived as a rather faint film with the naked eye. The outer ring is due to the O-ring seal on the outer surface of the window. *(d)* Fissures in the front end of the hollow waveguide.

level could not be restored to its former level by any realignment efforts. For this reason, the system was disassembled in order to control the condition of the optical components. Pictures of the back-reflecting mirror at the end of the waveguide, the window and the hollow waveguide itself taken after the disassembly are shown in figure 4.9.

The mirror exhibits a clearly visible spot in the center with a size approximately matching the outer diameter of the waveguide. The microscopic image reveals a droplet-like deposition which looks partly transparent, partly rather metallic (e.g. in the upper right). The center of the spot looks brighter and more diffuse in an area of about 0.3 mm diameter. The deposition could be fully removed by cleaning the mirror with ethanol. Some of this deposition might be due to moisture in the air. However, in this case, one would expect a similar effect already in earlier evacuation and venting tests, and an evaporation of the droplets within days after the disassembly. This was not observed. Another possibility

is that the deposition is silver ablated from the waveguide lining by high local laser power densities. Silver depositions on the mirror could lead to a misalignment of the back-reflecting beam, which would increase the fluorescence in the measured spectrum as observed. The damage occurred at an early stage of the prototype installation, where there was not yet a cap at the mirror end of the waveguide to protect its end face, and the cap at the waveguide front was not yet secured from moving by a clamp as shown in figure 4.2. The deposition could thus have been caused by an initial beam misalignment due to movements of components inside the gas system during evacuation or filling, causing the beam to directly strike the waveguide surface near the mirror end and burning it. Such burning had already previously been observed in tests by the Swansea group, leading to burnt spots on the waveguide front face and production of white smoke. A much slighter deposition was also observed on the inner window surface (see figure 4.9 (c)), probably due to the larger distance of the window from the waveguide.

In order to avoid similar optics damage in the future, an additional waveguide-protecting cap at the rear end and a clamp-secured front cap was introduced prior to reassembly of the system with new, undamaged components. In addition, the laser power was reduced to a maximum of 1.75 W; most measurements were done at 1 W laser power. Particular care was taken to ensure proper alignment at low power (in the mW range) before going up to high power.

It was not possible to discern damaged spots inside the small-diameter waveguide. However, the front waveguide end was found to be fissured over a length of about 14 mm (see figure 4.9 (d)). This indicates that the waveguide was exposed to mechanical stress, possibly due to movements of the front cap during evacuation or gas filling. It is not clear to what extent the silver lining was affected by the fissures. Since the waveguide end did not fall apart, it can be assumed that the fissures did not fully penetrate the glass walls, so that the lining might have remained intact. However, small fissures in the silver lining cannot be excluded. This would provide direct access of laser light to the glass substrate and thus enhance the fluorescence background. Mechanical stress on the waveguide was hereafter avoided by fixing the waveguide front cap inside the front block with a metal clamp.

Damage of optics after tritium exposure: After the new measures were implemented, no degradation of spectra was observed during further tests, re-commissioning with inactive gas mixtures and the first tritium run with low activity ('T-low'). The high-activity run ('T-high') was performed a week after the low-activity one. Afterwards, the system was evacuated. When it was filled with pure nitrogen two weeks later, the signal had decreased by about 57 %, and the shape of the background curve was significantly altered. Figure 4.10 shows that the previously comparably constant background changed into a curve steeply rising for increasing Raman shifts, even though this goes along with a small decrease at low Raman shifts. This curve was reproducibly obtained in several realignment attempts. Several months later, during which the contaminated system was kept evacuated, no reasonable Raman spectrum could be obtained any more. For this reason, the system was disassembled again.

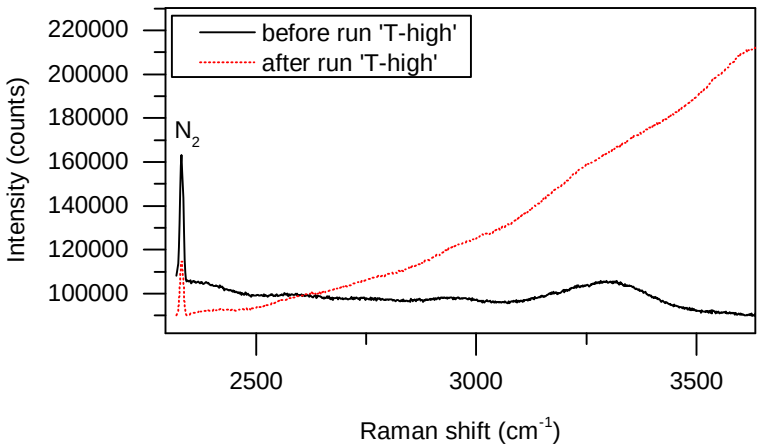

Figure 4.10.: Comparison of spectra of N_2 before and after high-activity tritium exposure. The first spectrum was acquired directly before the run 'T-high' started, the second one two weeks afterwards. Both spectra were acquired at an acquisition time of 1.7 s and a laser power of 1 W.

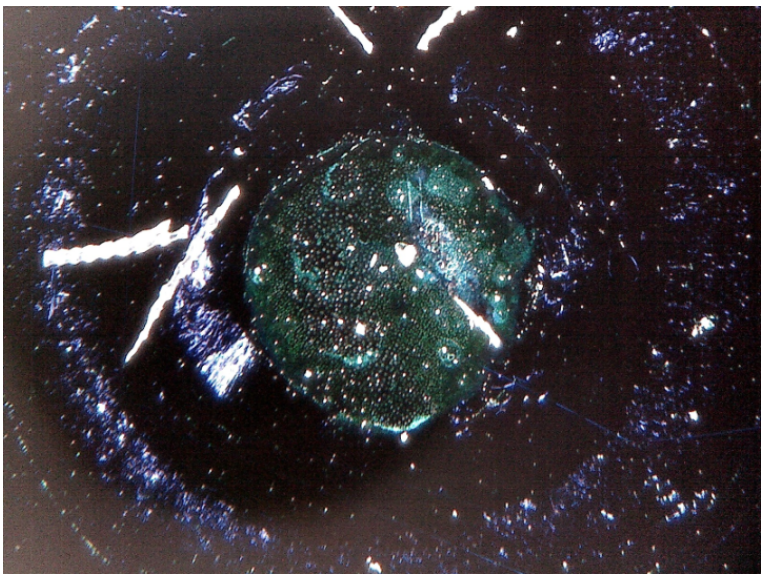

Figure 4.11.: Microscopic image of the back-reflecting mirror after tritium exposure. The greenish central spot has a diameter of about 0.9 mm. The surrounding mirror surface is partly scratched due to direct contact of the mirror with the steel surface of the waveguide protection cap. The bright, longish shapes are small fibers from the lens tissue in which the mirror was loosely wrapped after disassembly.

No damage of the window or the waveguide was visible, whereas the back-reflecting mirror showed clear signs of degradation. In figure 4.11, a microscopic image of the greenish spot which had appeared in the very center of the mirror is shown. The spot diameter is of about the same size as the central aperture of the cap covering the waveguide end. The steel surface of the cap was in direct contact with the mirror surface.

There are two possible damage sources: laser light and/or tritium β-radiation. The spot size seems to indicate an involvement of the laser, since tritium gas should have reached other parts of the mirror as well. However, the laser alone did not cause any fluorescence increase in the weeks before the tritium measurement, and no worsening was observed during the high-activity run where both laser and tritium were in contact with the mirror either. It is therefore more probable that β-radiation is the source of the observed damage, with a focus on the mirror center as the rest of the mirror was partly shielded by the cap and thus less exposed. The gradual degradation of the spectra observed following different laser-free periods after the high-activity run supports this conclusion: contamination of the inner surfaces in a gas system persists to a certain extent even if the system is evacuated and can thus lead to continuous degradation.

This indicates that the dielectric broadband HR-coating of the back-reflecting mirror is susceptible to radiation damage. This finding is in line with recent tests of the durability of window coatings under tritium exposure by LARA group member S. Fischer, where formation of spot-like features was observed on window coatings produced by electron beam deposition (EBD) [Fis14, Fis15].

The inner surface of the waveguide could not be optically examined due to the small inner diameter, so it could not be directly determined whether the silver lining was damaged as well. However, when the damaged mirror was removed from the system and replaced by a window, signal and fluorescence background went back almost to the former values (divided by two due to the missing back-reflection). Only a slight (relative) background increase and a signal decrease by 3 – 4 % was observed, which could be either due to the altered configuration or to damage of the waveguide lining. Thin metal coatings on glass had been found to be susceptible to damage in aggressive environments earlier, e.g. by Vessieres et al. when working with chlorinated organic solvents and gold coatings [Ves90]. It cannot by excluded that the waveguide was damaged by tritium as well, although not to the same extent as the mirror.

Conclusions: It was demonstrated that the waveguide-based Raman prototype is prone to damage in several respects:

(i) The waveguide itself is made of a thin glass tube and can thus easily be damaged mechanically.

(ii) Small beam misalignments at high powers can lead to damage and ablation of the silver lining on the inner surface of the waveguide.

(iii) Optical surfaces can be damaged and change their optical properties when exposed to tritium.

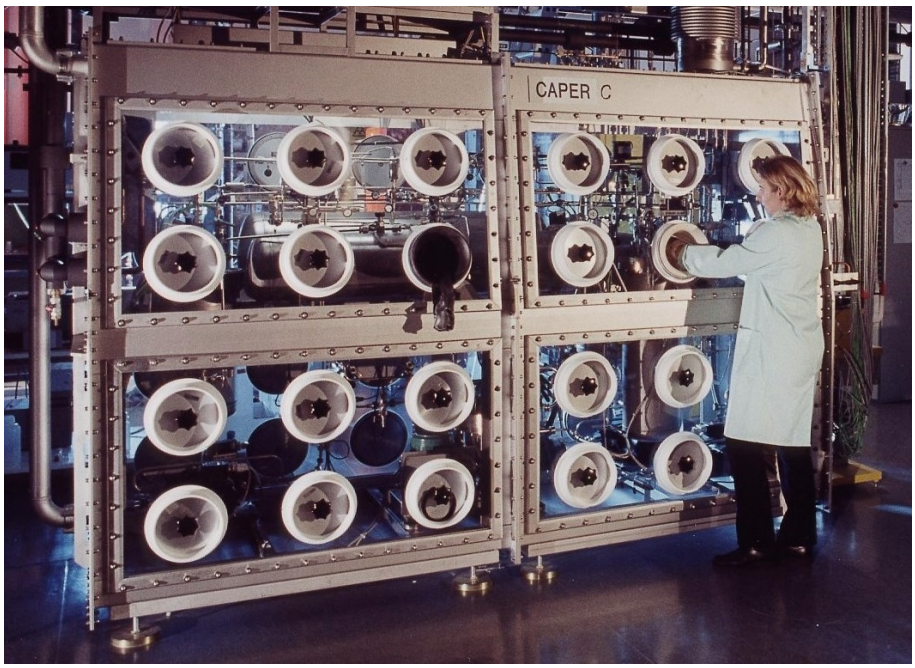

Figure 4.12.: Glove box at the Tritium Laboratory Karlsruhe.

In order to tackle the first two issues, alternative hollow waveguides less susceptible to damage were investigated within the scope of this work. This will be the topic of section 6.6. With respect to item (iii), it is of utmost importance to ensure constantly good optical properties of components inside the gas system for reliable long-term operation with tritium. For this reason, a test experiment to examine the durability of a range of reflecting optical surfaces under tritium exposure was conducted. Section 5.1 presents the experiment and the results, based on which further system developments could be advanced.

4.4.3. Limited suitability for glove box operation

The final Raman system will have to be located inside a glove box for tritium-related safety reasons; a picture of a glove box at TLK is shown in figure 4.12. This complicates alignment processes and system operation in several respects compared to setups in normal laboratory environments:

(i) Systems inside glove boxes can be accessed only via gloves installed at certain, fixed positions along the box window panes. For this reason, setups can be viewed and accessed only within very limited angles. Care has to be taken that all important components can be accessed and handled properly from outside. Also, the constrained view makes it harder to observe and assess the laser beam path and the overall system alignment.

(ii) The gloves themselves are made from halogen-free rubber (EPDM, or BIIR with CSM coating). They have a minimum thickness of 0.4 mm in order to prevent tritium

from permeating through the material, and to minimize the risk of damaging the gloves. In addition, the pressure in TLK glove boxes is lower than the ambient pressure for safety reasons, so that the gloves are sucked into the box away from the arm and fingers of the operator. For these reasons, fine motor manipulations of optics are handicapped to a certain extent.

(iii) Measurement conditions in a glove box are normally less controlled than in optical experiments outside. For instance, vibrations in a glove box are frequently encountered due to pumps within the box, and temperature changes in the range of few Kelvins are common, being influenced by a range of factors like the (varying) ambient temperature or operation of motors, light sources etc. in the box. To ascertain reliable operation under these conditions, measurement systems have to be either actively stabilized or intrinsically robust. The latter variant is preferable due to the risk of component failure in stabilization systems (especially in tritium environments); replacement of components inside of glove boxes can be time-consuming and expensive.

All in all, an easy-to-align and robust Raman setup should be envisaged for successful operation in a glove box. However, the current prototype implementation is very sensitive to misalignments. If the laser beam deviates slightly from running exactly parallel to the waveguide, fluorescence production inside the waveguide increases promptly. Also, the beam has to be well centered with respect to the waveguide, or the signal drops very fast. Figure 4.13 shows changes in a spectrum which resulted from minimal adjustments of the angular position of the laser guiding mirrors (M2 and M3 in figure 4.1): both signal and background vary easily by factors of 2 or more.

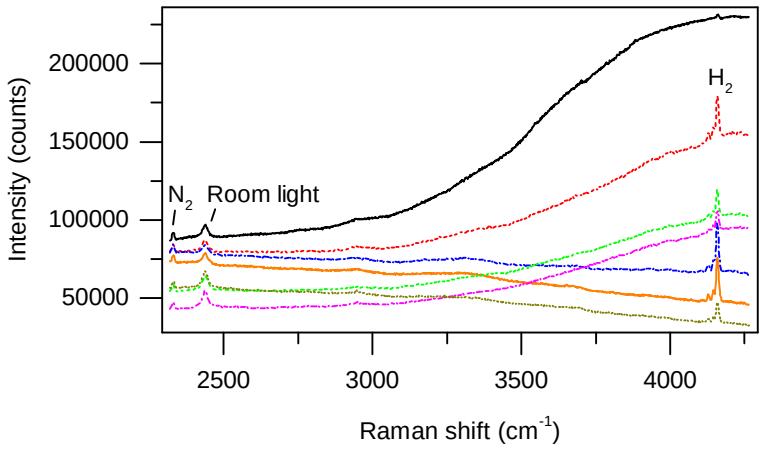

Figure 4.13.: Influence of the prototype alignment on the measured spectra. Spectra of the same sample taken with the same settings, but with slightly altered optical alignment between each acquisition are shown. The sample gas was pure H_2 at a pressure of 95 mbar. A laser power of 1 W and an acquisition time of 1 s was used. The two peaks at small Raman shifts belong to N_2 Raman light collected from ambient air, and to room light able to enter the system since the lid was partly opened for the alignment changes.

Also, to achieve proper alignment of the prototype system is not trivial even outside of a glove box, since the laser beam path directly in front of the window is too short to determine if the beam is strictly parallel to the waveguide, and one cannot directly see if the beam is well centered. As long as the gas system is not yet closed, the back-reflecting mirror can be removed and the transmitted laser beam be sent on a screen. The shape of the resulting spot gives a good indication if the alignment is good. However, this is not possible in regular operation mode with the mirror inserted and the back-reflected laser beam following the initial beam path. In this case, signal and background height in acquired spectra are the only feasible indicators for the alignment quality. In order to achieve sufficient signals, however, a relatively high laser power (in the range of few 100 mW) is required, which carries the risk to damage the waveguide during the alignment process. In addition, as soon as the system is operated with tritium and thus contaminated, it cannot be easily opened any more to go back to the first alignment method.

For these reasons, the final system has to be either rigidly stabilized to ensure that an initial, very good alignment is maintained over the whole period of operation, or it has to be designed in such a way that realignments are more easily possible than in the prototype setup. Possibilities to improve the suitability of the hollow waveguide based Raman system for operation in glove boxes will be discussed in section 5.2 in the following chapter. In addition, section 6.6 will be concerned with alternative waveguides which make the system less sensitive to minor changes in the laser beam angle or position.

4.5. Summary

The prototype of a hollow waveguide based Raman system for tritium measurements was successfully set up and tested to explore the potential of this technique for KATRIN. In the scope of different tests, works and measurements carried out with the system, several limitations of the current implementation with respect to the overall goals of this thesis – namely high sensitivity and tritium compatibility – could be identified. The findings allowed for the determination of the next steps towards these goals. The topic of how to improve the suitability of the system for operation in tritium environments is discussed in the following chapter, both with respect to an improved usability in glove boxes and tritium compatibility of optical components. Based on these findings, chapter 6 focuses on the investigation of fluorescence-reducing measures in order to achieve the target sensitivity.

5. Improvement of the system's suitability for operation in tritium environments

The test of a first hollow waveguide based prototype system for the use with tritiated gases, which was described in the previous chapter, allowed for the identification of the necessary steps towards a fully tritium compatible and reliable Raman system. Future operation within a tritium glove box requires improved system stability and options for facilitated alignment. Even more importantly, in order to guarantee reliable long-term operation it has to be ensured that optical properties of components inside the gas system – in particular the hollow waveguide itself – do not degrade with time due to tritium exposure. For this reason, a dedicated test experiment to examine the durability of reflecting optical surfaces under tritium exposure was conducted.

These topics are addressed in detail in this chapter, which is structured as follows: the durability test experiment is discussed in section 5.1, including concept outlines, the description of the measurement setup and a critical summary of the results. Afterwards, the possibility to improve the usability of the Raman system in a glove box by means of fiber delivery of the laser is addressed in section 5.2. Advantages of this approach are discussed, before concrete suggestions for a stable optical system and a suitable fiber feedthrough for the glove box are presented.

5.1. Durability test of reflective surfaces under tritium exposure

5.1.1. Motivation and measurement principle

As highlighted in subsection 4.4.2, damage of the broadband-coated dielectric mirror in the prototype system was observed after it had been exposed to almost pure tritium. It could not be determined if the silver lining of the waveguide itself was also affected. However, silver-plated metal gaskets employed in the CAPER facility at TLK (see e.g. [Bor05, Dem11]) were found to have turned black after a certain time of tritium operation. Since they are not exposed to air within the tritium gas system, this observation suggests a different – possibly tritium-related – damage mechanism than normal tarnishing for silver surfaces.

These observations are of high relevance for the planned hollow waveguide based Raman system for KATRIN, since a highly reflective inner surface of the hollow waveguide is

crucial to obtain high signals (cf. subsection 3.4.1). In order to use such a system for long-term monitoring of tritiated gases, good reflection properties have to be maintained over a period of several years, with respect to both the waveguide itself and mirrors located within the gas system. For this reason, it is vital to ensure the durability of reflecting surfaces under tritium exposure before they are installed in the final system, and to identify possible alternatives in case the established components turn out to be unsuitable for long-term tritium operation.

A dedicated durability test experiment was thus conducted within the scope of this work. In this experiment, a range of possible waveguide and mirror surfaces were exposed to tritium. The reflectance of these test specimens was compared to the values obtained before exposure, and to the reflectance of reference specimens of the same type which were stored in air and nitrogen atmosphere instead of tritium during the exposure period.

In the following, characteristics of different mirror surfaces and possible effects on their reflectance due to tritium exposure are discussed first. Afterwards, the chosen samples as well as the measurement setup and procedure are explained, before the obtained results are presented and discussed.

5.1.2. Introduction to highly reflective surfaces

In general, there are two types of highly reflective mirrors available: dielectric multilayer mirrors and metallic mirrors.

Multilayer dielectric coatings are obtained by stacking quarter-wave dielectric layers of alternate high and low index [Mac01], usually amorphous SiO_2 (fused silica) and metal oxides [Bau04]. By this means, light of a certain wavelength which is reflected from layer interfaces interferes constructively, leading to the effective reflection of a large fraction of the incident wavelength. Such optimized dielectric coatings allow for higher reflectances than many simple metal surfaces, with typical average values of $> 99\,\%$ in the design wavelength range [Tho14b]. It should be noted that the performance depends on the angle of incidence. Despite the good performance of multilayer dielectric coatings for normal mirror applications, they are not feasible for hollow waveguides for two reasons: the individual layers of multilayer coatings can hardly be uniformly applied within a long, thin tube [And04], and the angles of incidence of Raman light reflected in the waveguide are not restricted to the design value.

Metallic mirrors often use metal coatings on glass substrates due to the inherent smoothness of glass surfaces which is important for a high overall reflectance (cf. [Mat90, Osa95]). Alternatively, metal coatings can be applied to metal substrates, or polished metal surfaces can be directly used as mirrors. Typical metals used for mirrors are silver, gold or aluminum, depending on the intended application. The reflectances of these metals and copper are shown in figure 5.1 together with the reflectance of a broadband dielectric coating designed for a wavelength range of $400 - 750\,\mathrm{nm}$. In many cases, the reflectance varies considerably depending on the wavelength. The best reflection properties for both laser and Raman light are provided by silver and the dielectric coating, reaching about $98 - 99\,\%$ reflectance. The reflectance of aluminum is relatively constant over the wavelength range of interest ($\sim 530 - 700\,\mathrm{nm}$), but on a lower level of only about $91\,\%$. Gold

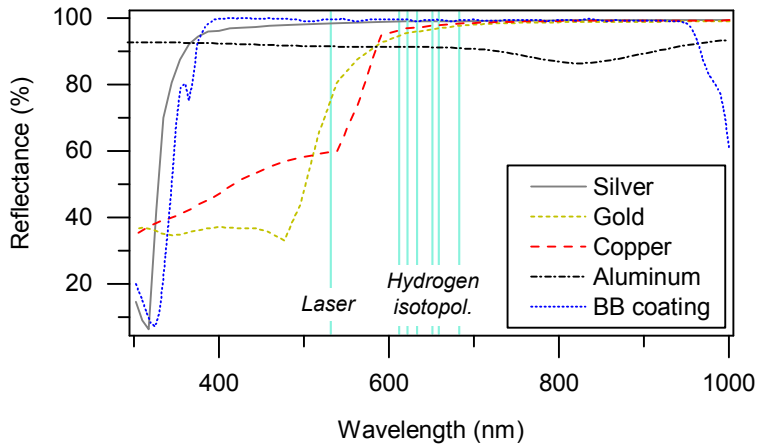

Figure 5.1.: Reflectances of different metals and a broadband dielectric coating at normal incidence. The wavelengths of the laser used in this work and the corresponding Q_1 branches of the six hydrogen isotopologues are indicated by vertical lines. The metal reflectance curves were calculated using the formula for normal incidence reflectance of opaque media [Hay13]: $R = \left[(1-n)^2 + k^2\right] / \left[(1+n)^2 + k^2\right]$ with n and k being the real and imaginary parts of the complex refractive index of each metal, and assuming light incident from vacuum or air with an approximate refractive index of 1. The values of n and k were taken from Babar and Weaver for silver, gold and copper [Bab15], and from Rakić et al. for aluminum [Rak98]. The broadband (BB) coating shown here is a E02 coating from Thorlabs designed for a wavelength range of 400 – 750 nm [Tho14b].

and copper provided reasonably high reflectances around the Q_1 branches of the hydrogen isotopologues, although these metals are less suitable as mirrors for the green laser light. It should be noted that metallic mirrors are often furnished with a thin protective overcoat (e.g. of SiO_2) to avoid tarnishing and/or scratches of the surface [Tho14b].

5.1.3. Possible effects on reflective surfaces in tritium atmospheres

In the case of dielectric multilayer coatings, the uppermost layer generally consists of amorphous SiO_2 [Bau04]. When exposed to radiation, this layer can suffer densifications which lead to a change of the refractive index [Dev94]. Densifications were observed for different irradiation scenarios by several research groups (see e.g. [Nor74, Dev94, Bus09]); Norris and EerNisse report this effect already for relatively low-energy electron irradiation in the range up to 18 keV [Nor74], which corresponds to the energy range of tritium β-electrons. The resulting refraction index change of up to 1 % [Dev94] affects the fined-tuned optical design of a multilayer coating and can thus influence the overall reflectance. In addition, densifications were observed to induce mechanical stress in SiO_2 [Nor74], which can lead to coating damages. For multilayer coatings of LARA windows, formation of spot-like features were observed after 17 days of tritium exposure if the windows were produced by electron beam deposition (EBD), whereas no indication for damage could be found in the case of denser coatings produced by methods such as magnetron sputtering or ion beam sputtering [Fis14, Fis15].

Less data is available for reflectance changes of metals under tritium exposure. Radiation damage in general is well studied for metals: many authors discuss the production of interstitial atoms and vacant lattice sites due to atoms displaced from their lattice site by radiation (see e.g. [Gib60, Luc62]). However, due to low energy transfers from electrons to the metal lattice, this effect is not expected for tritium radiation: typical threshold energies for this kind of damage are of the range of 20 – 40 eV [Luc62], while the energy transfer even from the highest energetic tritium β-electrons with kinetic energies of 18.6 keV amounts to only about 1 eV [Cas85a].

Other studies report embrittlement of metals by absorbed hydrogen isotopologues (see e.g. [Lou72, Bel95b]). While this effect is in principle not limited to tritium, Caskey points out differences between radioactive and inactive hydrogen isotopologues due to helium formation from tritium decays inside of metals [Cas85a]. In contrast to absorbed tritium, helium is easily trapped by lattice defects and thus less mobile within the metal structure [Cas85b]. The formation of defects of about 5 nm in size due to helium bubbles was observed in different metals within the microstructure and along grain boundaries, leading to material hardening and lower fracture resistance [Cas85a]. Bellanger reports dimension changes of palladium and palladium silver alloys in tritiated water electrolyzers due to tritium diffusion into the lattice, and resulting trans- and intergranular cracking [Bel95b]. Such effects could possibly damage metal surfaces exposed to tritium and affect their reflection properties.

Finally, some metals tarnish depending on the surrounding atmosphere, which decreases their reflectance. For silver and copper, this process is generally connected to sulfur compounds [Ric81, Fra85], which are present to a small extent e.g. in ambient air. They are not expected to be found in tritium gas systems, but their presence there cannot be unequivocally excluded.

5.1.4. Durability test samples

Six different types of reflective surfaces were chosen for the durability test to cover the most common mirror materials and a range of different metals with reasonable high reflectances: a broadband dielectric mirror as well as metallic mirrors made of gold, silver (protected and unprotected), copper and aluminum. As outlined above, all sample types can in principle be used as mirrors in the optical setup, although gold and copper perform well for Raman light reflection only and are not recommended for laser reflection. In addition, all unprotected metal surfaces are possible candidates for the hollow waveguide inner surface, while dielectric multilayer coatings cannot be used for the waveguide due to the reasons discussed above. Silver linings with SiO_2 protective layers are not feasible either due to the difficulty to apply a SiO_2 protective layer evenly to the inner surface of a long, thin tube.[1]

[1] SiO_2 layers are normally achieved by deposition or sputtering methods (e.g. electron beam deposition, chemical vapor deposition, ion or magnetron sputtering) which require direct accessibility to the sample surface, or by sol-gel processes which use dip or spin coating, both of which are not suitable for inner surfaces of small-diameter waveguides [Cra08, Bac03]. Instead, protective overcoats in waveguides are commonly made from polymers or silver halides (see e.g. [Dok07, Sha13]). However, these materials are not suitable for tritium atmospheres and can thus not be applied for the purposes discussed here.

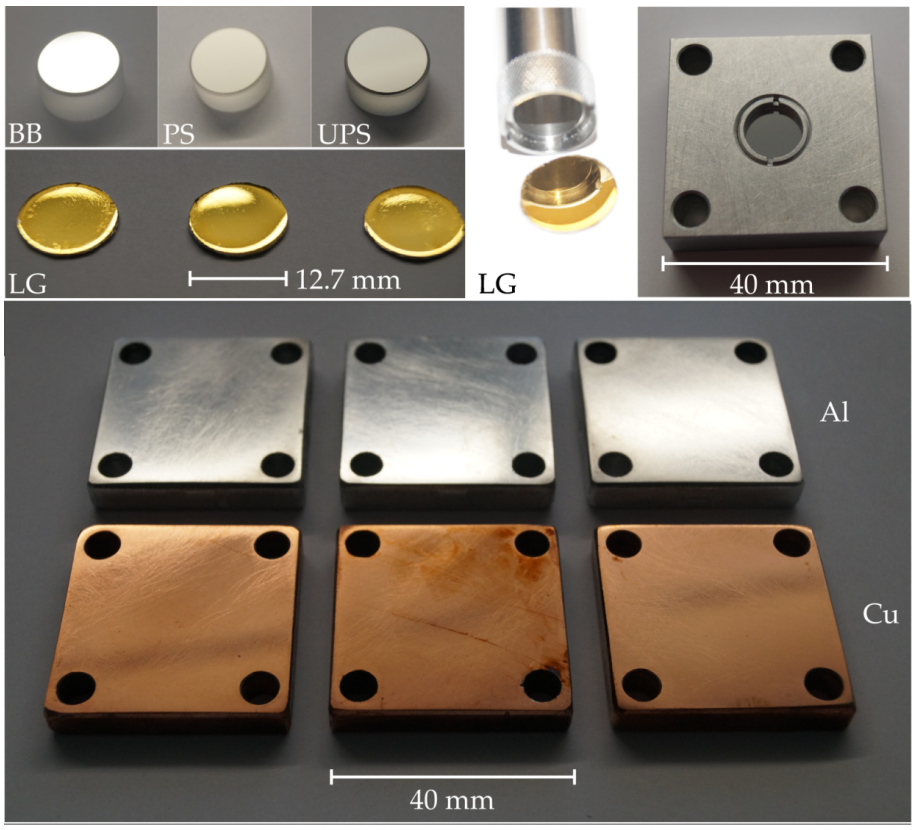

Figure 5.2.: Durability test samples. In the upper left corner, one specimen of each Thorlabs mirror – broadband dielectric (BB), protected silver (PS) and unprotected silver (UPS) – and the three Laser Gold samples (LG) are shown. The diameter of all these optics is $1/2'' = 12.7\,\text{mm}$. For the test experiment, they are inserted into a custom-made aluminum mount and fixed by a retaining ring, as shown in the upper right corner. The Laser Gold sample in the upper center reflects a metal instrument, demonstrating the good reflection properties despite comparably high surface roughness values. In the bottom panel, the aluminum (Al) and copper (Cu) samples are shown. They are manufactured in such a way that no separate sample holder is necessary.

Three test specimens of each type were produced, labeled 'T2', 'Box' and 'Air'. The first one is the one exposed to tritium. The other two are reference samples for comparison: Box specimens were stored within an inertized glove box, i.e. in a nitrogen atmosphere, and Air ones in normal ambient air during the exposition period. Apart from this period, all specimens of a certain sample type were treated in the same way to ascertain comparability. The surface roughness of the different samples was measured prior to exposition using a MarSurf mobile roughness measuring instrument from Mahr GmbH. The measured roughness values for each sample type are listed in table 5.1.

The samples are shown in figure 5.2. Details about each sample type can be found in table 5.1 and the following descriptions:

Table 5.1.: Overview of durability test specimens. The Thorlabs components were manufactured in a standardized way; in these cases, the surface roughness of just one of the specimens was exemplarily determined.

Sample	Code	Substrate	Coating	Manufacturer	Part No.	Roughness (nm)	
Broadband	BB	Fused silica	E02 broadband HR coating	Thorlabs Inc. Newton, NJ, USA	BB05-E02		31 ± 19
Protected silver	PS	Fused silica	Silver with SiO_2 overcoat	Thorlabs Inc. Newton, NJ, USA	PF05-03-P01		12 ± 3
Unprotected silver	UPS	Fused silica	Silver	Thorlabs Inc. Newton, NJ, USA	PF05-03-P01-UNPROT-SP		39 ± 23
Aluminum	Al	AlMg3/3.3535	-	in-house	custom	T2: Box: Air:	106 ± 22 194 ± 77 215 ± 61
Copper	Cu	Cu-ETP/2.0060	-	in-house	custom	T2: Box: Air:	102 ± 26 114 ± 27 131 ± 47
Laser Gold	LG	Nickel	Laser Gold	Epner Technology Inc. Brooklyn, NY, USA	custom	T2: Box: Air:	45 ± 12 147 ± 156 135 ± 76

- The broadband dielectric mirrors as well as protected and unprotected silver mirrors are standard 1/2" Thorlabs optics with low surface roughnesses. In order to prevent tarnishing in ambient air, the unprotected silver mirrors were stored in helium atmosphere prior to the durability experiment. All other optics were stored in closed boxes or plastic bags.
- The aluminum and copper samples were fabricated in-house from standard metal plates. The surfaces were smoothed to roughness values $\leq 300\,\mathrm{nm}$ by face-milling and subsequent polishing. Afterwards, they were cleaned with acetone in an ultrasonic bath. As the quality of the different specimens differs to a certain extent, the best available specimens were chosen as 'T2' samples.
- The Laser Gold samples were manufactured by Epner Technology Inc. [Epn14a], a company who provides waveguides with an inner gold lining on a nickel substrate [Epn14b]. In order to assess the potential of these so-called Light Pipes for hollow waveguide based Raman spectroscopy of tritiated gases, discs of the same substrate and coating were produced for the durability tests. Like the copper and nickel samples, these custom specimens are not as perfectly flat as the standardized Thorlabs components, since the company is not specialized in producing flat Laser Gold mirrors. Nevertheless, the samples are sufficient for a general test of reflectance changes of these materials under tritium influence.

5.1.5. Experimental setup

For the durability test, the measurement setup of the Coating Test Experiment (COATEX) at TLK was employed, which was initially constructed for window coating tests within the framework of the PhD thesis of S. Fischer [Fis14] and the diploma theses of K. Schönung and V. Schäfer [Sch11b, Sch13a]. This subsection gives a brief overview of the setup. A detailed description of the original setup can be found in [Sch11b]; modifications implemented later for improved stability and reproducibility are explained in [Sch13a].

The measurement setup used to test reflection properties of the samples before and after tritium exposure is shown in figure 5.3. Light from a laser light source is divided into two beams by a beam splitter. One beam is directed onto the sample surface. Light reflected from the sample reaches the beam splitter again, is partly reflected in a 90° angle and detected by a photodiode. The second part of the original beam is reflected by the beam splitter towards another photodiode for monitoring of the laser power. By this means, a reflection signal independent of laser power fluctuations can be obtained by taking the ratio of the two photodiode signals. The sample itself is mounted on a motorized translation stage which allows for stepwise scanning of the sample surface. The sample is kept in place by four cage rods and an additional mount in front which can be screwed to the cage rods. A polarization filter in front of the beam splitter provides constant polarization, so that the splitting ratio of the polarization-dependent beam splitter is not affected even in case of variations in the mode pattern of the laser [Sch13a].

A DPSS laser module with emission wavelength 593.5 nm is used. This wavelength lies well between the laser wavelength of 532 nm and the Q_1 branches of the hydrogen isotopologues ($\sim$ 612 nm – 683 nm) and thus in the very wavelength range for which

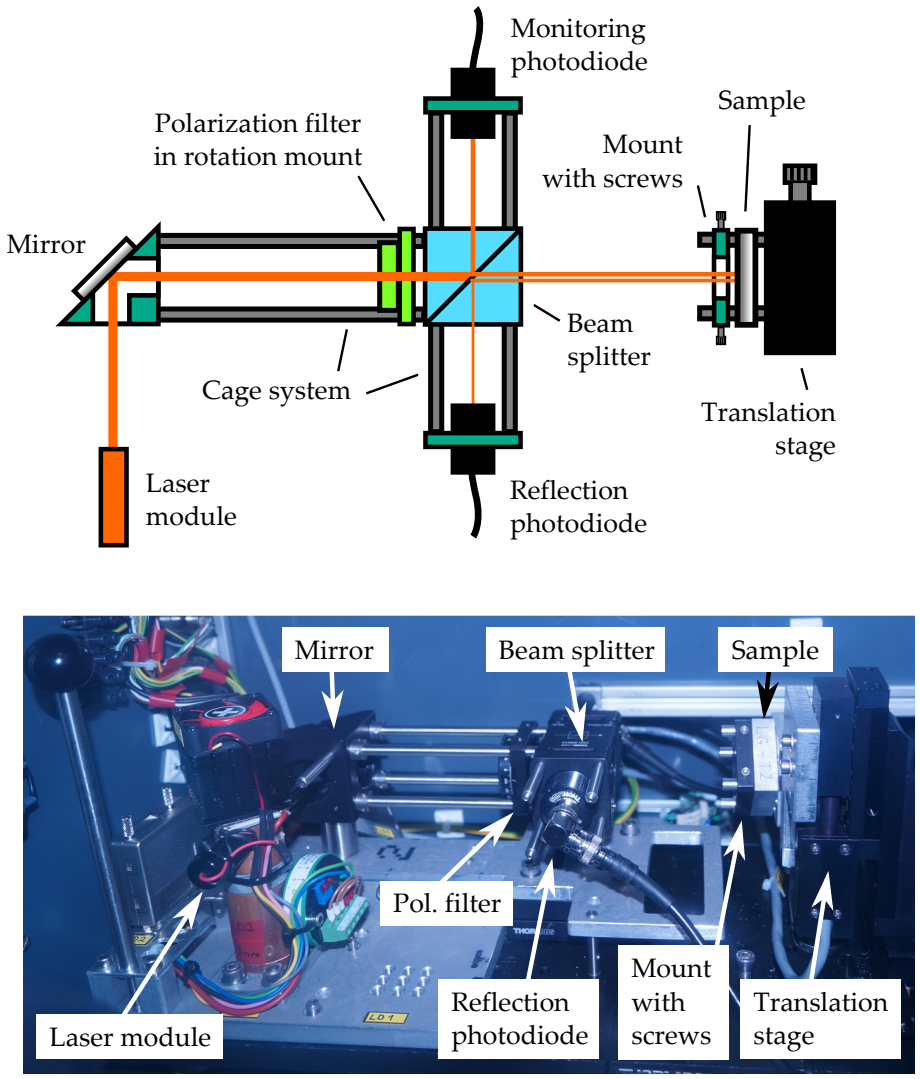

Figure 5.3.: Experimental setup of the durability test. *Top:* Schematic drawing. *Bottom:* Picture of the setup. The laser module is visible in the lower left; it is mounted in a copper block with a thermoelectric module and a fan on top to allow for effective temperature control. The whole experiment is located in the Omegatron glove box at TLK.

possible reflectance changes are of interest[2]. The laser temperature is controlled by means of a Pt100 temperature sensor and a thermoelectric module.

The optical setup is housed in a light-tight enclosure to avoid distortions of measurement results by ambient light. The temperature inside of the enclosure is monitored by another Pt100 sensor. A transimpedance amplifier converts the photodiode current signals into amplified voltage signals, with an amplification factor of 2000 V/A in case of the monitoring photodiode and 100,000 V/A for the reflection photodiode.

[2]In principle, different laser sources could be used to explicitly measure the reflectance at different wavelengths. However, this would involve modifications of the system possibly affecting the measurement reproducibility. As it is assumed that any reflectance changes will affect a broad wavelength range, it is sufficient to employ only one representative laser wavelength.

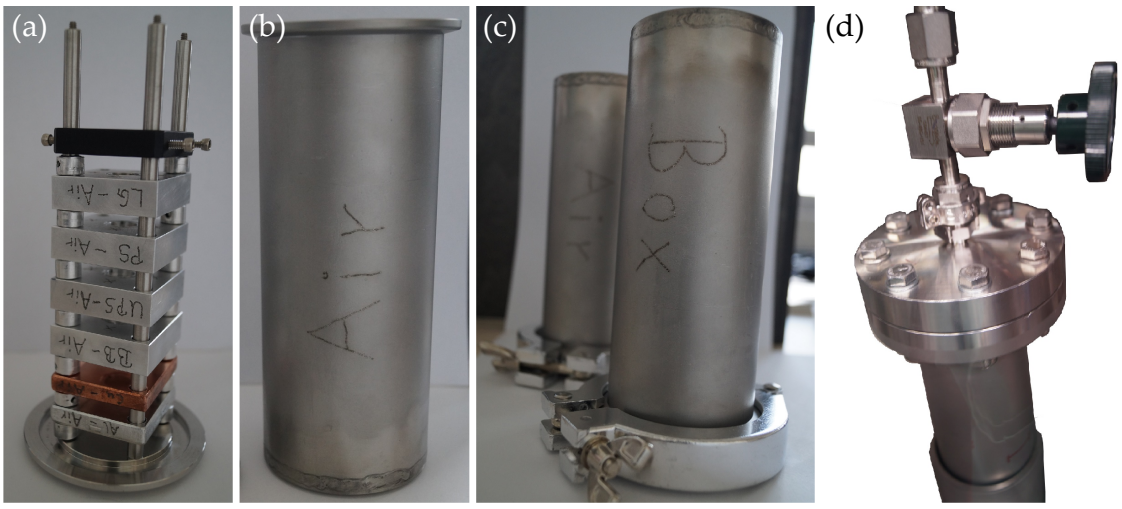

Figure 5.4.: Holder and containers for the durability test samples. *(a)* Sample holder for the Air samples. The six different sample types are stacked with placeholders in between and a plate on top which is screwed to the rods to fix all samples in place. The Box samples are stored in an identical holder, the T2 samples in a similar variant fully made of stainless steel. Note that in case of Air and Box holders, the rods holding the samples are attached to a KF blind flange which serves as the container lid. *(b)* Air sample container with open KF flange at its upper end. *(c)* Closed Air and Box sample containers. *(d)* Vessel for tritium exposure. The vessel is sealed tightly by a CF seal and filled with tritium via the gas inlet on top. The samples are transported to the filling vessel in a similar container without gas inlet. In contrast to the Air and Box case, the T2 sample holding structure is separate from the container lid.

Sample storage and handling: The samples of each batch (T2, Box and Air) are stacked on sample holding structures with sufficient space between the individual specimens to allow for contact of the surfaces with ambient gas, as shown in figure 5.4 (a). These holding structures can be integrated into closed containers. Aluminum containers (figure 5.4 (b) and (c)) are used for transport of the non-tritium samples as well as storage during measurement periods; during exposure time, the Air and Box samples are stored outside of their containers to provide sufficient air/gas exchange (see below). For tritium exposure of the T2 samples, a metal-sealed stainless steel vessel fulfilling the quality requirements of primary systems at TLK is used (figure 5.4 (d)).

5.1.6. Measurement procedure

Sample treatment: All samples were transferred into the Omegatron glove box and stored in their respective containers prior to the durability test. Reflectance measurements of all specimens were conducted in three runs (see below). Afterwards, the samples were transferred to different places for exposure:

- The T2 samples were transferred into the CAPER glove box. They were taken out of their transport container and inserted into the filling vessel shown in figure 5.4 (d). This vessel was evacuated and then filled with $p = 81.2\,\mathrm{mbar}$ of gas with a tritium

purity of $\epsilon_T = 92.35\,\%$. According to a gas chromatographic measurement, the gas mixture was composed of 90.9 % T_2, 1.4 % DT, 1.5 % HT as well as small amounts of tritiated methanes and nitrogen. The samples were exposed for $t_{exp} = 71$ days. The β-activity per volume is proportional to $p\epsilon_T \cdot t_{exp}$, so that above exposure is approximately equivalent to an exposure over five full years under KATRIN conditions, i.e. assuming a total ambient pressure of $p = 3\,\mathrm{mbar}$ at the position of the hollow waveguide based Raman measurement system and a tritium purity of $\epsilon_T = 95\,\%$ (cf. section 2.5).

- The Box samples were transferred into the CAPER glove box. Other than the Omegatron glove box, the CAPER glove box is inertized, i.e. contains an almost pure nitrogen atmosphere with $< 4\,\%$ oxygen content as well as water vapor in the ppm range. The box activity per volume was in the range of few $\mathrm{MBq/m^3}$, corresponding to a fraction of only about 10^{-9} of the one the T2 samples were exposed to. The Box samples were stored in the CAPER glove box outside of their container during the 71 days of exposure in order to provide sufficient gas exchange.
- The Air samples were transported into a fume hood providing continuous air exchange, and stored there outside of their container as well during the 71 days of exposure.

After exposure, all samples were transferred back into the Omegatron glove box and measured again with the COATEX setup.

Initial alignment of the measurement setup: Before measurements were started, the optical setup was initially aligned. In this process, the polarization filter (see figure 5.3) was adjusted such that the measured monitoring photodiode signal as well as the ratio between reflection and monitoring photodiode voltage were maximized. By adjusting the mirror positioning and the translation stage, the beam was aligned to be centered on the reflection photodiode when a standard, flat optical component from Thorlabs (neutral density filter ND10B) was inserted at the sample position. V. Schäfer stresses the importance of this centering in order to detect a maximum amount of reflected light [Sch13a]. However, it has to be mentioned that the measured signal is still very sensitive on the exact sample positioning. For this reason, even the same specimen can lead to different results when inserted in different positions (see figure 5.5) or when different surface areas are scanned. It should thus be noted that the system allows for relative comparisons of one sample before and after a certain treatment, but not for absolute reflectance measurements or direct comparisons between different samples.

Measurement runs: Measurements of each test specimen were conducted prior to and after exposure in three runs each, in which each specimen was measured three times in two different positions (see figure 5.5). The order in which the samples were measured was varied in each run. These arrangements were made in order to minimize the risk for systematic data shifts by means of multiple reinsertion of samples and an approximately even temperature distribution for all samples (see below and appendix H). The measurement order of each run is listed in table 5.2.

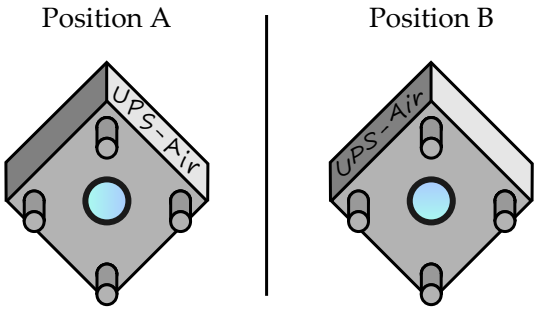

Figure 5.5.: Sample positioning. The sample was mounted on the translation stage in two different positions in order to be able to scan over a larger region of each surface. The positions are defined by the label at one side of the sample or optics mount which indicates the sample type and specimen. In order to change from position A to B, the sample was removed from the rods indicated in the figure, rotated by 90° and pushed back over the rods.

Table 5.2.: Measurement runs of the durability test. X stands for the sample type (e.g. Cu), the second part of each entry (T2 / Box / Air) for the respective specimen and the third part (A / B) for the sample positioning according to figure 5.5.

Run 1	**Run 2**	**Run 3**
3x X-T2-A	X-T2-A	3x X-Air-B
3x X-T2-B	X-Box-A	3x X-Air-A
3x X-Box-A	X-Air-A	3x X-Box-B
3x X-Box-B	X-T2-B	3x X-Box-A
3x X-Air-A	X-Box-B	3x X-T2-B
3x X-Air-B	X-Air-B	3x X-T2-A
	Repeat 3x	

Measurement procedure: Prior to each measurement period, the box electronics as well as the power supply and temperature control of the laser module were switched on. As is shown in figure 5.6, the photodiode voltage ratio is strongly dependent on the laser module temperature and fluctuates considerably especially during the first two minutes of laser stabilization. For this reason, the laser module temperature was allowed to stabilize for at least five minutes after switching on all electronics.

In order to test a certain specimen, it was mounted on the four rods attached to the translation stage in the right position according to figure 5.5. Afterwards, an additional, empty optics mount was pushed against the sample and fixed with a screw. By this means, measurement-distorting movements of the sample caused e.g. by vibrations of the step motor of the translation stage could be avoided. The lid of the light-tight enclosure around the setup was then closed and the measurement started. If the same specimen was measured in the same position multiple times in a row (in run 1 and run 3; see table 5.2), it was removed and reinserted between each measurement to minimize the risk for systematic data shifts, since the obtained results altered slightly with every reinsertion for some of the samples.

Measurements were performed only at glove box temperatures between 22 and 24 °C in order to minimize temperature-related signal fluctuations. This temperature range was chosen based on preliminary measurements investigating the influence of the glove box temperature on the measured data; these investigations are described in detail in appendix H.1. Consequently, the box light was never switched on during the durability test to prevent heating of the box. Since the measurement process itself increased the temperature in the glove box as well, measurements were frequently paused for a certain period of time when the temperature approached the upper limit, so that the system could cool down again. The box temperatures during the durability test measurements are listed in appendix H.2.

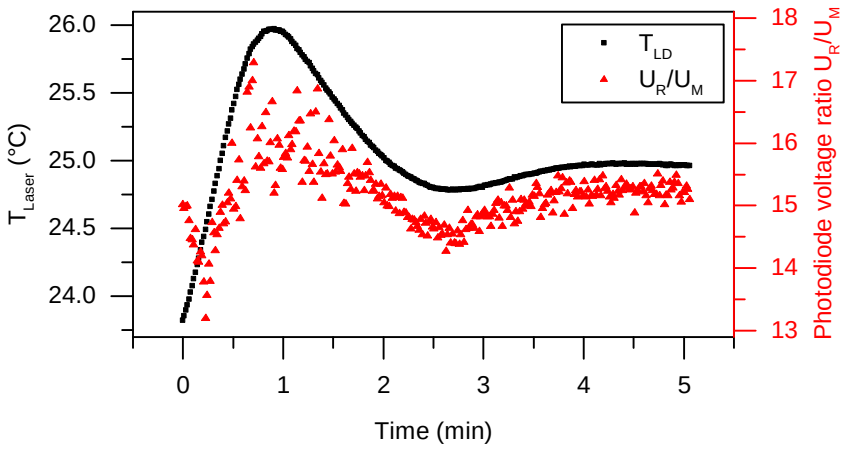

Figure 5.6.: Temporal development of laser temperature and photodiode voltage ratio after turning on the laser module.

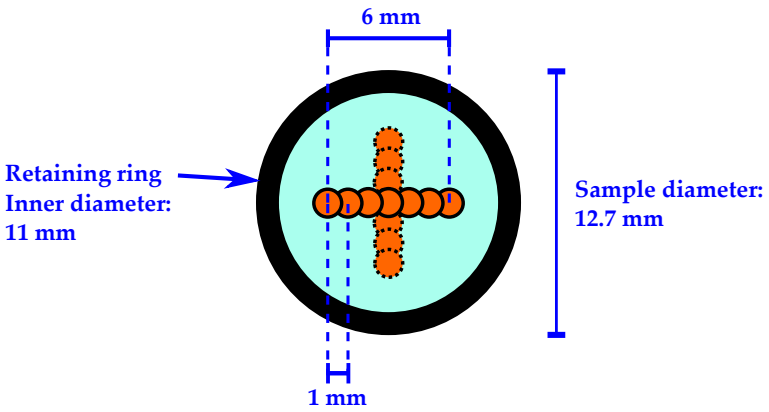

Figure 5.7.: Sample surface scan pattern. The orange circles represent the 1.5 mm laser beam illuminating the sample at seven different measurement points in one scan. The measurement points are approximately centered around the sample center. A safety margin to the sample edges is used to avoid the beam hitting the retaining ring. The dotted circles show the illumination pattern for a sample rotated by 90°. By using two different sample positions for the measurement (see figure 5.5), a larger area of the sample surface is covered.

The sample surface was scanned in horizontal direction by means of a motorized translation stage (EKSMA OPTICS, 960-0060-02, resolution 1.25 µm). At the beginning of each measurement, the position of the translation stage was calibrated via an end switch. For each sample position, 7 single measurement points evenly spaced 1 mm apart were used (see figure 5.7). Since the laser has a beam diameter of 1.5 mm, this leads to overlappings between the measurement points and thus a good coverage of the sample surface along the horizontal axis. The total acquisition time per measurement point was 10 s. In this time, 1000 photodiode voltage values per second were acquired and used to determine the 10 s average and standard deviation, which were then stored.

It should be noted that a loosening of retaining rings was discovered for some of the samples during the measurements after exposure. The loosening had probably occurred gradually in the course of the measurements due to vibrations of the step motor of the translation stage on which the samples were mounted for measurement. Loose retaining rings can lead to changes of the sample positioning and the angle of light incidence, so that measurement results can in principle be seriously affected. For this reason, all samples utilizing retaining rings (PS, UPS, BB, LG) were examined closely after the discovery. No loosening had occurred for the PS and LG samples. For the affected UPS and BB samples, previous measurements taken after exposure were repeated with retightened retaining rings. Of course, measurements taken before the exposure could not be repeated. However, in case of the UPS samples where all specimens were found to be affected to a small extent, all values before exposure were very similar and mostly exhibited low standard deviations of the order of 1 %. For this reason, the findings are still considered to be conclusive in that case. In case of the BB samples, only the Air and Box specimens were affected, but to a larger extent. The interpretation of the related data is discussed in the results section below.

5.1.7. Results and discussion

For each measurement point of a sample in a certain positioning, the photodiode voltage ratio U_R/U_M between the reflection and the monitoring photodiode was calculated. The voltage ratios of all nine measurements of a certain configuration (three measurements each in three runs, cf. table 5.2) were used to determine the weighted average for each measurement point. Finally, the data of all measurement points were averaged in order to characterize the configuration as a whole. The related uncertainty takes into account the uncertainty contributions due to (i) the reproducibility of sample reinsertions, (ii) the influence of temperature changes in the box and (iii) the statistical fluctuations determined for each 10 s acquisition from the single voltage signals received during this time. Details are given in appendix H.3.

The resulting voltage ratio data for each sample type and configuration before and after exposure are listed in the tables 5.3 – 5.5. Measurements in which the voltage ratio before and after exposure does not agree within the uncertainties are highlighted: the relative difference is written in bold in that case. The table shows that the initial voltage ratios are highest for protected and unprotected silver as well as broadband-coated samples, roughly 10 % lower for Laser Gold and considerably lower – by about 40 to 70 % – for aluminum and copper. Although the setup does not allow for absolute reflectance measurements, as discussed before, these results represent the qualitative expectation, given the lower reflectances of the last-named materials and the lower surface smoothness of these samples. The reaction of the different samples on exposure to tritium or air differs significantly:

Protected silver (PS): The protected silver samples were not measurably affected by any environment. Differences of the voltage ratio before and after exposure are of the order of 2 % or less and well within the measurement uncertainty.

Unprotected silver (UPS): In contrast, the unprotected silver coatings were clearly impaired when exposed to air and to tritium; only the sample stored in a nitrogen atmosphere showed no sign of degradation. About 70 % less light was reflected from the silver surface after it had been exposed to air, which can be attributed to normal tarnishing. Discoloration of the whole surface was visible to the naked eye.

In case of tritium exposure, the measured reflectance decrease was less pronounced, but still considerable with about 23 %. Since the Box reference samples were not affected, it can be excluded that this degradation is due to tarnishing in the short periods in which all unprotected silver samples were exposed to air (e.g. during measurements or visual inspection). For this reason, tritium-induced damage of the sample has to be assumed. Two dark spots on the surface were discernible on the surface after tritium exposure. Examining the larger one of these spots under the microscope, it proved to be a circular discoloration of about 0.5 mm in diameter, possibly with a slightly brighter dot in the center. The spot is shown in figure 5.8. Its structure is reminiscent of the tritium damage encountered for EBD dielectric window coatings by S. Fischer [Fis14]; in that case, however, more and smaller spots (diameter $\sim$ 0.1 mm) were found. Although the spot observed here does decrease the reflectance – the voltage ratio of the measurement point

Table 5.3.: Tritium durability test results of protected and unprotected silver. The photodiode voltage ratios measured for a certain configuration before and after exposure are compared in the last column. The relative difference is written in bold in cases where the values do not agree within the experimental uncertainty.

Sample	Position	Exposure	U_R/U_M	Difference
PS-T2	A	before	19.3 ± 0.2	-1 %
		after	19.1 ± 0.1	
	B	before	19.3 ± 0.2	0 %
		after	19.3 ± 0.2	
PS-Box	A	before	19.6 ± 0.2	-2 %
		after	19.2 ± 0.4	
	B	before	19.3 ± 0.2	-1 %
		after	19.0 ± 0.5	
PS-Air	A	before	19.8 ± 0.3	-2 %
		after	19.4 ± 0.4	
	B	before	19.4 ± 0.2	-1 %
		after	19.2 ± 0.1	
UPS-T2	A	before	19.3 ± 1.3	**-24 %**
		after	14.7 ± 0.5	
	B	before	19.5 ± 0.2	**-23 %**
		after	15.1 ± 0.4	
UPS-Box	A	before	19.3 ± 0.2	1 %
		after	19.5 ± 0.1	
	B	before	19.5 ± 0.2	0 %
		after	19.4 ± 0.2	
UPS-Air	A	before	19.8 ± 0.1	**-70 %**
		after	5.8 ± 0.3	
	B	before	18.0 ± 0.8	**-70 %**
		after	5.4 ± 0.8	

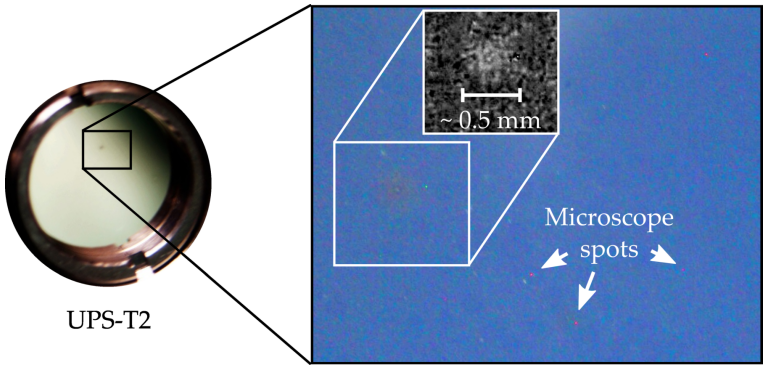

Figure 5.8.: Spot on the tritium-exposed unprotected silver surface. A second, smaller spot was visible to the eye, but is not discernible on the picture of the sample *(left)*. Under the microscope *(right)*, the spot is visible as a slight discoloration. In the inset, the marked surface area is shown with adjusted contrast and colors in order to improve the visibility of the spot. Note that the small, red dots visible in the image originate from the microscope, not from the sample.

closest to the spot is about 7 % lower than for the points at least 2 mm away from the spot – the observed total reflectance decrease of over 20 % concerns the whole measurement range. Possibly, the spot is a beginning macroscopic manifestation of tritium-induced microscopic damage occurring over the entire surface.

Broadband dielectric coating (BB): In case of the dielectric multilayer coating, the measurements support earlier assumptions that these coatings are prone to tritium-induced damage: although no visible damage as in the prototype system (see subsection 4.4.2) was observed under the microscope, the reflectance had decreased by about 16 % after tritium exposure.

Concerning the Box and Air reference samples, some caution is required in the data interpretation since a loosening of their retaining rings was discovered during the measurements after exposure; note that the T2 specimen was not affected. Although measurements of the Box and Air specimens after exposure were repeated with retightened retaining rings, high standard deviations and partly large differences between measured voltage ratios occurred already prior to exposure, especially in case of the Air specimen. For this reason, measurements involving the latter are not considered to be conclusive. Concerning the Box specimen, no further irregularities were observed after repetition of the runs after exposure, and differences between measurement in position A and B as well as before and after exposure are relatively small. For this reason, the Box values can be assumed to indicate unchanged reflection properties under nitrogen influence.

Laser Gold (LG): For most of the Laser Gold measurements, the voltage ratio values before and after exposure agree within the measured uncertainties. In particular, no degradation due to tritium β-radiation could be observed. A small deviation was found for the Air specimen in position B and a larger one for the Box specimen in position A. However, other than with the previously discussed deviations of unprotected silver and the

Table 5.4.: Tritium durability test results of the dielectric broadband coating and Laser Gold. The photodiode voltage ratios measured for a certain configuration before and after exposure are compared in the last column. The relative difference is written in bold in cases where the values do not agree within the experimental uncertainty. Note that the BB-Air measurements (in italics) are not considered conclusive due to loosened retaining rings. For details see main text.

Sample	Position	Exposure	U_R/U_M	Difference
BB-T2	A	before	19.2 ± 0.2	**-15 %**
		after	16.3 ± 0.2	
	B	before	20.4 ± 0.6	**-17 %**
		after	17.0 ± 0.2	
BB-Box	A	before	18.3 ± 1.2	5 %
		after	19.2 ± 0.3	
	B	before	20.5 ± 0.5	-3 %
		after	19.8 ± 0.2	
BB-Air	*A*	*before*	*16.7 ± 1.2*	*-3 %*
		after	*16.2 ± 1.4*	
	B	*before*	*19.3 ± 0.2*	***-25 %***
		after	*14.6 ± 1.8*	
LG-T2	A	before	17.4 ± 0.2	-3 %
		after	17.0 ± 0.2	
	B	before	16.2 ± 0.2	0 %
		after	16.2 ± 0.2	
LG-Box	A	before	6.5 ± 0.6	**-18 %**
		after	5.3 ± 0.3	
	B	before	13.6 ± 0.2	-4 %
		after	13.1 ± 0.7	
LG-Air	A	before	17.0 ± 0.3	-1 %
		after	16.8 ± 0.2	
	B	before	18.4 ± 0.2	**-3 %**
		after	17.9 ± 0.2	

broadband coating, no deviations were measured in the respective second positioning of the Laser Gold samples. Considering in addition the fact that no slow optical degradation of gold mirrors in air has been reported so far, it can thus be assumed that the reflection properties did not really change, but rather the uncertainties were underestimated.

Although the samples were stored face-down and inspected visually prior to measurements, very small dust particles on the surfaces cannot be excluded, which would decrease the amount of light reflected onto the photodiode. This effect should primarily affect Box and Air specimens which were stored openly during exposure, while the T2 specimens were housed in a closed container. Another possibility could be an underestimation of the temperature-related uncertainty. Although all measurements were conducted in the same temperature range between 22 and 24 °C, the ambient laboratory temperature was higher after exposure, so that the box temperature decreased more rapidly than in the initial measurements. For this reason, the mean box temperature during measurements increased from 23.2 °C before exposure to 23.5 °C after exposure, possibly leading to a small systematic shift towards lower photodiode voltage ratio in the measurements after exposure. The box temperatures during the durability test measurements are listed in appendix H.2.

Furthermore, the slight unevenness of the Laser Gold sample surfaces and the comparatively high surface roughness of the Box and Air specimens (cf. table 5.1) could play a role. The considerable difference between the total values measured in position A and B in case of the Box specimen – the values in position B are more than double the A values – suggests a major influence of the sample unevenness: apparently the reflected beam is not properly centered on the reflection photodiode any more in position A, so that light is lost. In that case, the measured value is expected to be rather sensitive on small positioning differences; this is also reflected in the large uncertainties of 9.2 % (before exposure) and 6.0 % (after exposure) in the Box-A measurements. For this reason, the reinsertion reproducibility could become worse, which might not be fully accounted for by the corrected standard deviation over nine reinsertions (cf. appendix H.3).

Aluminum and copper (Al, Cu): Similar to the Laser Gold samples, the voltage ratio values of aluminum and copper before and after exposure agree within the uncertainties in most cases. Deviations not covered by the uncertainties occur for the configurations Al-T2-A and Cu-T2-A (in both cases tending towards an improvement of reflectance by tritium exposure) as well as Al-Air-A and Cu-Box-B, but are not confirmed by the respective second measurement of each specimen in the other position. It is therefore assumed that at least in case of the Air and Box specimens, the same reasons as considered above for the Laser Gold deviations played a role, especially considering the relatively high surface roughnesses of these specimens (see table 5.1). With respect to the T2 results, the same could be the case; at any rate, the tendency towards an improvement rather than a decline of the observed voltage ratio shows that a degradation of aluminum and copper reflection properties due to tritium is not to be expected.

Table 5.5.: Tritium durability test results of aluminum and copper. The photodiode voltage ratios measured for a certain configuration before and after exposure are compared in the last column. The relative difference is written in bold in cases where the values do not agree within the experimental uncertainty.

Sample	Position	Exposure	U_R/U_M	Difference
Al-T2	A	before	7.9 ± 0.3	**7 %**
		after	8.5 ± 0.1	
	B	before	7.9 ± 0.3	-2 %
		after	7.7 ± 0.1	
Al-Box	A	before	7.3 ± 0.1	1 %
		after	7.4 ± 0.1	
	B	before	6.7 ± 0.3	-1 %
		after	6.6 ± 0.1	
Al-Air	A	before	5.5 ± 0.2	-1 %
		after	5.4 ± 0.2	
	B	before	6.2 ± 0.2	**-11 %**
		after	5.5 ± 0.2	
Cu-T2	A	before	10.1 ± 0.1	**10 %**
		after	11.1 ± 0.4	
	B	before	10.2 ± 0.6	3 %
		after	10.5 ± 0.4	
Cu-Box	A	before	7.2 ± 0.7	-13 %
		after	6.2 ± 0.3	
	B	before	8.8 ± 0.1	**-6 %**
		after	8.3 ± 0.2	
Cu-Air	A	before	11.6 ± 0.2	-3 %
		after	11.2 ± 0.3	
	B	before	11.0 ± 0.3	-9 %
		after	10.0 ± 0.8	

Summary: Clear evidence for degradation due to tritium influence was found for unprotected silver as well as broadband dielectric multilayer coatings. In these cases, the difference between measurements before and after exposure is between 2.6 (position A) and 7.9 times (B) larger than the sum of the single uncertainties for unprotected silver, and between 7.7 (A) and 4.5 times (B) for the broadband coating. Thus, the degrading influence of tritium on these surfaces can be considered confirmed despite the supposed underestimation of uncertainties: even assuming, for the sake of argument, a severe underestimation by a factor of 2 (which is easily sufficient to cover the minor deviations observed in some of the Air and Box configurations), this would not be sufficient to explain the observed deviation between measurements before and after tritium exposure. Using the weighted average of the measured voltage ratio difference in the two positionings, the tritium-induced reflectance decrease amounts to $23 \pm 2\,\%$ for unprotected silver and $15 \pm 1\,\%$ for broadband multilayer coatings.

For all other sample types, no degradation due to tritium influence was observed. Minor trends towards decreased reflectances outside of the stated uncertainty limits concerned only several Air and Box reference samples, but none of the T2 samples of protected silver, Laser Gold, aluminum and copper. The summed-up uncertainties measured for T2 samples are $\leq 1.7\,\%$ for protected silver and $\leq 2.7\,\%$ for Laser Gold, so that a possible interaction between these surfaces and tritium β-radiation can be assumed to affect the reflectance marginally at most. Uncertainties are larger in case of aluminum and copper, but here the trend is towards a reflectance increase instead of a deterioration. For this reason, these materials can be considered as suitable for optical applications in tritium atmospheres as well.

5.1.8. Implications for an improved hollow waveguide based Raman system

The durability test shows that a silver-lined glass waveguide as employed in the prototype setup is not suitable for use in a hollow waveguide based Raman system for KATRIN. In general, light guided by the waveguide undergoes multiple reflections, so that an intensity decrease over the course of the KATRIN measurements of up to 23 % in every reflection would lead to considerable signal losses and thus to a serious deterioration of the achievable sensitivity.[3] This finding rules out the majority of commercially available hollow waveguides for the visible range, which are commonly based on silver linings on glass.[4]

Protected silver, on the other hand, is an excellent option for mirrors in the gas system, being both highly reflective and unaffected by tritium. However, as briefly discussed in subsection 5.1.4, it is not applicable for waveguides. For this reason, Laser Gold, aluminum and copper are the only ones of the samples tested in the scope of this work which are

[3] As an example, the intensity of light undergoing only three reflections with reflection losses of 23 % in the waveguide would already be reduced to $0.23^3 \sim 1\,\%$, while ten reflections are sufficient to decrease the initial intensity to a fraction of only about $4 \cdot 10^{-7}$.

[4] As mentioned further above, commercially available hollow waveguides are usually offered with protective coatings made of polymers or silver halides, which, however, are not compatible to tritium and can thus not be applied here.

both tritium-compatible and in principle suitable for waveguide applications. From a reflectance point of view, aluminum could be used as a compromise with reasonably high reflectance at both the laser and the Raman light wavelengths (see figure 5.1). In the case that waveguide diameters are chosen large enough to allow the laser beam to pass through without being reflected from the waveguide walls, Laser Gold or copper become feasible as well. In any case, very smooth inner waveguide surfaces are required to achieve reasonably high reflectances. Investigations of alternatives to the current, not tritium-compatible waveguide solution will be discussed in detail in the following chapter in section 6.6.

With respect to (flat) mirrors, the durability test has shown that all tested mirror surfaces apart from broadband multilayer coatings and unprotected silver can be used in tritium systems. Protected silver mirrors provide the best reflectance for visible light and should thus be the mirror type of choice in an improved hollow waveguide based Raman system.

5.2. Fiber coupling for improved usability in glove boxes

In order to improve the usability of hollow waveguide based Raman systems in glove boxes, fiber coupling of the excitation laser is proposed. Placing the laser head outside of the glove box and delivering the beam inside via suitable fiber optics has several advantages over free-space beam delivery:

Laser head placement: Apart from saving space in the glove box, placing the laser outside of the glove box avoids contamination of the laser with tritium, and maintenance and repair are facilitated. Furthermore, the laser can be placed well outside any strong magnetic fields in the vicinity of the WGTS superconducting solenoids which could disturb proper laser operation.[5]

Flexibility: In the current LARA system, the laser is placed outside of the glove box as well. In that case, however, the laser beam is focused into the LARA cell in a free-space solution via a custom-made hardware interface housing the cell ('Appendix'), which is permanently attached to one of the glove box walls (see appendix A). A fiber-delivered laser offers much more flexibility concerning the location of the Raman cell in a glove box: the laser can be delivered to basically anywhere in the box without the laser safety risks connected to extended free-space beam delivery.

Alignment: In addition, fiber-optic beam delivery allows for easier and more reliable alignment of the hollow waveguide based Raman system. As detailed in subsection 4.4.3, achieving proper alignment within a glove box is complicated by (i) the constrained view and accessibility, (ii) limited possibilities of fine-motor manipulations and (iii) the need for the laser beam to be well-centered and parallel with respect to the hollow waveguide. In the prototype setup, position and angle of the laser beam were determined by two

[5] Note that these arguments apply to the spectrometer and CCD detector as well. In contrast to the laser light, however, fiber delivery of the Raman light is already used as a standard in TLK Raman systems (cf. section 4.1.1 and appendix A).

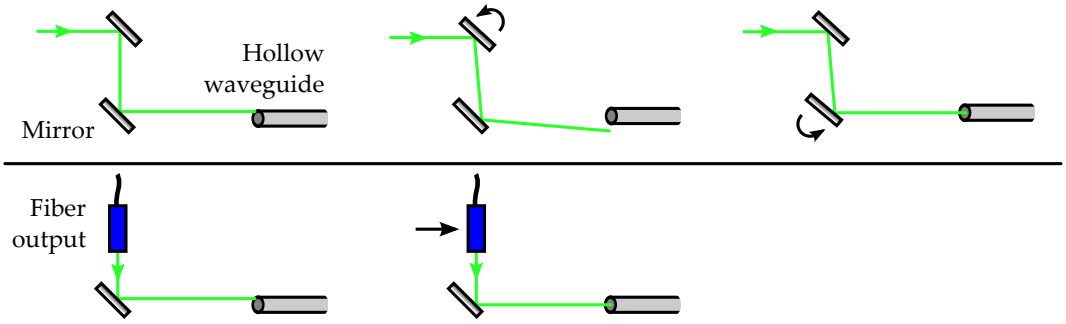

Figure 5.9.: Alignment possibilities. *Top:* Alignment via two mirrors at fixed positions. *Bottom:* Alignment via movable fiber output. See main text for details.

laser guiding mirrors (M2 and M3 in figure 4.1). Adjusting the orientation of only one mirror changes both the angle of the laser beam and its position at the waveguide front, as illustrated in the upper panel of figure 5.9; both mirrors have to be adjusted in order to achieve a positional shift without changing the angle, or a modification of the angle without altering the beam position.

The alignment is much simplified when the beam is launched from a fiber mounted in a stable xy translation stage.[6] In this case, when alignment parallel to the waveguide is achieved once, the beam can easily be centered with respect to the waveguide without altering the angle again (cf. figure 5.9, lower panel). Also, fine adjustments at high power to maximize the Raman signal are possible by this means without risk of damaging the waveguide, since the beam angle does not change and the position can be carefully adjusted by micrometer screws with direct feedback on the alignment quality via the Raman measurement instead of poorly visible beam paths.

5.2.1. Proposed optical system

An optical fiber for laser delivery has to fulfill the following requirements:

- It has to be suitable for a high laser power of several watts.
- It has to be single-mode. In multi-mode fibers, interference of the various guided modes exiting the fiber with noticeable phase differences leads to a 'speckled' output pattern [Tel07]. This pattern is highly sensitive on fiber movements due to their influence on the individual ray paths, so that any translation of the fiber as intended here would affect the output pattern and power, rendering quantitative measurements impossible.
- It has to allow for stable coupling, with a low risk of damaging the fiber in case of minor misalignments.

[6] Note that the same effect can also be achieved by mounting one of the two mirrors in the two-mirror-solution on a translation stage instead of screwing it to the optical breadboard in a fixed position like in the prototype setup. When fiber delivery of the laser is used, however, it is advantageous to directly make the fiber output end movable to save space and optical components.

In standard optical fibers based on total internal reflection, the transmittable power depends strongly on the fiber core size [Tel07]. For single-mode fibers, with core sizes typically in the range of $4 - 10\,\mu\text{m}$, power transmission is limited to only a few hundred mW at most since higher powers would lead to internal power densities above the damage threshold; for this reason, large-core multimode fibers are usually employed for high-power transmission.

One possibility to achieve both high-power transmission and single-mode propagation is the use of Photonic Crystal Fibers (PCFs) [Kni98]. These fibers utilize a periodic lattice of microscopic air holes around a solid or hollow core in order to confine the fundamental mode to this core: in solid-core PCFs, the mean refractive index of the cladding is lowered below the core refractive index by the hole structure, so that guidance is achieved by a modified variant of total internal reflection [Pin12], while hollow-core PCFs rely on photonic band gaps to prevent the fundamental mode from leaving the core [Rus03]. Higher order modes, in contrast, can leak out of the core through the gaps between the air holes [Rus06], so that single-mode guidance is achieved even for large-mode areas. For this reason, it is possible to transmit much higher powers than through conventional single-mode fibers [Rus06].

An 'aeroGUIDE-Power' fiber from NKT Photonics [NKT13, NKT14] is proposed for the task at hand. Its structure and beam profile are shown in figure 5.10. Apart from being endlessly single-mode with a mode field diameter of $12.2 \pm 1.5\,\mu\text{m}$ ($1/\text{e}^2$, at 532 nm), the fiber is equipped with high power SMA-905 connectors with integrated mode strippers for good performance at high power and low damage risk: uncoupled light is prevented from entering the fiber by the mode strippers, and excess heat is efficiently dissipated by the copper-based connector body (see figure 5.11). In addition, the fiber is polarization-maintaining with a measured maximum extinction ratio of 32 dB. Attenuation at 532 nm is $< 40\,\text{dB/km}$ [NKT14].

In order to account for long-term stability during KATRIN operation, an actively stabilized fiber coupling system ('FiberLock', TEM Messtechnik [TEM14, TEM15]) is recommended. Such a system monitors the fiber output and provides feedback to a piezo-driven mirror directly in front of the fiber coupling lens. The 2D actuator rapidly (with kHz repetition rate) scans the fiber input aperture with the laser beam, and uses the feedback to lock to maximum coupling efficiency by performing small circular modulations of the scanner angle. Alternatively, it is possible to actively stabilize the output power by changing the circular modulation to a geodesic orbit canceling any intensity noise. By this means, mechanical and thermal drifts as well as laser power fluctuations are actively compensated for [TEM14].

The proposed optical setup is shown in figure 5.12. It provides all necessary adjustment possibilities to achieve good coupling to the single-mode fiber, which depends on a range of degrees of freedom [TEM15]:

- **Beam convergence angle:** The geometry of the light cone which can be coupled with maximum efficiency into the fiber is determined by fiber properties. The optimal light cone is achieved by suitable choice of the focal length f of the aspheric

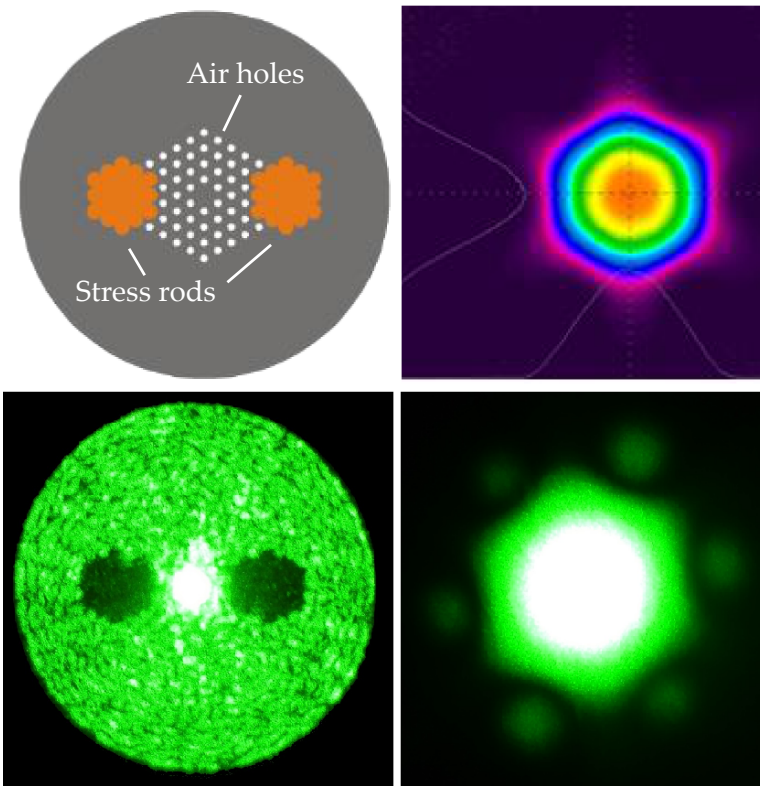

Figure 5.10.: Structure and beam profile of the 'AeroGUIDE Power' large mode-area PCF. The schematic pictures in the upper panel are taken from [NKT14], courtesy of NKT photonics. *Left:* PCF structure. The fundamental mode is guided through the solid center of the air hole structure. The stress rods are made of a different material than the fiber body; their relative orientation defines the slow axis parallel to which the laser polarization direction is aligned in order to be maintained during transmission. The picture in the lower left was obtained by illuminating the FC-APC fiber output end with low-power laser light; in that configuration, higher order modes were not stripped, so that the whole fiber structure was illuminated and could be imaged onto a screen. *Right:* Output pattern of the AeroGUIDE power. The fundamental mode is not completely Gaussian due to the hexagonal air hole lattice [Jin13]; nevertheless, a good beam quality is provided, with a M^2 value of about 1.1 (C. Fagermo, NKT Photonics, private communication, 27.10.2015).

focusing lens, taking into account the original $1/e^2$ laser beam diameter d_L and the laser wavelength λ:

$$f = \frac{\pi \cdot d_L \cdot d_{MF}}{4\lambda} \tag{5.1}$$

for coupling into a fiber of mode field diameter d_{MF} [New16].

- **Position of the beam waist in z-direction (along the optical axis of the fiber):** The position can be adjusted by moving the aspheric focusing lens along the optical axis to vary the distance between lens and fiber entrance. For stable and uncomplicated coupling, it is recommended to integrate the aspheric focusing lens in a fiber coupler which can be attached to the SMA connector (60FC-SMA-T-23-A*f*-01, Schäfter+Kirchhoff GmbH [Sch14a]). The coupler allows to adjust the

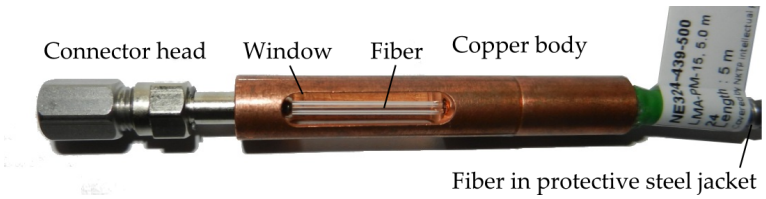

Figure 5.11.: High-power SMA connector of the AeroGUIDE Power. The copper body for efficient heat dissipation contains windows through which stripped light can exit the connector. Note that this light should be captured in a suitable beam dump configuration when using high laser powers in the watt range.

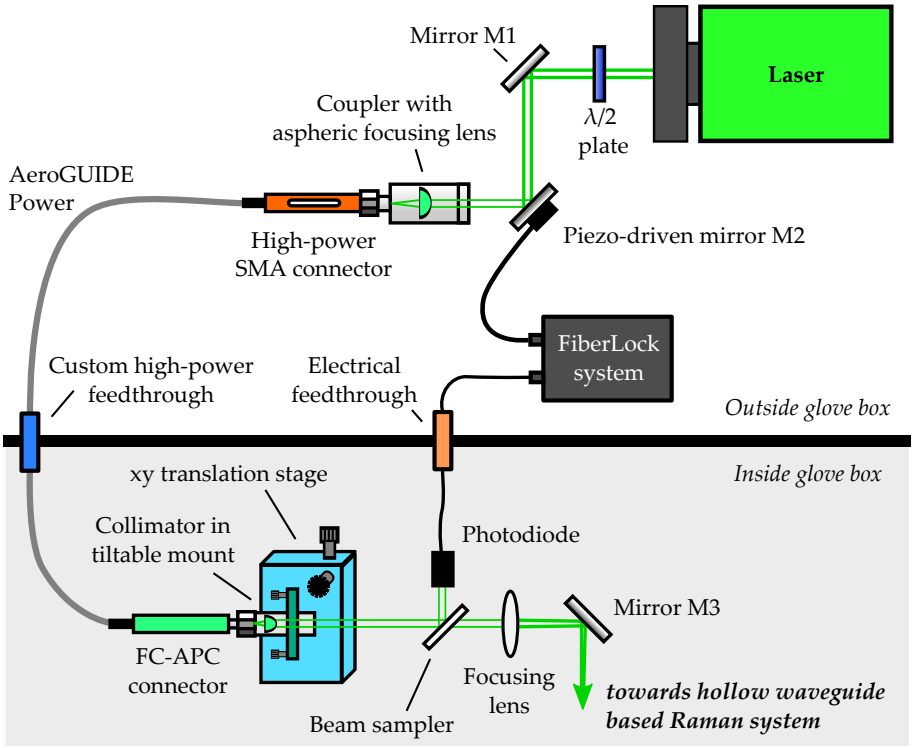

Figure 5.12.: Optical setup for stable fiber based laser delivery (schematic). See main text for details.

lens position as well as the fiber tilt to align the optical axis along the mechanical axis of the coupler.

- **Position and angle of the beam waist in x- and y-direction (perpendicular to the optical axis):** As illustrated in figure 5.9, the four degrees of freedom related to position and angle of a beam can be covered by two tiltable mirrors. In the proposed setup, one is mounted in a conventional mirror mount (M1 in figure 5.12) and the second one is the piezo-driven FiberLock mirror (M2).
- **Polarization direction:** In addition, a half-wave plate allows one to adjust the laser polarization direction to the slow axis of the fiber (cf. figure 5.10).

At the fiber output, a collimator (60FC-4-A*f*-01, Schäfter+Kirchhoff GmbH) is attached to the fiber end connector (see figure 5.12). It is inserted in a tiltable mirror mount on an xy translation stage to allow for flexible beam alignment in the hollow waveguide based Raman system. A beam sampler after the collimator is used to send a small fraction of the laser beam behind the fiber onto a photodiode to provide feedback about the transmitted power to the FiberLock system, which controls the Piezo-driven mirror in front of the fiber as described above.

5.2.2. Selection of a suitable glove box feedthrough

In order to deliver the laser into a glove box through an optical fiber, a leak-tight fiber feedthrough is required to keep the protective function of the glove box intact. There are two different types of fiber feedthroughs available:

- **Connector feedthroughs:** This type of feedthrough is a sealing component with fiber connectors at its two sides, one in the glove box and one outside. Fibers can be attached to these connectors, and light is coupled from one fiber into the other via the feedthrough. However, apart from disadvantages like the associated coupling losses and the need for two fibers, this solution is not well suitable for high-power applications: the coupling reproducibility is in general not good enough to guarantee damage-free operation in the case of laser powers above 1 W, according to consistent statements by a number of different connector feedthrough suppliers.[7]
- **Continuous feedthrough:** Alternatively, a fiber can be fed through a glove box wall without being interrupted itself. This technique relies on hermetic sealing around the fiber at one position along the fiber length. This type of feedthrough is suitable for high-power applications and should thus be utilized for laser delivery into a glove box.

Extensive product research yielded no continuous feedthrough solutions feasible for the task at hand: commercially available continuous feedthroughs are either restricted to certain fibers not suitable for high-power, single-mode laser delivery, or they contain halogens and can thus not be used for sealing applications in tritium glove boxes. For this reason, a custom solution is proposed. It is illustrated in figure 5.13: during production, the AeroGUIDE Power cable is provided with a gap in the protective steel jacket as well

[7] Note that a connector feedthrough is nevertheless well suitable for delivering the Raman light out of the glove box towards spectrometer and detector, as only low-power light is involved in this case.

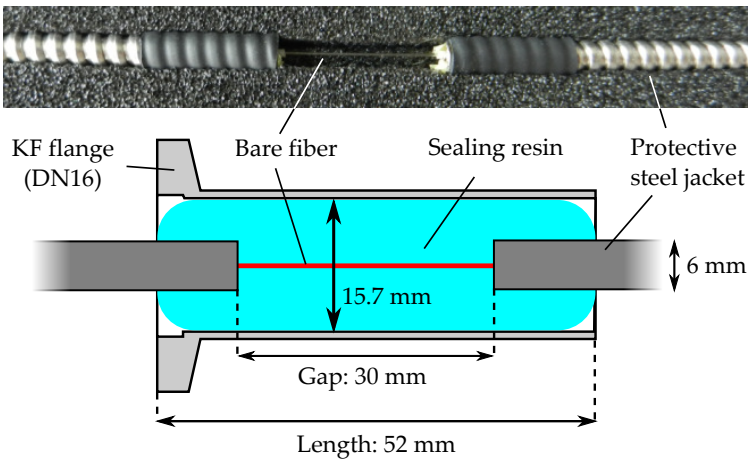

Figure 5.13.: Custom fiber feedthrough design. *Top:* Gap in the protective fiber jacket. *Bottom:* Schematic drawing of the resin-sealed feedthrough solution. The KF flange and tubing diameter is large enough for the SMA connector (diameter: 9.5 mm) to be fed through.

as in the plastic protection sleeve directly surrounding the fiber.[8] The fiber is fed through a piece of tubing ending in a KF flange until the gap is located inside the tube. The bare fiber is then embedded in a halogen-free polyurethane resin (e.g. Electrolube UR5604) which fills the entire tube for air-tight sealing. The resin provides good adhesion to both the bare fiber and the tubing metal, while not exhibiting too much stress on the fiber during curing. The feedthrough can then be attached to a glove box via a matching KF port at the glove box side.

Summary

Reliable, safe and flexible laser delivery to a hollow waveguide based Raman system inside a glove box can be achieved by means of an actively stabilized single-mode fiber setup. Suitable components and configurations for this purpose have been identified within the scope of this work. With respect to practical considerations, a fiber feedthrough tailored to the special requirements of tritium glove boxes can be realized by the custom solution presented above. The fiber-based laser delivery system proposed here offers easy laser maintainability as well as flexibility in the glove box, while greatly facilitating the optical alignment of a hollow waveguide based Raman system located in a glove box compared to free-space laser delivery.

[8] Note that the removal of the protective sleeves is necessary since (i) the steel jacket itself is not air-tight, so that a sealing around the jacket would have no effect, and (ii) the plastic protection sleeve might contain halogens and would in that case not be suitable for glove box sealings.

6. Fluorescence-reducing measures and optimization of measurement parameters

It was discussed in section 3.4 that a hollow waveguide based Raman system has the potential to increase the Raman signal significantly compared to a conventional 90° Raman system. However, the sensitivity achieved with a hollow waveguide based prototype setup for the use with tritiated gases was found to be only of the same order as the one achieved with the standard LARA system, as shown in section 4.3: it was heavily impaired by the occurrence of strong fluorescence in the system, which led to a high shot noise level and consequently a deteriorating signal-to-noise ratio, with the signal gain being practically neutralized by the high noise values. In order to achieve the targeted sensitivity increase, it is thus vital to minimize the influence of fluorescence contributions in the hollow waveguide based Raman system while maintaining high Raman signals. This is the topic of the present chapter.

A range of fluorescence-minimizing approaches were investigated, in particular modifications of the system setup in the form of rearrangement and replacement of fluorescent optical components. The effect of each suggested approach on signal and noise, and hence the signal-to-noise ratio, was determined experimentally; these investigations were performed together with A. Off and are discussed in full detail in his Master's thesis [Off15]. In addition, the influence of various measurement parameters on the sensitivity was studied to optimize the system settings towards highest possible signal-to-noise ratios.

The chapter starts with an introduction to the topic of fluorescence production in optical components in section 6.1. In section 6.2, general options to reduce the detected fluorescence background are considered. In the following sections (6.3 – 6.6), concepts as well as experimental testing and evaluation of approaches to minimize fluorescence contributions from the various optical components in the hollow waveguide based Raman system are presented; note that the contents of these sections were subject to a publication by the author and co-workers in the journal "Sensors" [Rup15]. The optimization of measurement parameters is the topic of section 6.7. Finally, the results of the various investigations presented in this chapter are summarized in section 6.8.

6.1. Introduction: fluorescence in optical components

The term fluorescence denotes radiative transitions between the vibronic levels of an excited electronic state and those of the electronic ground state [Hak06]. The basic process is illustrated in the left panel of figure 6.1: in a system excited for instance by

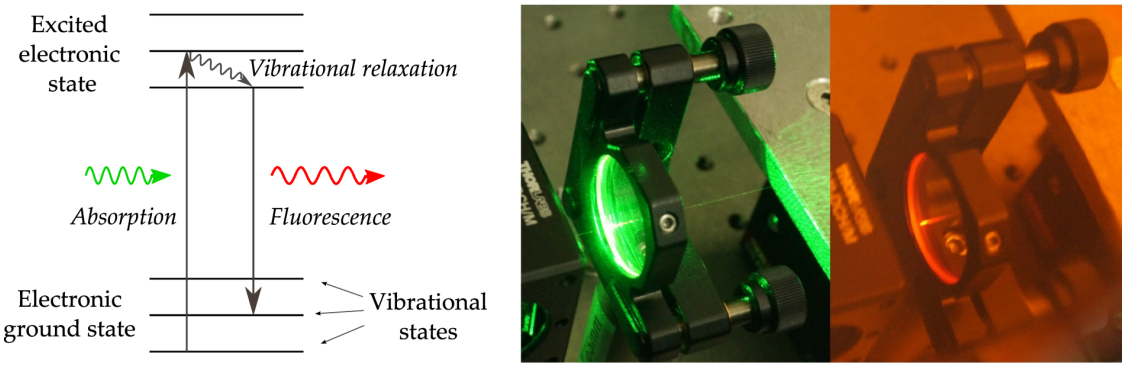

Figure 6.1.: Fluorescence in optical components. *Left:* Basic principle of fluorescence generation. The system is excited by absorption of incident light. It can release parts of the excitation energy by (radiationless) vibrational relaxation, before de-exciting via fluorescence light emission. *Right:* Fluorescence in a window exposed to 532 nm laser light. Both pictures show the same window. In the right picture, an edge filter in front of the camera was used to block the laser wavelength. By this means, the less intense red fluorescence light generated along the laser beam path becomes visible.

incident laser light, fluorescence light is emitted spontaneously, with an energy which is smaller than or equal to the energy of the absorbed photon. Since transitions can occur between a multitude of different vibronic states, fluorescence is emitted over a broad wavelength range. Note that for all excitation wavelengths in the visible range but very long ones, this broadband fluorescence wavelength range coincides with the wavelengths of the hydrogen Raman lines. Therefore, the fluorescence background is hard to eliminate and contributes to the overall noise in a spectrum, as outlined in subsection 3.2.3.

In optical components in a Raman system, fluorescence arises due to absorption of a small fraction of the incident laser beam in the optical material. While the bulk of the absorbed light is transformed non-radiatively into phonons and generates heat, some is re-emitted as fluorescence light. In optical glasses, e.g. fused silica (SiO_2) glass, the main origins of fluorescence are impurities and point defects such as color centers in the glass matrix [Wey42, Mae96, Sch10]. In the right panel of figure 6.1, fluorescence in an optical window due to 532 nm laser excitation is shown. As could be seen in figure 4.7, the intensity of collected fluorescence light easily competes with or even surpasses the Raman intensity, thus leading to non-negligible noise contributions. Possibilities for fluorescence reduction in a Raman system are therefore discussed in the following section.

6.2. Minimizing the fluorescence in a hollow waveguide based Raman system

In principle, there are several options to reduce the fluorescence of optical components:

- One possibility is to change the excitation laser wavelength. As discussed before in section 3.3.4, the wavelengths of Raman lines and fluorescence light are separated for excitation lasers in the middle to far UV region. This solution is not favored,

though, due to practical considerations as well as budgetary constraints. Another possibility is to shift the excitation laser into the near-IR wavelength region, where many electronic excitations are not excited due to the lower excitation energy, so that the fluorescence background is considerably weaker [McC05]. However, due to the approximate $\tilde{\nu}_i^4$ dependence of the Raman signal on the excitation wavelength (cf. equation 3.39), this goes along with a non-negligible signal decrease: for a 1064 nm DPSS laser, for instance, the signal decreases by a factor of 16, thus seriously denting the sensitivity again.

- Another possibility is temperature quenching: higher temperatures increase molecular motion and collisions within the optical material, which provide an alternative de-excitation channel to radiative transitions [Gui90]. A certain decrease of the fluorescence background was indeed observed in the prototype measurements in the first minutes after the system was exposed to high-power laser light. However, going to high temperatures $> 100\,°C$ for more effective temperature quenching would not only require extensive external heating of all fluorescent components in the system – an approach which is complicated by the low thermal conductivity of glass –, but also bear the risk of influencing the gas composition e.g. by enhanced self-equilibration.
- A very effective possibility to decrease the fluorescence-related noise while maintaining high Raman signals is to avoid fluorescence production within the line-of-sight of the Raman light collection to the greatest possible extent. This can be achieved by avoiding any contact between laser light and optical components, by placing fluorescent components outside of the line-of-sight of the light collection, or by using non-fluorescing components only. The investigation of such fluorescence reduction measures is the main focus of this chapter.

In order to achieve the goal to avoid fluorescence production in a hollow waveguide based Raman system as far as possible, it is necessary to take into account all optical components in the prototype system contributing to the detected fluorescence background. Contributions are expected from all glass-based components which are both exposed to laser light and located within the line-of-sight of the collection optics, namely (according to figure 4.1)

- the dichroic beam splitter,
- the window at the waveguide entrance,
- the back-reflecting mirror at the exit-end, and
- the hollow waveguide itself.

In the following, the investigation of a range of measures to avoid or minimize the detected fluorescence contributions from these components is addressed, with a focus on their replacement and/or rearrangement.

For the sake of simplicity, the systematic investigations undertaken here were not performed in a closed gas system as the prototype setup, but in an open setup where Raman spectra of ambient air were recorded. Care was taken that all described modifications are suitable for later integration of the system in a closed gas loop for *in situ* measurements. Note that

a SP2150i spectrometer (PI Acton) was used in these measurements instead of the SP500i spectrometer employed in the prototype setup. The following settings were maintained for all comparison measurements:

- The laser power was 1 W.
- 50 acquisitions of 1 s each were averaged for noise reduction.
- The CCD detector was cooled to -73 °C.
- The 400 vertical CCD pixels were combined to 25 bins of 16 pixels each.
- Dark measurements were performed during the measurements with the laser turned off to quantify thermal and read-out noise.

The acquired data were analyzed according to the procedure described in subsection 4.2.2. The analysis settings are listed in appendix F.2.

6.3. Investigation of alternatives to the beam splitter

According to the product specifications, the dichroic beam splitter separating laser and Raman light (LPD01-532RS, see table 4.1) reflects more than 98 % of the incident 532 nm laser beam, while 0.14 % are transmitted [Sem16a]. This leaves up to 1.96 % of the incident light being absorbed within the fused silica substrate, corresponding to almost 20 mW already for an incident laser power of 1 W. Although not all of the absorbed light is transformed into fluorescence light, the amount of fluorescence produced by several milliwatts of 532 nm radiation is by no means negligible (cf. figure 6.1, right panel). In addition, the beam splitter is located directly in the Raman light detection cone – although not in its focus – , so that fluorescence contributions from this component are rather efficiently collected and detected.

For this reason, alternatives to the standard beam splitter configuration were investigated within the scope of this work. Note that this study was part of the Master's thesis of Andreas Off [Off15] and partly based on preliminary studies by H. Seitz-Moskaliuk [Sei14]; both theses were supervised by the author within the frame of this PhD thesis. This section follows closely the line of thought published by the author and co-workers in [Rup15].

6.3.1. Alternative options for laser and Raman light separation

The dichroic beam splitter separates laser and Raman light by means of an optical coating, sending the respective wavelength components into different directions. An alternative to this approach would be direct spatial separation of the two light beams, which can be achieved either (i) by a small pick-off mirror, or (ii) by a larger mirror with a central hole, as illustrated in figure 6.2. In the former case, the laser beam is reflected into the waveguide by the pick-off mirror, while the bulk of the back-scattered Raman light passes around the small mirror and can be collected. A metal coating instead of a glass-based dichroic coating as in the beam splitter case is applied for fluorescence reduction. In the

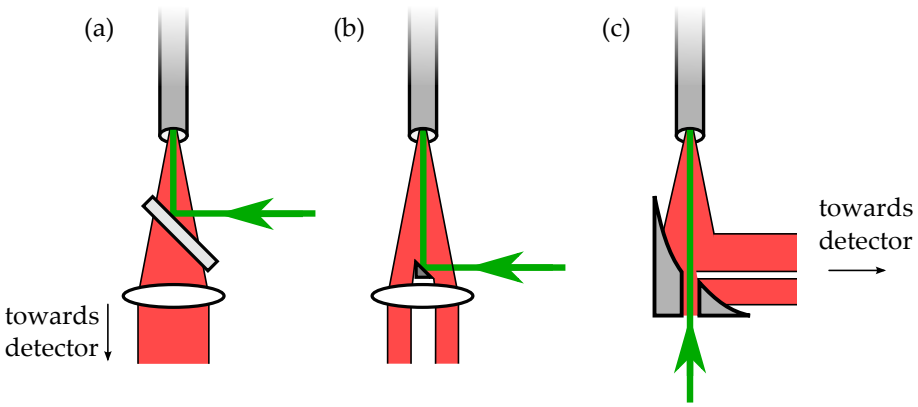

Figure 6.2.: Options for laser and Raman light separation. The paths of laser *(green)* and Raman light *(red)* when using *(a)* a dichroic beam splitter, *(b)* a pick-off mirror, or *(c)* an off-axis parabolic mirror with central hole for light separation are shown.

mirror-with-hole approach, the laser beam enters the waveguide through a small hole in a mirror, which reflects the back-scattered Raman-light in a 90° angle towards a side-arm where the Raman light collection optics are placed. Fluorescence production is avoided in this case as no direct contact between laser light and the mirror-with-hole occurs.

The drawback of the aforementioned alternatives is that a certain fraction of the Raman light – more specifically the part which is directly back-scattered (scattering angles close to 180°) and which thus suffers the least losses due to reflections in the waveguide – is lost for detection: it is either blocked by the laser pick-off mirror, or leaves the system through the laser access hole. For this reason it is crucial that the dimensions of the pick-off mirror or the hole are not larger than necessary with respect to the laser beam size, and that the distance to the waveguide (which is limited by the focal length of the collection lens) is as large as possible.

Nevertheless, it should be noted that in the beam splitter solution, the signal is reduced both by reflection losses of the laser beam ($\sim 2\,\%$) and transmission losses of the Raman light ($\sim 4\,\%$ in the region of the Q_1 lines of the hydrogen isotopologues) [Sem16a]. In contrast, just one reflection occurs in case of the pick-off mirror (only laser reflection) or mirror-with-hole solution (only Raman light reflection). By choosing the mirror/hole dimensions appropriately, the total losses can be even lower for these solutions than for the beam splitter. For instance, a hole of 2 mm diameter in a 25.4 mm mirror-with-hole takes up less than 1 % of the total mirror area, so that less light is lost due to the hole in this configuration than due to Raman transmission through the beam splitter in the original setup.

6.3.2. Experimental setup

All three light separation options were compared experimentally with respect to their fluorescence and signal properties. The following components were used for this investigation:

Pick-off mirror: A 2x2 mm right-angle prism mirror with protected aluminum-coated hypotenuse surface (PTK0203, Knight Optical) was used as the pick-off mirror. It was inserted directly in front of the Raman light collection lens in a custom-made mount, fitting the Thorlabs cage system for standard 25.4 mm-optics. The mount is shown in figure 6.3: the prism mirror was attached to the end of a thin metal sheet of 0.5 mm thickness, reaching from top into the center of the mount with the thin side facing the waveguide exit. By this means, only a minimal amount of the Raman light was blocked by the metal holder.

Off-axis mirror-with-hole: In the mirror-with-hole configuration (see figure 6.2 (c)), an off-axis parabolic mirror based on an aluminum substrate and coated with protected silver was used (MPD249H-P01, Thorlabs). It exhibited an on-axis through-hole of 2 mm diameter (custom-dimension) at a total mirror diameter of 50.8 mm. The reflective focal length was 101.6 mm. The mirror-with-hole is shown in figure 6.4.

Measurement setup: The general optical setup up to the beam splitter as well as the collection optics were the same as in the prototype measurements (see subsection 4.1.1 and figure 4.1). For the comparison measurements, the beam splitter was subsequently replaced by (i) the pick-off mirror and (ii) the mirror-with-hole. In the latter case, the collimating lens was left away since the parabolic mirror-with-hole itself served as collimator. Note that because of the size of this off-the-shelf mirror, the lens imaging the Raman light onto the fiber bundle had to be changed to the same diameter ($D = 50.8\,\mathrm{mm}$) to capture the full illuminated area of the mirror-with-hole; its focal length ($f = 75\,\mathrm{mm}$) was selected so that the maximum light collection solid angle of the system did not

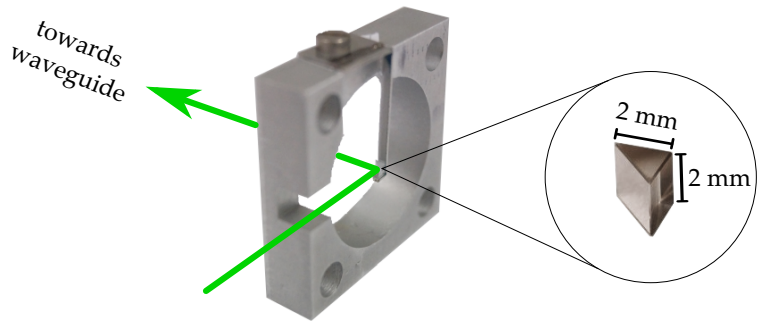

Figure 6.3.: Pick-off mirror mount. The laser beam is directed onto the pick-off mirror surface through an opening in the mount.

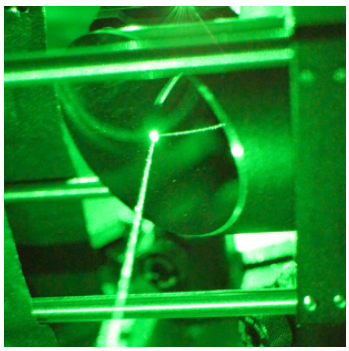

Figure 6.4.: Off-axis parabolic mirror-with-hole. The mirror is mounted in a cage system to provide optimal alignment with the lens focusing the Raman light onto the fiber bundle (towards the left side of the picture, not shown here). Picture taken by A. Off.

change significantly from the standard 25.4 mm-optic setups used for the beam splitter and pick-off mirror measurements.

In order to minimize fluorescence contributions from components other than the one separating laser and Raman light, the cell entrance window and the back-reflecting mirror were not included in the setup used for this investigation. In addition, a 200 mm long silver tube of 4.5 mm inner diameter was used instead of the glass-based hollow waveguide. Due to the overly large diameter of the tube, the laser beam did not come in contact with the tube walls, and thus no fluorescence from the waveguide was expected. These measures allow one to compare only the influence of the beam splitter and its alternatives on background and shot noise. Note that while this large-diameter tube guarantees minimal fluorescence generation, at the same time it comes at the expense of decreased Raman collection efficiency, due to the severe solid-angle mismatch between the opening of the light-guiding tube and the fiber bundle diameter.

6.3.3. Results and discussion

The results from the comparison measurement between the beam splitter and its alternatives are listed in table 6.1. The tabulated data reveal the following:

Pick-off mirror: With respect to fluorescence, it is noticeable that the noise level did not decrease when using a pick-off mirror instead of a beam splitter. This is explained by the fact that fluorescence was still generated in this configuration; the measurements revealed that laser stray light could easily interact with both the glass substrate of the mirror and the collection lens right behind the mirror. In addition, the data show that a considerable fraction of the total signal was lost in comparison to the beam splitter configuration. This can be partly attributed to the comparatively low reflectance of the aluminum coating of only about 90 % [Kni16], as well as to Raman light being blocked by the mirror itself and its mount, which shade about 3 % of the lens area. Nevertheless, the signal loss of about 30 % is higher than could be expected by these effects only. In this context, it should be noted that mirror positioning and optical alignment were quite

Table 6.1.: Comparison of beam splitter, pick-off mirror and mirror-with-hole with respect to their influence on signal (S), noise (N) and signal-to-noise ratio (SNR).

	S (10^3 counts)	N (counts)	SNR (10^3)
Beam splitter	98.7 ± 1.0	5.8 ± 0.7	17.0 ± 2.2
Pick-off mirror	70.7 ± 0.7	7.2 ± 0.9	9.8 ± 1.2
Mirror-with-hole	98.8 ± 1.0	2.8 ± 0.4	35.3 ± 4.5
Dark measurement	—	2.6 ± 0.3	—

challenging in this configuration due to the tiny size of the mirror. For this reason, parts of the signal loss are in all likelihood due to misalignment of the laser beam path relative to the Raman collection cone.

Accordingly, the signal-to-noise ratio achieved using a pick-off mirror is comparatively low. All in all, this solution cannot be considered a viable alternative to the standard beam splitter configuration.

Mirror-with-hole: For the metal-based mirror-with-hole, in contrast, the achieved SNR could be approximately doubled compared to the original setup. This is primarily due to the considerable background decrease: the noise level diminished practically to the level of a dark spectrum, i.e. the thermal and read-out noise from the detector.

The above findings demonstrate that fluorescence contributions from the wavelength-separating element can be eliminated nearly completely if direct contact with the laser beam is avoided, and if a full-metal component is used instead of glass-substrate optics to diminish the influence of laser stray light. In addition, the signal reached levels which were comparable to those achieved using the dichroic beam splitter, due to its highly reflective protected silver surface ($R > 98\,\%$ in the region of the Q_1 lines of the hydrogen isotopologues [Tho14b]) and only little (sub-percent) loss of Raman light through the hole.

For all these reasons, the use of a mirror-with-hole instead of a standard dichroic beam splitter is strongly recommended in hollow waveguide based Raman setups.

6.4. Investigation of a reduction of the cell window fluorescence

As described in subsection 4.1.1, fluorescence production in the window through which the laser beam enters the gas system was already minimized in the prototype system by an appropriate choice of window thickness and material according to the investigations described in [Jam15]. Nevertheless, as the window is not only exposed to the full laser beam, but also located very close to the waveguide end (in about 6 mm distance) and thus

to the focus of the collection optics, the remaining amount of fluorescence light produced in the window is very efficiently collected. For this reason, a noticeable amount of the total detected fluorescence background originates from the window.

In contrast to the beam splitter discussed above, it is not possible to avoid contact between laser beam and window, or to replace the window by a non-fluorescing metal alternative: a window is indispensable for the laser to enter the gas system containing the tritiated sample gas in a closed Raman system. Since fluorescence is thus inevitably produced, a background reduction has to rely on minimizing the amount of fluorescence light which reaches the detector. A possible rearrangement of optical components to achieve this goal will be discussed in the following. It was investigated within the Master's thesis of Andreas Off supervised by the author [Off15]. Note that this section follows closely the reasoning published by the author and co-workers in [Rup15].

6.4.1. Rearrangement of the optical configuration at the waveguide front end

If a mirror-with-hole is used instead of the beam splitter, as proposed in section 6.3 above, another window configuration is possible. It was shown in the previous chapter that a protected silver coating can be employed in a tritium atmosphere without being damaged. In contrast to the dielectric-coated beam splitter, the mirror-with-hole can thus be placed inside the gas system. The resulting new window configuration is shown in figure 6.5: laser and Raman light enter/exit the system through two separate windows in this case. This has two advantages with respect to fluorescence: first, the window through which the laser beam enters the system is placed directly in front of the mirror-with-hole, so that the generated fluorescence is almost completely blocked from the line-of-sight of the Raman light collection. Second, the window through which the Raman light exits the gas system is not exposed to laser light at all.

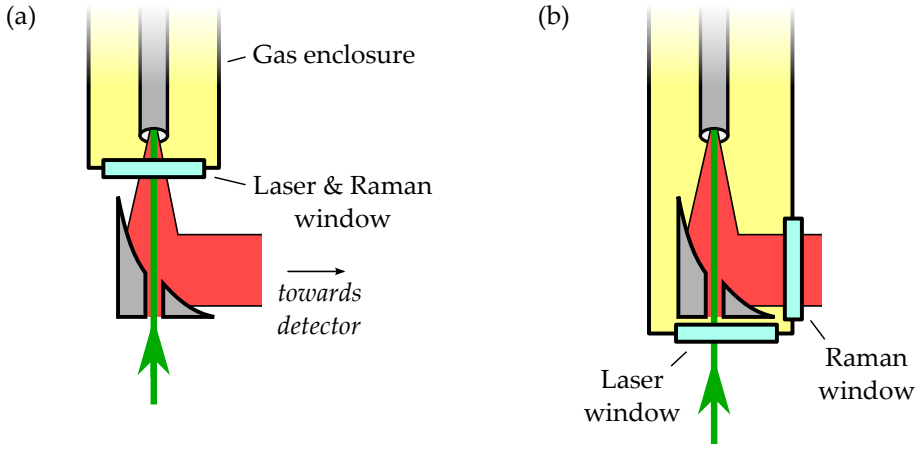

Figure 6.5.: Cell window configurations at the waveguide front end. *(a)* Original configuration. *(b)* New configuration.

6.4.2. Experimental setup

In order to compare the two configurations shown in figure 6.5, once again a silver tube with an inner diameter of 4.5 mm was used as the waveguide, and the back-reflecting mirror was removed, as described in subsection 6.3.2. In addition, the aforementioned mirror-with-hole configuration was implemented instead of the beam splitter. The fused silica laser window was anti-reflection coated for both laser and Raman wavelengths (Thorlabs WG41050-A, thickness $d = 5$ mm, coating BBAR = 350 – 700 nm). In the measurement corresponding to the original configuration, it was placed 11 mm in front of the waveguide, corresponding to the distance of the window in the prototype setup. In the test of the new configuration, it was placed directly in front of the mirror-with-hole.

6.4.3. Results and discussion

The comparison between the old front-window position, i.e. directly in front of the waveguide, and the revised position, where the laser window is placed before the mirror-with-hole, is shown in table 6.2. While the signal amplitude is comparable for the two configurations, the noise differs considerably: for the new configuration, it is now at the level of the dark measurement. This leads to a vast improvement by almost a full order of magnitude of the signal-to-noise ratio. For this reason, the suggested and tested window repositioning is an important step towards a fluorescence-free hollow waveguide based Raman system.

6.5. Investigation of a reduction of the mirror fluorescence

The back-reflecting mirror at the waveguide end consists of a dielectric-coated glass substrate. Despite its excellent reflectance of 99.6 % at 532 nm [Tho14b], few milliwatts of laser light are absorbed by the mirror material. Since the mirror is located directly behind the waveguide rear end, in a distance of only about 0.2 mm due to the protective cap, a large fraction of the resulting fluorescence is coupled into the waveguide, guided to its front exit and collected.

Table 6.2.: Influence of the front cell window configuration on the fluorescence background. Configurations (a) and (b) refer to figure 6.5. Note that the tabulated results are not directly comparable to the ones of table 6.1 due to the altered experimental setup.

	S (10^3 counts)	N (counts)	SNR (10^3)
Original configuration (a)	97.8 ± 1.0	27.9 ± 3.6	3.5 ± 0.5
New configuration (b)	93.3 ± 0.9	2.8 ± 0.4	33.3 ± 4.3
Dark measurement	—	2.7 ± 0.3	—

In addition, it was discussed in subsection 4.4.3 that proper alignment of the system is difficult with the back-reflecting mirror inserted, since the transmitted beam cannot be observed in this case. For these reasons, a different configuration of optics at the rear end of the waveguide is discussed in the following. The configuration was proposed by A. Off [Off15] and tested experimentally within the scope of the present work. Note that this section follows closely the reasoning published by the author and co-workers in [Rup15].

6.5.1. Rearrangement of the optical configuration at the waveguide rear end

The first step in a rearrangement of optics at the waveguide rear end is to replace the back-reflecting mirror integrated into the system by a window through which the laser beam can leave the system at the waveguide rear end. By this means, alignment of the laser beam traversing the waveguide is much facilitated, while back-reflection of the beam is still possible using an external mirror in some distance behind the window.

However, the issue of fluorescence generated in optical components at the waveguide rear end and coupled into the waveguide persists. In addition, one disadvantage of the mirror-with-hole configuration arises when the laser is back-reflected through the waveguide: a divergent beam is not fully coupled back out of the system through the central hole, but partly reflected by the mirror-with-hole into the Raman exit window, where it generates fluorescence directly in the line-of-sight of the detector. For these reasons, the following configuration is suggested, which is illustrated in figure 6.6.

- If back-reflection of the laser beam is desired, a concave mirror should be employed instead of a flat one to be able to refocus the beam through the hole in the mirror-with-hole.

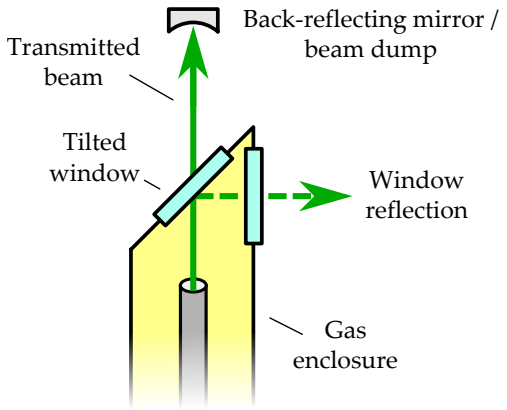

Figure 6.6.: New optical configuration at the waveguide rear end. Light reflected from the rear window is coupled out of the system through another window. Second-order back-reflections from this window are negligible. The bulk of the laser beam transmitted through the waveguide is either back-reflected and refocused by a concave mirror, or absorbed in a beam dump.

- In order to account for (divergent) back-reflections from the rear cell window, the window should be tilted with respect to the laser beam axis, thus preventing window reflections from being coupled back into the waveguide and reflected into the Raman exit window. Any anti-reflection coating of the tilted rear window has to be suitable for non-perpendicular incidence to avoid further fluorescence production; alternatively, an uncoated window can be used.
- The detection of fluorescence generated in the rear cell window can be reduced by allowing for a larger distance between waveguide end and window, i.e. several centimeters instead of a sub-millimeter distance only. Optionally, an additional aperture located behind the waveguide exit can block some fluorescence; care has to be taken that it is large enough to let the laser pass through unimpeded.

6.5.2. Experimental setup

In order to test the light return from a window at the exit end of the waveguide, a thin, uncoated fused silica window (Thorlabs WG41010, thickness $d = 1\,\mathrm{mm}$) was placed at a distance of 30 mm behind the exit of the waveguide; the large-diameter silver tube was used as the waveguide again. Starting at perpendicular laser beam incidence, the window was tilted in steps of 5° with respect to the laser beam axis. In addition, a measurement without the rear window was made to provide a "base-line" value, free of any back-scattering. Again, the mirror-with-hole configuration was used instead of the beam splitter. The laser beam was absorbed in a beam dump behind the tilted window; a possible back-reflection of the beam by a concave mirror is investigated in subsection 6.7.2 further below.

6.5.3. Results and discussion

The results of the rear window tilt measurements are collated in table 6.3. Here, the measurement at a tilting angle of 45° was chosen as an example, since the results for all tilting angles were very similar, most of them within the uncertainty of the measurement.

As expected, the fluorescence background and hence the noise is higher for the perpendicular window compared to the tilted one and the no-window configuration. It should be

Table 6.3.: Influence of the rear cell window configuration on the fluorescence background.

	S (10^3 counts)	N (counts)	SNR (10^3)
Perpendicular laser incidence	99.7 ± 1.0	8.7 ± 1.1	11.5 ± 1.5
Window tilted by 45° to beam	94.4 ± 0.9	3.5 ± 0.5	27.0 ± 3.5
No window	95.2 ± 1.0	2.8 ± 0.4	34.0 ± 4.4
Dark measurement	—	3.1 ± 0.4	—

noted that the signal is also slightly higher for the perpendicular window; this is due to the Raman contribution of the reflected laser beam instigating an additional amount of Raman light. However, this small signal gain does by far not outweigh the higher noise, so that the signal-to-noise ratio is less than half the value achieved with a tilted window. Overall, it is evident from the measurements that the noise level can be decreased almost to the level of a dark measurement by avoiding back-reflections from the window.

It should be noted that a small amount of background still remains due to fluorescence light originating from components behind the waveguide, in particular the window. In the measurements reported here, it was placed 30 mm behind the waveguide exit. In another test measurement, full elimination of detected background light could be achieved when the distance of the tilted window from the waveguide end was at least 60 mm.

6.6. Investigation of an alternative waveguide configuration

As was detailed in subsection 4.1.1, the hollow waveguide used in the prototype setup consists of a glass substrate which is internally lined with a 200 nm thick layer of unprotected silver. The inner diameter of the waveguide is 1 mm. In order to prevent laser light from entering the waveguide glass substrate at its end faces and fluorescence light from leaving the waveguide towards the detector, steel caps with a central aperture of 0.8 mm diameter were installed at both ends of the waveguide in the prototype setup (cf. figures 4.1 and 4.2). Despite this measure, non-negligible fluorescence contributions from the waveguide were observed even for optimal laser alignment; possible reasons for this will be discussed in the following subsection.

As already highlighted in the previous chapters, apart from this fluorescence background additional issues connected to the waveguide arise which make it necessary to change the current configuration. In particular, the durability test described in section 5.1 has shown that unprotected silver degrades under tritium influence, so that the current waveguide cannot be expected to maintain its good transmission properties in long-term measurements of tritiated gases. Also, the waveguide is prone to damage – both mechanical and laser-induced, as related in subsection 4.4.2 – and very sensitive to small misalignments of the laser beam (see subsection 4.4.3).

For these reasons, an altered waveguide configuration was investigated in the scope of this work. The general idea is described in subsection 6.6.2; it is partly based on preliminary studies from the Master's thesis of H. Seitz-Moskaliuk [Sei14]. Afterwards, the experimental setup and results of a test of the new waveguide are presented. The experimental test was conducted within the framework of the Master's thesis of Andreas Off supervised by the author [Off15].

6.6.1. Fluorescence from the glass-based hollow waveguide

In a first step, possible reasons for fluorescence originating from the waveguide are discussed. Although the waveguide substrate consists of glass and is thus prone to fluorescence generation when in contact with laser light, the inner silver lining as well as

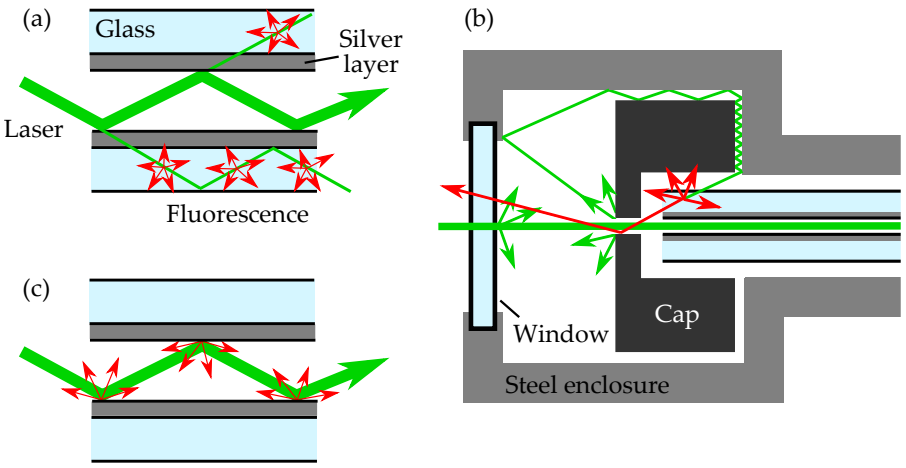

Figure 6.7.: Possible reasons for observed waveguide fluorescence. *(a)* Light leaking through the silver layer. *(b)* Diffuse scattering of laser and Raman light. *(c)* Fluorescence generation due to laser-wall interactions.

the steel caps at the waveguide end faces should prevent laser light from entering and fluorescence light from leaving towards the detector.

One possibility why fluorescence is still observed is light leaking through the silver lining (see figure 6.7 (a)). However, for 532 nm laser light, the skin depth in silver is only about 12 nm and thus much smaller than the silver layer thickness of 200 nm.[1] According to Beer's law [Dem13], only a fraction of about 10^{-7} of the incident light is transmitted through the 200 nm thick layer into the glass substrate in case of normal incidence; even less light is transmitted here considering the shallow angle of incidence of the almost parallel laser beam. It seems thus very unlikely that the observed fluorescence is due to laser light leaking into the glass substrate through the silver layer, much less – taking into account the considerably lower intensity of fluorescence light produced in the substrate – that fluorescence light from the substrate should leak back into the waveguide.

Another possibility is diffusely scattered light in the system (figure 6.7 (b)). A small fraction of the incident laser light is distributed throughout the system by Rayleigh scattering and diffuse scattering (e.g. due to wings of the incident beam hitting the outer cap surface) as well as by subsequent reflections within the stainless steel enclosure of the gas system. For this reason, light of the laser wavelength can enter the waveguide substrate through its (uncoated) outer surface and generate fluorescence there. As this fluorescence light is also distributed within the system by diffuse scattering, some of it can be detected despite the fluorescence-blocking caps at the waveguide ends.

However, waveguide-related fluorescence was observed even for waveguides tested outside of the gas system in open air (though still with protective caps), which leaves fewer possibilities for the distribution of diffusely scattered light. A certain fraction of the observed background light can thus be assumed to originate directly from the waveguide interior (figure 6.7 (c)). In contrast to fluorescence from the glass substrate, fluorescence

[1] The skin depth is calculated as $d_s = \lambda/(4\pi k)$ [Dem13]. For silver, the imaginary part of the refractive index at 532 nm is $k = 3.4215$ [Bab15], so that $d_s = 532\,\text{nm}/(4\pi \cdot 3.4215) = 12.4\,\text{nm}$.

generated directly in the waveguide would be very efficiently collected together with the Raman light. For this reason, it has to be assumed that some background contributions trace back to the silver-lined inner surface of the waveguide itself, e.g. due to impurities in or on the material. The reaction of the silver surface to laser exposure could not be directly observed because of the small diameter. However, emission of light in the orange to red wavelength range could be observed when directing a high-power laser beam (in the watt range) onto different metal surfaces, indicating that some background light is generated by metal surfaces as well, although to a lesser extent than in case of glasses.

In order to minimize fluorescence contributions from the waveguide, measures against background light both from the substrate and the interior of the waveguide have to be considered. Alterations to the current configuration, which in addition address the other waveguide-related issues mentioned above, are proposed in the following subsection.

6.6.2. Alterations to the waveguide configuration

The following alterations with regard to the waveguide configuration are proposed:

1. **Gold instead of silver lining:** According to the durability test (section 5.1), silver degrades when exposed to tritium, while gold, aluminum and copper maintain their reflectance. The current silver lining should thus be exchanged by one of these materials. The favored material is gold: it provides not only a good reflectance in the wavelength region of the Raman lines of interest (cf. figure 5.1), but is frequently used in tritium systems due to its chemical inertness and low tritium adsorption [Bab14].

2. **Larger inner diameter:** To increase the waveguide diameter and thus minimize interactions between the laser beam and the inner waveguide walls has several advantages:

   - Fluorescence produced in such interactions is minimized.
   - Strong laser attenuation in the waveguide due to the comparatively low reflectance of gold at the laser wavelength is avoided. At the same time, Raman attenuation is also reduced as light is reflected less often in a waveguide with a larger inner diameter.
   - High laser densities at the waveguide surface, which could lead to damage, are avoided.
   - The system becomes less sensitive to small beam misalignments (e.g. if the beam is not strictly parallel to the waveguide).
   - In addition, a larger inner diameter improves the gas flow through the waveguide.

   On the downside, a lower fraction of the Raman light leaving the waveguide can be collected in case of a larger-diameter waveguide due to its increased étendue (cf. subsection 3.4.1). The optimal choice of waveguide diameter will therefore be discussed in detail in subsection 6.7.1. Note that a reduction of the laser beam

diameter is in principle also possible to minimize interactions between the laser beam and the inner waveguide walls; however, in general this goes along with a larger beam divergence, which as a consequence leads again to laser interaction with the wall when long waveguides are used.

3. **Full-metal instead of glass-based waveguide:** Fluorescence potentially produced in the waveguide glass substrate can be avoided by using a full-metal waveguide instead. In addition, this greatly improves the mechanical stability of the waveguide.

With respect to the last item, it has to be mentioned that metal waveguides have been traditionally used to a much lesser degree than glass-based ones. The latter profit from the intrinsically smooth surface of glass, while the achievable reflectance of metal waveguides is usually limited by their rougher inner surface and the difficulties to accomplish a sufficiently good internal polish in long tubes with a small inner diameter. Consequently, the use of full-metal waveguides was long restricted to either very large diameters – Eaglesfield considers the use of a silver-lined steel pipe with 25.4 mm inner diameter as an optical pipeline [Eag62] – or very short waveguides: by using mechanical polishing, Vessieres et al. produced a gold-coated light pipe of 1 mm inner diameter, but with a total length of only 20 mm [Ves90]. Seitz-Moskaliuk tested the possibility to assemble a full-metal waveguide from separately polished metal plates, with a groove acting as the waveguide in one plate and the other plate serving as the lid [Sei14]. However, signal losses due to light leaking into the slit between the plates were too high for this approach to be competitive to other waveguides.

In order to obtain metal tubes which (i) are long, (ii) have a small inner diameter in the few-millimeter range and (iii) provide a highly reflective inner surface at the same time, an alternative to conventional polishing techniques is thus employed in the frame of this work: electroforming. In this technique, articles are produced by electro-deposition on a mandrel, which is subsequently removed [AST13]. A highly polished mandrel leads to a very smooth surface of the deposit. For this reason, a highly reflective waveguide with inner gold lining can be obtained by electroplating a long, cylindrical mandrel with a small diameter and highly polished surface with gold, followed by deposition of a thicker nickel layer for mechanical stability, before the mandrel is removed [Ove14].

6.6.3. Experimental setup

The new waveguides tested in the scope of this work are so-called “Light Pipes” manufactured by Epner Technology Inc. [Epn14b] by electroforming as described above. The substrate consists of pure nickel, the hard gold coating (“Laser Gold”) is made of 99.99 % purity gold [Epn14a]. In order to test the influence of material and diameter on the measured fluorescence background and the Raman signal, four sample waveguides of 200 mm length each were compared:

- a glass-based, silver-lined waveguide with an inner diameter of ID = 1 mm, i.e. the same type as used in the prototype measurements;
- a gold-coated, full-metal Light Pipe with ID = 1 mm for direct comparison to the glass-based, silver-coated waveguide;

- another Light Pipe with a larger inner diameter of ID = 2 mm; and
- an unpolished silver tube with ID = 4.5 mm to test an even larger diameter.[2]

For completeness, a 180° Raman measurement was also taken without any waveguide inserted, to ascertain a fluorescence-free base line. In the Raman setup used for the comparison, the mirror-with-hole configuration was again implemented instead of the beam splitter, and the front cell-window and back-reflecting mirror were not installed to probe exclusively fluorescence originating from the waveguides. All waveguides were inserted into a groove fitting their outer diameter to ensure their straightness. Instead of steel caps as used in the prototype setup, an x-y adjustable 0.8 mm pinhole was placed in front of the glass waveguide to prevent laser light from entering the glass walls directly and fluorescence light from exiting.

6.6.4. Results and discussion

The results of the comparison between the different waveguides are shown in table 6.4. Several points are noteworthy regarding the fluorescence-related background noise:

First of all, it becomes clear that a non-negligible background is produced even when full-metal waveguides are employed. For comparison, the background curves obtained with the 1 mm Light Pipe (LP1) and the glass-based waveguide are shown in figure 6.8. Both the observed background in the spectrum of the full-metal waveguide and the absence of SiO_2 Raman peaks in the spectrum of the glass-based waveguide indicate that the glass substrate is not the main origin of fluorescence related to a waveguide, but interactions between laser light and the metal inner waveguide walls play a major role. Regardless of this, the background is reduced by more than a factor of two when replacing the glass-based waveguide with a Light Pipe of the same diameter. Assuming that the substrate does not have a major influence, possible reasons for this are the different inner surface materials (silver vs. gold) themselves, or less or different impurities in/on the Light Pipe lining. Note that subsequent cleaning of both waveguides types with ethanol did not lead to any change of either signal or noise.

The second important observation related to the data in table 6.4 is the clear influence of the waveguide diameter on the measured noise: the larger the diameter, the lower the noise. For the large-diameter silver tube, in which practically no interaction between laser and tube wall occurs, the noise level even approaches the level of a dark or 'no-waveguide' measurement. Fluorescence can thus be successfully avoided by choosing a large enough waveguide diameter.

On the other hand, as expected, the measured signal drops as well with increased waveguide diameter since a smaller fraction of the Raman light can be imaged onto / coupled into the light collection fiber bundle. This will be discussed in detail in subsection 6.7.1. In addition, the signal is reduced in the 1 mm Light Pipe compared to the glass-based waveguide due to the lower reflectance of gold compared to silver at the laser wavelength (cf. figure 5.1). Nevertheless, the overall signal loss of about 45 % when changing from

[2] A silver tube was chosen since a third Light Pipe was not available due to budgetary constraints, while large-diameter glass waveguides (ID > 3 mm) could not be delivered without being damaged.

Table 6.4.: Performance of different waveguide types with different inner diameters (ID).

	ID (mm)	S (10^3 counts)	N (counts)	SNR (10^3)
Glass-based waveguide	1.0	317.6 ± 3.2	26.2 ± 3.4	12.1 ± 1.6
Light Pipe LP1	1.0	235.9 ± 2.4	10.9 ± 1.4	21.6 ± 2.8
Light Pipe LP2	2.0	178.2 ± 1.8	4.7 ± 0.6	37.9 ± 4.9
Silver tube	4.5	98.6 ± 1.0	3.1 ± 0.4	32.0 ± 4.1
No waveguide	—	33.4 ± 0.34	2.8 ± 0.4	11.9 ± 1.6
Dark measurement	—	—	2.7 ± 0.3	—

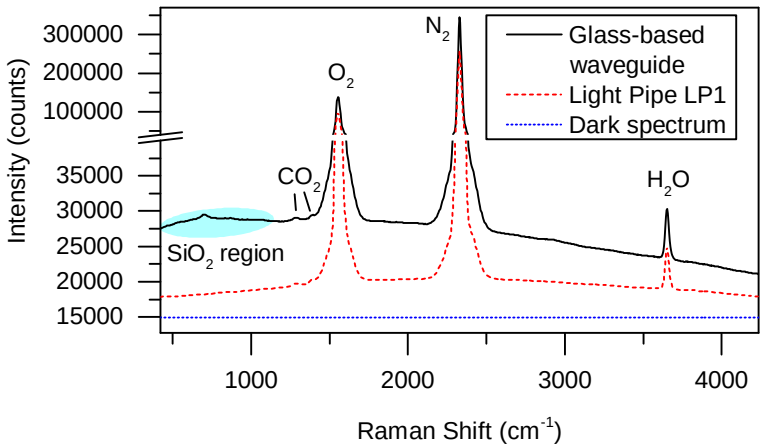

Figure 6.8.: Fluorescence background from glass-based waveguide and Light Pipe. The respective spectra of air are shown. The Q_1 branches of nitrogen and oxygen as well as the peaks corresponding to CO_2 (Fermi-diad, ν_1 symmetric stretch and $2\nu_2$ bending overtone) and H_2O (ν_1 symmetric stretch) are labeled. No Raman peaks of SiO_2 (i.e. fused silica glass) are visible in the spectrum of the glass-based waveguide; these would be expected at several positions in the highlighted Raman shift region below 1200 cm^{-1} according to Walrafen and Krishnan [Wal82].

the standard 1 mm glass waveguide to the 2 mm Light Pipe is more than compensated for by a noise reduction of $> 80\,\%$. As a consequence, this leads to an overall sensitivity improvement by more than a factor of three.

Considering this improvement and the various additional advantages of the alteration of the waveguide configuration discussed in subsection 6.6.2 – namely tritium compatibility, lower susceptibility to mechanical and laser damage, better alignment stability and improved gas flow –, turning away from standard glass-based waveguides with small diameters, as usually employed in the literature, to larger-diameter all-metal waveguides is highly recommendable for Raman gas sensing applications. The choice of suitable waveguide parameters for the final hollow waveguide based Raman system, i.e. the exact length and diameter, is discussed in the following section.

6.7. Optimization of measurement parameters

Apart from implementing the various fluorescence-reducing measures discussed above, several parameters of the new hollow waveguide based Raman system have to be optimized in order to achieve the highest possible sensitivity. First of all, this concerns length and diameter of the waveguide, which are discussed in the following subsection. Subsection 6.7.2 focuses on the question if the double-pass configuration of the prototype setup, in which a mirror behind the waveguide reflects the laser beam back to achieve a higher power density in the waveguide, is still advantageous over a single-pass solution in the new setup. Finally, the influence of acquisition parameters on the sensitivity is investigated in subsection 6.7.3 to identify the optimal measurement settings.

6.7.1. Optimization of waveguide parameters

As outlined in section 3.4, the measured Raman signal in a hollow waveguide based Raman system depends on a range of parameters such as the reflectance of the inner surface, the length and the diameter of the waveguide. The reflectance is fixed by the choice of a gold-lined Light Pipe with very smooth inner surface. With respect to waveguide length and diameter, model calculations of their respective influence on the measured signal have been performed within the scope of this work. Parts of the results are used in the following; the detailed calculations can be found in Appendix I.

Waveguide length: It was shown in the previous section that interactions between the laser beam and the inner waveguide walls should be avoided as far as possible in order to minimize the background noise. In that case, laser attenuation is reduced practically to zero, so that the intensity at the waveguide exit is determined by Raman light attenuation only. For this reason, the Raman intensity can be maximized by making the waveguide as long as possible: increasing the waveguide length always leads to an (ever smaller) additional Raman contribution from the additional waveguide segment and a gradual saturation of the intensity curve. The scattering geometry is thus basically the backward Raman case shown in figure 3.9 and discussed in section 3.4, even if a back-reflecting

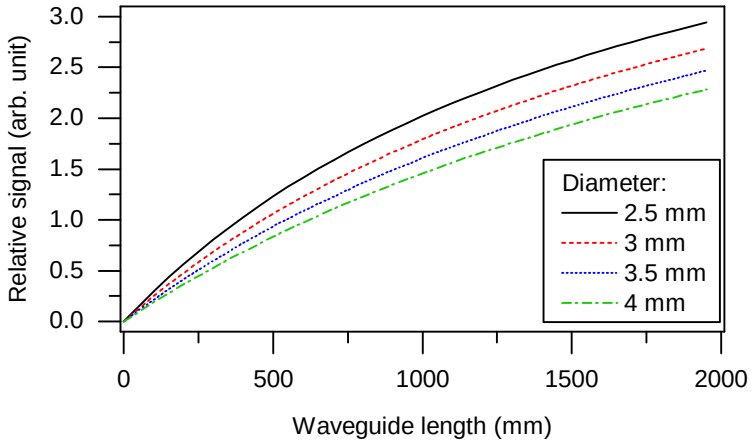

Figure 6.9.: Dependence of the relative Raman signal on the waveguide length for large-diameter waveguides. The curves were calculated based on equation I.10 for nitrogen in a gold-coated waveguide. See appendix I for details.

mirror is employed.[3] The theoretically calculated length dependence of the measured Raman signal for large-diameter waveguides is shown in figure 6.9: attenuation is so low that the signal does not saturate even for a waveguide length of up to two meters. In practice, however, space restrictions in the glove boxes housing the Inner Loop limit the waveguide length to about 800 mm.[4] This maximum length should thus be used in the final hollow waveguide system in order to achieve highest possible Raman signals.

Waveguide diameter: According to equation 3.33, two different factors related to the waveguide geometry have to be taken into account when considering the measured Raman signal: the total intensity of the Raman light generated in the waveguide and the light collection properties, which determine the fraction of generated Raman light which is actually detected. Both factors are related to the waveguide diameter. On the one hand, the attenuation decreases for larger diameters due to the lower number of reflections in the waveguide, which leads to a higher Raman intensity at the waveguide exit. On the other hand, a lower fraction of the total emitted light can be imaged onto the collection fiber bundle in case of a larger waveguide diameter. The model calculations (appendix I) show that the latter effect dominates, so that a diameter increase results in a lower signal, as shown in figure 6.10. This is also reflected in the signal values shown in table 6.4 above for waveguides of different diameters.

Nevertheless, the results discussed in the previous section demonstrated that the waveguide diameter should not be chosen too small despite the higher signal, since background

[3] According to figure 3.9 and the corresponding equations discussed in section 3.4, there is an optimum cell length when a back-reflecting mirror is used in a backward scattering configuration. Due to the missing laser attenuation in the case discussed here, however, the mirror just leads to an approximately doubled signal in this case, but does not affect the general relation between cell length and relative Raman signal.

[4] For the same reason, i.e. space restrictions, the off-the-shelf mirror with hole with a focal length of 101.6 mm and a diameter of 50.8 mm is replaced by a custom-made one with dimensions reduced by a factor of 2, i.e. $f = 50.8$ mm and $D = 25.4$ mm. The hole diameter remains at 2 mm.

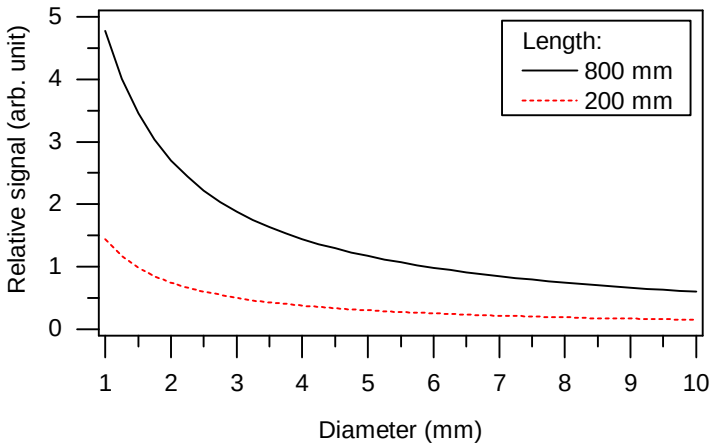

Figure 6.10.: Dependence of the relative Raman signal on the waveguide diameter. Note that the underlying calculations of light attenuation in the waveguide are based on literature reflectance values (see appendix I for details). Measured attenuations have been found to be higher than the theoretical values, leading to lower absolute signals than calculated. This is probably due to the imperfect smoothness of real waveguide inner surfaces. As small-diameter waveguides are affected more strongly by higher attenuations, realistic curves of the relative signal can be assumed to decline more slowly with increasing diameter than the ones shown here.

noise rises as well in small-diameter waveguides: the noise reduction connected to a larger diameter outweighs the signal loss up to a certain point when calculating the signal-to-noise ratio. At some stage, however, a further diameter increase will not cause a significant noise decrease any longer, while the signal will still become lower and approach the limit of the "no waveguide" measurement, so that the overall sensitivity will decrease again. This tendency is already observed in the 4.5 mm silver tube measurement shown in table 6.4 above. For this reason, the diameter should be just as large as necessary for fluorescence avoidance.

Based on the measurements presented in the last section, where a certain fluorescence background was still observed in the 2 mm Light Pipe, it can be assumed that background production is related to the laser beam being not perfectly centered and parallel to the waveguide: the maximum $1/e^2$ laser beam diameter[5] is $D_{\max} \approx 0.6\,\mathrm{mm}$, so that just a negligible fraction of the total laser intensity in the wings of the Gaussian beam,

$$\frac{I_{\text{wing}}}{I_{\text{tot}}} = e^{-2\cdot\left(\frac{D_{\text{WG}}}{D_{\max}}\right)^2} = e^{-2\cdot\left(\frac{2}{0.6}\right)^2} \approx 10^{-10}\ , \tag{6.1}$$

would interact with the walls of the waveguide with inner diameter $D_{\text{WG}} = 2\,\mathrm{mm}$ in case of a strictly parallel and centered beam. Also, an angle of only 0.6° between laser beam and waveguide is sufficient to let the full 1 W beam collide with the waveguide wall at least once in a 2 mm waveguide. Such minor alignment inaccuracies cannot be fully avoided despite using micrometer screws. Therefore, a certain safety margin between laser and waveguide diameter has to be allowed for when choosing the waveguide diameter.

[5] The $1/e^2$ diameter of a Gaussian beam in a distance z from the beam waist (radius) $w_0 = \lambda z_0/\pi = \lambda f/(\pi r_{\text{Laser}})$ is given by $D = 2w(z) = 2w_0 \cdot \sqrt{1+(z/z_0)^2} = w_0 \cdot \sqrt{1+(z\lambda/\pi w_0^2)^2}$ [Mes15].

Based on this consideration, a 3 mm diameter is suggested for the 800 mm long final waveguide. The laser beam exiting the laser-guiding PCF (cf. section 5.2) is collimated to a diameter of 1 mm, and focused into the waveguide by a 750 mm lens. With the focal point located in the center of the waveguide, the beam reaches its maximum diameter at both waveguide ends, at a distance of 400 mm from the beam waist. At this distance, the beam has a diameter of about 0.74 mm, i.e. 24.6 % of the waveguide diameter for a 3 mm Light Pipe; this is larger than in the case of the 2 mm Light Pipe (30 %) to provide a larger safety margin. In preliminary measurements with aluminum waveguides, the background was consequently reduced practically to the level of a dark measurement for a 3 mm diameter, while a 2.5 mm diameter was not yet sufficient to suppress all fluorescence production. Note that according to the theoretical data shown in figure 6.10, increasing the waveguide diameter from 2 mm to 3 mm in a 800 mm long Light Pipe leads to a signal loss of less than ca. 30 %, while the measurement data from table 6.4 indicate that a noise reduction by more than 40 % is possible.

6.7.2. Single-pass vs. double-pass configuration

In the original prototype setup, a mirror at the rear end of the waveguide was used to reflect the laser back through the waveguide ("double-pass configuration") to achieve approximately doubled signals compared to a single-pass setup. The returning beam was decoupled from the backward scattered Raman light by the dichroic beam splitter, following the initial laser beam path (cf. figure 6.2) in inverse direction. In principle, such a double-pass configuration is also possible in the new setup comprising the various alteration discussed in the previous sections. However, since the beam splitter is exchanged by a mirror-with-hole, care has to be taken that the back-reflected laser beam is well focused and aligned to leave the system through the small hole in the mirror-with-hole: any laser light hitting the surface of the mirror-with-hole would be reflected into the Raman window (see figure 6.5) and produce fluorescence background. For this reason, a concave mirror should be used as the back-reflecting mirror.

The double-pass mode was tested with the new 800 mm long Light Pipe in the fluorescence-reduced setup. All windows were installed as described in the sections 6.4 and 6.5. The collection optics comprised the $f = 50.8$ mm mirror-with-hole as well as a $f = 50$ mm lens to focus the collected light into the fiber bundle leading to the spectrometer. The laser beam was focused by a $f = 750$ mm lens into the waveguide, with the focal point located in the middle of the waveguide (i.e. in a distance of $L/2 = 400$ mm from the waveguide end). A dielectric-coated, concave mirror with $f = 500$ mm (CM750-500-E02, Thorlabs) was placed in a distance of $d = 425$ mm behind the waveguide rear end to refocus the laser beam approximately at the position of the mirror with hole.[6]

The double-pass configuration was directly compared to a single-pass one, in which the concave mirror was replaced by a beam dump. The results of both measurements are listed in table 6.5: despite the almost doubled signal in the double-pass configuration, the

[6] The original beam is maximally focused in the distance $d_o = d + L/2 = 825$ mm from the mirror. According to the mirror equation, $1/f = 1/d_o + 1/d_i$ [Dem06], the reflected beam is focused in a distance $d_i = (1/500 + 1/825)^{-1}$ mm $= 1269$ mm from the mirror, i.e. 44 mm behind the waveguide front end and 6.8 mm before the mirror-with-hole.

sensitivity was similar in both cases, since the noise increased as well by about a factor of 2. This indicates that the back-reflected laser beam is not fully coupled out of the system, so that small amounts of laser light still reach the Raman window and produce fluorescence there. It should be noted that the signal in the double-pass configuration suffers from the laser beam passing the uncoated rear window twice, with reflection losses of the order of 8 % in each pass (calculated based on [Mal65]). However, even if a practically doubled signal was achieved by using a custom anti-reflection coating suitable for 45° incidence, this would lead to a signal-to-noise ratio of only approximately $35 \cdot 10^3$. Within the measurement uncertainties, this value is still not higher than the value achieved in single-pass configuration. Weighing the additional alignment efforts connected to the double-pass configuration – in particular inside a glove box – against a potential minor sensitivity increase, it seems thus advisable to refrain from using a double-pass configuration in the final hollow waveguide based Raman system.

Table 6.5.: Comparison of single-pass and double-pass mode in the new hollow waveguide based Raman setup. Measurement settings: $P_{\mathrm{Laser}} = 0.5\,\mathrm{W}$, $t_{\mathrm{acq}} =$ 50 x 0.37 s, 5 vertical bins.

	S (10^3 counts)	N (counts)	SNR (10^3)
Single-pass	54.5 ± 0.5	1.6 ± 0.2	33.6 ± 4.3
Double-pass	94.1 ± 0.9	3.1 ± 0.4	30.6 ± 3.9
Dark measurement	—	1.2 ± 0.2	—

6.7.3. Optimization of the light acquisition settings

The measured signal-to-noise ratio depends not only on the Raman system used, but also on the acquisition settings, in particular

- the acquisition time for a single spectrum, t_{acq},
- the number of single acquisitions over which is averaged, n_{acq},
- the number of vertical detector bins, n_{bin}.

These parameters are only partly fixed by experimental requirements: cosmic ray removal requires at least two averages ($n_{\mathrm{acq}} \geq 2$, cf. subsection 4.2.2), and a bin number of $n_{\mathrm{bin}} \geq 5$ is recommended to be able to correct acquired spectra for astigmatism aberration[7] [Fis14]. The maximum allowed total acquisition time, $t_{\mathrm{acq,tot}} = t_{\mathrm{acq}} \cdot n_{\mathrm{acq}}$, is also fixed. However, it can be reached by taking either few long acquisitions or a many short ones. In addition, it has to be taken into account that saturation of the CCD detector – 2^{16} counts per bin cannot be exceeded – should be avoided, which requires a sufficiently high number of bins or single acquisitions.

[7] Note that astigmatism correction was not applied within the framework of this study. However, it is recommended for the final measurements for KATRIN, especially when a low f-number spectrometer (as used in the LARA system) is employed.

In the investigations conducted so far within the scope of this work, the acquisition settings were chosen in a way which allowed for a certain flexibility in the evaluation of acquired data by using many bins and many short single acquisitions. In the actual Raman measurements for KATRIN, the acquisition settings should rather be optimized with respect to maximum sensitivity. In order to determine the optimal settings, measurements with the hollow waveguide based Raman system were conducted for a range of combinations of different acquisition settings, with $t_{\mathrm{acq}} = 0.1 - 5\,\mathrm{s}$, $n_{\mathrm{acq}} = 2 - 50$ and $n_{\mathrm{bin}} = 1 - 25$.

Representative plots of the dependence of signal, noise and signal-to-noise ratio on each parameter are shown in figure 6.11, demonstrating the characteristics of each:

- The advantage of a long acquisition time is the high achievable signal. Since it rises approximately linearly with acquisition time, while shot noise and thermal noise increase only with the square root of t_{acq}, the signal-to-noise ratio follows an approximate square root curve. Note that the third noise contribution, the readout noise, is independent of t_{acq}.
- An increased number of acquisitions does not lead to a higher signal compared to a single acquisition. On the other hand, the sensitivity benefits as the total noise decreases with $\sqrt{n_{\mathrm{acq}}}$ by averaging.
- The number of bins influences the read-out noise only; it becomes larger the more bins have to be read out. According to the manufacturer of the CCD used, the signal-to-noise ratio improves approximately linearly with the number of pixels grouped together (with $n_{\mathrm{pixel}} \propto 1/n_{\mathrm{bin}}$) in the read-out noise limited case, and roughly proportional to $\sqrt{n_{\mathrm{pixels}}} \propto 1/\sqrt{n_{\mathrm{bin}}}$ if shot noise predominates [Pri15b].

In figure 6.12, the signal-to-noise ratios of measurements with a constant total acquisition time of $t_{\mathrm{acq,tot}} = t_{\mathrm{acq}} \cdot n_{\mathrm{acq}} = 10\,\mathrm{s}$ are shown. The plot demonstrates that few long measurements are clearly to be preferred to many short ones to maximize the sensitivity achieved in a given total acquisition time: for instance, when changing the acquisition settings from $t_{\mathrm{acq,tot}} = 2$ x 5 s to 50 x 0.2 s, the signal-to-noise ratio decreases by 61 % (independent of the number of bins used), despite the total acquisition time being the same in both cases.

The difference is due to the read-out noise, which is independent of the acquisition time. According to above considerations, the signal-to-noise ratio follows the proportionality

$$\mathrm{SNR} \propto \frac{t_{\mathrm{acq}}}{\sqrt{N_{\mathrm{R}}^2 + \left(c_1\sqrt{t_{\mathrm{acq}}}\right)^2}} \cdot \sqrt{n_{\mathrm{acq}}}\ , \tag{6.2}$$

with N_{R} being the read-out noise and c_1 the proportionality constant related to the time-dependent noise contributions (shot noise and thermal noise) $\propto \sqrt{t_{\mathrm{acq}}}$. When the total acquisition time is fixed and thus $n_{\mathrm{acq}} \propto 1/t_{\mathrm{acq}}$, this expression becomes

$$\mathrm{SNR}\big|_{t_{\mathrm{acq,tot}}=\mathrm{const.}} \propto \frac{t_{\mathrm{acq}}}{\sqrt{N_{\mathrm{R}}^2 + \left(c_1\sqrt{t_{\mathrm{acq}}}\right)^2}} \cdot \frac{1}{\sqrt{t_{\mathrm{acq}}}} = \sqrt{\frac{t_{\mathrm{acq}}}{N_{\mathrm{R}}^2 + c_1^2 \cdot t_{\mathrm{acq}}}}\ . \tag{6.3}$$

While the read-out noise thus becomes increasingly negligible for long acquisition times, it contributes noticeably to the total noise in short acquisitions and limits the achievable signal-to-noise ratio.

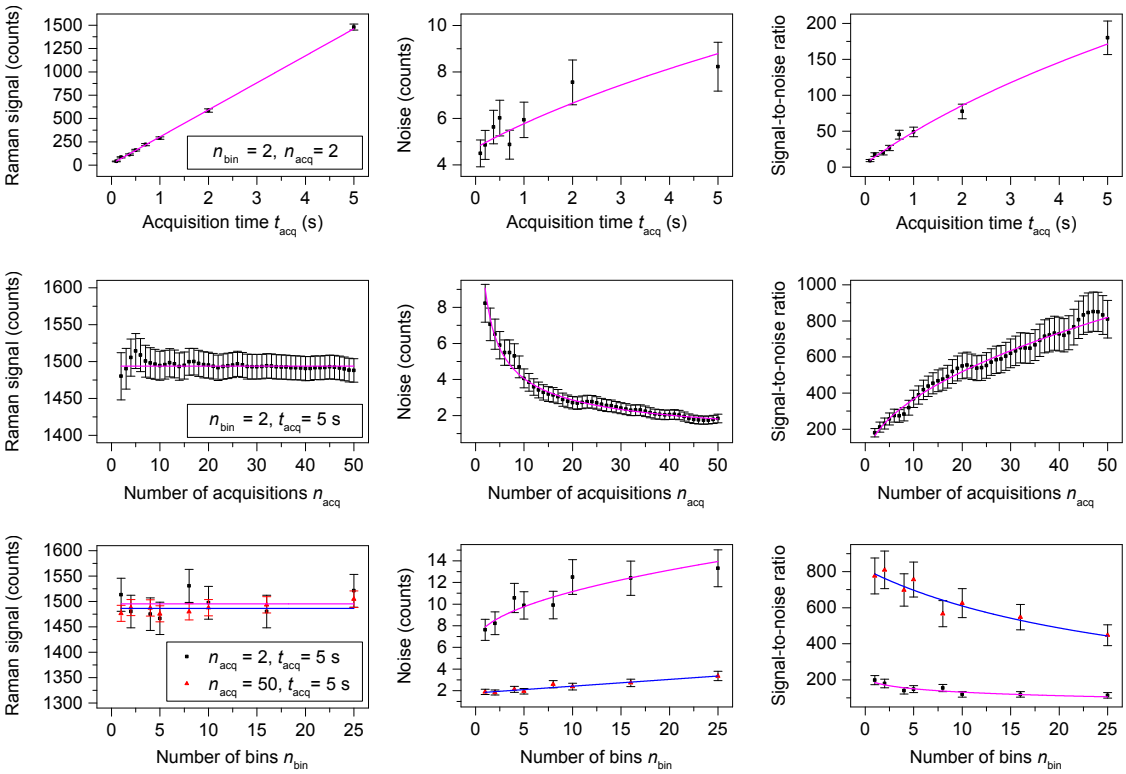

Figure 6.11.: Dependence of signal, noise and signal-to-noise ratio on measurement parameters. *Top:* Dependence on the acquisition time. *Center:* Dependence on the number of acquisitions. *Bottom:* Dependence on the number of bins. The other parameters were fixed in each case to the values stated in the 'Raman signal' plot legend. Fit curves are shown to guide the eye. The following fit functions with fit parameters A, B, C were used according to the considerations in the main text:

- $S(t_{\mathrm{acq}}) = A + B \cdot t_{\mathrm{acq}}$, with the fit parameter A taking into account the small, constant signal offset due to light detected during the CCD read-out process.
- $N(t_{\mathrm{acq}}) = \sqrt{A + B \cdot t_{\mathrm{acq}}}$, with A related to the constant read-out noise contribution.
- $\mathrm{SNR}(t_{\mathrm{acq}}) = A \cdot (B + t_{\mathrm{acq}}) / \sqrt{C + t_{\mathrm{acq}}}$.
- $S(n_{\mathrm{acq}}) = A$.
- $N(n_{\mathrm{acq}}) = A / \sqrt{n_{\mathrm{acq}}}$.
- $\mathrm{SNR}(n_{\mathrm{acq}}) = A \cdot \sqrt{n_{\mathrm{acq}}}$.
- $S(n_{\mathrm{bin}}) = A$.
- $N(n_{\mathrm{bin}}) = A + B \cdot \sqrt{n_{\mathrm{bin}}}$ (for $n_{\mathrm{acq}} = 2 \Rightarrow$ shot noise limited case),
  $N(n_{\mathrm{bin}}) = A + B \cdot n_{\mathrm{bin}}$ (for $n_{\mathrm{acq}} = 50 \Rightarrow$ read-out noise limited case).
- $\mathrm{SNR}(n_{\mathrm{bin}}) = A / (B + \sqrt{n_{\mathrm{bin}}})$ (for $n_{\mathrm{acq}} = 2$),
  $\mathrm{SNR}(n_{\mathrm{bin}}) = A / (B + n_{\mathrm{bin}})$ (for $n_{\mathrm{acq}} = 50$).

The peak corresponding to the Q_2 branch of N_2 was used to determine the signal in each case in order to avoid detector saturation as partly observed for the Q_1 branch. All analysis settings are listed in appendix F.3. Note that in the case of the n_{acq} plots, subsets of the same batch of 50 acquisitions were averaged and analyzed, so that the single data points shown here are not fully independent.

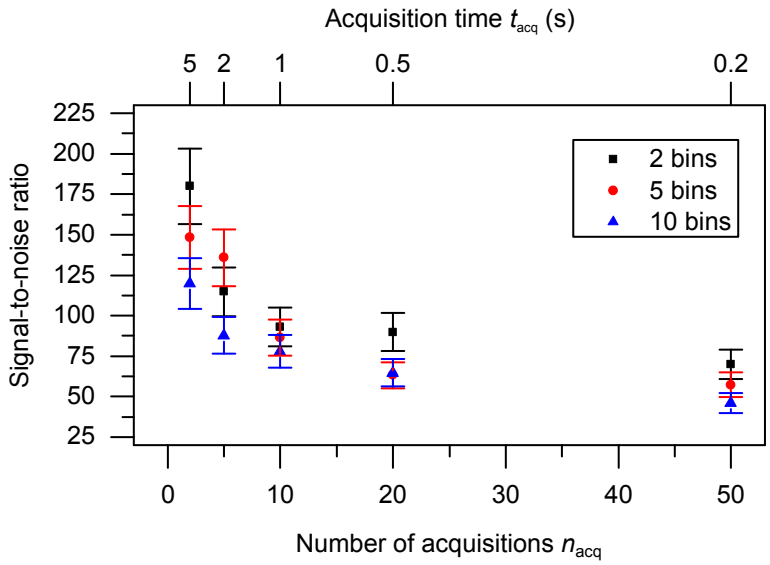

Figure 6.12.: Signal-to-noise ratios of measurements with a total acquisition time of 10 s.

Based on above considerations, the following settings can be recommended for high-sensitivity measurements limited to a maximum total acquisition time of $t_{\mathrm{acq,tot}}$:

- As cosmic ray removal requires at least two averages, the acquisition time for a single acquisition should be chosen as $t_{\mathrm{acq}} = 0.5 \cdot t_{\mathrm{acq,tot}}$.
- The number of bins used should be limited to the smallest possible value, i.e. five bins to allow for astigmatism correction.

It should be noted that using long acquisition times increases the risk of detector saturation. In this case, either the number of bins has to be increased or the number of single acquisitions (with t_{acq} accordingly decreased in the latter case). A comparison between these two alternatives is shown in table 6.6. The data prove that both are comparable with respect to sensitivity.

6.8. Summary

In this chapter, a number of approaches were investigated to minimize the influence of fluorescence contributions in the hollow waveguide based Raman system while maintaining high Raman signals. The overall goal was to decrease fluorescence-related noise as far as possible in order to fully profit from the signal-enhancing effect of the hollow waveguide technique, thus enabling a considerable sensitivity increase by about two orders of magnitude compared to the standard LARA system.

For this purpose, modifications of the system setup in the form of rearrangement and replacement of fluorescent optical components were suggested and tested experimentally. By replacing the standard beam splitter by a tritium compatible, full-metal mirror-with-hole and rearranging the windows and other optics at both waveguide ends in such a way

Table 6.6.: Comparison between the influence of more bins and more acquisitions on the signal-to-noise ratio. n_{bin} and n_{acq} were multiplied by the same factor in comparison to the original measurement settings to compare the resulting SNR. Note that t_{acq} has to be decreased by the same factor when changing n_{acq} to keep the total acquisition time $t_{\mathrm{acq,tot}} = n_{\mathrm{acq}} \cdot t_{\mathrm{acq}} = 4\,\mathrm{s}$ constant.

	n_{bin}	$n_{\mathrm{acq}} \cdot t_{\mathrm{acq}}$ (s)	SNR
Original measurement	5	2 · 2	148 ± 19
n_{bin} x 2	10	2 · 2	62 ± 8
n_{acq} x 2, t_{acq} / 2	5	4 · 1	63 ± 8
n_{bin} x 5	25	2 · 2	40 ± 5
n_{acq} x 5, t_{acq} / 5	5	10 · 0.4	40 ± 5

that produced fluorescence was no longer as efficiently collected as before, the noise related to these components could be decreased practically to the level of a (fluorescence-free) dark measurement, while no or only marginal Raman signal losses were suffered. The rearrangement of the front window configuration alone – which originally was responsible for a particularly large fraction of the total fluorescence background –, led already to an improvement of the signal-to-noise ratio by about one order of magnitude.

In case of the waveguide itself, fluorescence reduction was achieved by utilizing a larger-diameter, full-metal waveguide instead of the former glass-based one. Although this alteration was connected to some loss in the collected Raman signal, the latter proved to be more than compensated for by the lower noise, so that a sensitivity increase by about a factor of 3 could still be achieved. In addition, the new, full-metal waveguide has further advantages like being tritium compatible and less susceptible to mechanical and laser damage than the previous glass-based one.

After suitable components and arrangements for a fluorescence-minimized hollow waveguide based Raman setup had been identified, the diameter and length of the waveguide, the scattering geometry as well as acquisition settings were optimized in further studies in order to be able to obtain highest possible signal-to-noise ratios.

All investigations and optimizations described in this chapter were based on theoretical considerations and/or rigorously defined comparison measurements. The next step is thus to evaluate the performance of the complete new Raman system, with all fluorescence-reducing measures and further optimizations implemented. This is the topic of the following chapter.

7. Results: Performance of the optimized setup

In the previous chapters, a range of systematic studies were presented concerning tritium compatibility and suitability of a hollow waveguide based Raman system for operation in glove box environments, as well as fluorescence minimization in order to achieve highest sensitivities. Based on the results gained from these investigations, an optimized Raman system was set up and tested within the scope of this work. This chapter presents the detection limits achieved with the new system and discusses its performance with respect to the intended application within the framework of the KATRIN experiment.

First, a summary of the features of the new system design is given is section 7.1. Afterwards, the measurement setup and settings of the performance test as well as specifics of the data analysis are treated in section 7.2. Section 7.3 contains the results obtained with the new setup. Finally, the results are discussed and assessed with respect to KATRIN in section 7.4.

7.1. Summary of the new system design

The complete new design of the hollow waveguide based Raman system resulting from the investigations presented in the previous chapters is shown in figure 7.1 in comparison to the original prototype setup. The new optical setup comprises

- a fiber-delivered laser beam for improved system usability in glove boxes,
- a tritium compatible, full-metal mirror-with-hole instead of a glass-based beam splitter to separate laser and Raman light without fluorescence generation,
- fluorescence-minimizing window configurations at the waveguide front and rear end,
- single-pass configuration for facilitated alignment without loss of sensitivity,
- a full-metal, large-diameter waveguide lined with gold for reduced fluorescence, tritium compatibility, low susceptibility to mechanical and laser damage, good alignment stability and improved gas flow.

Results achieved with this new, improved setup are presented and discussed with respect to the KATRIN requirements in the following.

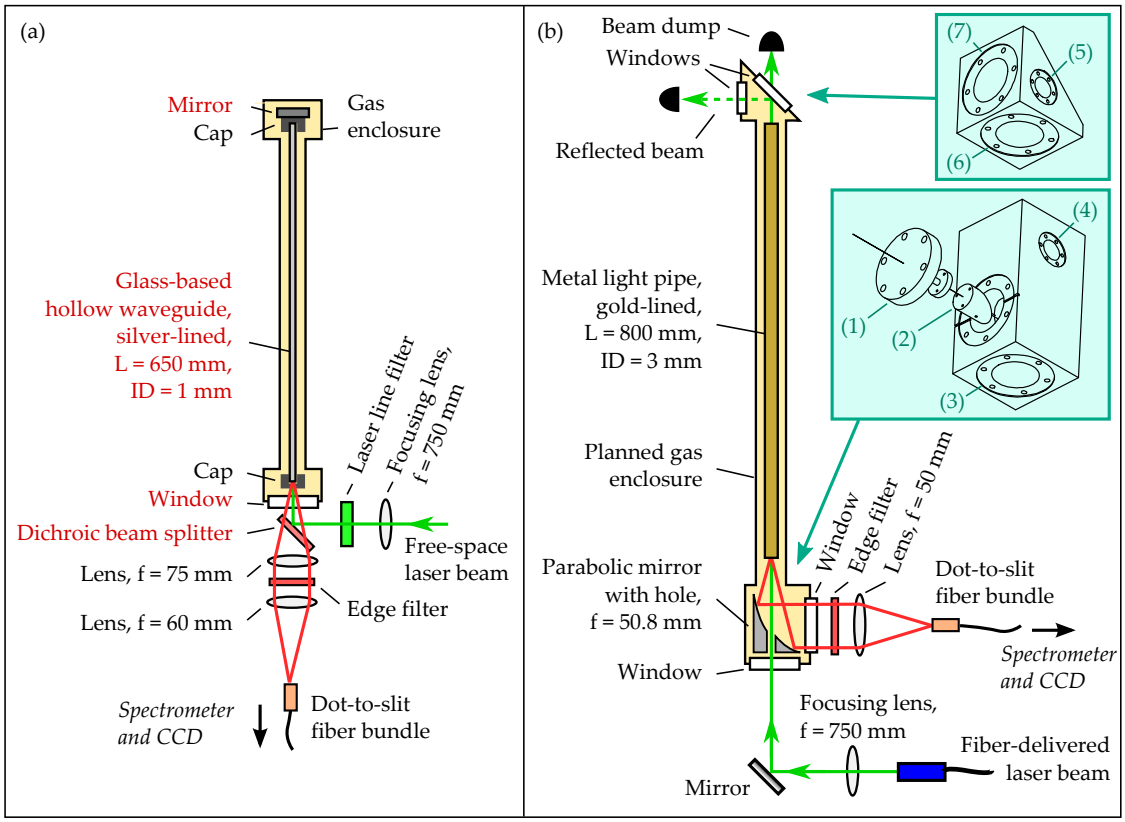

Figure 7.1.: Schematic sketch of the optical setup of *(a)* the prototype and *(b)* the optimized hollow waveguide based Raman system (not to scale). The components annotated in red are the ones responsible for the high fluorescence background in the prototype setup. The gas inlets and outlets located on top of the gas enclosure are not shown in the top view for reasons of clearness; note that the prototype system only has one gas inlet above the front cap, while the final system is designed for continuous inline measurements with a gas inlet over the mirror-with-hole and an outlet at the other end of the waveguide. In the upper right corner, CAD drawings of the gas inlet block housing the mirror-with-hole *(bottom, exploded view)* and the gas outlet block at the rear end of the waveguide *(top)* are shown with the following annotations: (1) Mirror-with-hole mount. The mirror-with-hole (2) is screwed to the extrusion on the right side of the mount. The left side of the mount is a CF flange which can be attached in a leak-tight way to the block. (3) CF socket for laser window. The windows are integrated in CF flanges by diffusion-bonding. (4), (5) CF sockets for gas inlet and outlet. (6) CF socket for hollow waveguide. The waveguide is integrated into a CF-flange, where it is fixed in place and made leak-tight by electrowelding the nickel substrate to the flange material. (7) CF socket for rear end window. Note that all optics including the mirror-with-hole have a diameter of 1” = 25.4 mm in the final setup due to space restrictions.

7.2. Performance test

Setup and settings:

The performance of the new hollow waveguide based Raman system was tested using the principal optical setup shown in figure 7.1 (b). However, free-space instead of fiber-coupled laser beam delivery was used since an appropriate fiber coupler was not yet available at the time of measurement. A 'gem 532' laser (532 nm, cw) from Laser Quantum was utilized, providing a similar M^2 value (1.1) and a similar beam diameter as the fiber collimator (0.9 mm ± 0.2 mm in a distance of 25 cm behind the laser output) [Las16]. The laser power was 1.5 W.

Raman spectra of air were acquired with $n_{\mathrm{acq}} = 2$ and $n_{\mathrm{bin}} = 5$, according to the considerations of subsection 6.7.3. Two different acquisition times of $t_{\mathrm{acq}} = 10\,\mathrm{s}$ and 29.5 s were chosen to provide a comparison to the standard LARA system measurements reported in [Sch13b] (2x 10 s), and to assess the system performance at a total measurement period of about 1 minute (2x 29.5 s plus up to 1 s for automated data processing, cf. [Fis14]).

Data analysis:

(i) Peak height and area approach: For the final system performance test, the data were analyzed in two different ways. The first method is the one used for all data analyses in this work so far, which is described in subsection 4.2.2. In this method, the height of the Raman peak of interest is used as a measure for the Raman signal, and the noise is given by the standard deviation of a flat part of the spectrum; this method was used in the comparison measurements for reasons of simplicity and is applied here as well to maintain comparability to the measurement reported in [Sch13b]. For KATRIN gas analysis applications, however, it is recommended to use the peak area instead of the height as a measure for the Raman signal due to better precision and accuracy properties [Sch09]. For this reason, this alternative analysis method was utilized in parallel, in order to gauge the detection limit in this performance test.

Both analysis methods are illustrated in figure 7.2. In the peak area based method, the related noise – i.e. the standard deviation of the blank measures, cf. subsection 3.2.1 – has to be determined differently than in the peak height method, by estimating the fluctuation of the total background intensity summed up over the pixel range used for the peak area determination. For this purpose, a Gaussian distributed random intensity with mean value $\mu = 0$ and standard deviation σ, which is determined as previously from a flat part of the spectrum, is simulated for each pixel in the range of the peak area determination. The intensities simulated for all pixels are subsequently added up. The noise in the peak area is obtained by simulating the full process very often and calculating the standard deviation of the obtained results; one million simulations were used in this work in order to obtain a good estimate of the noise. All analysis settings used in both methods are listed in appendix F.4.

(ii) Analyzed peak: Due to the long measurement times, detector saturation occurred for the Q_1 branch of N_2, which had been used for previous analyses. Therefore, the less intense peak corresponding to the Q_2 branch (vibrational overtone) of nitrogen was used

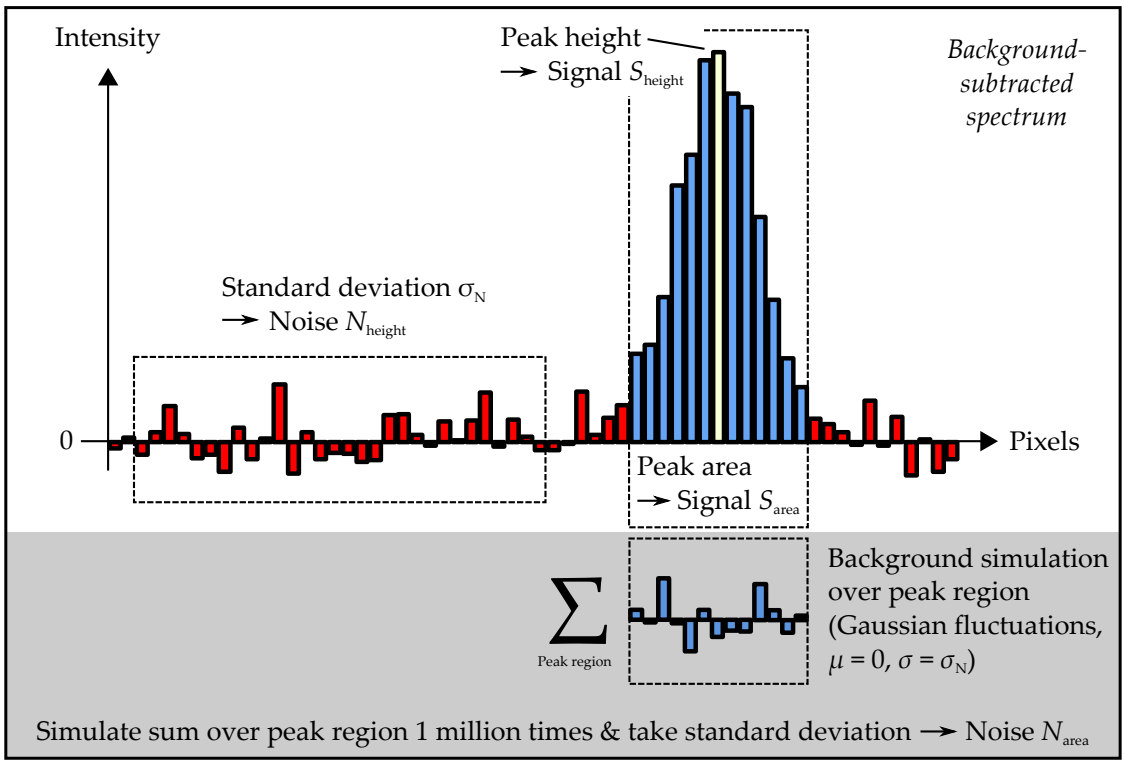

Figure 7.2.: Determination of signal and noise in the peak height and the peak area approach.

to determine the signal of each measurement. A spectrum comprising both peaks is shown in figure 7.3. As the use of the low-intensity Q_2 branch leads to lower signal-to-noise ratios for nitrogen than those actually achievable with the system, the inherent detection limit should still be calculated based on the Q_1 rather than the Q_2 branch to enable proper evaluation of the system performance. For this reason, the ratio R between the signals obtained from the Q_2 and Q_1 branches of nitrogen was determined both for the height and the area approach from 32 unsaturated spectra acquired independently at a range of different acquisition settings, yielding the following results:

$$R_{\text{height}} = \frac{S_{\text{height}}(\text{N}_2\ \text{Q}_2)}{S_{\text{height}}(\text{N}_2\ \text{Q}_1)} = (0.077 \pm 0.002)\,\%, \tag{7.1}$$

$$R_{\text{area}} = \frac{S_{\text{area}}(\text{N}_2\ \text{Q}_2)}{S_{\text{area}}(\text{N}_2\ \text{Q}_1)} = (0.091 \pm 0.003)\,\%. \tag{7.2}$$

Based on these ratios and the nitrogen partial pressure of $p_{\text{N}_2} = 790.97 \pm 0.12\,\text{mbar}$[1], an effective partial pressure could be assigned to the nitrogen Q_2 peak:

$$p_{\text{N}_2,\text{eff,height}} = R_{\text{height}} \cdot p_{\text{N}_2} = 0.62 \pm 0.02\,\text{mbar}, \tag{7.3}$$

$$p_{\text{N}_2,\text{eff,area}} = R_{\text{area}} \cdot p_{\text{N}_2} = 0.72 \pm 0.02\,\text{mbar}. \tag{7.4}$$

[1]This value assumes a total atmospheric pressure of 1013 mbar and a nitrogen fraction of 0.78082 ± 0.00012 [Kay12].

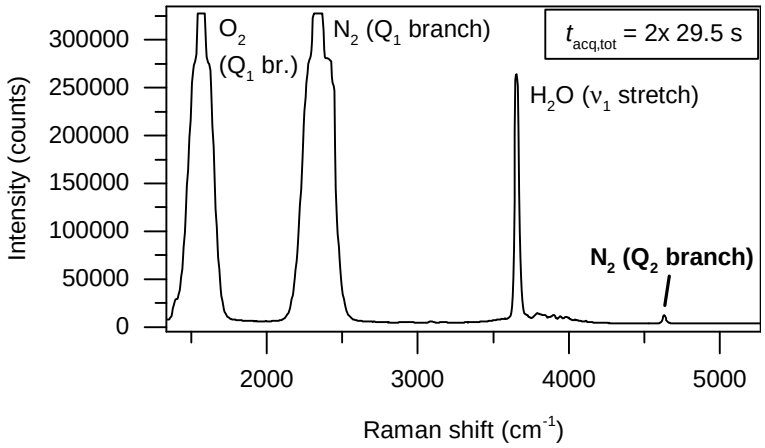

Figure 7.3.: Spectrum acquired using the optimized hollow waveguide based Raman system. The high Raman intensities of the Q_1 branches of oxygen and nitrogen at long acquisition times lead to detector saturation, which manifests itself in the plateaus at the top of the corresponding Raman peaks. The observed 'shoulders' correspond to the unresolved S_1 and O_1 branches.

The effective partial pressure corresponds to that partial pressure of nitrogen which would yield a Q_1 branch signal of the same value as the signal obtained at atmospheric pressure from the Q_2 branch. Thus, it was used to determine the detection limit according to equation 3.32. Note that the calculated values for $p_{N_2,\mathrm{eff}}$ are of a similar order of magnitude as the ones projected for Raman measurement after the KATRIN WGTS.

7.3. Results

The results obtained with the optimized hollow waveguide based Raman system are listed in tables 7.1 and 7.2. In the first table, signal and noise extracted from the acquired spectra as well as the resulting signal-to-noise ratio are listed. The data reveal that the minute fluorescence remaining after implementation of the fluorescence-reducing measures described in the previous chapter still leads to a noise of several counts above dark level due to the long acquisition times and few averages used. Regardless, the noise level is now of the same order as the one encountered in measurements with the standard LARA system – e.g. $N = 13$ counts in the 2x 10 s measurement at 5 W laser power reported in [Sch13b] – and thus significantly improved compared to the high-background prototype system.

In addition, the data demonstrate that the area approach for signal extraction leads to signals increased by a factor of 7.3 – 7.5 compared to the peak height approach, while the noise only rises by a factor of 3.8. For this reason, the overall signal-to-noise ratio profits from an improvement by a factor of about 2.

Based on the data of table 7.1 and the effective partial pressures calculated above, the detection limit for nitrogen at a laser power of 1.5 W could be determined according to equation 3.32. This is shown in the first LOD column of table 7.2. The second LOD

Table 7.1.: Signal, noise and signal-to-noise ratio obtained with the optimized hollow waveguide based Raman system. The results achieved for the two different acquisition times used and both signal extraction methods (peak height vs. peak area) are shown. The last column lists the purely detector-related noise, N_{D}, which was obtained from dark spectra acquired and analyzed with the same settings as used for the Raman spectra.

	$t_{\mathrm{acq,tot}}$ (s)	S (10^2 counts)	N (counts)	SNR (10^1)	N_{D} (counts)
Height	20 (2 x 10)	30 ± 1	11 ± 1	29 ± 4	8 ± 1
	59 (2 x 29.5)	87 ± 1	21 ± 3	42 ± 5	8 ± 1
Area	20 (2 x 10)	224 ± 3	39 ± 11	57 ± 15	29 ± 8
	59 (2 x 29.5)	642 ± 7	78 ± 21	82 ± 22	32 ± 8

Table 7.2.: Nitrogen and tritium detection limits obtained with the optimized hollow waveguide based Raman system. The specified laser power values refer to the power at the position of the Raman measurement system. The tritium detection limits were calculated from the nitrogen ones using the ratio of their Raman scattering cross sections, $\sigma_{\mathrm{T_2}}/\sigma_{\mathrm{N_2}}$. The $\mathrm{LOD_{sc}}$ values are scaled to a higher laser power. See main text for details.

	$t_{\mathrm{acq,tot}}$ (s)	LOD N_2 (10^{-3} mbar), $P_{\mathrm{Laser}} = 1.5\,\mathrm{W}$	LOD T_2 (10^{-3} mbar), $P_{\mathrm{Laser}} = 1.5\,\mathrm{W}$	$\mathrm{LOD_{sc}}$ N_2 (10^{-3} mbar), $P_{\mathrm{Laser}} = 4\,\mathrm{W}$	$\mathrm{LOD_{sc}}$ T_2 (10^{-3} mbar), $P_{\mathrm{Laser}} = 4\,\mathrm{W}$
Height	20 (2 x 10)	6.4 ± 0.9	2.5 ± 0.4	3.2 ± 0.5	1.2 ± 0.2
	59 (2 x 29.5)	4.3 ± 0.6	1.7 ± 0.2	2.5 ± 0.4	1.0 ± 0.2
Area	20 (2 x 10)	3.8 ± 1.0	1.5 ± 0.4	1.9 ± 0.6	0.7 ± 0.2
	59 (2 x 29.5)	2.6 ± 0.7	1.0 ± 0.3	1.5 ± 0.4	0.6 ± 0.2

column lists the corresponding detection limits for tritium instead of nitrogen, taking into account the different Raman scattering cross sections for nitrogen and tritium[2]. In the last two columns (LOD_{sc}), the values for nitrogen and tritium are scaled to a higher laser power of 4 W in order to estimate the detection limit which can be expected in the actual Raman measurements for KATRIN. In these measurements, a 5 W laser (as used in the standard LARA system) will be employed. Fiber coupling of the laser beam leads to a power of about 4 W at the measurement position in the glove box due to the coupling efficiency of about 80 % (cf. section 5.2). The equations used for scaling can be found in appendix D.1.

7.4. Discussion of the results and assessment with respect to KATRIN

The results presented in table 7.2 show that the sensitivity goal of this work, a tritium detection limit of the order of 10^{-3} mbar within total acquisition times of a minute or less, is achievable with the optimized hollow waveguide based Raman system presented here. A low detection limit of about $1.5 \cdot 10^{-3}$ mbar is reached already at a reduced laser power of 1.5 W and a short total acquisition time of 20 s with the area approach. By using the full design laser power of 4 W at the measurement system and measuring for up to one minute, even detection limits in the 10^{-4} mbar range start to come into reach.

These results can be compared to measurements with the standard LARA setup performed by M. Schlösser in his PhD thesis [Sch13b].[3] In these measurements, the same spectrometer (SP2150i, PI Acton) and the same total acquisition time of 2x 10 s was used. Raman spectra of a gas mixture of H_2, HD and D_2 (about 25 % : 50 % : 25 %) were acquired at a laser power of 5 W. Using the peak height approach, a detection limit of $LOD_{H_2-HD-D_2} = 6.8 \cdot 10^{-2}$ mbar for the inactive hydrogen isotopologues was obtained, corresponding to an approximate tritium detection limit of $LOD_{T_2} = 8.4 \cdot 10^{-2}$ mbar (cf. appendix G). Comparing this to the high-power tritium detection limit obtained with the hollow waveguide based Raman system in 2x 10 s yields a sensitivity improvement by a factor of about 70, i.e. almost two orders of magnitude.

When using a longer total acquisition time of 2x 29.5 s, which is still sufficient to fulfill the KATRIN requirements, the limit of detection improves by a factor of 88 compared to the reported standard LARA measurement. Based on pressure values of 150 – 200 mbar at the position of the LARA system in the KATRIN Inner Loop, a comparable measurement performance can thus be reached with the new hollow waveguide based Raman system at 88 times lower total pressures of 1.7 – 2.3 mbar. This corresponds well to the expected pressure after the WGTS second pumping stage, which is estimated to lie in the single-digit

[2] The ratio between the cross-sections for the different hydrogen isotopologues and nitrogen can be found in appendix G.

[3] It should be noted that more recent results of the LARA system performance are reported in [Fis14]. However, these data are not directly comparable to the ones obtained within this work, as a different spectrometer with higher light throughput was used. In addition, a too optimistic estimation of the detection limit is given there due to a mistake in the data analysis: the signal is evaluated via the peak area approach, while the standard deviation of a flat part of the spectrum is used as in the peak height approach, leading to a LOD value overestimated by about one order of magnitude.

millibar range. For this reason, the new, hollow waveguide based Raman system makes it possible for the first time to monitor the source gas composition after the WGTS, in addition to the LARA measurement before injection.

The improved detection limit also allows one to detect trace impurities down to the permille level. The ratio of the Raman cross sections for many gases to the nitrogen cross section is typically in the range of 0.5 to 8 [Dan81], so that detection limits of impurities can be expected to range between about $2 \cdot 10^{-4}$ and $3 \cdot 10^{-3}$ mbar at a total acquisition time of 2x 29.5 s and full laser power. It should be noted that a quantification limit (LOQ) can be defined analogous to the detection limit, with a higher confidence level represented by a recommended value of $k = 10$ [Mac80] in equation 3.29:

$$\mathrm{LOQ} = \frac{10p}{\mathrm{SNR}} = \frac{10}{3} \cdot \mathrm{LOD} \ . \tag{7.5}$$

Based on this equation, it can be concluded that trace impurities with partial pressures of about $7 \cdot 10^{-4}$ to $1 \cdot 10^{-2}$ mbar can not only be detected by the new Raman system within a minute, but even quantified. Information about impurity formation is of high interest with respect to a comprehensive understanding of processes in the Inner Loop which affect the gas composition. As the standard LARA system is located in close proximity to the gas-purifying permeator, such information can be gained only by the new Raman system at a measurement position further down the line in the Inner Loop.

In summary, highly sensitive, Raman spectroscopic measurements of the composition of tritiated gases at low pressures have been made possible by the investigations described in the previous chapters, namely the development of a tritium compatible hollow waveguide based Raman system for very high signals combined with the successful implementation of fluorescence-reducing measures for minimized background noise. The sensitivity of the new measurement system exceeds the predecessor system by almost two orders of magnitude, thus enabling important measurements within the framework of the KATRIN experiment which were formerly out of reach. These measurements will contribute significantly to our understanding of processes in the Inner Loop and consequently of the gas composition inside the actual source tube, so that a reliable estimation of the uncertainties connected to source systematics is rendered possible.

8. Summary and outlook

Summary: This work focused on the development of a highly sensitive Raman spectroscopic system for compositional analyses of the KATRIN tritium source gas. The KATRIN experiment aims to measure the neutrino mass with an unprecedented sensitivity of 200 meV/c^2 (90 % C.L.), improving the current upper limit by one order of magnitude. Thus, KATRIN will contribute significantly to the advance of such fundamental research topics as the origin of neutrino masses and structure formation in the universe.

In order for KATRIN to reach its challenging design sensitivity, it is vital that systematic uncertainties are minimized throughout the experiment. Due to the various systematic effects connected to the tritium source, a range of parameters of the WGTS have to be stabilized and/or monitored on the 0.1 % level. An important source parameter influencing the measured β-spectrum is the isotopic composition of the gas, which is therefore continuously monitored by Raman spectroscopy. A dedicated Raman spectroscopic system (LARA) has been developed over the last years in cooperation between the Karlsruhe Institute of Technology and Swansea University, and been demonstrated to fulfill the KATRIN requirements.

However, it is not possible to measure the isotopic composition directly in the source tube due to technical and experimental constraints. As the source composition can change between the position of measurement and the source tube due to a range of effects like wall interactions and separation phenomena, an additional composition measurement after the WGTS is envisaged to gain a quantitative understanding of compositional changes. This understanding is indispensable in order for KATRIN to produce a neutrino mass measurement result with reliable uncertainties. As the sensitivity of the existing Raman system is not sufficient for measurements at the low gas pressures after the WGTS, the additional composition measurement requires a new, highly sensitive Raman system. The development of such a system was the main goal of this thesis, with a focus on achieving a sufficiently high sensitivity, i.e. tritium detection limits of the order of 10^{-3} mbar within acquisition times of a minute or less, in a system which is tritium compatible and suitable for the use in glove box environments.

For this reason, a range of possible methods to enhance the sensitivity of Raman spectroscopic systems were considered within the scope of this work. Hollow waveguide based Raman spectroscopy was identified as the most promising candidate for low-pressure gas applications under the KATRIN frame conditions. In this method, signal enhancements by about two orders of magnitude are achieved by using a hollow waveguide with a reflective inner surface as the Raman gas cell, through which the laser beam passes longitudinally. By this means, the Raman interaction region is greatly increased compared to conventional Raman gas cell designs: the laser beam can interact with gas molecules over the full

length of the waveguide, with the waveguide guiding the Raman scattered light towards the exit, so that light generated over the entire waveguide length can be collected.

Existing hollow waveguide based Raman systems described in the literature have the drawback of being generally not tritium compatible on the one hand, and either not sensitive enough for the task at hand or not providing sufficient gas throughput due to extremely small waveguide diameters on the other hand. For this reason, a hollow waveguide based prototype system for the use with tritiated gas was set up within the framework of this study to test the principle of this measurement method with respect to the envisaged application at KATRIN. Based on the experiences gained during construction, commissioning and tritium operation of the prototype system, necessary steps towards a fully tritium compatible and highly sensitive Raman system were identified and subsequently taken in the further course of this work.

First of all, tritium-induced damage of optical components encountered in the prototype system stressed the importance of preventing degradation of optical surfaces under tritium exposure, so that reliable long-term operation for KATRIN can be guaranteed. In order to be able to ensure stable optical properties of components inside the tritium gas system, a dedicated test experiment to examine the durability of a range of reflecting optical surfaces under tritium exposure was conducted. The investigation revealed that silver-lined waveguides, as commonly applied for light in the visible range, are not suited for long-term use in a system for tritium gas analysis due to degrading reflection properties. Alternative materials suitable for this task could be identified in the scope of the same test. Based on the obtained results, a gold-lined waveguide is recommended for use in a hollow waveguide based Raman system for tritium gas analysis. Also, it could be shown that silver mirrors protected by an SiO_2 layer (which cannot be applied to the inside of a waveguide, though) are resistant against tritium-induced damage, offering the opportunity to place such a mirror in the gas system.

Taking into account these results, a new optical design of the hollow waveguide based Raman system was investigated which deviates in several respects from systems described in the literature. The main focus of these investigations was to minimize the fluorescence background in order to limit the related shot noise contributions to a minimum, thus enabling a high signal-to-noise ratio and consequently a high sensitivity to be reached. A range of approaches based on rearrangement and replacement of fluorescent optical components was tested and evaluated with respect to the signal-to-noise ratio achieved in each scenario, namely (i) replacement of the standard dichroic beam splitter for separation of laser and Raman light by a mirror-with-hole solution, (ii) rearrangement of the optical configuration of windows and mirrors at both ends of the waveguide, and (iii) replacement of the standard (i.e. glass-based, silver-lined and small-diameter) waveguide by a full-metal waveguide lined with gold and with an inner diameter of few millimeters. By implementing these measures, the fluorescence background could be successfully reduced down to a minimum value close to the level achieved in the low-fluorescence standard LARA system.

In addition, a range of further optimizations were investigated in order to achieve highest sensitivities and guarantee proper usability of the final system inside of a glove box for tritium operation. On the one hand, the length and diameter of the waveguide were optimized with respect to both low noise and a high signal, the use of a back-reflecting

mirror at the waveguide end was examined, and the optimal acquisition settings for high sensitivities were determined. On the other hand, fiber-based laser delivery to the hollow waveguide based Raman system inside a glove box was proposed, offering flexibility in the glove box as well as uncomplicated laser maintainability, while greatly facilitating the optical alignment compared to free-space laser delivery. Suitable components and configurations for reliable and safe laser delivery were identified, and a custom fiber feedthrough solution tailored to the special requirements of tritium glove boxes was introduced.

Based on the various investigations summarized above, a hollow waveguide based Raman system optimized for the use with tritium and high sensitivities could be set up and tested. With this new system, the sensitivity goal given by a tritium detection limit of the order of 10^{-3} mbar within total acquisition times of a minute or less was reached already at a comparatively low laser power of 1.5 W, and can even be expected to be exceeded when using higher powers. The new system surpasses the sensitivity of the standard Raman system by almost two orders of magnitude, making it possible for the first time to monitor the source gas composition after the WGTS, in principle. In addition, impurities previously unaccounted for can now be detected, down to trace impurities on the permille level. The results of this work thus enable important measurements in the framework of the KATRIN experiment, which will contribute significantly to our understanding of processes in the Inner Loop and consequently the gas composition inside the actual source tube. By this means, a reliable estimation of the uncertainties connected to source systematics will be rendered possible, allowing KATRIN to produce a final neutrino mass result with accurate uncertainties.

Next steps: This work was primarily focused on the optical design of the new, highly sensitive Raman system for tritium gas analysis. In order to reach full operational readiness of the system, the following tasks still have to be completed:

- The system has to be equipped with a high-power and high-stability laser, as used in the current LARA system. The performance under dynamic gas circulation conditions should then be tested in a closed gas loop without tritium, before integrating it in the actual KATRIN Inner Loop.

- In order to properly quantify the measured gas composition, it is necessary to calibrate the system. The calibration standard used for intensity calibration in the LARA system [Sch13b, Sch15c] cannot be applied to the hollow waveguide based Raman system due to the different system geometry and setup. Instead, calibration can be achieved by measuring tritiated gas mixtures of precisely known composition. A gas mixing loop to provide these gas mixtures, the so-called TriHYDE loop, is currently under construction at TLK and will be commissioned this year.[1]

- In order to be able to interpret the combined composition data acquired with the LARA system and the hollow waveguide based Raman system correctly, gas dynamical simulations for the gas loop between both systems are required.

[1] S. Niemes, PhD thesis in preparation, Karlsruhe Institute of Technology, 2016.

Outlook: In addition to the primarily intended use for a second compositional measurement after the WGTS, there are a range of further possible application scenarios for the new, high-sensitivity Raman system:

- **Measurement of the rotational temperature of tritium at 30 K:** It is currently not known how well the rotational state distribution of the source gas thermalizes between the pressure controlled buffer vessel at 300 K and the WGTS tube at 30 K. Since transitions between ortho and para states of tritium are strongly suppressed due to the required nuclear spin flip, the rotational state distribution might not fully thermalize while the gas is transported through the 5 m long injection capillary into the WGTS. If not taken into account in the KATRIN analysis, such incomplete thermalization would be a source of uncertainty with respect to the final state distribution, translating into a shift in the neutrino mass squared e.g. of the order of $1 \cdot 10^{-3}\,\mathrm{eV}^2/c^4$ if the effective rotational temperature is 10 % higher than the assumed 30 K [Bod15]. In order to tackle this issue, the rotational temperature of tritium after being cooled down from 300 to 30 K in a straight tube could in principle be measured by a Raman system using a high-resolution spectrometer. While the standard LARA cell is not designed for operation at 30 K, the use of a full-metal waveguide (with relatively high thermal conductivity) as the Raman cell in the new system could offer the opportunity to construct a cryogenic Raman measurement system.
- **Measurement of the ortho-para ratio after the WGTS:** With respect to the ortho-para ratio of the source gas, it is expected that the ratio in the source is close to the high-temperature equilibrium of 3:1 due to the short time the gas molecules spend in the cooled sections of the Inner Loop [Bod15]. According to simulations, realistic ortho-para transitions will thus only lead to a shift of $0.44 \cdot 10^{-3}\,\mathrm{eV}^2/c^4$ in the neutrino mass squared [Bod15]. Nevertheless, further studies of the ortho-para ratio can be worthwhile to test existing models and potentially get a better estimate on the related uncertainty. Although the new Raman system will not be able to measure the ortho-para ratio in the source itself either, due to its position after the WGTS turbo-molecular pumps, a measurement of the ortho-para ratio at that position can still provide experimental input to probe our understanding of the ortho-para evolution in the Inner Loop.
- **Optimization of Inner Loop / permeator operation settings:** A certain fraction of the gas stream pumped off from the WGTS is diverted from the Inner Loop at the permeator in order to remove impurities generated in the Loop (cf. figure 2.5). This fraction has to be chosen large enough that all impurities accumulating at the permeator are removed; otherwise, these non-permeable impurities will clog the permeator in the long run. As the rate of impurity formation is currently unknown, the fraction of gas to be diverted has to be estimated with a certain safety margin. By measuring the amount of generated impurities with the hollow waveguide based Raman system, it will be possible in the future to chose the gas stream appropriately based on measured data instead of estimations. This eliminates the need for a safety margin and makes the operation of the Loop system more efficient.
- **Detection of helium in tritiated gases by using β-radioluminescence:** While Raman spectroscopy in general is not able to detect monoatomic species like

helium, it is possible to utilize a Raman measurement system for helium detection in case of tritium-helium gas mixtures: helium atoms excited electronically by tritium β-decay electrons can de-excite under emission of luminescence light, which can be detected together with Raman light in a Raman spectroscopic system. This concept was successfully tested with the standard LARA system [Sch15a]. However, long acquisition times in the range of 1000 s had to be used to obtain reasonably high helium signals, as only a very small fraction of the total luminescence light produced in the cell was emitted within the region covered by the collection optics. By using a hollow waveguide based Raman system instead, significantly higher signals can be expected as β-luminescence light produced anywhere in the waveguide is confined and guided towards the waveguide exit, allowing for simultaneous detection of hydrogen isotopologues and helium. This technique could be utilized for instance to determine the amount of ^{3}He accumulating in the KATRIN feed gas during tritium storage. Another possible (non-KATRIN) application is tritium accountancy in the breeder blankets of future fusion reactors [Bor13], as the tritium-to-helium ratio of the ^{4}He gas purging the blankets could be determined by this technique.

- **Process monitoring and control:** Owing to the high sensitivity of the new Raman system, it also allows for next-to-real-time gas analysis of tritiated (and other) gases in process applications, where total gas pressures are typically higher than the ones considered in this work. A tritium detection limit better than $1 \cdot 10^{-1}$ mbar in only 2x 0.1 s total acquisition time was reached already at a relatively low laser power of 1 W using the peak approach, making the hollow waveguide based Raman system suitable for process monitoring and control applications where short feedback times are required.
- **High-sensitivity composition measurements for future β-decay experiments:** Finally, the high-sensitivity, tritium compatible Raman system developed in this work could replace the current LARA implementation in future β-decay experiments where higher-sensitivity monitoring systems might be required, for instance within the scope of new challenges like the search for sterile neutrinos.

Appendix

A. Setup of the standard LARA system for KATRIN

The optical setup of the standard LARA system is sketched in figure A.1. Note that multiple LARA systems with a comparable setup have been in use for tritium analytics at the Tritium Laboratory Karlsruhe. The following description focuses on the so-called LARA3 system, which will be employed in the KATRIN experiment. The contents of this appendix are based on [Fis14].

The standard LARA system uses a 90° collection geometry: the laser beam is focused into the LARA cell containing the sample gas. The Raman scattered light leaves the cell at an 90° angle to the beam direction and is subsequently collected and detected. A double-pass configuration is used, i.e. the laser beam is back-reflected through the cell by a mirror (mirror M3 in figure A.1) for doubled laser power in the cell. In the following, details about the purpose and characteristics of the main components are given.

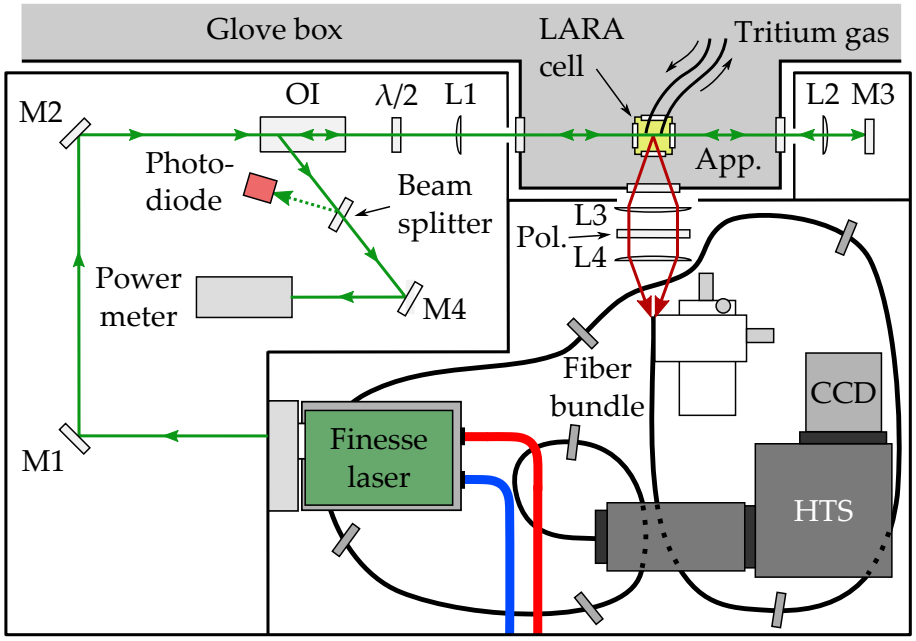

Figure A.1.: Setup of the standard LARA system for KATRIN. All components are mounted on an optical breadboard. In operation mode, the whole system is surrounded by a light tight enclosure. Abbreviations: Mi – laser mirror i, OI – optical isolator, $\lambda/2$ – half-wave plate, Li – plano-convex lens i, App. – Appendix, Pol. – linear sheet polarizer, HTS – HTS spectrometer, CCD – Pixis CCD detector. Figure adapted from [Fis14].

Laser: A Finesse laser from Laser Quantum is employed. It is a diode-pumped solid state (DPSS) Nd:YVO_4 laser, which operates in continuous wave (cw) mode with an output wavelength of 532 nm. It provides a maximum power of 5 W and horizontal output polarization. The laser is cooled with a water chiller.

Mirrors: The laser mirrors (Thorlabs, NB1-K12) have a dielectric coating which offers a high reflectance of $> 99.5\,\%$ for s-polarized light [Tho16].

Optical isolator, half-wave plate and power meter: The optical isolator (Thorlabs, IO-5-532-HP) provides a clean linear polarization of the laser beam. The initially horizontal polarization is subsequently rotated by a half-wave plate to vertical polarization in order to maximize the intensity of the Raman scattered light detected in the 90° collection geometry. In addition, the optical isolator has the task to prevent the back-reflected laser beam from re-entering the laser head, which would cause laser instabilities and might lead to permanent damage of the laser. The back-reflected beam is deflected from the initial beam path by the optical isolator and absorbed in a thermopile power meter (Coherent, LM-10), which measures the intensity and position of the beam.

Focusing lens: The plano-convex lenses L1 and L2 focus the laser beam into the center of the sample cell with a focal length of 250 mm. The lenses have an anti-reflection coating which minimize intensity losses due to reflection to $< 0.5\,\%$ [Tho14a].

Raman cell: The Raman sample cell (LARA cell) contains the gas sample which is to be analyzed. It consists of a hollow cubic body made from stainless steel, which is equipped with view ports at its side surfaces to allow the laser and Raman light to enter or leave the cell. The view ports consist of anti-reflection coated fused silica windows which are diffusion bonded into CF16-flanges to achieve a leak-tight connection to the cell body. Valve-bearing inlets at the top of the cell allow for either flowing or static gas samples. The cell is fully tritium compatible and located inside a separate compartment attached to a glove box, the so-called appendix. By this means, only the tritium-bearing parts of the system are located in a glove box, while the rest of the optical system is not exposed to radioactivity and can easily be accessed.

Safety equipment: For safety reasons, a shutter is inserted behind the laser, which is closed if the top cover of the system is opened or if the beam diverges from its reference path. To check for beam displacements or component failure, a small fraction of the back-reflected and deflected laser beam is coupled out by a beam splitter and monitored by a photodiode. The laser shutter is triggered if the photodiode signal drops under a certain threshold.

Achromatic lenses: The scattered light is collected and focused onto an optical fiber by two achromatic, plano-convex 2" lenses (L3, L4 in figure A.1) with a focal length of 75 mm and anti-reflective coating (Thorlabs, AC508-075-A-ML). The achromatic lenses reduce chromatic aberrations compared to standard lenses, so that the influence of the collection optics on the measured spectrum is minimized.

Polarizer: A sheet polarizer is inserted in the region of collimated light between the two achromats, so that only vertical polarized light enters the following fiber bundle.

This is necessary to be able to correctly determine the polarization-dependent line strength function (cf. appendix C), which is required for calibration of the system [Sch13b].

Fiber: An optical fiber bundle comprising 48 individual, adjoining fibers with a core diameter of 100 µm and a cladding diameter of 125 µm transfers the scattered light to the spectrometer. The individual fibers are aligned in a slit-to-slit configuration at both ends of the fiber bundle to image the Raman scattering region (corresponding to the longitudinal laser beam profile in the LARA cell) onto the entrance slit of the spectrometer. The fiber has a numerical aperture of NA= 0.22.

Edge filter: An edge filter (Semrock, LP03-532RU-25) at the spectrometer entrance slit suppresses the Rayleigh scattered light at the laser wavelength of 532 nm by a factor of more than 10^6 [Sem16b]. By this means, stray light in the spectrometer which would induce a high background on the CCD detector is prevented. The edge filter is not visible in figure A.1.

Spectrometer: A high-throughput lens spectrometer (Princeton Instruments, HTS) with a low f-number of f/1.8 is used for the spectral analysis of the Raman light. The medium resolution diffraction grating with 600 grooves/mm allows for simultaneous monitoring of the Q_1 branches of all hydrogen isotopologues.

CCD detector: A CCD (Charged Coupled Device) array detector is used to convert the scattered photons into electric charges (Princeton Instruments, PIXIS2KB). A high quantum efficiency of approximately 95 % is provided by the back-illumination technique [Pri15b]. The detector can be cooled down to -75 °C for reduction of dark noise (cf. subsection 3.2.3).

B. Flow diagram of the Inner Loop at the WGTS

The flow diagram of the Inner Loop at the WGTS is shown in figure B.1.

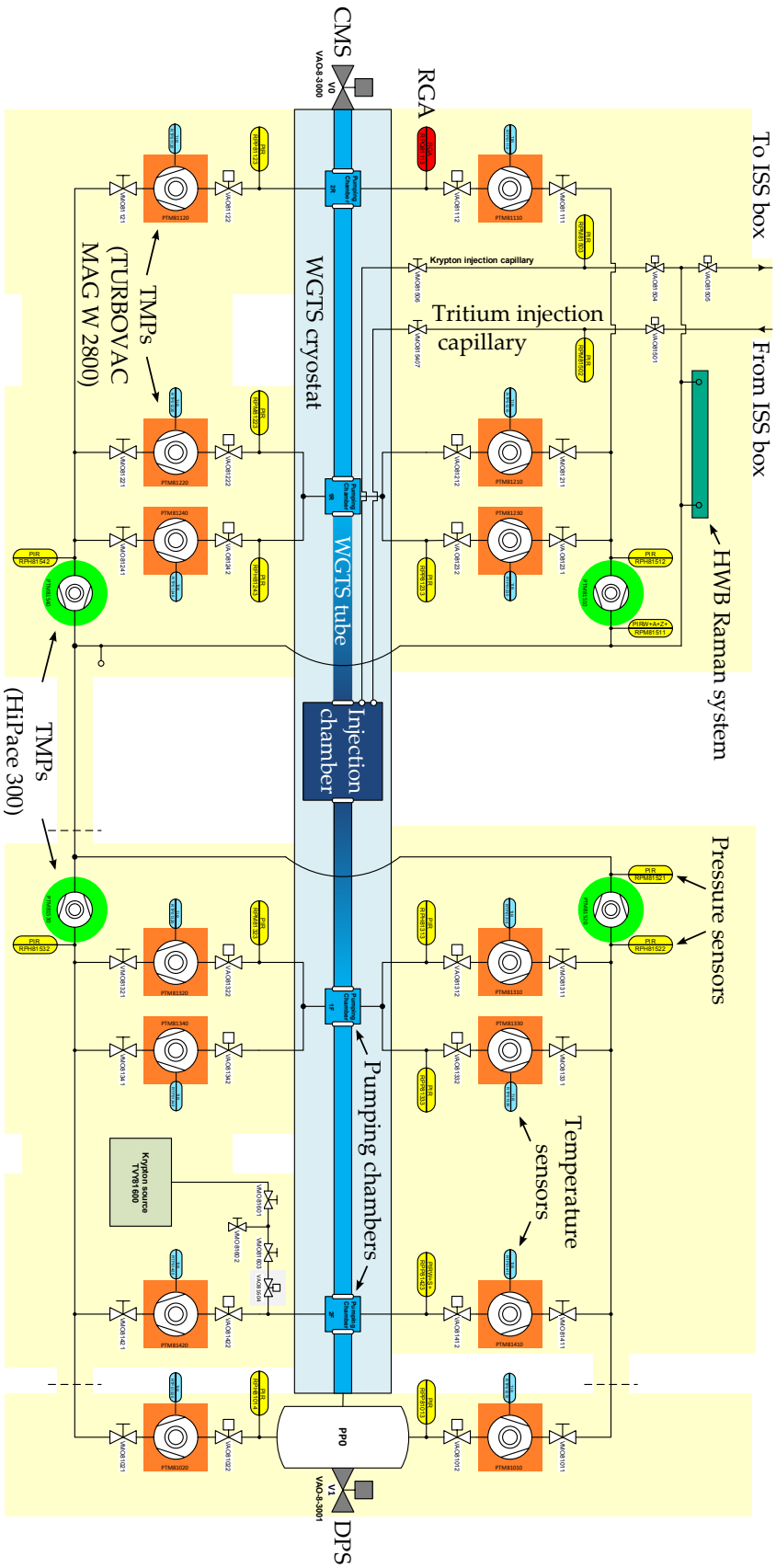

Figure B.1.: Flow diagram of the Inner Loop at the WGTS. 14 TURBOVAC MAG W 2800 turbo molecular pumps (Oerlikon Leybold Vacuum GmbH [Oer16], *orange squares*) form the first pumping stage, four HiPace 300 turbo molecular pumps (Pfeiffer Vacuum [Pfe16], *green circles*) the second one. Abbreviations: CMS – calibration and monitoring system; DPS – Differential Pumping Section; HWB Raman system – hollow waveguide based Raman system; ISS – Isotope Separation System; RGA – rest gas analyzer; TMPs – turbo molecular pumps.

C. The line strength function

The line strength function $\Phi(\varphi, \theta, a, \gamma)_{p^{\mathrm{i}}, p^{\mathrm{s}}}$ describes the transition probability of a certain Raman transition. For this reason, the line intensity related to a given transition is proportional to $\Phi(\varphi, \theta, a, \gamma)_{p^{\mathrm{i}}, p^{\mathrm{s}}}$ (cf. equation 3.24). As outlined in subsection 3.1.3, the line strength function depends on the polarization of incident and scattered light (p^{i}, p^{s}) as well as on the scattering geometry. The latter is described by the angles θ and φ, which define the direction of the scattered beam relative to reference coordinate system, as illustrated in figure C.1.

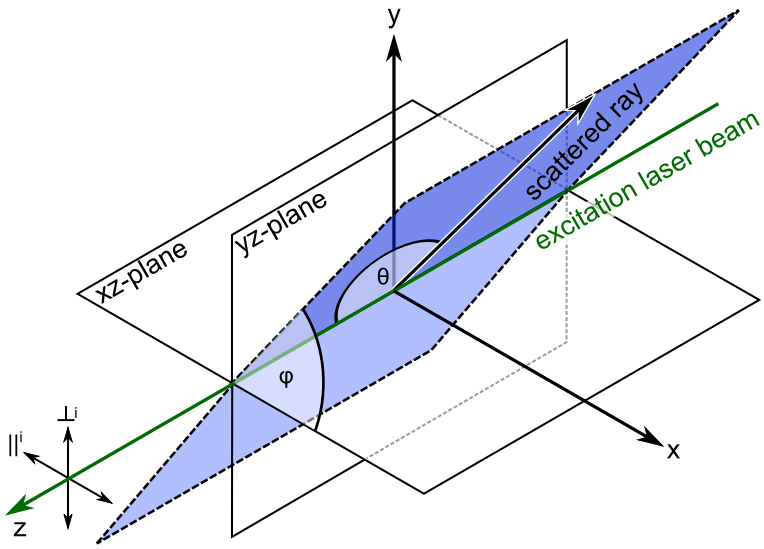

Figure C.1.: Definition of Raman scattering angles and the polarization directions. The polarization directions $\perp$ and $\parallel$ are defined relative to the xz-plane, which is parallel to the breadboard surface of the optical setup. The zenith angle θ is defined as the angle between the scattered ray and the z-axis, which corresponds to the direction of the excitation laser beam. The azimuth angle φ is defined as the angle between the scattered ray and the x-axis, which is perpendicular to the z-axis. The scattering plane *(blue)* is determined by the direction of the excitation laser beam (z-axis) and the scattered ray. Figure adapted from [Sch13b].

The four line strength functions for $\perp$- and $\parallel$-polarized laser and Raman light in dependence of the average polarizability, a, and the anisotropy of the polarizability, γ, are given by [Lon02]

$$\Phi(\varphi,\theta,a,\gamma)_{\perp^{\mathrm{i}},\perp^{\mathrm{s}}} = a^2\cos^2\varphi + b^{(2)}\frac{\gamma^2}{45}\cdot\left(4-\sin^2\varphi\right)\ , \tag{C.1}$$

$$\Phi(\varphi,\theta,a,\gamma)_{\parallel^{\mathrm{i}},\perp^{\mathrm{s}}} = a^2\sin^2\varphi + b^{(2)}\frac{\gamma^2}{45}\cdot\left(3+\sin^2\varphi\right)\ , \tag{C.2}$$

$$\Phi(\varphi,\theta,a,\gamma)_{\parallel^{\mathrm{i}},\parallel^{\mathrm{s}}} = a^2\cos^2\theta\cos^2\varphi + b^{(2)}\frac{\gamma^2}{45}\cdot\left(3+\cos^2\theta\cos^2\varphi\right)\ , \tag{C.3}$$

$$\Phi(\varphi,\theta,a,\gamma)_{\perp^{\mathrm{i}},\parallel^{\mathrm{s}}} = a^2\cos^2\theta\sin^2\varphi + b^{(2)}\frac{\gamma^2}{45}\cdot\left(3+\cos^2\theta\sin^2\varphi\right)\ . \tag{C.4}$$

$$\tag{C.5}$$

In these expressions, $b^{(2)}$ is the Placzek-Teller factor. It is given by [Lon02]

$$b^{(2)}_{J''} = \frac{J''(J''+1)}{(2J''-1)(2J''+3)} \tag{C.6}$$

for rotational states J'' of the molecule.

The line strength function assumes its maximum value of $a^2 + b^{(2)}\cdot\gamma^2/45\cdot 4$ under the following conditions:

- $\perp^{\mathrm{i}},\perp^{\mathrm{s}}$: $\varphi = 0°$, θ arbitrary,
- $\parallel^{\mathrm{i}},\perp^{\mathrm{s}}$: $\varphi = 90°$, θ arbitrary,
- $\parallel^{\mathrm{i}},\parallel^{\mathrm{s}}$: $\varphi = 0°$, $\theta = 0°$ or $180°$,
- $\perp^{\mathrm{i}},\parallel^{\mathrm{s}}$: $\varphi = 90°$, $\theta = 0°$ or $180°$.

This shows that the Raman intensity is independent of the laser polarization direction in case of forward or backward scattering ($\theta = 0°$ or $180°$), which is connected to the rotational symmetry of these configurations. In addition, these expressions show that the line strength function is maximized when the scattering angles and polarization configurations are chosen such that the direction in which the Raman light is scattered is perpendicular to the polarization axis of the incident laser light.

It should be noted that integrations are required to obtain the total line strength function for a measurement configuration, since realistic measurement systems collect Raman light over a certain solid angle instead of a just from a single distinct angle. This is described in detail in [Sch13d].

D. Scaling of SNR and LOD

D.1. Scaling of SNR and LOD to a higher laser power

In chapter 7, the results obtained in the performance test of the optimized hollow waveguide based Raman system had to be scaled in order to estimate the system performance at a higher laser power. The equations used for scaling are explained in the following.

According to equation 3.38, the measured Raman signal is proportional to the laser irradiance, $\mathcal{I}$, and thus the laser power, P:

$$S(P) = C_1 \cdot P \tag{D.1}$$

with the proportionality constant C_1.

The measured noise is composed of three individual noise contributions, as related in subsection 3.2.3. While the detector-related thermal noise (N_T) and read-out noise (N_R) are independent of the laser power, the shot noise contribution (N_S) is proportional to the square root of the intensity of background light (cf. equation 3.36). In a Raman system well screened from external light sources such as room light, this background is practically exclusively related to the excitation laser radiation (e.g. due to fluorescence generation in the optical system), so that

$$N_\mathrm{S}(P) = \sqrt{C_2 \cdot P} \tag{D.2}$$

with the proportionality constant C_2. The total noise is thus given by

$$N(P) = \sqrt{N_\mathrm{S}^2(P) + N_\mathrm{T}^2 + N_\mathrm{R}^2} \overset{(D.2)}{=} \sqrt{C_2 \cdot P + N_\mathrm{T}^2 + N_\mathrm{R}^2} \equiv \sqrt{C_2 \cdot P + N_\mathrm{D}^2} \tag{D.3}$$

with the purely detector-related noise $N_\mathrm{D} = \sqrt{N_\mathrm{T}^2 + N_\mathrm{R}^2}$; the latter is determined experimentally from a dark spectrum with the laser turned off. The power-dependent term is thus related to the measured values of the total and the detector-related noise by the following relation:

$$C_2 \cdot P = N^2(P) - N_\mathrm{D}^2 \ . \tag{D.4}$$

Using equations D.1 and D.3, the signal-to-noise ratio obtained when using a certain laser power P_0 is given by

$$\mathrm{SNR(P_0)} = \frac{S(P_0)}{N(P_0)} = \frac{C_1 \cdot P_0}{\sqrt{C_2 \cdot P_0 + N_\mathrm{D}^2}} \ . \tag{D.5}$$

The signal-to-noise ratio scaled to a different laser power $P_x = P_0 \cdot x$ is thus described by the following expression:

$$\mathrm{SNR_{sc}}(P_x) = \frac{C_1 \cdot P_x}{\sqrt{C_2 \cdot P_x + N_\mathrm{D}^2}} = \frac{C_1 \cdot P_0 \cdot x}{\sqrt{C_2 \cdot P_0 \cdot x + N_\mathrm{D}^2}} \tag{D.6}$$

$$\overset{(D.1,D.4)}{=} \frac{S(P_0) \cdot x}{\sqrt{(N^2(P_0) - N_\mathrm{D}^2) \cdot x + N_\mathrm{D}^2}} \,. \tag{D.7}$$

This equation can be used to scale the signal-to-noise ratio to a certain laser power P_x based on

- the signal and noise values $S(P_0)$ and $N(P_0)$ measured using a laser power P_0,
- the detector-related noise N_D determined from a dark measurement, and
- the scaling factor $x = P_x/P_0$.

The related uncertainty is obtained using Gaussian error propagation:

$$\begin{aligned}\Delta\mathrm{SNR_{sc}}(P_x) = \Bigg[&\left(\mathrm{SNR_{sc}}(P_x) \cdot \frac{\Delta S(P_0)}{S(P_0)}\right)^2 + \left(\mathrm{SNR_{sc}}(P_x) \cdot \frac{x \cdot N(P_0) \cdot \Delta N(P_0)}{(N^2(P_0) - N_\mathrm{D}^2) \cdot x + N_\mathrm{D}^2}\right)^2 \\ &+ \left(\frac{S(P_0) \cdot \Delta x}{\sqrt{(N^2(P_0) - N_\mathrm{D}^2) \cdot x + N_\mathrm{D}^2}} \cdot \left(1 - \frac{0.5x(N^2(P_0) - N_\mathrm{D}^2)}{(N^2(P_0) - N_\mathrm{D}^2) \cdot x + N_\mathrm{D}^2}\right)\right)^2 \Bigg]^{\frac{1}{2}} \,.\end{aligned} \tag{D.8}$$

The scaled detection limit is determined according to equation 3.32 from the scaled signal-to-noise ratio and the partial pressure p of the analyte:

$$\mathrm{LOD_{sc}} = \frac{3p}{\mathrm{SNR_{sc}}} \,. \tag{D.9}$$

The uncertainty is obtained using Gaussian error propagation:

$$\Delta\mathrm{LOD_{sc}} = \mathrm{LOD_{sc}} \cdot \sqrt{\left(\frac{\Delta p}{p}\right)^2 + \left(\frac{\Delta\mathrm{SNR_{sc}}}{\mathrm{SNR_{sc}}}\right)^2} \,. \tag{D.10}$$

D.2. Scaling of detection limits from the literature to a different laser power and acquisition time

In order to be able to compare own results or sensitivity targets to the results of other research groups who used different acquisition settings, it is in general necessary to scale detection limits with respect to laser power and acquisition time. However, the equations D.7 or D.9 can usually not be used when scaling of the literature values is desired, since normally only the detection limits themselves are stated, but neither the signal and noise values used to calculate them nor the detector-related noise.

Approximate scaling can be achieved nevertheless by neglecting constant noise contributions, i.e. those which are independent of the laser power and the acquisition time. This approximation can be assumed to be valid in the presence of a certain non-negligible fluorescence background as is usually observed in hollow waveguide based Raman measurements utilizing a 532 nm laser. The noise is then approximated by the shot noise contribution only. As both the Raman and the background intensity (B_{ext}) increase linearly with the laser power, P, and the acquisition time, t_{acq}, signal and noise are described by the following proportionalities:

$$S(P, t_{\mathrm{acq}}) \propto P \cdot t_{\mathrm{acq}} \ , \tag{D.11}$$

$$N(P, t_{\mathrm{acq}}) \approx N_{\mathrm{s}}(P, t_{\mathrm{acq}}) = \sqrt{B_{\mathrm{ext}}(P, t_{\mathrm{acq}})} \propto \sqrt{P \cdot t_{\mathrm{acq}}} \ , \tag{D.12}$$

leading to a signal-to-noise ratio of

$$\mathrm{SNR}(P, t_{\mathrm{acq}}) = \frac{S(P, t_{\mathrm{acq}})}{N(P, t_{\mathrm{acq}})} = C \cdot \frac{P \cdot t_{\mathrm{acq}}}{\sqrt{P \cdot t_{\mathrm{acq}}}} = C \cdot \sqrt{P \cdot t_{\mathrm{acq}}} \tag{D.13}$$

with the proportionality constant C.

Scaling a given signal-to-noise ratio $\mathrm{SNR}(P_0, t_{\mathrm{acq},0})$ to a different laser power $P_x = P_0 \cdot x$ and a different acquisition time $t_{\mathrm{acq},y} = t_{\mathrm{acq},0} \cdot y$ leads to the following expression:

$$\mathrm{SNR}_{\mathrm{sc}}(P_x, t_{\mathrm{acq},y}) = C \cdot \sqrt{x P_0 \cdot y t_{\mathrm{acq},0}} \overset{(D.13)}{=} \sqrt{xy} \cdot \mathrm{SNR}(P_0, t_{\mathrm{acq},0}) \ . \tag{D.14}$$

As the detection limit is inversely proportional to the signal-to-noise ratio, the scaled LOD is given by

$$\mathrm{LOD}_{\mathrm{sc}}(P_x, t_{\mathrm{acq},y}) = \frac{1}{\sqrt{xy}} \cdot \mathrm{LOD}(P_0, t_{\mathrm{acq},0}) = \mathrm{LOD}(P_0, t_{\mathrm{acq},0}) \cdot \sqrt{\frac{P_0}{P_x} \frac{t_{\mathrm{acq},0}}{t_{\mathrm{acq},y}}} \ . \tag{D.15}$$

This equation was used to scale results obtained by the group around Buric et al. [Bur13] to a higher laser power and an increased acquisition time in subsection 3.4.2.

E. Schematic drawing of the prototype gas cell

A schematic drawing of the gas cell of the hollow waveguide based prototype system (see chapter 4) is shown in figure E.1.

Figure E.1.: Schematic drawing of the prototype gas cell. Exploded component view. The dimensions of all components are true to scale (approximately 1:1.4); only the thickness of the copper sealings (drawn in red) between the front/rear block and the Swagelok connectors is increased in this drawing for better visibility (real thickness: 0.5 mm). The blue circles at the front and rear block facing the respective end caps represent O-ring seals. Note that the waveguide itself is not included in this drawing. It is inserted in a stainless steel tube with an inner diameter of about 1.7 mm, which is connected at each end to the front and rear block by the copper-sealed Swagelok connectors shown in the drawing (cf. figure 4.2).

F. Analysis settings

Signal and noise were extracted from the spectra measured within the scope of this work using the procedures described in the (sub-)sections 4.2.2 and 7.2 for the peak height and the peak area approach, respectively. The peak area approach was only used in the final performance test in addition to the peak height approach; details about the chosen analysis settings are given below in section F.4.

When using the peak height approach, the following general settings were used in all analyses:

- The SCARF routine for signal extraction was applied in two iterations. A polynomial order of $n = 3$ was used for the Savitzky-Golay smoothing process (cf. [Jam13b]).

- Noise extraction utilized a polynomial fitting routine based on least square fitting and using a Cholesky algorithm to compute the best polynomial fit in order to obtain the background curve. A polynomial order of $n = 7$ was used for the fit in each case.

The other analysis settings were chosen in dependence of the position of the peak of interest and characteristics of the background curve to allow for appropriate signal and noise extraction. The signal extraction settings comprise

- the Rolling Circle Filter (RCF) radius used in each SCARF iteration ("RCF radius I" and "RCF radius II"),

- the number of side points included in the Savitzky Golay (SG) algorithm in each SCARF iteration ("SG side points I" and "SG side points II"),

- the pixel range of the background-subtracted spectrum from which the signal is extracted by taking the maximum value ("signal extraction range").

The noise extraction settings comprise

- the pixel range to which the polynomial fit is applied ("fit range"),

- the (smaller) pixel range from which the noise is extracted by taking the standard deviation of the fit residual ("noise extraction range").

The settings used in each data analysis are listed in the following.

F.1. Prototype measurements

The results of the measurements with the hollow waveguide based prototype system discussed in section 4.3 were obtained using the peak height approach with the following analysis settings:

'T-low' run (H_2 signal from Q_1 branch):

- Signal extraction:
  - RCF radius I: 20
  - SG side points I: 40
  - RCF radius II: 15
  - SG side points II: 20
  - Signal extraction range: 1200 – 1320
- Noise extraction:
  - Fit range: 120 – 190
  - Noise extraction range: 125 – 185

'T-high' runs (T_2 signal from Q_1 branch):

- Signal extraction:
  - RCF radius I: 5
  - SG side points I: 20
  - RCF radius II: 10
  - SG side points II: 20
  - Signal extraction range: 75 – 110
- Noise extraction:
  - Fit range: 120 – 190
  - Noise extraction range: 125 – 185

F.2. Investigation of fluorescence-reducing measures

The various investigations of fluorescence-reducing measures described in the sections 6.3 – 6.6 were analyzed using the peak height approach with the following settings:

N_2 signal from Q_1 branch:

- Signal extraction:
  - RCF radius I: 180
  - SG side points I: 210
  - RCF radius II: 120
  - SG side points II: 150
  - Signal extraction range: 520 – 620
- Noise extraction:
  - Fit range: 455 – 525
  - Noise extraction range: 460 – 520

F.3. Optimization of measurement parameters

The investigations concerning the optimization of measurement parameters for the hollow waveguide based Raman system, which are described in section 6.7, were analyzed using the peak height approach with the following settings:

Single-pass vs. double-pass (N_2 signal from Q_1 branch):

- Signal extraction:
  - RCF radius I: 180
  - SG side points I: 210
  - RCF radius II: 120
  - SG side points II: 150
  - Signal extraction range: 520 – 620
- Noise extraction:
  - Fit range: 455 – 525
  - Noise extraction range: 460 – 520

Optimization of acquisition settings (N_2 signal from Q_2 branch):

- Signal extraction:
  - RCF radius I: 180
  - SG side points I: 210
  - RCF radius II: 120
  - SG side points II: 150
  - Signal extraction range: 1090 – 1150
- Noise extraction:
  - Fit range: 1235 – 1305
  - Noise extraction range: 1240 – 1300

F.4. Performance of the optimized setup

The data of the performance test with the optimized hollow waveguide based Raman setup, which is described in chapter 7, were analyzed using both the peak height and the peak area approach. The respective analysis settings are given in the following.

F.4.1. Peak height approach

N_2 signal from Q_2 branch:

- Signal extraction:
  - RCF radius I: 60
  - SG side points I: 100
  - RCF radius II: 60
  - SG side points II: 50
  - Signal extraction range: 1110 – 1140
- Noise extraction:
  - Fit range: 1235 – 1305
  - Noise extraction range: 1240 – 1300

F.4.2. Peak area approach

In the data analysis based on the peak area approach, the signal was determined by summing up all intensities in the pixel range 1220 – 1133. This range corresponded to the width of the peak related to the Q_2 branch of N_2 at which the intensity had decreased to approximately $1/e^2$, so that a large fraction of the total peak area was taken into account in the analysis.

In order to obtain the noise N_{area} according to the procedure described in section 7.2, background fluctuations were simulated over the same number of pixels as used for the signal determination, i.e. 14 pixels. The noise determined in the peak height approach was used as the standard deviation of the simulated Gaussian fluctuations, i.e. $\sigma_{\mathrm{N}} = N_{\mathrm{height}}$ (cf. section 7.2 and figure 7.2). One million simulations were performed.

The detector-related noise $N_{\mathrm{D,area}}$ was obtained via the same procedure, i.e. based on the simulation of background fluctuations over 14 pixels, but using the detector-related noise of the peak height approach as the standard deviation ($\sigma_{\mathrm{N_D}} = N_{\mathrm{D,height}}$).

G. Raman scattering cross sections for the hydrogen isotopologues

The Raman scattering cross sections for all six hydrogen isotopologues relative to the scattering cross section for N_2 were determined at the Tritium Laboratory Karlsruhe by T. James and M. Schlösser based on theoretical line strength calculations as well as measurements with accurately known gas mixtures.[1] The obtained values are listed in table G.1.

Table G.1.: Ratio of the Raman scattering cross sections for all six hydrogen isotopologues to the cross section for nitrogen. The numbers were determined for the respective Q_1 branches and for an excitation laser wavelength of 532 nm.

i	σ_i/σ_{N_2}
H_2	3.4 ± 0.1
HD	3.2 ± 0.1
HT	3.1 ± 0.1
D_2	2.9 ± 0.1
DT	2.8 ± 0.1
T_2	2.6 ± 0.1

[1] T. James, private communication, March 2015

H. Measurement reproducibility and uncertainties in the durability test of reflective surfaces

A test of the durability of reflective surfaces under tritium exposure was presented in section 5.1. This appendix gives additional information about the influence of temperature on the measurement reproducibility (section H.1), the temperatures in the Omegatron glove box during the durability test measurements (section H.2) as well as the uncertainty calculation used in the analysis of the results (section H.3).

H.1. Influence of temperature on the measurement reproducibility

The reproducibility which can be achieved using the COATEX measurement setup was thoroughly investigated and improved by V. Schäfer in her diploma thesis [Sch13a]. With respect to the mechanical reproducibility, e.g. in case of repeated reinsertion and repositioning of a sample, she reports a maximum deviation of measurement results by 2.1 %. This value being of the same order as the statistical measurement uncertainty, it is concluded that the COATEX performance is sufficiently reproducible with regard to necessary mechanical interventions [Sch13a].

In a long-term run over several days, however, measurement results differed by up to 5.6 %, and a correlation between ambient temperature and measured signal was discovered [Sch13a]. For this reason, another long-term run was performed within the scope of the present work to further study this correlation, and thus to be able to determine suitable experimental frame conditions with respect to temperature-related measurement parameters. The long-term measurement lasted 77.8 h. It was conducted using a reflective neutral density filter (Thorlabs ND10B) as the sample. Its surface was not scanned, but a fixed point near the sample center was continuously monitored. The acquisition time for each single measurement was 10 s.

The temperature in the glove box during the long-term run is shown in figure H.1. After the measurement was started, it increased by more than 2 °C within few hours; a more or less stable box temperature was reached after 15 h. Since the ambient laboratory temperature did not rise as well during this time and no other devices were active in the Omegatron glove box, this temperature curve indicates that the measurement itself (e.g. operation and temperature stabilization of the laser module) increases the temperature in the box. Another temperature rise occurred when turning on the box light, i.e. lamps

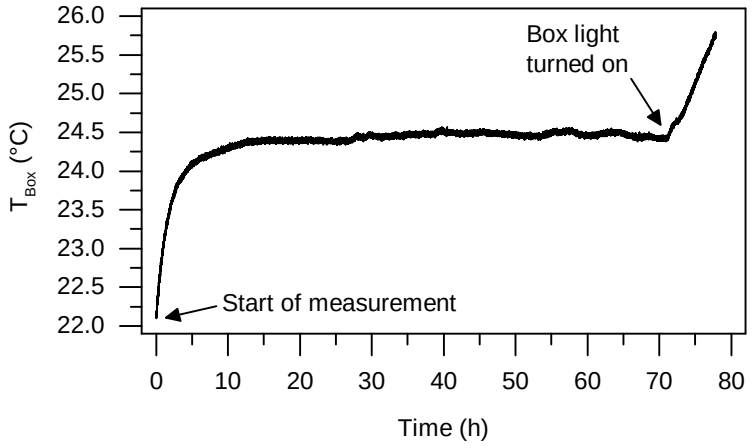

Figure H.1.: Box temperature during long-term run. The measurement was started directly after all necessary electronics in the box (laser module supply, photodiode amplifier etc.) had been turned on.

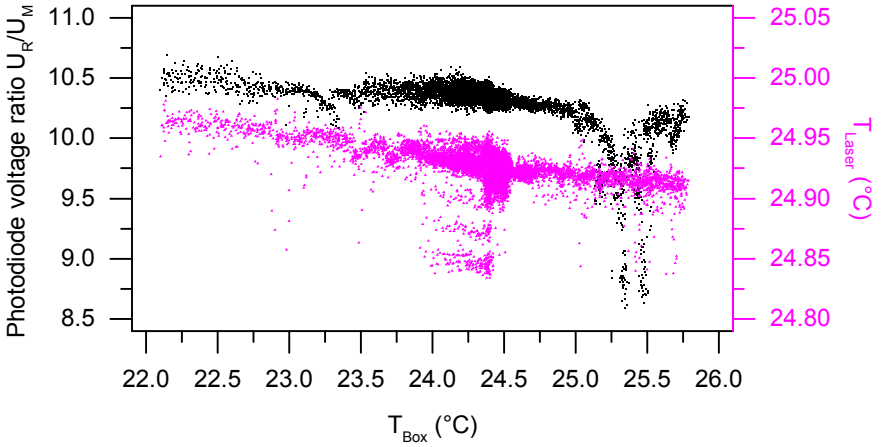

Figure H.2.: Photodiode voltage ratio and laser module temperatures plotted in dependence of the box temperature.

integrated into the Omegatron box, towards the end of the measurement; this led to an approximately linear increase with a slope of 0.23 K/h over a period of more than 5 h, with no indication of approaching a limit soon.

The relation between box temperature and the measured ratio between reflection and monitoring photodiode voltage is shown in figure H.2. For box temperatures between 22 and 25 °C, the ratio decreases by about 3 % with increasing temperature, with a slight irregularity in the curve around 23.2 °C. Above a temperature of about 25 °C, however, the ratio suddenly drops by approximately 16 % before returning to the previous level.

In addition, the temperature measured for the laser module is included. Its main trend is a decrease by approximately 0.05 °C with rising box temperatures, but with irregularities mainly in the box temperature range around 24 - 24.5 °C, i.e. after about 3.5 h of

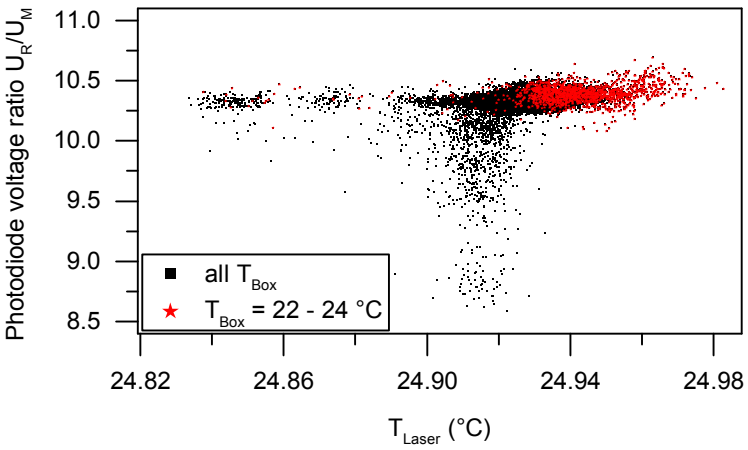

Figure H.3.: Photodiode voltage ratio plotted in dependence of the laser module temperature. The red symbols represent the data subset measured at a box temperature between 22 and 24 °C.

measurement. At higher box temperatures, when the photodiode voltage ratio starts to drop, the laser module temperature is relatively stable again. The observed irregularities of the measured laser module temperature at certain box temperatures are probably related to the PID-regulation of the stabilizing Peltier unit. Since both sides of the latter are influenced by the same ambient temperature, slight regulation-loop instabilities can occur for particular temperatures, depending on the selected P-, I- and D-settings.

As the irregularities in the photodiode voltage signal are observed at a different box temperature than the ones of the laser module temperature, it can be assumed that both effects are not connected. V. Schäfer discusses possible other temperature-related effects on the signal like a temperature dependence of the photodiodes or the amplifier [Sch13a]. However, she finds that these effects are not sufficient to explain the observed deviations. It is therefore assumed that other effects lead to the observed signal change, for instance misalignments of the system by thermal expansion of components.

In order to minimize measurement uncertainties by large signal fluctuations, the measurements performed in the scope of this work were thus restricted to box temperatures between 22 and 24 °C by leaving the box light turned off and letting the box cool down again after a number of measurements. Apart from the signal-influencing high temperature region, this temperature range excludes also the region in which the main laser module temperature changes occurred to avoid any yet unobserved harmful effects, such as possible temperature-induced variations in the mode pattern of the laser module.[1] In figure H.3, the relation between laser module temperature and photodiode voltage ratio is shown for all box temperatures and when restricted to the stated region: in the latter case, the vast majority of measurement points is found to be located in a similar laser module temperature range (24.94 ± 0.02 °C), and even those at lower laser module temperatures exhibit similar voltage ratio values as the rest.

[1] Note that a change of the PID-regulation settings would likely lead to laser module temperature instabilities in a different box temperature region.

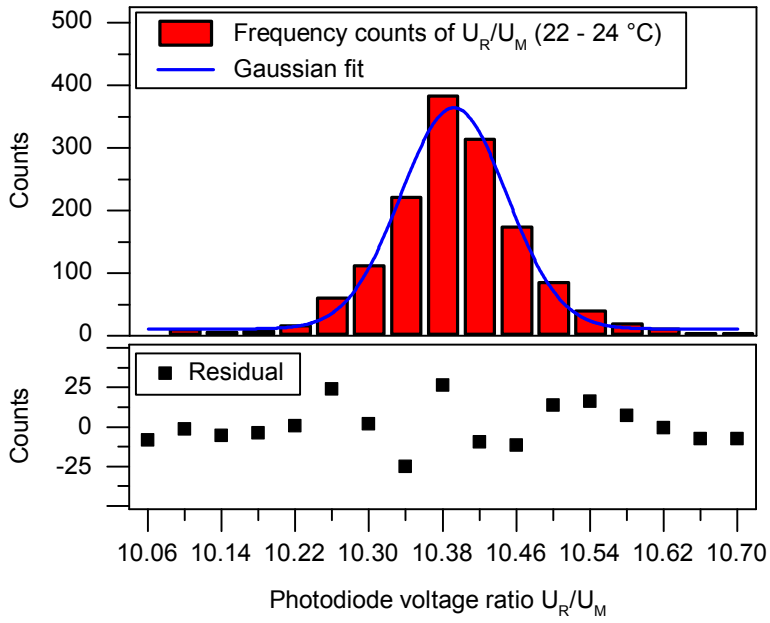

Figure H.4.: Histogram of measured photodiode voltage ratios for a box temperature between 22 and 24 °C.

The lower variance of signals is another reason for the chosen temperature limit. A histogram of of all photodiode voltage ratios for box temperature values between 22 and 24 °C is plotted in figure H.4. Even though single measurement points vary by a maximum of 5.88 % – similar to the observation in [Sch13a] – the data can be approximated by a Gaussian fit with $\sigma = 0.057$. This corresponds to only 0.55 % of the mean value, indicating a good reproducibility for measurements of a few hours in duration.

H.2. Box temperatures during the durability test measurements

The temperatures measured in the Omegatron glove box during each measurement run of each sample type are listed in table H.1. The mean box temperature was higher in the measurements after exposure due to the increased ambient temperature in the laboratory.

H.3. Uncertainties

The uncertainty of the photodiode voltage ratios $U_\mathrm{R}/U_\mathrm{M}$ given in the tables 5.3 – 5.5 is calculated according to

$$\sigma_\mathrm{tot} = \sqrt{\sigma_\mathrm{stat}^2 + \sigma_\mathrm{temp}^2 + \sigma_\mathrm{repr}^2} \tag{H.1}$$

from the different uncertainty contributions:

Table H.1.: Box temperatures during the durability test measurements.

	Sample type	Box temperature range (°C)			$T_{\mathrm{Box,mean}}$ (°C)
		Run 1	Run 2	Run 3	
before exposure	PS	22.8 – 23.6	23.3 – 23.9	22.1 – 23.1	23.2
	UPS	23.6 – 24.0	22.1 – 23.2	22.5 – 23.3	23.2
	BB	22.6 – 23.5	23.6 – 24.0	22.1 – 23.1	23.0
	LG	22.6 – 23.5	22.7 – 23.6	23.4 – 23.7	23.3
	Al	22.5 – 23.6	22.1 – 23.4	23.3 – 23.7	23.1
	Cu	23.7 – 24.0	22.9 – 23.9	22.1 – 23.1	23.2
after exposure	PS	23.3 – 23.9	23.2 – 23.9	22.8 – 23.8	23.5
	UPS	23.2 – 23.8	22.9 – 23.8	23.0 – 23.8	23.5
	BB	23.3 – 23.8	22.9 – 23.9	23.3 – 23.9	23.5
	LG	22.9 – 23.8	23.4 – 23.9	22.8 – 23.9	23.5
	Al	23.4 – 23.8	22.9 – 23.8	23.1 – 23.9	23.5
	Cu	23.0 – 23.8	23.4 – 23.9	23.5 – 23.7	23.6

- σ_{stat} is the uncertainty related to statistical fluctuations of the measured photodiode voltages. In each measurement i, the uncertainty σ_i of the voltage ratio between reflection and monitoring photodiode is calculated by Gaussian error propagation from the experimental standard deviations of the two measured voltage ratios. (See section 5.1.7 for a description of the photodiode voltage ratio calculation.) When the weighted average over all single measurements i is calculated for each measurement point, the related uncertainty is given by $\sigma_{\mathrm{p}} = \left(\sum_i \sigma_i^{-2}\right)^{-1/2}$. The statistical uncertainty of the photodiode voltage ratio averaged over all seven measurement points is then calculated by Gaussian error propagation again:

$$\sigma_{\mathrm{stat}} = \frac{1}{7} \cdot \sqrt{\sum_{n=1}^{7} \sigma_{\mathrm{p},n}^2} \; . \tag{H.2}$$

- σ_{temp} is the 0.55 % uncertainty due to temperature changes, as detailed above in section H.1:

$$\sigma_{\mathrm{temp}} = 0.55\,\% \cdot \frac{U_{\mathrm{R}}}{U_{\mathrm{M}}} \; . \tag{H.3}$$

- σ_{repr} is the uncertainty connected to the reproducibility of sample reinsertion. It is given by the standard deviation of the photodiode voltage ratios which were measured in a certain run for a certain measurement configuration (e.g. sample

UPS, specimen T2, position A) and averaged over all seven measurement points, $< \frac{U_\mathrm{R}}{U_\mathrm{M}}(\mathrm{run},\ \mathrm{config}) >$. Each sample is reinserted nine times in a certain configuration within the three measurement runs prior to or after exposure, respectively. In order to account for the low number of repetitions, the standard deviation is corrected by the Student t-factor for $(9-1) = 8$ degrees of freedom, $t_{68.27}(8) = 1.07$ [GUM08]:

$$\sigma_\mathrm{repr} = t_{68.27}(8) \cdot \sigma_{<\frac{U_\mathrm{R}}{U_\mathrm{M}}(\mathrm{run},\ \mathrm{config})>} \ . \tag{H.4}$$

I. Model calculation of the dependencies of the Raman signal on the waveguide properties

As outlined in section 3.4, the measured Raman signal in a hollow waveguide based Raman system depends on a range of parameters such as the reflectance of the inner surface, the length and the diameter of the waveguide. In order to estimate the influence of the latter on the measured signal, model calculations have been performed within the scope of this work.

According to equation 3.33, two different factors related to the waveguide geometry, i.e. length and inner diameter, have to be taken into account when considering the measured Raman signal: the total intensity of the Raman light generated in the waveguide and the light collection properties, which determine the fraction of generated Raman light which is actually detected. Both will be examined more closely in the following paragraphs to provide a basis for the subsequent signal calculations.

Light collection: The light collection properties of a hollow waveguide based Raman system are independent of the waveguide length, but they are related to the waveguide diameter as the latter determines both the emission angle and the spot size of Raman light at the waveguide exit. The fraction of generated Raman light which is detected is related to these parameters due to the limited acceptance cone of the light collection system, as is discussed in the following.

- **Emission angle:** In subsection 3.4.1, it was discussed that a larger diameter allows more modes to propagate in the waveguide with low losses, leading to a larger emission angle at the waveguide exit. Hollow waveguides with diameters in the millimeter range can be expected to guide a large number of modes, so that the light collection system rather than the choice of diameter is most likely the limiting factor with respect to detecting light with large emission angles: the maximum emission angle which can be collected is limited by the acceptance of the spectrometer (f-number: $f/4.0$) to a value of $\theta_{\max} = 7.1°$.

  In order to determine the maximum collected emission angle of the Light Pipes, a diaphragm was placed in a distance of 40 mm in front of the waveguide exit. The Raman signal was measured at different diaphragm apertures ≥ 1 mm, which correspond to different maximum emission angles being detected. The resulting curves obtained with the two Light Pipes are shown in figure I.1. The two curves agree well with each other: rising quickly at first, the signal soon approaches a constant value. No change of signal can be observed any longer for angles above about 7°, which matches the spectrometer-limited value. The measurement indicates

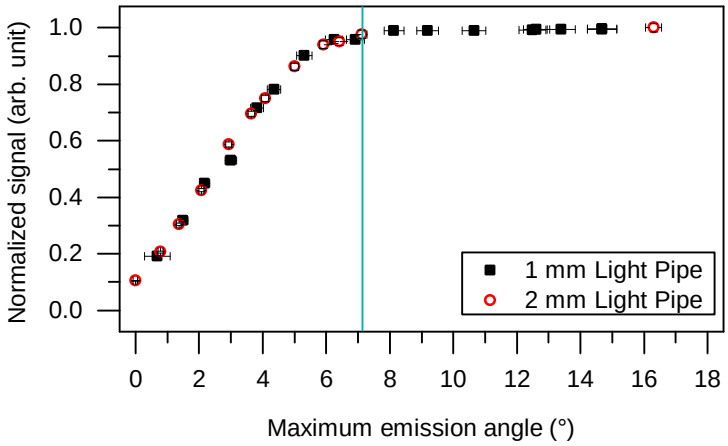

Figure I.1.: Angular dependence of the measured Raman signal. The vertical line represents the maximum emission angle which can be collected by the collection system.

that the cut-off of high-order modes is indeed due to the collection optics rather than to suppression of these modes by high attenuation in the waveguide; in the latter case, one would expect different curves for the two Light Pipes due to the higher attenuation of higher-order modes in small-diameter waveguides. The existence of undetected higher-order modes is also confirmed by the theoretical calculations presented further below. In summary, with respect to the emission angle, the choice of diameter does not have a significant effect on the measured signal in the case of large-diameter waveguides as employed within the scope of this work.

- **Spot size:** However, the collection of light exiting the waveguide is not only limited by the emission angle, but also by the exit point of a light ray. Two optics of the same focal length used to collect and refocus the Raman light can image a spot of 1 mm diameter onto the entrance of the 1 mm diameter collection fiber bundle in its original size, so that all light rays emerging from this spot with angles $\leq \theta_{\mathrm{max,FB}}$ – the maximum fiber bundle acceptance angle – can enter the fiber bundle and be transmitted. This is illustrated in figure I.2 (a_1). If the waveguide diameter is larger than the fiber bundle, rays exiting the waveguide outside of this 1 mm spot are not imaged and detected any more (figure I.2 (a_2)).[1] As illustrated in figure I.2 (b), the question if a ray (with sufficiently small emission angle) is within the imaged spot or not depends on where in the waveguide it is produced. As Raman light is generated uniformly along the waveguide length, the ratio between light being imaged and total produced light is approximately equal to the ratio between imaged spot diameter D_{im} and total waveguide diameter D_{wg}. This can be expressed by an imaging constant $c_{\mathrm{im}} = D_{\mathrm{im}}/D_{\mathrm{wg}}$ for all waveguide diameters $D_{\mathrm{wg}} > D_{\mathrm{im}}$. Note that realistic values of c_{im} can be assumed to be slightly larger than this calculated value due to the focal depth of the collection optics.

[1] Since the étendue $A\Omega$ never decreases in an optical system, it does not help to alter the collection and focusing focal length in such a way that a larger spot is focused down to 1 mm diameter: the solid angle Ω of the light cone increases with any decrease of spot area A, so that parts of the light are not coupled into the fiber bundle any more due to too large entrance angles.

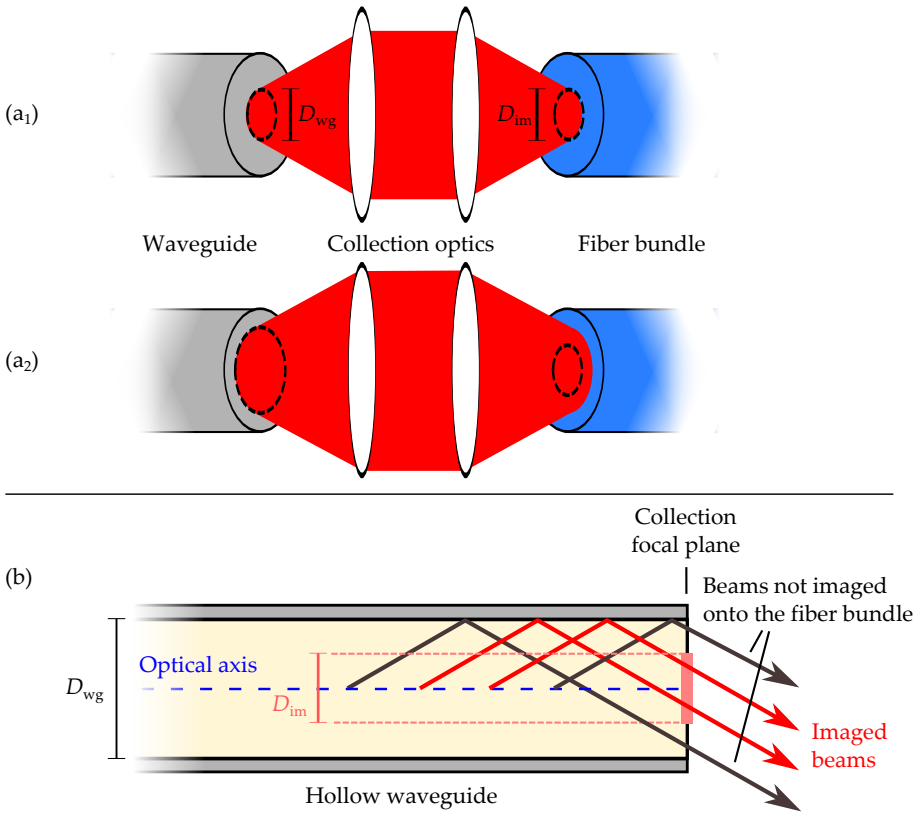

Figure I.2.: Imaging of Raman light from the hollow waveguide onto the fiber bundle. The top panel illustrates imaging of light from a waveguide with inner diameter D_{wg} onto a fiber bundle with diameter D_{fb} by collection optics of the same focal length. *(a_1)* If $D_{\mathrm{wg}} = D_{\mathrm{fb}}$, all light exiting the waveguide is imaged onto the fiber bundle. *(a_2)* If $D_{\mathrm{wg}} > D_{\mathrm{fb}}$, the refocused spot is larger than the fiber bundle aperture, so that light is lost. The diameter of the spot still imaged is equal to the fiber bundle diameter: $D_{\mathrm{im}} \equiv D_{\mathrm{wg}}$. *(b)* The bottom panel illustrates how the point of light emission in the waveguide determines whether the light is imaged onto the fiber bundle or not. For reasons of clarity, only rays emitted along the optical axis are shown here. In the illustration, the waveguide diameter is around twice as large as the imaged spot diameter, so that about half of the emitted rays are imaged.

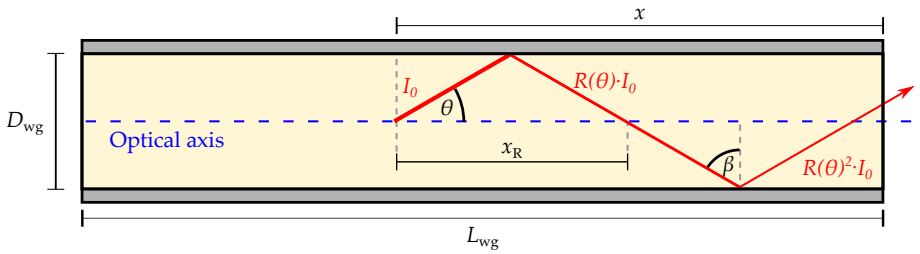

Figure I.3.: Light attenuation in the waveguide. See main text for details.

Attenuation in the waveguide: Next, the dependence of the waveguide diameter on light attenuation in the waveguide is examined. Since only waveguides with diameters in the millimeter range ($\gg \lambda_{\text{Laser}}, \lambda_{\text{Raman}}$) are considered, ray optics is used to approximate the propagation and attenuation of light in the Light Pipes.

Consider a ray of light which is guided along a distance x in the waveguide at an angle θ to the waveguide axis, as shown in figure I.3. In each reflection from the waveguide wall, the intensity is reduced by the angular dependent reflectance of the wall material, $R(\theta)$.[2] After n reflections, the initial intensity I_0 has decreased to

$$I_n(\theta) = I_0 \cdot R(\theta)^n = I_0 \cdot \mathrm{e}^{\ln(R(\theta))\cdot n} \ . \tag{I.1}$$

There is one reflection per distance $x_R = D_{wg}/\tan\theta$ (cf. figure I.3), so that the number of reflections over the total distance x is given by

$$n = \frac{x}{x_R} = \frac{x \cdot \tan\theta}{D_{wg}} \ . \tag{I.2}$$

By inserting equation I.2 into equation I.1, one obtains the following exponential function which describes the attenuation of a ray of initial intensity I_0 guided along a distance x in the waveguide at an angle θ to the waveguide axis:

$$I(x,\theta) = I_0 \cdot \exp\left(\frac{x \cdot \tan\theta \cdot \ln R(\theta)}{D_{wg}}\right) \equiv I_0 \cdot \mathrm{e}^{-\alpha(\theta)\cdot x} \tag{I.3}$$

with the attenuation coefficient

$$\alpha(\theta) = -\frac{\tan\theta \cdot \ln R(\theta)}{D_{wg}} \ . \tag{I.4}$$

A larger waveguide diameter D_{wg} leads to less attenuation in the waveguide.

Total signal calculation: Based on above considerations about light collection and attenuation properties, the total detected Raman signal can be estimated, as shown in the following.

[2] $R(\theta)$ can be calculated from the complex reflective index of the wall material by using the Fresnel equations with the angle of incidence $\beta = 1 - \theta$. Since the waveguide is circular symmetric, p- and s-polarization can be assumed to contribute equally to the total incident light: $R = (R_s + R_p)/2$.

The intensity $I_{\mathrm{R}}(x,\theta)$ of Raman light produced at a distance x from the waveguide exit (= the focal point of the collection optics) at an angle θ to the waveguide axis in a backward scattering geometry is determined by the attenuation of the incident laser in the waveguide up to the distance x, and the attenuation of the Raman light (defined by $\alpha_{\mathrm{R}}(\theta)$) traveling back through the waveguide over the same distance. According to equation I.3, the attenuation of the laser light is described by

$$I_{\mathrm{L}}(x) = I_{0,\mathrm{L}} \cdot \mathrm{e}^{-\alpha_{\mathrm{L}}(\theta_{\mathrm{L}})\cdot x} \tag{I.5}$$

with the initial laser intensity $I_{0,\mathrm{L}}$ and the laser attenuation coefficient $\alpha_{\mathrm{L}}(\theta_{\mathrm{L}})$. This leads to the following relation for the attenuated Raman intensity:

$$I_{\mathrm{R}}(x,\theta) \propto I_{\mathrm{L}}(x) \cdot \mathrm{e}^{-\alpha_{\mathrm{R}}(\theta)\cdot x} = I_{0,\mathrm{L}} \cdot \mathrm{e}^{-(\alpha_{\mathrm{L}}(\theta_{\mathrm{L}})+\alpha_{\mathrm{R}}(\theta))\cdot x} \ . \tag{I.6}$$

In contrast to the attenuation of the Raman light, which depends on the angle of each emitted ray, the laser attenuation is a fixed value: $\alpha_{\mathrm{L}}(\theta_{\mathrm{L}}) \equiv \alpha_{\mathrm{L}}$. Assuming a laser beam parallel to the waveguide, the maximum laser angle θ_{L} is determined by the focal length of the focusing lens, f, and the initial beam diameter, D_{L}, via $\theta_{\mathrm{L}} = \arctan(D_{\mathrm{L}}/(2f))$.

Integration of equation I.6 over the full waveguide length L_{wg} leads to the following expression:

$$I_{\mathrm{R,wg}}(\theta) = \int_0^{L_{\mathrm{wg}}} I_{\mathrm{R}}(x,\theta)\mathrm{d}x \propto \frac{I_{0,\mathrm{L}}}{(\alpha_{\mathrm{L}} + \alpha_{\mathrm{R}}(\theta))} \cdot \left(1 - \mathrm{e}^{-(\alpha_{\mathrm{L}}+\alpha_{\mathrm{R}}(\theta))\cdot L_{\mathrm{wg}}}\right) \ . \tag{I.7}$$

In order to obtain the detected (relative) Raman signals to compare different diameters and waveguide lengths, this expression is multiplied with the imaging constant $c_{\mathrm{im}} = D_{\mathrm{im}}/D_{\mathrm{wg}}$ and integrated over the observed solid angle, with θ up to $\theta_{\mathrm{max}} = 7.1°$:

$$I_{\mathrm{tot}} \propto c_{\mathrm{im}} \int_0^{2\pi} \mathrm{d}\varphi \int_0^{\theta_{\mathrm{max}}} I_{\mathrm{R,wg}}(\theta) \sin\theta \ \mathrm{d}\theta \tag{I.8}$$

$$\overset{(I.4)}{=} 2\pi \cdot I_{0,\mathrm{L}} \cdot \frac{D_{\mathrm{im}}}{D_{\mathrm{wg}}} \int_0^{\theta_{\mathrm{max}}} \frac{-D_{\mathrm{wg}}}{\tan\theta \cdot \ln(R_{\mathrm{L}} + R_{\mathrm{R}}(\theta))} \tag{I.9}$$

$$\cdot \left(1 - \mathrm{e}^{-\frac{L_{\mathrm{wg}}}{D_{\mathrm{wg}}}\cdot\tan\theta\cdot\ln(R_{\mathrm{L}}+R_{\mathrm{R}}(\theta))}\right) \sin\theta \ \mathrm{d}\theta \ . \tag{I.10}$$

The expression was evaluated numerically using Mathematica for different waveguide diameters and lengths in order to obtain the plots shown in the figures 6.9 and 6.10 in chapter 6. Note that only relative Raman signals were calculated for comparison. For this reason, constant factors (2π, $I_{0,\mathrm{L}}$, D_{im}) were omitted in the calculation.

It should be noted that these model calculations serve as an approximation only to obtain an understanding of the general dependence of the measured Raman signal on the waveguide length and diameter. The calculations are based on literature reflectance values. The measured attenuation of laser light propagating through the glass-based, silver-lined waveguide or through the 1 and 2 mm Light Pipes has been found to be higher than the theoretical values, probably due to the imperfect smoothness of real waveguide inner surfaces. The observed deviations correspond to ca. 4 – 6.5 % lower reflectance values.

Bibliography

[Aba11] K. N. Abazajian et al., *Cosmological and astrophysical neutrino mass measurements*, Astropart. Phys. **35**, 4 (2011) 177–184.

[Aba15] K. N. Abazajian et al., *Neutrino physics from the cosmic microwave background and large scale structure*, Astropart. Phys. **63** (2015) 66–80.

[Aga11] S. Agarwal et al., *The effect of massive neutrinos on the matter power spectrum*, Mon. Not. R. Astron. Soc. **410**, 3 (2011) 1647–1654.

[ALE98] ALEPH Collaboration, R. Barate et al., *An upper limit on the τ neutrino mass from three-and five-prong τ decays*, Eur. Phys. J. C **2**, 3 (1998) 395–406.

[ALE06] ALEPH, DELPHI, L3, OPAL, SLD Collaborations, the LEP Electroweak Working Group, the SLD Electroweak and Heavy Flavour Groups, *Precision electroweak measurements on the Z resonance*, Phys. Rep. **427**, 5 (2006) 257–454.

[Alt01] R. Altkorn et al., *Intensity Considerations in Liquid Core Optical Fiber Raman Spectroscopy*, Appl. Spectrosc. **55**, 4 (2001) 373–381.

[Ams15] J. Amsbaugh et al., *Focal-plane detector system for the KATRIN experiment*, Nucl. Instrum. Methods Phys. Res., Sect. A **778** (2015) 40–60.

[And04] D. R. Anderson et al., *Troubleshooting Optical Fiber Networks*, Academic Press, San Diego, CA, USA, 2nd edition (2004).

[Ass96] K. Assamagan et al., *Upper limit of the muon-neutrino mass and charged-pion mass from momentum analysis of a surface muon beam*, Phys. Rev. D **53**, 11 (1996) 6065.

[AST13] ASTM International, *ASTM B832-93(2013), Standard Guide for Electroforming with Nickel and Copper*, Book of Standards Volume 02.05, West Conshohocken, PA, USA (2013).

[Atk06] P. W. Atkins et al., *Physical chemistry*, Oxford University Press, Oxford, UK, 8th edition (2006).

[Bab12] M. Babutzka et al., *Monitoring of the properties of the KATRIN Windowless Gaseous Tritium Source*, New J. Phys. **14** (2012) 103046.

[Bab14] M. Babutzka, *Design and development for the Rearsection of the KATRIN experiment*, Ph.D. thesis, Karlsruhe Institute of Technology (2014).

[Bab15] S. Babar et al., *Optical constants of Cu, Ag, and Au revisited*, Appl. Opt. **54**, 3 (2015) 477–481.

[Bac03] H. Bach et al., *Thin Films on Glass*, Springer, Berlin/Heidelberg, Germany, 1st edition (2003).

[Bah64] J. N. Bahcall, *Solar neutrinos. I. Theoretical*, Phys. Rev. Lett. **12**, 11 (1964) 300.

[Bah76] J. N. Bahcall et al., *Solar neutrinos: a scientific puzzle*, Science **191** (1976) 264–267.

[Bar56] W. H. Barkas et al., *Mass-ratio method applied to the measurement of L-meson masses and the energy balance in pion decay*, Phys. Rev. **101**, 2 (1956) 778.

[Bau04] P. Baumeister, *Optical Coating Technology*, SPIE Press monograph, SPIE Optical Engineering Press, Bellingham, WA, USA (2004).

[BC14] G. B. e. a. Borexino Collaboration, *Neutrinos from the primary proton-proton fusion process in the Sun*, Nature **512**, 7515 (2014) 383–386.

[Bel95a] A. I. Belesev et al., *Results of the Troitsk experiment on the search for the electron antineutrino rest mass in tritium beta-decay*, Phys. Lett. B **350**, 2 (1995) 263–272.

[Bel95b] G. Bellanger, *Embrittlement of palladium and palladium-silver alloy cathode membranes by tritium*, Fusion Technol. **27**, 1 (1995) 36–45.

[Bet34] H. Bethe et al., *The 'neutrino'*, Nature **133**, 3362 (1934) 532.

[Blo67] N. Bloembergen, *The Stimulated Raman Effect*, Am. J. Phys. **35**, 11 (1967) 989–1023.

[Bod15] L. I. Bodine et al., *Assessment of molecular effects on neutrino mass measurements from tritium beta decay*, Phys. Rev. C **91**, 3 (2015) 035505.

[Bor05] B. Bornschein et al., *Successful experimental verification of the Tokamak Exhaust Processing concept of ITER with the CAPER facility*, Fusion Sci. Technol. **48**, 1 (2005) 11–16.

[Bor08] B. Bornschein, *Absolute Neutrino Mass Measurements*, in F. Soler et al., editors, *Neutrinos in Particle Physics, Astrophysics and Cosmology*, Scottish Graduate Series, CRC Press, Boca Raton, FL, USA (2008), pp. 261–286.

[Bor10] B. Bortnik et al., *Rugged compact metallized capillary Raman probe for material identification in hostile environments*, IEEE Aerospace Conference Proceedings (2010) 1–7.

[Bor11] B. Bornschein, *Between Fusion and Cosmology - The Future of the Tritium Laboratory Karlsruhe*, Fusion Sci. Technol. **60**, 3 (2011) 1088–1091.

[Bor13] B. Bornschein et al., *Tritium management and safety issues in ITER and DEMO breeding blankets*, Fusion Eng. Des. **88**, 6 (2013) 466–471.

[Bur10] M. P. Buric et al., *Multimode metal-lined capillaries for Raman collection and sensing*, J. Opt. Soc. Am. B **27**, 12 (2010) 2612–2619.

[Bur12] M. P. Buric et al., *Field tests of the Raman gas composition sensor*, FIIW 2012 - 2012 Future of Instrumentation International Workshop Proceedings (2012) 29–32.

[Bur13] M. P. Buric et al., *Design and industrial testing of ultra-fast multi-gas Raman spectrometer*, Proc. of SPIE **8726** (2013) 87260.

[Bus09] G. Buscarino et al., *Polyamorphic transformation induced by electron irradiation in a-SiO_2 glass*, Phys. Rev. B **80**, 9 (2009) 094202.

[Cap14] F. Capozzi et al., *Status of three-neutrino oscillation parameters, circa 2013*, Physical Review D **89**, 9 (2014) 093018.

[Car96] W. F. Carlsen et al., *System for collecting weakly scattered radiation*, US Patent No. 5,506,678 (1996).

[Cas85a] G. R. Caskey Jr., *Effects of tritium on material properties*, Technical report, E. I. du Pont de Nemours & Co., Savannah River Laboratory (1985).

[Cas85b] G. R. Caskey Jr., *Tritium-helium effects in metals*, Technical report, E. I. du Pont de Nemours & Co., Savannah River Laboratory (1985).

[Cha14] J. Chadwick, *Intensitätsverteilung im magnetischen Spectrum der β-Strahlen von Radium B + C*, Verhandl. Dtsc. Phys. Ges. **16** (1914) 383.

[Cha89] A. Chambers et al., editors, *Basic vacuum technology*, Hilger, Bristol, UK (1989).

[Cha05] C. Charlton et al., *Midinfrared sensors meet nanotechnology: Trace gas sensing with quantum cascade lasers inside photonic band-gap hollow waveguides*, Appl. Phys. Lett. **86**, 19 (2005) 194102.

[Cla07] E. A. Clark et al., *Effects of Tritium Exposure on UHMW-PE , PTFE, and Vespel Polyimide*, Fus. Sci. Techn. **52** (2007) 1007–1011.

[Coh77] C. Cohen-Tannoudji et al., *Quantum mechanics*, volume 1, Wiley, New York, NY, USA (1977).

[Cra08] R. J. Crase et al., *Optical Thin-Film Coating Methods*, Photonics Spectra (2008), `http://www.photonics.com/Article.aspx?PID=5&VID=22&IID=158&AID=35232`, accessed: 04.03.2016.

[Dan62] G. Danby et al., *Observation of high-energy neutrino reactions and the existence of two kinds of neutrinos*, Phys. Rev. Lett. **9**, 1 (1962) 36.

[Dan81] S. A. Danichkin et al., *Raman scattering parameters for gas molecules (survey)*, J. Appl. Spectrosc. **35**, 4 (1981) 1057–1066.

[Day16] Daya Bay Collaboration, F. P. An et al., *Measurement of the Reactor Antineutrino Flux and Spectrum at Daya Bay*, Phys. Rev. Lett. **116** (2016) 061801.

[Dem06] W. Demtröder, *Experimentalphysik: Elektrizität und Optik*, volume 2, Springer-Verlag, Berlin, Germany, 4th edition (2006).

[Dem08a] W. Demtröder, *Laser spectroscopy 1: Basic principles*, Springer, Berlin, Germany, 4th edition (2008).

[Dem08b] W. Demtröder, *Laser spectroscopy 2: Experimental techniques*, Springer, Berlin, Germany, 4th edition (2008).

[Dem11] D. Demange et al., *CAPER modifications and first experimental results on highly tritiated water processing with PERMCAT at the Tritium Laboratory Karlsruhe*, Fusion Sci. Technol. **60**, 4 (2011) 1317–1322.

[Dem13] W. Demtröder, *Experimentalphysik 2: Elektrizität und Optik*, Springer, Berlin/Heidelberg, Germany, 6th edition (2013).

[Des15] E. Desimoni et al., *About Estimating the Limit of Detection by the Signal to Noise Approach*, Pharm. Anal. Acta **6**, 4 (2015) 1000355.

[Dev94] R. A. B. Devine, *Macroscopic and microscopic effects of radiation in amorphous SiO_2*, Nucl. Instrum. Methods Phys. Res., Sect. B **91** (1994) 378–390.

[Dav64] R. Davis Jr, *Solar neutrinos. II. Experimental*, Phys. Rev. Lett. **12**, 11 (1964) 303.

[Dav68] R. Davis Jr et al., *Search for neutrinos from the sun*, Phys. Rev. Lett. **20**, 21 (1968) 1205.

[Dok07] Doko Engineering, *Hollow glass fibers for infrared lasers*, Product specifications (2007), `http://www.do-ko.jp/specs.html`, accessed: 08.02.2016.

[Dos06] N. Doss et al., *Molecular effects in investigations of tritium molecule β decay endpoint experiments*, Phys. Rev. C **73** (2006) 025502.

[Dos07] N. Doss, *Calculated final state probability distributions for T_2 β-decay measurements*, Ph.D. thesis, University College London (2007).

[Dou12] Double Chooz Collaboration, Y. Abe et al., *Reactor ν_e disappearance in the Double Chooz experiment*, Phys. Rev. D **86**, 5 (2012) 052008.

[Dre13] G. Drexlin et al., *Current direct neutrino mass experiments*, Adv. High Energy Phys. **2013** (2013) 1–39.

[Eag62] C. C. Eaglesfield, *Optical pipeline: a tentative assessment*, Proceedings of the IEE-Part B: Electronic and Communication Engineering **109**, 43 (1962) 26–32.

[ECH14] ECHo Collaboration, L. Gastaldo et al., *The Electron Capture ^{163}Ho Experiment ECHo*, J. Low Temp. Phys. **176**, 5-6 (2014) 876–884.

[Efr08] E. Efremov et al., *Achievements in resonance Raman spectroscopy - Review of a technique with a distinct analytical chemistry potential*, Anal. Chim. Acta **606** (2008) 119–134.

[Epn14a] Epner Technology Inc., *Laser Gold*, Processes and products (2014), `http://www.epner.com/processes-and-products/laser-gold/`, accessed: 24.02.2016.

[Epn14b] Epner Technology Inc., *Light Pipes*, Capabilities (2014), `http://www.epner.com/capabilities/light-pipes/`, accessed: 24.02.2016.

[Fel98] G. J. Feldman et al., *Unified approach to the classical statistical analysis of small signals*, Phys. Rev. D **57** (1998) 3873–3889.

[Fer34] E. Fermi, *Versuch einer Theorie der β-Strahlen. I*, Zeitschrift für Physik **88**, 3-4 (1934) 161–177.

[Fey58] R. P. Feynman et al., *Theory of the Fermi Interaction*, Phys. Rev. **109** (1958) 193–198.

[Fis11] S. Fischer et al., *Monitoring of tritium purity during long-term circulation in the KATRIN test experiment LOOPINO using laser Raman spectroscopy*, Fusion Sci. Technol. **60** (2011) 925–930.

[Fis14] S. Fischer, *Commissioning of the KATRIN Raman system and durability studies of optical coatings in glove box and tritium atmospheres*, Ph.D. thesis, Karlsruhe Institute of Technology (2014).

[Fis15] S. Fischer et al., *Investigation of durability of optical coatings in highly purified tritium gas*, Fusion Sci. Technol. **67** (2015) 76–79.

[Fle74] M. Fleischmann et al., *Raman spectra of pyridine absorbed at a silver electrode*, Chem. Phys. Lett. **26**, 2 (1974) 163–166.

[Fra85] J. Franey et al., *The corrosion of silver by atmospheric sulfurous gases*, Corros. Sci. **25**, 2 (1985) 133–143.

[GAL99] GALLEX Collaboration, W. Hampel et al., *GALLEX solar neutrino observations: Results for GALLEX IV*, Phys. Lett. B **447**, 1 (1999) 127–133.

[Gar14] A. Garfagnini, *Neutrinoless double beta decay experiments*, in *Int. J. Mod. Phys.: Conference Series*, volume 31, World Scientific (2014), p. 1460286.

[GER15] GERDA Collaboration, M. Agostini et al., *Limit on Neutrinoless Double Beta Decay of ^{76}Ge by GERDA*, Physics Procedia **61** (2015) 828–837.

[Gib60] J. B. Gibson et al., *Dynamics of Radiation Damage*, Phys. Rev. **120** (1960) 1229–1253.

[Gil80] J. T. Gill, *Effect of container preparation on the growth of protium and methane impurities into tritium gas*, J. Vac. Sci. Technol. **17**, 2 (1980) 645–654.

[Giu12] A. Giuliani et al., *Neutrinoless double-beta decay*, Adv. High Energy Phys. **2012** (2012) 1–38.

[Glü13] F. Glück et al., *Electromagnetic design of the large-volume air coil system of the KATRIN experiment*, New J. Phys. **15**, 8 (2013) 083025.

[GNO05] GNO Collaboration, M. Altmann et al., *Complete results for five years of GNO solar neutrino observations*, Phys. Lett. B **616**, 3 (2005) 174–190.

[Gol58] M. Goldhaber et al., *Helicity of Neutrinos*, Phys. Rev. **109** (1958) 1015–1017.

[Gri69] V. Gribov et al., *Neutrino astronomy and lepton charge*, Phys. Lett. B **28**, 7 (1969) 493–496.

[Gro06] J. Gross, *Mass Spectrometry: A Textbook*, Springer, Berlin/Heidelberg, Germany (2006).

[Gro13] S. Grohmann et al., *The thermal behaviour of the tritium source in KATRIN*, Cryogenics **55-56** (2013) 5–11.

[Gro15] S. Groh, *Modeling of the response function and measurement of the transmission properties of the KATRIN experiment*, Ph.D. thesis, Karlsruhe Institute of Technology (2015).

[Gui90] G. Guilbault, *Practical Fluorescence*, Modern Monographs in Analytical Chemistry, Taylor & Francis, 2nd edition (1990).

[Hak06] H. Haken et al., *Molekülphysik und Quantenchemie: Einführung in die experimentellen und theoretischen Grundlagen*, Springer, Berlin, Germany, 5th edition (2006).

[Han04] S. Hannestad, *Neutrinos in cosmology*, New J. Phys. **6** (2004) 108.

[Han14] S. Hanf et al., *Fiber-enhanced Raman multigas spectroscopy: A versatile tool for environmental gas sensing and breath analysis*, Anal. Chem. **86**, 11 (2014) 5278–5285.

[Hay05] C. Haynes et al., *Surface-Enhanced Raman Spectroscopy*, Anal. Chem. **77**, 17 (2005) 338A–346A.

[Hay13] W. Haynes, *CRC Handbook of Chemistry and Physics*, CRC Press, Boca Raton, FL, USA, 94th edition (2013).

[Her63] G. Herzberg, *Molecular Spectra and Molecular Structure: I. Spectra of Diatomic Molecules*, D. Van Nostrand Company, Inc., Princeton, NJ, USA (1963).

[Hip15] M. Hippler, *Cavity-Enhanced Raman Spectroscopy of Natural Gas with Optical Feedback cw-Diode Lasers*, Anal. Chem. **87** (2015) 7803–7809.

[Höt12] M. Hötzel, *Simulation and analysis of source-related effects for KATRIN*, Ph.D. thesis, Karlsruhe Institute of Technology (2012).

[Ice14] IceCube-PINGU Collaboration, M. G. Aartsen et al., *Letter of Intent: The Precision IceCube Next Generation Upgrade (PINGU)*, arXiv preprint **arXiv:1401.2046** (2014).

[IUP76] International Union of Pure and Applied Chemistry (IUPAC), Analytical Chemistry Division, *Nomenclature, Symbols, Units and their Usage in Spectrochemical Analysis - II. Data Interpretation*, Pure Appl. Chem. **45** (1976) 99–103.

[IUP97] International Union of Pure and Applied Chemistry (IUPAC), Analytical Chemistry Division, *A statistical overview of standard (IUPAC and ACS) and new procedures for determining the limits of detection and quantification: Application to voltametric and stripping techniques*, Pure Appl. Chem. **69**, 2 (1997) 297–328.

[Jam13a] T. M. James, *Quantitative Raman spectroscopy of gases related to KATRIN*, Ph.D. thesis, Swansea University, Wales (2013).

[Jam13b] T. M. James et al., *Automated quantitative spectroscopic analysis combining background subtraction, cosmic ray removal, and peak fitting*, Appl. spectrosc. **67**, 8 (2013) 949–959.

[Jam15] T. M. James et al., *Trace gas and dynamic process monitoring by Raman spectroscopy in metal-coated hollow glass fibres*, Anal. Methods **7**, 6 (2015) 2568–2576.

[Jan15] A. Jansen, *The Cryogenic Pumping Section of the KATRIN Experiment – Design Studies and Experiments for the Commissioning*, Ph.D. thesis, Karlsruhe Institute of Technology (2015).

[Jin13] W. Jin et al., *Photonic crystal fibers, devices, and applications*, Front. Optoelectron. **6**, 1 (2013) 3.

[GUM08] Joint Committee for Guides in Metrology, *JCGM 100: Evaluation of Measurement Data - Guide to the Expression of Uncertainty in Measurement*, Technical report, JCGM (2008).

[Jou08] K. H. Jousten, editor, *Handbook of vacuum technology*, WILEY-VCH, Weinheim, Germany (2008).

[JUN16] JUNO Collaboration, F. An et al., *Neutrino physics with JUNO*, J. Phys. G: Nucl. Part. Phys. **43**, 3 (2016) 030401.

[Käf12] W. Käfer, *Sensitivity studies of the KATRIN experiment*, Ph.D. thesis, Karlsruhe Institute of Technology (2012).

[Kam11] KamLAND Collaboration, A. Gando et al., *Constraints on θ_{13} from a three-flavor oscillation analysis of reactor antineutrinos at KamLAND*, Phys. Rev. D **83**, 5 (2011) 052002.

[KAT05] KATRIN collaboration, J. Angrik et al., *KATRIN Design Report 2004*, FZKA Scientific Report **7090** (2005).

[KAT16] KATRIN Collaboration, M. Arenz et al., *Commissioning of the vacuum system of the KATRIN Main Spectrometer*, J. Instrum. **11**, 04 (2016) P04011.

[Kay08] B. Kayser, *Neutrino Oscillation Phenomenology*, in F. Soler et al., editors, *Neutrinos in Particle Physics, Astrophysics and Cosmology*, Scottish Graduate Series, CRC Press, Boca Raton, FL, USA (2008), pp. 51–64.

[Kay12] Kaye & Laby Online, *Tables of Physical & Chemical Constants. 3.1.4 Composition of the Earth's atmosphere*, Version 2.0 (2012), `http://www.kayelaby.npl.co.uk/chemistry/3_1/3_1_4.html`, accessed: 07.04.2016.

[Kra08] S. Kraft-Bermuth et al., *Development and characterization of microcalorimeters for a next generation ^{187}Re beta-decay experiment*, J. Low Temp. Phys. **151**, 3-4 (2008) 619–622.

[Kei14] R. Keiner et al., *Enhanced Raman multigas sensing – a novel tool for control and analysis of $^{13}CO_2$ labeling experiments in environmental research*, Analyst **139**, 16 (2014) 3879–3884.

[Kla06] H. V. Klapdor-Kleingrothaus et al., *The evidence for the observation of $0\nu\beta\beta$ decay: the identification of $0\nu\beta\beta$ events from the full spectra*, Mod. Phys. Lett. A **21**, 20 (2006) 1547–1566.

[Kni98] J. Knight et al., *Large mode area photonic crystal fibre*, Electron. Lett. **34**, 13 (1998) 1347–1348.

[Kni16] Knight Optical (UK) Ltd, *Optical coatings: Protected aluminium / visible use (MV2)*, Product specifications (2016), `https://www.knightoptical.com/_public/documents/1383918552_coatingmirror450650nmprotvismv2.pdf`, accessed: 17.03.2016.

[Kod01] K. Kodama et al., *Observation of tau neutrino interactions*, Phys. Lett. B **504**, 3 (2001) 218–224.

[Kom05] Y. Komachi et al., *Raman probe using a single hollow waveguide.*, Opt. Lett. **30**, 21 (2005) 2942–2944.

[Kra05] C. Kraus et al., *Final results from phase II of the Mainz neutrino mass search in tritium β decay*, Eur. Phys. J. C **40** (2005) 447–468.

[Kru83] P. Kruit et al., *Magnetic field paralleliser for 2π electron-spectrometer and electron-image magnifier*, J. Phys. E: Sci. Instrum. **16**, 4 (1983) 313.

[Kry96] V. Krylov et al., *Stimulated Raman amplification of femtosecond pulses in hydrogen gas*, Opt. Lett. **21**, 24 (1996) 2005–2007.

[Kuc16] L. Kuckert, *The windowless gaseous tritium source of the KATRIN experiment – Characterisation of gas dynamical and plasma properties*, Ph.D. thesis, Karlsruhe Institute of Technology (2016).

[Kun08] Y. Kuno, *Superbeam, Beta Beam, and Neutrino Factory*, in F. Soler et al., editors, *Neutrinos in Particle Physics, Astrophysics and Cosmology*, Scottish Graduate Series, CRC Press, Boca Raton, FL, USA (2008), pp. 301–300.

[Las04] R. Lascola et al., *Isotopic hydrogen analysis via conventional and surface-enhanced fiber optic Raman spectroscopy*, Proc. SPIE **5586** (2004).

[Las16] Laser Quantum, *gem – High specification OEM CW lasers*, Data sheet (2016), `http://www.laserquantum.com/download-ds.cfm?id=773`, accessed: 07.04.2016.

[Lei14] B. Leiber, *Investigations of background due to secondary electron emission in the KATRIN-experiment*, Ph.D. thesis, Karlsruhe Institute of Technology (2014).

[Lew07] R. Lewis, *Development of a Raman System for In-Line Monitoring of Tritium at the Karlsruhe Tritium Neutrino (KATRIN) Experiment*, Ph.D. thesis, Swansea University (2007).

[Li11] J.-F. Li et al., *Core-shell nanoparticle based SERS from hydrogen adsorbed on a rhodium(111) electrode*, Chem. Commun. **47** (2011) 2023–2025.

[Løv02] O. M. Løvvik et al., *Density functional calculations on hydrogen in palladium-silver alloys*, J. Alloys Compd., Proceedings of the International Symposium on Metal-Hydrogen Systems, Fundamentals and Applications (MH2000) **330–332** (2002) 332 – 337.

[Lob85] V. Lobashev et al., *A method for measuring the electron antineutrino rest mass*, Nucl. Instrum. Methods Phys. Res., Sect. A **240**, 2 (1985) 305–310.

[Lon83] G. L. Long et al., *Limit of Detection: A closer look at the IUPAC definition*, Anal. Chem. **55**, 7 (1983) A712–A724.

[Lon02] D. A. Long, *The Raman effect: a unified treatment of the theory of Raman scattering by molecules*, Wiley, Chichester, UK (2002).

[Lor02] T. J. Loredo et al., *Bayesian analysis of neutrinos observed from supernova SN 1987A*, Phys. Rev. D **65**, 6 (2002) 063002.

[Lou72] M. Louthan et al., *Hydrogen embrittlement of metals*, Mater. Sci. Eng. **10** (1972) 357–368.

[Luc62] P. G. Lucasson et al., *Production and Recovery of Electron-Induced Radiation Damage in a Number of Metals*, Phys. Rev. **127** (1962) 485–500.

[Luk12] S. Lukić et al., *Measurement of the gas-flow reduction factor of the KATRIN DPS2-F differential pumping section*, Vacuum **86**, 8 (2012) 1126–1133.

[Mac80] D. MacDougall et al., *Guidelines for data acquisition and data quality evaluation in environmental chemistry*, Anal. Chem. **52**, 14 (1980) 2242–2249.

[Mac01] H. Macleod, *Thin-Film Optical Filters*, Series in Optics and Optoelectronics, CRC Press, Boca Raton, FL, USA, 3rd edition (2001).

[Mae96] C. F. Maes et al., *Laser induced fluorescence in fused silica and other optical materials*, SPIE Proceedings **2705** (1996) 93–102.

[Mak62] Z. Maki et al., *Remarks on the unified model of elementary particles*, Progr. Theoret. Phys. **28**, 5 (1962) 870–880.

[Mal65] I. Malitson, *Interspecimen Comparison of the Refractive Index of Fused Silica*, J. Opt. Soc. Am. **55**, 10 (1965) 1205–1209.

[Mar64] E. Marcatili et al., *Hollow metallic and dielectric waveguides for long distance optical transmission and lasers*, Bell Syst. Techn. J. **43**, 4 (1964) 1783–1809.

[MAR13] MARE collaboration, E. Ferri et al., *Neutrino mass measurement with ^{187}Re and ^{163}Ho in the framework of MARE*, Nucl. Phys. B Proc. Suppl. **237** (2013) 54–56.

[Mat90] Y. Matsuura et al., *Loss reduction of dielectric-coated metallic hollow waveguides for CO_2 laser light transmission*, Opt. Laser Technol. **22**, 2 (1990) 141–145.

[Mat98] Y. Matsuura et al., *Flexible hollow waveguides for delivery of excimer-laser light.*, Opt. Lett. **23**, 15 (1998) 1226–1228.

[McC05] R. L. McCreery, *Raman Spectroscopy for Chemical Analysis*, John Wiley and Sons Inc. New York, NY, USA (2005).

[McC06] R. L. McCreery, *Photometric Standards for Raman Spectroscopy*, in: Handbook of Vibrational Spectroscopy, John Wiley and Sons, Hoboken, NJ, USA (2006).

[Mer13] S. Mertens et al., *Background due to stored electrons following nuclear decays in the KATRIN spectrometers and its impact on the neutrino mass sensitivity*, Astropart. Phys. **41** (2013) 52–62.

[Mes15] D. Meschede, *Gerthsen Physik*, Springer Spektrum, Berlin/Heidelberg, Germany, 25th edition (2015).

[MIN14] MINOS Collaboration, P. Adamson et al., *Combined analysis of ν_μ disappearance and $\nu_\mu \rightarrow \nu_e$ appearance in MINOS using accelerator and atmospheric neutrinos*, Phys. Rev. Lett. **112**, 19 (2014) 191801.

[Mit96] J. R. Mitchell, *Diode laser pumped Raman gas analysis system with reflective hollow tube gas cell*, US Patent No. 5,521,703 (1996).

[MKS16] MKS Instruments, *HPQ3 High Pressure RGA*, Product specifications (2016), `http://www.mksinst.com/docs/UR/HPQ3-HPQ3S-specifications.aspx`, accessed: 03.05.2016.

[Moh07] R. N. Mohapatra et al., *Theory of neutrinos: a white paper*, Rep. Progr. Phys. **70**, 11 (2007) 1757.

[Mon09] B. Monreal et al., *Relativistic cyclotron radiation detection of tritium decay electrons as a new technique for measuring the neutrino mass*, Phys. Rev. D **80**, 5 (2009) 051301.

[New16] Newport Corporation, *Fiber Optic Coupling: Coupling Laser Light into a Single-Mode Fiber*, Technical note (2016), `http://www.newport.com/Fiber-Optic-Coupling/144877/1033/content.aspx`, accessed: 09.03.2016.

[NKT13] NKT photonics, *aeroGUIDE-Power: Broadband High Power PM Fiber Delivery*, Data sheet (2013), `http://www.nktphotonics.com/wp-content/uploads/2015/03/aeroGUIDE-POWER.pdf`, accessed: 08.03.2016.

[NKT14] NKT photonics, *LMA-PM-15: Single mode 15 µm polarization-maintaining fiber*, Data sheet (2014), `http://www.nktphotonics.com/wp-content/uploads/2015/01/LMA-PM-15.pdf`, accessed: 08.03.2016.

[Nor74] C. B. Norris et al., *Ionization dilatation effects in fused silica from 2 to 18 keV electron irradiation*, J. Appl. Phys. **45**, 9 (1974) 3876–3882.

[NOv07] NOvA Collaboration, D. S. Ayres et al., *The NOvA Technical Design Report*, FERMILAB-DESIGN-2007-01 (2007), available online: `http://inspirehep.net/record/774999/files/fermilab-design-2007-01.pdf?version=1` (accessed: 09.05.2016).

[Oer16] Oerlikon Leybold Vacuum GmbH, *TURBOVAC MAG W 2800*, Technical Data (2016), `https://leyboldproducts.oerlikon.com/de/de/produktkatalog_03.aspx?cid=40_10_20_100`, accessed: 03.05.2016.

[Off15] A. Off, *Untersuchungen zur Fluoreszenzreduzierung in einem Kapillar-Raman-System für hochsensitive Gasanalytik am Tritiumlabor Karlsruhe (TLK)*, Master's thesis, Karlsruhe Institute of Technology (2015).

[Oki10] Y. Okita et al., *A Raman cell based on hollow optical fibers for breath analysis*, Proc. of SPIE **7559** (2010) 755908.

[Osa95] M. Osawa et al., *Fabrication of fluorocarbon polymer-coated silver hollow-glass waveguides for the infrared by the liquid-phase coating method*, Opt. Laser Technol. **27**, 6 (1995) 393–396.

[Ove14] G. Overton, *Photonic Materials: Epner gold: The Midas touch for laser cavities and sensing applications*, Laser Focus World **50**, 4 (2014).

[Pag10] G. Pagliaroli et al., *Neutrino mass bound in the standard scenario for supernova electronic antineutrino emission*, Astropart. Phys. **33**, 5 (2010) 287–291.

[PDG14] Particle Data Group, K. A. Olive et al., *Review of particle physics*, Chin. Phys. C **38**, 9 (2014) 090001.

[Pas08] S. Pastor, *Cosmological Aspects of Neutrino Physics*, in F. Soler et al., editors, *Neutrinos in Particle Physics, Astrophysics and Cosmology*, Scottish Graduate Series, CRC Press, Boca Raton, FL, USA (2008), pp. 357–382.

[Pau30] W. Pauli, *Offener Brief an die Gruppe der Radioaktiven bei der Gauvereins-Tagung zu Tübingen (1930).*, In: Wissenschaftlicher Briefwechsel mit Bohr, Einstein, Heisenberg u.a., Band II: 1930 – 1939, Springer, Berlin/Heidelberg, Germany (1985).

[Pea08a] W. F. Pearman et al., *Multipass capillary cell for enhanced Raman measurements of gases.*, Appl. Spectrosc. **62**, 3 (2008) 285–289.

[Pea08b] W. F. Pearman et al., *Quantitative measurements of CO_2 and CH_4 using a multipass Raman capillary cell.*, Appl. Opt. **47**, 25 (2008) 4627–32.

[Per09] D. H. Perkins, *Particle astrophysics*, Oxford University Press, Oxford, UK, 2nd edition (2009).

[Pfe16] Pfeiffer Vacuum GmbH, *HiPace 300*, Product details (2016), `https://www.pfeiffer-vacuum.com/en/products/turbopumps/hybrid-bearing/hipace-300/?request_locale=en_US`, accessed: 03.05.2016.

[Pic92] A. Picard et al., *A solenoid retarding spectrometer with high resolution and transmission for keV electrons*, Nucl. Instrum. Methods Phys. Res., Sect. B **63**, 3 (1992) 345–358.

[Pin12] A. M. R. Pinto et al., *Photonic Crystal Fibers for Sensing Applications*, J. Sens. **2012** (2012) 1–21.

[Pla14] Planck Collaboration, P. A. R. Ade et al., *Planck 2013 results. XVI. Cosmological parameters*, Astron. Astrophys. **571** (2014) A16.

[Pla15a] Planck Collaboration, P. A. R. Ade et al., *Planck 2015 results. XIII. Cosmological parameters*, arXiv preprint **arXiv:1502.01589v2** (2015).

[Pla15b] Planck Collaboration, R. Adam et al., *Planck 2015 results. I. Overview of products and scientific results*, arXiv preprint **arXiv:1502.01582v2** (2015).

[Pon58] B. Pontecorvo, *Inverse beta processes and nonconservation of lepton charge*, Sov. Phys. JETP **7** (1958) 172–173.

[Pon68] B. Pontecorvo, *Neutrino experiments and the problem of conservation of leptonic charge*, Sov. Phys. JETP **26**, 5 (1968) 984–988.

[Pra12] M. Prall et al., *The KATRIN pre-spectrometer at reduced filter energy*, New J. Phys. **14**, 7 (2012) 073054.

[Pri13a] F. Priester, *Tritiumtechnologie für die fensterlose Quelle WGTS von KATRIN*, Ph.D. thesis, Karlsruhe Institute of Technology (2013).

[Pri13b] F. Priester et al., *TriToP – A compatibility experiment with turbomolecular pumps under tritium atmosphere*, Vacuum **98**, 0 (2013) 22–28.

[Pri15a] F. Priester et al., *Commissioning and detailed results of KATRIN inner loop tritium processing system at Tritium Laboratory Karlsruhe*, Vacuum **116** (2015) 42–47.

[Pri15b] Princeton Instruments, *PIXIS System*, Manual (2015), `ftp://ftp.princetoninstruments.com/public/Manuals/Princeton%20Instruments/PIXIS%20System%20Manual.pdf`, accessed: 01.04.2016.

[Pro13] Project 8 Collaboration, P. J. Doe et al., *Project 8: Determining neutrino mass from tritium beta decay using a frequency-based method*, arXiv preprint **arXiv:1309.7093** (2013).

[Rae10] S. Rae et al., *Surface enhanced Raman spectroscopy (SERS) sensors for gas analysis*, Analyst **135** (2010) 1365–1369.

[Rak98] A. D. Rakić et al., *Optical properties of metallic films for vertical-cavity optoelectronic devices*, Appl. Opt. **37**, 22 (1998) 5271–5283.

[Ram28] C. V. Raman et al., *A New Type of Secondary Radiation*, Nature **121** (1928) 501–502.

[Ran12] P.-O. Ranitzsch et al., *Development of metallic magnetic calorimeters for high precision measurements of calorimetric ^{187}Re and ^{163}Ho spectra*, J. Low Temp. Phys. **167**, 5-6 (2012) 1004–1014.

[Rei56] F. Reines et al., *The Neutrino*, Nature **178** (1956) 446–449.

[REN15] RENO Collaboration, J. H. Choi et al., *Observation of Energy and Baseline Dependent Reactor Antineutrino Disappearance in the RENO Experiment*, arXiv preprint **arXiv:1511.05849** (2015).

[Ric81] D. Rice et al., *Atmospheric Corrosion of Copper and Silver*, J. Electrochem. Soc. **128**, 2 (1981).

[Rob91] R. G. H. Robertson et al., *Limit on $\overline{\nu}_e$ mass from observation of the β decay of molecular tritium*, Phys. Rev. Lett. **67** (1991) 957–960.

[Röl13] M. Röllig et al., *Activity monitoring of a gaseous tritium source by beta induced X-ray spectrometry*, Fusion Eng. Des. **88**, 6–8 (2013) 1263–1266, proceedings of the 27th Symposium On Fusion Technology (SOFT-27); Liège, Belgium, September 24-28, 2012.

[Röl15] M. Röllig, *Tritium analytics by beta induced X-ray spectrometry*, Ph.D. thesis, Karlsruhe Institute of Technology (2015).

[Rup15] S. Rupp et al., *Improving the Detection Limit in a Capillary Raman System for In Situ Gas Analysis by Means of Fluorescence Reduction*, Sensors **15**, 9 (2015) 23110–23125.

[Rus03] P. Russell, *Photonic Crystal Fibers*, Science **299** (2003) 358–362.

[Rus06] P. S. J. Russell, *Photonic-Crystal Fibers*, J. Lightwave Technol. **24**, 12 (2006) 4729–4749.

[SAG02] SAGE Collaboration, J. N. Abdurashitov et al., *Solar neutrino flux measurements by the Soviet-American gallium experiment (SAGE) for half the 22-year solar cycle*, J. Exp. Theor. Phys. **95**, 2 (2002) 181–193.

[Sal12] R. Salter et al., *Cavity-enhanced Raman spectroscopy with optical feedback cw diode lasers for gas phase analysis and spectroscopy*, Analyst **137**, 20 (2012) 4669.

[Sch09] M. Schlösser, *First Laser Raman measurements with tritium for KATRIN and studies of systematic effects of the LARA system*, Diploma thesis, Karlsruhe Institute of Technology (2009), available online: `https://www.katrin.kit.edu/publikationen/091216_MS_diploma_thesis_with_Cover.pdf` (accessed: 09.05.2016).

[Sch10] Schott AG, *Fluorescence of optical glass*, TIE36: Technical Information – Advanced Optics (2010), `http://www.schott.com/advanced_optics/german/download/schott_tie-36_fluorescence_of_optical_glass_eng.pdf`, accessed: 15.03.2016.

[Sch11a] M. Schlösser et al., *Design Implications for Laser Raman Measurement Systems for Tritium Sample-Analysis, Accountancy or Process-Control Applications*, Fusion Sci. Technol. **60** (2011) 976–981.

[Sch11b] K. Schönung, *Entwicklung eines Experiments zur Untersuchung optischer Fenster in Tritiumumgebung und Bewertung der ersten Untersuchungen*, Diploma thesis, Karlsruhe Institute of Technology (2011), available online: `https://www.katrin.kit.edu/publikationen/dth_KSchoenung.pdf` (accessed: 09.05.2016).

[Sch13a] V. Schäfer, *Charakterisierung des "Coating Test Experiments" zur Verbesserung der Langzeitstabilität und der Reproduzierbarkeit*, Diploma thesis, Karlsruhe Institute of Technology (2013), available online: `https://www.katrin.kit.edu/publikationen/1dth-VeraSchaefer-2013.pdf` (accessed: 09.05.2016).

[Sch13b] M. Schlösser, *Accurate calibration of the Raman system for the Karlsruhe Tritium Neutrino Experiment*, Ph.D. thesis, Karlsruhe Institute of Technology (2013).

[Sch13c] M. Schlösser et al., *Accurate calibration of the laser Raman system for the Karlsruhe Tritium Neutrino Experiment*, J. Mol. Struct. **1044** (2013) 61–66.

[Sch13d] M. Schlösser et al., *Evaluation method for Raman depolarization measurements including geometrical effects and polarization aberrations*, J. Raman Spectrosc. **44**, 3 (2013) 453–462.

[Sch14a] Schäfter+Kirchhoff GmbH, *Fiber Collimators: Fiber Couplers 60FC-SMA-... for SMA-905 High Power Connectors*, Catalog extract (2014), `http://www.sukhamburg.com/download/fk60fc_e.pdf`, accessed: 09.03.2016.

[Sch14b] J. Schwarz, *The detector system of the KATRIN experiment – Implementation and first measurements with the spectrometer*, Ph.D. thesis, Karlsruhe Institute of Technology (2014).

[Sch15a] M. Schlösser et al., *How To Make Raman-Inactive Helium Visible in Raman Spectra of Tritium-Helium Gas Mixtures*, Fusion Sci. Technol. **67**, 3 (2015) 559–562.

[Sch15b] M. Schlösser et al., *Raman spectroscopy at the Tritium Laboratory Karlsruhe*, Fusion Sci. Technol. **67** (2015) 555–558.

[Sch15c] M. Schlösser et al., *Relative Intensity Correction of Raman Systems with National Institute of Standards and Technology Standard Reference Material 2242 in 90°-Scattering Geometry*, Appl. Spectrosc. **69**, 5 (2015) 597–607.

[Sch16] K. Schönung, *Development of a Rear Wall for the KATRIN Rear Section and investigation of tritium compatibility of Rear Section components*, Ph.D. thesis, Karlsruhe Institute of Technology (2016).

[SDS15] SDSS Collaboration, S. Alam et al., *The eleventh and twelfth data releases of the Sloan Digital Sky Survey: final data from SDSS-III*, Astrophys. J. Suppl. Ser. **219**, 1 (2015) 12.

[Sem16a] Semrock, Inc., *532 nm RazorEdge Dichroic laser-flat beamsplitter, Part Number: LPD01-532RS-25*, Product specifications (2016), `https://www.semrock.com/FilterDetails.aspx?id=LPD01-532RS-25`, accessed: 08.02.2016.

[Sem16b] Semrock Inc., *532 nm RazorEdge ultrasteep long-pass edge filter (LP03-532RU-25)*, Product specifications (2016), `https://www.semrock.com/FilterDetails.aspx?id=LP03-532RU-25`, accessed: 03.05.2016.

[Sem16c] Semrock, Inc., *UV Raman Spectroscopy*, Laser & Optical Systems (2016), `https://www.semrock.com/uv-raman-spectroscopy.aspx`, accessed: 14.03.2016.

[Sha05] F. Sharipov et al., *Separation phenomena for gaseous mixture flowing through a long tube into vacuum*, Phys. Fluids **17**, 12 (2005) 1–8.

[Sha12] B. Sharma et al., *SERS: Materials, applications, and the future*, Mater. Today **15**, 1–2 (2012) 16–25.

[Sha13] J. Shannon, *Hollow Silica Waveguides for Mid-Infrared Power Transmission and Spectroscopy*, Polymicro Technologies, White Paper (2013), `http://www.photonics.com/images/Web/WhitePapers/496/White%20Paper-%20HSW%20Usage%20Molex.pdf`, accessed: 04.03.2016.

[Sis04] M. Sisti et al., *New limits from the Milano neutrino mass experiment with thermal microcalorimeters*, Nucl. Instrum. Methods Phys. Res., Sect. A **520**, 1 (2004) 125–131.

[Sei14] H. Seitz-Moskaliuk, *Investigation of metal capillaries for fluorescence reduction in a capillary Raman system for high-sensitivity gas analysis*, Master's thesis, Karlsruhe Institute of Technology (2014).

[Sme23] A. Smekal, *Zur Quantentheorie der Dispersion*, Naturwissenschaften **11** (1923) 873–875.

[Smi05] E. Smith et al., *Modern Raman spectroscopy: a practical approach*, Repr. with corr., Wiley, Chichester, UK (2005).

[SNO01] SNO Collaboration, Q. R. Ahmad et al., *Measurement of the Rate of* $\nu_e + d \rightarrow p + p + e^-$ *Interactions Produced by* ^8B *Solar Neutrinos at the Sudbury Neutrino Observatory*, Phys. Rev. Lett. **87**, 7 (2001) 071301.

[SNO02] SNO Collaboration, Q. R. Ahmad et al., *Direct Evidence for Neutrino Flavor Transformation from Neutral-Current Interactions in the Sudbury Neutrino Observatory*, Phys. Rev. Lett. **89** (2002) 011301.

[SNO16] SNO Collaboration, A. Bellerive et al., *The Sudbury Neutrino Observatory*, Nucl. Phys. B **908** (2016) 30–51.

[Sou86] P. C. Souers, *Hydrogen Properties for Fusion Energy*, University of California Press, Berkeley, CA, USA (1986).

[Stu10] M. Sturm, *Aufbau und Test des Inner-Loop-Systems der Tritiumquelle von KATRIN*, Ph.D. thesis, Karlsruhe Institute of Technology (2010).

[Sud58] E. C. G. Sudarshan et al., *Chirality Invariance and the Universal Fermi Interaction*, Phys. Rev. **109** (1958) 1860–1862.

[Sup98a] Super-Kamiokande Collaboration, Y. Fukuda et al., *Evidence for Oscillation of Atmospheric Neutrinos*, Phys. Rev. Lett. **81** (1998) 1562–1567.

[Sup98b] Super-Kamiokande Collaboration, Y. Fukuda et al., *Measurements of the solar neutrino flux from Super-Kamiokande's first 300 days*, Phys. Rev. Lett. **81**, 6 (1998) 1158.

[Sup13] Super-Kamiokande Collaboration, K. Abe et al., *Evidence for the appearance of atmospheric tau neutrinos in super-kamiokande*, Phys. rev. lett. **110**, 18 (2013) 181802.

[T2K15] T2K Collaboration, K. Abe et al., *Measurements of neutrino oscillation in appearance and disappearance channels by the T2K experiment with* $6.6 \cdot 10^{20}$ *protons on target*, Phys. Rev. D **91** (2015) 072010.

[Tay01] D. J. Taylor et al., *Enhanced Raman sensitivity using an actively stabilized external resonator*, Rev. Sci. Instrum. **72**, 4 (2001) 1970–1976.

[Tel07] H. H. Telle et al., *Laser Chemistry: Spectroscopy, Dynamics and Applications*, Wiley, Chichester, UK (2007).

[TEM14] TEM Messtechnik GmbH, *FiberLock: Automatic single-mode fiber coupling*, Data sheet (2014), `http://www.tem-messtechnik.de/index_htm_files/FL_Digital_FlyerWeb.pdf`, accessed: 08.03.2016.

[TEM15] TEM Messtechnik GmbH, *FiberLock: Actively Stabilized Fiber Coupling*, White Paper (2015), `http://www.tem-messtechnik.de/index_htm_files/fiberLockArticle.pdf`, accessed: 08.03.2016.

[Nob15] The Royal Swedish Academy of Sciences, *The Nobel Prize in Physics 2015*, Press release (2015), `http://www.nobelprize.org/nobel_prizes/physics/laureates/2015/press.html`, accessed: 19.04.2016.

[Tho14a] Thorlabs Inc., *Optical coatings: AR Coating*, Optical Tutorials (2014), `https://www.thorlabs.de/newgrouppage9.cfm?objectgroup_id=5840`, accessed: 18.02.2016.

[Tho14b] Thorlabs Inc., *Optical coatings: HR Coating*, Optical Tutorials (2014), `https://www.thorlabs.de/newgrouppage9.cfm?objectgroup_id=5840`, accessed: 23.02.2016.

[Tho16] Thorlabs Inc., *Nd:YAG Laser Mirror, 2nd Harmonic, NB1-K12*, Product specifications (2016), `http://www.thorlabs.de/newgrouppage9.cfm?objectgroup_id=3793`, accessed: 03.05.2016.

[Tol77] W. Tolles et al., *A Review of the Theory and Application of Coherent Anti-Stokes Raman Spectroscopy (CARS)*, Appl. Spectrosc. **31**, 4 (1977) 253–271.

[Tro11] Troitsk Collaboration, V. N. Aseev et al., *An upper limit on electron antineutrino mass from Troitsk experiment*, Phys. Rev. **D84** (2011) 112003.

[Uda92] T. Uda et al., *Hydrogen Isotope Exchange Reaction Rates in Tritium, Hydrogen and Deuterium Mixed Gases*, Radiochim. Acta **56** (1992) 209–214.

[Vac08] R. Vaccarone et al., *The design of a frequency multiplexed Ir-Au TES array*, J. Low Temp. Phys. **151**, 3-4 (2008) 921–926.

[Val10] K. Valerius, *The wire electrode system for the KATRIN main spectrometer*, Prog. Part. Nucl. Phys. **64**, 2 (2010) 291–293, neutrinos in Cosmology, in Astro, Particle and Nuclear Physics. International Workshop on Nuclear Physics, 31st course.

[Val11] K. Valerius et al., *Prototype of an angular-selective photoelectron calibration source for the KATRIN experiment*, J. Instrum. **6**, 01 (2011) P01002.

[Ves90] A. Vessieres et al., *Ultra-low-volume gold light-pipe cell for the IR analysis of dilute organic solutions*, Appl. Spectrosc. **44**, 6 (1990) 1092–1094.

[Wal72] G. Walrafen et al., *Intensification of spontaneous Raman spectra by use of liquid core optical fibers*, Appl. Spectrosc. **26**, 6 (1972) 585–589.

[Wal82] G. E. Walrafen et al., *Model analysis of the Raman spectrum from fused silica optical fibers*, Appl. Opt. **21**, 3 (1982) 359–360.

[Wei03] C. Weinheimer, *Laboratory Limits on Neutrino Masses*, in K. Winter et al., editors, *Neutrino Mass*, volume 190 of *Springer Tracts in Modern Physics*, Springer, Berlin/Heidelberg, Germany (2003), pp. 25–52.

[Wey42] W. A. Weyl, *Fluorescence of Glass*, Ind. Eng. Chem. **34**, 9 (1942) 1035–1041.

[Wil87] J. F. Wilkerson et al., *Limit on ν_e Mass from Free-Molecular-Tritium Beta Decay*, Phys. Ref. Lett. **58** (1987) 2023–2026.

[Yan13] X. Yang et al., *High sensitivity gas sensing by Raman spectroscopy in photonic crystal fiber*, Sens. Actuators, B **176** (2013) 64–68.

[Zub12] K. Zuber, *Neutrino physics*, Series in high energy physics, cosmology, and gravitation, CRC Press, Boca Raton, FL, USA, 2nd edition (2012).

Danksagung

Diese Arbeit wäre ohne die Unterstützung vieler Personen nicht möglich gewesen. Ich möchte mich bei all jenen bedanken, die mich während meiner Promotion begleitet und zum Gelingen der Arbeit beigetragen haben.

Ein herzliches Dankeschön gilt zunächst meinen Betreuern:

Prof. Dr. Guido Drexlin danke ich für die Gelegenheit, meine Doktorarbeit im Rahmen eines so spannenden Projekts wie des KATRIN-Experiments durchführen zu können.

Prof. Dr. Helmut H. Telle möchte ich herzlich danken für die Betreuung meiner Arbeit über Ländergrenzen hinweg sowie für viele hilfreiche Anregungen, gute Tipps und natürlich die unschätzbare Tellerisierung von Paper-Texten.

Dr. Beate Bornschein danke ich für ihre stets offene Tür ebenso wie für ihre Förderung des wissenschaftlichen Nachwuchses und die vielen Weiterbildungsmöglichkeiten.

Ebenfalls herzlich danken möchte ich der gesamten Laser-Raman-Gruppe für die gute Zusammenarbeit, die hilfreichen Diskussionen und das tolle Arbeitsklima, insbesondere Beate Bornschein, Tim Brunst, Sebastian Fischer, Timothy James, Andreas Off, Magnus Schlösser, Hendrik Seitz-Moskaliuk, Michael Sturm und Helmut Telle.

Ganz besonders danken möchte ich Sebastian Fischer: einerseits für seine stete Hilfsbereitschaft und Unterstützung auf fachlicher Seite, aber auch dafür, dass er in schwierigen Zeiten immer ein offenes Ohr, Zeit und aufbauende Worte parat hatte.

Furthermore, I'd like to thank Tim James for the fruitful collaboration in hollow waveguide matters, many helpful discussions and interesting insights into the English language.

Magnus Schlösser danke ich sehr herzlich für seine hervorragende Unterstützung noch über Diplomarbeitszeiten hinaus und sein großes persönliches Engagement auf fachlicher wie menschlicher Ebene.

Ein großer Dank gebührt zudem meinen Bachelor- und Masterstudenten Tim Brunst, Hendrik Seitz-Moskaliuk und Andreas Off für die tolle Zusammenarbeit und ihren Einsatz, mit dem sie maßgeblich zu meiner Arbeit beigetragen haben.

Michael Sturm danke ich für seine Hilfsbereitschaft und Unterstützung in vielen Fragen.

Auch den Kollegen von der TApIR-Gruppe, insbesondere Robin Größle und Sebastian Mirz, möchte ich für ihre Diskussionsbereitschaft und die gute Zusammenarbeit danken.

Von technischer Seite her bin ich einer ganzen Reihe von Leuten zu großem Dank verpflichtet.

Ganz besonders herzlich möchte ich Dieter Adami danken, der mir in der Werkstatt viel beigebracht und noch mehr in Windeseile selbst gefertigt, repariert, weichgeglüht, gekürzt oder zusammengeschweißt hat, wenn mein System mal wieder nicht so laufen wollte, wie es sollte.

Aber auch ohne die folgenden Personen und ihren vielfältigen Einsatz beim Schweißen, Fräsen oder Polieren sowie ihre Unterstützung in technischen Fragen wäre die vorliegende Arbeit nicht möglich gewesen: Klaus Mehret, Nancy Tuchscherer, Florian Priester, Marco Röllig, Witalij Hinz, Stefan Welte, Adalbert Braun, Manfred Göckel und Norbert Kernert. Ihnen allen möchte ich meinen herzlichen Dank aussprechen.

Der CAPER-Gruppe, insbesondere Thanh-Long Le und Eleonore Fanghänel, danke ich zudem für die Bereitstellung und Analyse von Tritium-Gasmischungen.

Bernhard Heinle möchte ich gerne danken für seine große Sorgfalt im Strahlenschutz, die einen immer mit gutem Gefühl im Labor arbeiten lässt, und seine unkomplizierte Unterstützung beim Umgang mit Tritium.

Auch möchte ich den Mitgliedern der Infrastruktur-, Betriebs- sowie der Mess- und Regelungsgruppe danken, die experimentelles Arbeiten am TLK erst ermöglichen. Ich danke Dr. Uwe Besserer, Dirk Osenberg und Dr. Jürgen Wendel für ihre Unterstützung in verschiedenen Fragen.

Eva Porter und Sylvia Krieger danke ich sehr herzlich für ihre Hilfe in administrativen Angelegenheiten.

Der Graduiertenschule KSETA danke ich für die Finanzierung meiner Arbeit und das interessante Seminarangebot.

Für ihre Mühe danke ich herzlich den Korrekturlesern dieser Arbeit: Helmut Telle, Sebastian Fischer, Robin Größle, Hendrik Seitz-Moskaliuk, Magnus Schlösser, Michael Sturm, Simon Niemes, Beate Bornschein.

Meinen wechselnden Büro-Kollegen danke ich sehr für die stets gute Arbeitsatmosphäre und die lustige gemeinsame Zeit: Tim Brunst, Bennet Krasch, Andreas Off, Oskari Paskari, Hendrik Seitz-Moskaliuk und Sebastian Wozniewski.

Auch danke ich meinen Mitdoktoranden und den anderen DiDoBaMaNaWis bei KATRIN, EDELWEISS und am ITEP für die schöne Zeit und die gemeinsamen Erlebnisse.

Allen Mitarbeitern am TLK möchte ich herzlich danken für das angenehme Arbeitsklima und die große Hilfsbereitschaft.

Zu guter Letzt möchte ich besonders herzlich meiner Familie und meinem Freund Philip danken, die mich immer in jeder Hinsicht unterstützt haben und auch in den stressigsten Phasen an meiner Seite standen.